

**DECONVOLUTION OF ION VELOCITY
DISTRIBUTIONS FROM LASER-INDUCED
FLUORESCENCE SPECTRA OF XENON
ELECTROSTATIC THRUSTER PLUMES**

by

Timothy B. Smith

A dissertation submitted in partial fulfillment
of the requirements for the degree of
Doctor of Philosophy
(Aerospace Engineering)
in The University of Michigan
2003

Doctoral Committee:

Associate Professor Alec D. Gallimore, Chair
Professor R. Paul Drake
Professor Iain D. Boyd
Dr. George J. Williams Jr., NASA Glenn Research Center

© Timothy B. Smith 2003
All Rights Reserved

To Ruth H. Smith (1924-1996),
Who proved “It can’t be done that way”
was wrong. Repeatedly.

“Is that the comet?” he whispered.

“Yes,” said the professor.

“But it’s not moving at all,” said Sniff in a puzzled voice. “And I don’t see any tail either.”

“Its tail is behind,” explained the professor. “It is rushing straight *towards* the earth, that’s why it doesn’t look as if it’s moving. But you can see that it gets bigger every day.”

“When will it arrive?” asked Sniff, staring in fascinated curiosity at the little red spark through the telescope.

“According to my reckoning it should hit the earth on the seventh of October at 8.42 p.m. Possibly four seconds earlier,” said the professor.

“And what will happen then?” asked Sniff.

“What will happen?” said the professor in surprise. “Well, I hadn’t thought about that. But I shall record the events in great detail, you may be sure.”

– Tove Jansson, *Comet in Moominland*, New York: Avon, 1976, p. 92.

ACKNOWLEDGEMENTS

No research is performed in a vacuum. This is especially true in vacuum research. Billions of atoms per cubic centimeter bounce around in our high-vacuum systems, with frequent interactions with their confines. The research summarized in this thesis has similarly resulted in frequent collisions with the limits of my knowledge, and occasionally with the boundaries of our field; as we all learned in thermodynamics, the expansion of these boundaries under pressure requires real work. These atoms also undergo less-frequent, but often more significant, interactions with their companions. Likewise, interactions with my professors, fellow students, departmental technicians and secretaries over the last six years could less often be described as collisions, and the information exchange was usually beneficial to all concerned.

First of all, I would like to thank my advisors, Professors Alec Gallimore and Paul Drake, for their unwavering support—intellectual, professional, personal and financial. Alec has not only built PEPL up from an abandoned vacuum tank and empty high bay to the top tier of academic labs for electric propulsion research, but has also fostered a sense of camaraderie and community among his students. Furthermore, his patience with the glacial progress typical in laser diagnostics has been exemplary. Professor Drake was gracious enough to take in an unusually-old first-year graduate student and introduce him to the world of experimental plasma physics. In the years since I transferred to PEPL, he has regularly taken time to meet, discuss my research, and point out both flaws and opportunities with amazing speed and acuity.

I would also like to thank the other members of my committee, Professor Iain Boyd and Dr. George Williams, for their guidance. The departmental technicians (Dave, Tom and Mike) and machinist (Terry) all contributed in their unique fashion, while we all know that the department would grind to a halt without our secretaries (Margaret, Sharon and Suzanne).

My fellow students at PEPL have gracefully put up with me for four years now. The past masters (and doctorates), who showed me the ropes in this new field, include Colleen, Matt, Farnk, Jimmy, and especially George—here’s your chance to avenge years of snide comments about rough-sawn Unistrut, “high-precision” alignment of monochromators and the magic Fluke. Dan has been a solid coauthor, while he and the rest of the grad students (Peter, Rich, Brian, Mitchell and Allen) have patiently listened to my ramblings, pointed out what valve I forgot to turn, and helped me figure out what was wrong with the power supplies this time. Finally, I can’t forget the undergrads (Kathryn, Yoshi, Rafael and Josh), though it might have seemed like I did at the time; they did a lot of work, and might even have learned something in the process.

Love and thanks to Dad, who financed many years of primary and secondary education with little apparent return. Thanks, also, to Len and Gail, who raised a wonderful daughter and have spent many afternoons and evenings looking after a cranky baby while I was busy.

Finally, I simply must thank Sarah for putting up with me over the last six years—I’m looking forward to a few score like those, but perhaps with a little better income—and for giving us Alexander, who’s exactly the boy we asked for. (And a good thing too, since we didn’t keep the receipt.)

And Mom, wherever you are: I hope the craftsmanship approaches your standards.

PREFACE

This thesis presents a method for extracting singly-ionized xenon (Xe II) velocity distribution estimates from single-point laser-induced fluorescence (LIF) spectra at 605.1 nm. Unlike currently-popular curve-fitting methods for extracting bulk velocity and temperature data from LIF spectra, this method makes no assumptions about the velocity distribution, and thus remains valid for non-equilibrium and counterstreaming plasmas.

The well-established hyperfine structure and lifetime of the $5d^4D_{7/2} - 6p^4P_{5/2}^0$ transition of Xe II provide the computational basis for a Fourier-transform deconvolution. Computational studies of three candidate deconvolution methods show that, in the absence of *a priori* knowledge of the power spectra of the velocity distribution and noise function, a Gaussian inverse filter provides an optimal balance between noise amplification and filter broadening.

Deconvolution of axial-injection and multiplex LIF spectra from the P5 Hall thruster plume yields near-field and far-field axial velocity distributions. Near-field LIF spectra provide velocity distributions that cannot be measured by probe-based methods, while far-field LIF spectra provide a basis for comparison with mass spectrometer data. Transforming far-field ion axial velocity distributions to an ion energy basis reproduces all Xe II features found in mass spectrometer data taken at the same location and conditions. Axial profiles of ion axial velocity show a zone of increasing velocity extending 20 cm downstream of the thruster exit plane, with decreasing velocity from 20 to 50 cm, and demonstrate repeatabilities within 2%. Vertical-beam LIF reveals unexpectedly strong in-

teractions between counterflowing streams in the inward divergence region at the thruster centerline.

Deconvolution of multiplex LIF spectra taken from the FMT-2 ion engine plume provides beamwise velocity distributions from 1.4 mm to 30 cm. Axial profiles of axial velocity fail to disclose the location of the neutralization plane, while radial sweeps of axial velocity show no discernable trend. Radial profiles of radial velocity show increasing divergence with radial position.

TABLE OF CONTENTS

DEDICATION	ii
ACKNOWLEDGEMENTS	iv
PREFACE	vi
LIST OF FIGURES	ix
LIST OF TABLES	x
NOMENCLATURE	xi
CHAPTER	
I. INTRODUCTION	1
1.1 Problem statement	1
1.1.1 Laser-induced fluorescence	2
1.1.2 The curve-fitting analysis method	3
1.1.3 Limitations of Cedolin's method	3
1.2 Aim	5
1.3 Organization	5
II. ELECTRIC PROPULSION	7
2.1 Historical background	7
2.2 Advantages of electric propulsion	9
2.2.1 The rocket equation	9
2.2.2 Performance parameters	11
2.3 Electrostatic thrusters	13
2.3.1 Hall thrusters	14
2.3.2 Ion engines	18
2.4 Kinematic compression	20
2.5 Summary	23
III. FOURIER-TRANSFORM DECONVOLUTION	24

3.1	Convolution	25
3.1.1	Definition and properties	25
3.1.2	Fourier transforms	25
3.1.3	Convolution theorem	30
3.2	Deconvolution	30
3.2.1	Simple inverse filter	31
3.2.2	Rectangular inverse filter	32
3.2.3	Gaussian inverse filter	33
3.2.4	Wiener filter	33
3.2.5	Constraints	34
3.3	Benchmarking	35
3.4	Summary	37
IV. LASER-INDUCED FLUORESCENCE OF XE II		38
4.1	Historical background	38
4.2	Xe II spectroscopy	40
4.2.1	Lines for Xe II LIF	41
4.3	LIF line model	42
4.3.1	Two-level model	43
4.3.2	Four-level model	47
4.3.3	Line shape	49
4.4	Hyperfine structure at 605.1 nm	49
4.4.1	Isotopic splitting	50
4.4.2	Nuclear-spin splitting	51
4.4.3	Hyperfine line intensity	52
4.5	Line broadening	53
4.5.1	Natural broadening	53
4.5.2	Doppler shift and broadening	56
4.5.3	Saturation broadening	58
4.6	Summary	60
V. COMPUTATIONAL METHODS		62
5.1	Noise analysis of LIF spectra	63
5.1.1	Reference cell	63
5.1.2	P5 plume	67
5.2	Deconvolution	69
5.2.1	Simple inverse filter	70
5.2.2	Rectangular inverse filter	73
5.2.3	Gaussian inverse filter	78
5.3	Summary	80

VI. EXPERIMENTAL APPARATUS AND METHODS	82
6.1 Facility	82
6.2 Thrusters	84
6.2.1 UM/AFRL P5 Hall thruster	84
6.2.2 NASA FMT-2 ion engine	87
6.3 Beam-injection schemes	88
6.3.1 Off-axis multiplex	88
6.3.2 Axial-injection	92
6.4 External optics	92
6.4.1 Laser	92
6.4.2 Beam-handling	93
6.5 LVTF optics	95
6.5.1 Off-axis multiplex	95
6.5.2 Axial-injection	97
6.6 LIF collection	98
VII. P5 PLUME LIF	100
7.1 Axial-injection LIF of P5 plume	100
7.1.1 Axial sweep along discharge centerline	102
7.1.2 Lateral sweep across discharge	111
7.1.3 Axial sweep along thruster centerline	117
7.2 Multiplex LIF of P5 plume	123
7.2.1 3 kW condition	124
7.2.2 Test condition 9	128
7.2.3 Test condition 10	135
7.2.4 Test condition 1	140
7.2.5 Test condition 2	144
7.3 Discussion	147
7.4 Summary	151
VIII. FMT-2 PLUME LIF	153
8.1 Multiplex LIF of FMT plume	153
8.1.1 TH15 without neutralizer	154
8.1.2 TH19 without neutralizer	158
8.1.3 TH15 with neutralizer	161
8.1.4 TH19 with neutralizer	165
8.2 Summary	170
IX. CONCLUSIONS AND FUTURE WORK	171
9.1 Deconvolution	171

9.2	P5 Hall thruster	172
9.3	FMT-2 ion engine	173
9.4	Future work	173
APPENDICES		177
BIBLIOGRAPHY		253

LIST OF FIGURES

Figure

1.1	Radial LIF at P5 Hall thruster centerline. Dashed line is a curve-fit to the left peak by Cedolin's method.	4
2.1	Hall thruster schematic.	15
2.2	Ion engine schematic.	18
2.3	Kinematic distortion of an initially-Maxwellian distribution ($T = 10^4$ K, $u_0 = 4$ km/s) by electrostatic acceleration ($U = 1100$ V).	22
3.1	Fourier transform pairs.	29
3.2	Positivity forcing function examples for $\epsilon = [10^{-3}, 10^{-2}, 10^{-1}, 10^0]$	35
4.1	Partial Grotrian diagram for Xe II metastable lines [74].	41
4.2	Two-level model for laser absorption, line emission and quenching.	43
4.3	Upper state population fraction N_2/N_1^0 as a function of the dimensionless saturation parameter $S(\nu) = I_\nu/I_s(\nu)$	46
4.4	Four-level model for laser absorption, line emission, collisional excitation and quenching.	47
4.5	Fine and hyperfine structure of Xe II LIF.	52
4.6	Hyperfine splitting $h(\nu)$ for the Xe II $5d^4 D_{7/2} - 6p^4 P_{5/2}^0$ line.	53
4.7	Cold-plasma spectrum $c(\nu)$ for the Xe II $5d^4 D_{7/2} - 6p^4 P_{5/2}^0$ line.	56
4.8	Warm-plasma spectrum $w(\nu)$ for the Xe II $5d^4 D_{7/2} - 6p^4 P_{5/2}^0$ line, $T = 600$ K.	58

4.9	Minimum saturation intensity $I_s(\nu)$ as a function of temperature for the simple two-level model of Eqn. ??	59
5.1	Reference cell LIF spectra.	64
5.2	Signal-to-noise ratio for reference cell LIF spectra.	65
5.3	Noise power $\phi_n(\tau)$ for reference cell LIF spectra.	66
5.4	P5 LIF spectra, 10 cm downstream of discharge channel, 1.6 kW.	68
5.5	Signal-to-noise ratio for P5 LIF spectra.	69
5.6	Noise power $\phi_n(\tau)$ for P5 LIF spectra.	69
5.7	Cold-plasma spectrum and transform (computational kernel).	70
5.8	Velocity distribution estimate $\hat{f}(v_k)$ for warm-plasma (600 K) spectrum, deconvolved by the simple inverse filter.	72
5.9	Noise amplification factor as a function of signal-to-noise ratio for simple inverse filter deconvolution of a warm-plasma (600 K) spectrum.	73
5.10	Velocity distribution estimate $\hat{f}(v_k)$ for warm-plasma (600 K) spectrum, SNR = 100, deconvolved by the rectangular inverse filter.	74
5.11	Noise amplification factor as a function of filter bandwidth for rectangular inverse filter transform deconvolution of a warm-plasma (600 K) spectrum, SNR = 33.	75
5.12	Line broadening as a function of filter bandwidth for the rectangular inverse filter.	77
5.13	Velocity distribution estimate $\hat{f}(v_k)$ for warm-plasma (600 K) spectrum, SNR = 100, deconvolved by the Gaussian inverse filter transform.	78
5.14	Noise amplification factor as a function of filter bandwidth for Gaussian inverse filter transform deconvolution of a warm-plasma (600 K) spectrum, SNR = 33.	79
5.15	Line broadening as a function of filter bandwidth for the Gaussian inverse filter.	80
6.1	Photograph of the P5 Hall thruster.	85

6.2	Dimensioned half-section of the P5 Hall thruster.	85
6.3	Photograph of the FMT-2 ion thruster.	87
6.4	Beam and thruster orthogonal axes for the off-axis multiplex technique.	89
6.5	Beam and thruster orthogonal axes for the off-axis multiplex technique.	92
6.6	Laser division and modulation.	93
6.7	Typical velocity distribution estimate $\hat{f}(v)$ from stationary plasma in a xenon opto-galvanic cell	94
6.8	Multiplex laser beam delivery and fluorescence collection optics schematic, looking upstream (north) from behind thruster.	95
6.9	Axial-injection and LIF collection optics, looking upstream (north) from behind thruster.	97
6.10	Axial-injection periscope, looking west.	98
7.1	Coordinate grid for P5 LIF experiments, looking down.	101
7.2	Deconvolved $f(v_x)$ (solid) & curve-fit (dashed) at $(x, y) = (50, 7.37)$ cm.	102
7.3	Deconvolved $f(v_x)$ (solid) & curve-fit (dashed) at $(x, y) = (20, 7.37)$ cm.	102
7.4	Deconvolved $f(v_x)$ (solid) & curve-fit (dashed) at $(x, y) = (10, 7.37)$ cm.	103
7.5	Deconvolved $f(v_x)$ (solid) & curve-fit (dashed) at $(x, y) = (5.0, 7.37)$ cm.	103
7.6	Deconvolved $f(v_x)$ (solid) & curve-fit (dashed) at $(x, y) = (2.0, 7.37)$ cm.	104
7.7	Deconvolved $f(v_x)$ (solid) & curve-fit (dashed) at $(x, y) = (1.0, 7.37)$ cm.	104
7.8	Deconvolved $f(v_x)$ (solid) & curve-fit (dashed) at $(x, y) = (0.5, 7.37)$ cm.	105
7.9	Deconvolved $f(v_x)$ (solid) & curve-fit (dashed) at $(x, y) = (0.2, 7.37)$ cm.	105
7.10	Deconvolved $f(v_x)$ (solid) & curve-fit (dashed) at $(x, y) = (0.1, 7.37)$ cm.	106
7.11	Deconvolved $f(v_x)$ (solid) & curve-fit (dashed) at $(x, y) = (0.05, 7.37)$ cm.	106

7.12	Averaged, twin-peaked distribution at 1.6 kW, $(x, y) = (20., 7.37)$ cm.	107
7.13	Axial ion velocity vs. axial position along P5 discharge centerline ($y = 7.37$ cm).	107
7.14	Axial ion energy vs. axial position along P5 discharge centerline ($y = 7.37$ cm).	109
7.15	Axial ion temperature vs. axial position along P5 discharge centerline ($y = 7.37$ cm). Dashed line shows predicted kinematic compression.	110
7.16	Deconvolved $f(v_x)$ (solid) & curve-fit (dashed) at $(x, y) = (0.1, 6.37)$ cm.	111
7.17	Deconvolved $f(v_x)$ (solid) & curve-fit (dashed) at $(x, y) = (0.1, 6.62)$ cm.	111
7.18	Deconvolved $f(v_x)$ (solid) & curve-fit (dashed) at $(x, y) = (0.1, 6.87)$ cm.	112
7.19	Deconvolved $f(v_x)$ (solid) & curve-fit (dashed) at $(x, y) = (0.1, 7.12)$ cm.	112
7.20	Deconvolved $f(v_x)$ (solid) & curve-fit (dashed) at $(x, y) = (0.1, 7.37)$ cm.	113
7.21	Deconvolved $f(v_x)$ (solid) & curve-fit (dashed) at $(x, y) = (0.1, 7.62)$ cm.	113
7.22	Deconvolved $f(v_x)$ (solid) & curve-fit (dashed) at $(x, y) = (0.1, 7.87)$ cm.	114
7.23	Deconvolved $f(v_x)$ (solid) & curve-fit (dashed) at $(x, y) = (0.1, 8.12)$ cm.	114
7.24	Deconvolved $f(v_x)$ (solid) & curve-fit (dashed) at $(x, y) = (0.1, 8.37)$ cm.	115
7.25	Axial ion velocity vs. lateral position 1 mm downstream of P5 discharge ($x = 0.1$ cm).	117
7.26	Axial ion temperature vs. lateral position 1 mm downstream of P5 discharge ($x = 0.1$ cm).	118
7.27	Deconvolved $f(v_x)$ (solid) & curve-fit (dashed) at $(x, y) = (50, 0)$ cm.	118
7.28	Deconvolved $f(v_x)$ (solid) & curve-fit (dashed) at $(x, y) = (40, 0)$ cm.	119
7.29	Deconvolved $f(v_x)$ (solid) & curve-fit (dashed) at $(x, y) = (30, 0)$ cm.	119
7.30	Deconvolved $f(v_x)$ (solid) & curve-fit (dashed) at $(x, y) = (20, 0)$ cm.	120

7.31	Deconvolved $f(v_x)$ (solid) & curve-fit (dashed) at $(x, y) = (10, 0)$ cm.	120
7.32	Axial ion velocity vs. axial position along P5 centerline ($y = 0$ cm).	122
7.33	Axial ion temperature vs. axial position along P5 centerline ($y = 0$ cm).	122
7.34	Axial ion velocity & energy vs. radial position at $x = 10.01$ cm for 3kW.	125
7.35	Radial & vertical ion velocity vs. radial position at $x = 10.01$ cm for 3kW.	126
7.36	Axial, radial and vertical temperatures vs. radial position at $x = 10.01$ cm for 3kW.	127
7.37	Axial ion velocity & energy vs. radial position at $x = 50.02$ cm for TC9.	128
7.38	Axial ion velocity & energy vs. radial position at $x = 63.14$ cm for TC9.	129
7.39	Axial ion velocity & energy vs. radial position at $x = 75.00$ cm for TC9.	129
7.40	Radial & vertical ion velocity vs. radial position at $x = 50.02$ cm for TC9.	129
7.41	Axial, radial and vertical temperatures vs. radial position at $x = 50.02$ cm for TC9.	132
7.42	Radial & vertical ion velocity vs. radial position at $x = 63.14$ cm for TC9.	132
7.43	Axial, radial and vertical temperatures vs. radial position at $x = 63.14$ cm for TC9.	133
7.44	Radial & vertical ion velocity vs. radial position at $x = 75.00$ cm for TC9.	133
7.45	Axial, radial and vertical temperatures vs. radial position at $x = 75.00$ cm for TC9.	134
7.46	Axial ion velocity & energy vs. radial position at $x = 63.14$ cm for TC 10.	135
7.47	Axial ion velocity & energy vs. radial position at $x = 75.00$ cm for TC 10.	136
7.48	Radial & vertical ion velocity vs. radial position at $x = 63.14$ cm for TC 10.	136
7.49	Radial & vertical ion velocity vs. radial position at $x = 75.00$ cm for TC 10.	137

7.50	Axial, radial and vertical temperatures vs. radial position at $x = 63.14$ cm for TC 10.	138
7.51	Axial, radial and vertical temperatures vs. radial position at $x = 75.00$ cm for TC 10.	139
7.52	Axial ion velocity & energy vs. radial position at $x = 63.14$ cm for TC 1.	140
7.53	Radial & vertical ion velocity vs. radial position at $x = 63.14$ cm for TC 1.	141
7.54	Axial, radial and vertical temperatures vs. radial position at $x = 63.14$ cm for TC 1.	142
7.55	Axial ion velocity & energy vs. radial position at $x = 63.14$ cm for TC 2.	144
7.56	Radial & vertical ion velocity vs. radial position at $x = 63.14$ cm for TC 2.	145
7.57	Axial, radial and vertical temperatures vs. radial position at $x = 63.14$ cm for TC 2.	146
7.58	Two-dimensional velocity distribution $f(v_x, v_z)$ downstream of P5 centerline, normalized so $f \leq 1.0$. Contour lines are at $f = [0.1, 0.2, \dots 0.9]$.	149
7.59	Ion energy distributions at 1.6 kW, $(x, y) = (10., 7.37)$ cm.	151
8.1	Axial ion velocity & energy vs. radial position at $x = 0.140$ cm for unneutralized TH15.	156
8.2	Radial & vertical ion velocity vs. radial position at $x = 0.140$ cm for unneutralized TH15.	156
8.3	Axial ion velocity & energy vs. radial position at $x = 5.017$ cm for unneutralized TH15.	158
8.4	Radial & vertical ion velocity vs. radial position at $x = 5.017$ cm for unneutralized TH15.	158
8.5	Axial ion velocity & energy vs. radial position at $x = 5.090$ cm for unneutralized TH19.	161
8.6	Radial & vertical ion velocity vs. radial position at $x = 5.090$ cm for unneutralized TH19.	161

8.7	Axial ion velocity & energy vs. axial position at $y = 0.000$ cm for neutralized TH15.	164
8.8	Radial & vertical ion velocity vs. axial position at $y = 0.000$ cm for neutralized TH15.	164
8.9	Axial ion velocity & energy vs. radial position at $x = 5.100$ cm for neutralized TH19.	167
8.10	Radial & vertical ion velocity vs. radial position at $x = 5.100$ cm for neutralized TH19.	167
8.11	Axial ion velocity & energy vs. radial position at $x = 0.142$ cm for neutralized TH19.	169
8.12	Radial & vertical ion velocity vs. radial position at $x = 0.142$ cm for neutralized TH19.	169
A.1	Unsaturated (solid curve) and saturation-broadened warm-plasma spectra (dashed curves for βP_L values of $10^0, 10^1, 10^2, 10^3, 10^4$ and 10^5 MHz) for the Xe II $5d^4 D_{7/2} - 6p^4 P_{5/2}^0$ line, $T = 600$ K.	183
A.2	Desaturation example for lightly-saturated ($\beta P_L = 10^3$ MHz) warm-plasma (600 K) spectrum with SNR = 33.	186
A.3	Desaturation example for moderately-saturated ($\beta P_L = 10^4$ MHz) warm-plasma (600 K) spectrum SNR = 33.	186
A.4	Desaturation example for heavily-saturated ($\beta P_L = 3 \times 10^4$ MHz) warm-plasma (600 K) spectrum with SNR = 33.	187
A.5	Desaturation noise amplification factor as a function of saturation βP_L for SNR = 100 (solid curve), 33, 10 and 3.3 (dashed curves).	188
B.1	Deconvolved $f(v_k)$ & curve-fit at 3 kW, $(x, y) = (10.01, 0.00)$ cm (3kwa).	189
B.2	Deconvolved $f(v_k)$ & curve-fit at 3 kW, $(x, y) = (10.01, 6.37)$ cm (3kwb).	190
B.3	Deconvolved $f(v_k)$ & curve-fit at 3 kW, $(x, y) = (10.01, 7.37)$ cm (3kwc).	190
B.4	Deconvolved $f(v_k)$ & curve-fit at 3 kW, $(x, y) = (10.01, 8.37)$ cm (3kwd).	191
B.5	Deconvolved $f(v_k)$ & curve-fit at 3 kW, $(x, y) = (50.02, 0.00)$ cm (3kwe).	191

B.6	Deconvolved $f(v_k)$ & curve-fit at TC 9, $(x, y) = (50.02, 0.00)$ cm (tc9a).	192
B.7	Deconvolved $f(v_k)$ & curve-fit at TC 9, $(x, y) = (50.02, -1.00)$ cm (tc9b).	193
B.8	Deconvolved $f(v_k)$ & curve-fit at TC 9, $(x, y) = (50.02, 1.00)$ cm (tc9c).	193
B.9	Deconvolved $f(v_k)$ & curve-fit, TC 9, $(x, y) = (50.02, 2.00)$ cm (tc9d).	194
B.10	Deconvolved $f(v_k)$ & curve-fit, TC 9, $(x, y) = (50.02, -2.00)$ cm (tc9e).	194
B.11	Deconvolved $f(v_k)$ & curve-fit, TC 9, $(x, y) = (50.02, -5.00)$ cm (tc9f).	195
B.12	Deconvolved $f(v_k)$ & curve-fit, TC 9, $(x, y) = (50.02, 5.00)$ cm (tc9g).	195
B.13	Deconvolved $f(v_k)$ & curve-fit, TC 9, $(x, y) = (63.14, 0.00)$ cm (tc9h).	196
B.14	Deconvolved $f(v_k)$ & curve-fit, TC 9, $(x, y) = (63.14, -1.00)$ cm (tc9i).	196
B.15	Deconvolved $f(v_k)$ & curve-fit, TC 9, $(x, y) = (63.14, 1.00)$ cm (tc9j).	197
B.16	Deconvolved $f(v_k)$ & curve-fit, TC 9, $(x, y) = (63.14, 2.00)$ cm (tc9k).	197
B.17	Deconvolved $f(v_k)$ & curve-fit, TC 9, $(x, y) = (63.14, -2.00)$ cm (tc9l).	198
B.18	Deconvolved $f(v_k)$ & curve-fit, TC 9, $(x, y) = (63.14, -5.00)$ cm (tc9m).	198
B.19	Deconvolved $f(v_k)$ & curve-fit, TC 9, $(x, y) = (63.14, 5.00)$ cm (tc9n).	199
B.20	Deconvolved $f(v_k)$ & curve-fit, TC 9, $(x, y) = (75.00, 0.00)$ cm (tc9o).	199
B.21	Deconvolved $f(v_k)$ & curve-fit, TC 9, $(x, y) = (75.00, 1.00)$ cm (tc9p).	200
B.22	Deconvolved $f(v_k)$ & curve-fit, TC 9, $(x, y) = (75.00, -1.00)$ cm (tc9q).	200
B.23	Deconvolved $f(v_k)$ & curve-fit, TC 9, $(x, y) = (75.00, -2.00)$ cm (tc9r).	201
B.24	Deconvolved $f(v_k)$ & curve-fit, TC 9, $(x, y) = (75.00, 2.00)$ cm (tc9s).	201
B.25	Deconvolved $f(v_k)$ & curve-fit, TC 9, $(x, y) = (75.00, 5.00)$ cm (tc9t).	202
B.26	Deconvolved $f(v_k)$ & curve-fit, TC 9, $(x, y) = (75.00, -5.00)$ cm (tc9u).	202
B.27	Deconvolved $f(v_k)$ & curve-fit, TC 10, $(x, y) = (63.14, 0.00)$ cm (tc10a).	203

B.28	Deconvolved $f(v_k)$ & fit, TC 10, $(x, y) = (63.14, -1.00)$ cm (tc10b). . .	204
B.29	Deconvolved $f(v_k)$ & curve-fit, TC 10, $(x, y) = (63.14, 1.00)$ cm (tc10c).	204
B.30	Deconvolved $f(v_k)$ & curve-fit, TC 10, $(x, y) = (63.14, 2.00)$ cm (tc10d).	205
B.31	Deconvolved $f(v_k)$ & fit, TC 10, $(x, y) = (63.14, -2.00)$ cm (tc10e). . .	205
B.32	Deconvolved $f(v_k)$ & fit, TC 10, $(x, y) = (63.14, -5.00)$ cm (tc10f). . .	206
B.33	Deconvolved $f(v_k)$ & curve-fit, TC 10, $(x, y) = (63.14, 5.00)$ cm (tc10g).	206
B.34	Deconvolved $f(v_k)$ & curve-fit, TC 10, $(x, y) = (75.00, 0.00)$ cm (tc10h).	207
B.35	Deconvolved $f(v_k)$ & curve-fit, TC 10, $(x, y) = (75.00, 1.00)$ cm (tc10i).	207
B.36	Deconvolved $f(v_k)$ & fit, TC 10, $(x, y) = (75.00, -1.00)$ cm (tc10j). . .	208
B.37	Deconvolved $f(v_k)$ & fit, TC 10, $(x, y) = (75.00, -2.00)$ cm (tc10k). . .	208
B.38	Deconvolved $f(v_k)$ & curve-fit, TC 10, $(x, y) = (75.00, 2.00)$ cm (tc10l).	209
B.39	Deconvolved $f(v_k)$ & curve-fit, TC 10, $(x, y) = (75.00, 5.00)$ cm (tc10m).	209
B.40	Deconvolved $f(v_k)$ & curve-fit, TC 10, $(x, y) = (75.00, -5.00)$ cm (tc10n).	210
B.41	Deconvolved $f(v_k)$ & curve-fit at TC 1, $(x, y) = (63.14, 0.00)$ cm (tc01a).	211
B.42	Deconvolved $f(v_k)$ & fit at TC 1, $(x, y) = (63.14, -1.00)$ cm (tc01b). . .	212
B.43	Deconvolved $f(v_k)$ & curve-fit at TC 1, $(x, y) = (63.14, 1.00)$ cm (tc01c).	212
B.44	Deconvolved $f(v_k)$ & curve-fit at TC 1, $(x, y) = (63.14, 2.00)$ cm (tc01d).	213
B.45	Deconvolved $f(v_k)$ & fit at TC 1, $(x, y) = (63.14, -2.00)$ cm (tc01e). . .	213
B.46	Deconvolved $f(v_k)$ & fit at TC 1, $(x, y) = (63.14, -5.00)$ cm (tc01f). . .	214
B.47	Deconvolved $f(v_k)$ & curve-fit at TC 1, $(x, y) = (63.14, 5.00)$ cm (tc01g).	214
B.48	Deconvolved $f(v_k)$ & fit at TC 1, $(x, y) = (63.14, 15.00)$ cm (tc01h). . .	215
B.49	Deconvolved $f(v_k)$ & fit at TC 1, $(x, y) = (63.14, -15.00)$ cm (tc01i). . .	215

B.50	Deconvolved $f(v_k)$ & fit at TC 1, $(x, y) = (63.14, -7.50)$ cm (tc01j). . .	216
B.51	Deconvolved $f(v_k)$ & curve-fit at TC 1, $(x, y) = (63.14, 7.50)$ cm (tc01k).	216
B.52	Deconvolved $f(v_k)$ & curve-fit at TC 2, $(x, y) = (63.14, 0.00)$ cm (tc02a).	217
B.53	Deconvolved $f(v_k)$ & curve-fit at TC 2, $(x, y) = (63.14, 7.50)$ cm (tc02b).	218
B.54	Deconvolved $f(v_k)$ & fit at TC 2, $(x, y) = (63.14, -7.50)$ cm (tc02c). . .	218
B.55	Deconvolved $f(v_k)$ & fit at TC 2, $(x, y) = (63.14, -15.00)$ cm (tc02d). .	219
B.56	Deconvolved $f(v_k)$ & fit at TC 2, $(x, y) = (63.14, 15.00)$ cm (tc02e). . .	219
C.1	Deconvolved $f(v)$ & curve-fit at TH15, $(x, y) = (0.14, 0.000)$ cm (th15a).	220
C.2	Deconvolved $f(v)$ & curve-fit at TH15, $(x, y) = (0.14, 1.372)$ cm (th15b).	221
C.3	Deconvolved $f(v)$ & curve-fit at TH15, $(x, y) = (0.14, 2.540)$ cm (th15c).	221
C.4	Deconvolved $f(v)$ & curve-fit at TH15, $(x, y) = (0.14, 3.912)$ cm (th15d).	222
C.5	Deconvolved $f(v)$ & curve-fit at TH15, $(x, y) = (0.14, 5.080)$ cm (th15e).	222
C.6	Deconvolved $f(v)$ & curve-fit at TH15, $(x, y) = (0.14, 6.452)$ cm (th15f).	223
C.7	Deconvolved $f(v)$ & curve-fit at TH15, $(x, y) = (0.14, 7.772)$ cm (th15g).	223
C.8	Deconvolved $f(v)$ & curve-fit at TH15, $(x, y) = (0.14, 8.992)$ cm (th15h).	224
C.9	Deconvolved $f(v)$ & curve-fit at TH15, $(x, y) = (0.14, 10.160)$ cm (th15i).	224
C.10	Deconvolved $f(v)$ & curve-fit at TH15, $(x, y) = (0.14, 11.557)$ cm (th15j).	225
C.11	Deconvolved $f(v)$ & curve-fit at TH15, $(x, y) = (5.02, 0.00)$ cm (th15l). .	226
C.12	Deconvolved $f(v)$ & curve-fit at TH15, $(x, y) = (5.02, 1.27)$ cm (th15m).	227
C.13	Deconvolved $f(v)$ & curve-fit at TH15, $(x, y) = (5.02, 2.24)$ cm (th15n).	227
C.14	Deconvolved $f(v)$ & curve-fit at TH15, $(x, y) = (5.02, 3.81)$ cm (th15o).	228
C.15	Deconvolved $f(v)$ & curve-fit at TH15, $(x, y) = (5.02, 5.08)$ cm (th15p).	228

C.16	Deconvolved $f(v)$ & curve-fit at TH15, $(x, y) = (5.02, 6.35)$ cm (th15q).	229
C.17	Deconvolved $f(v)$ & curve-fit at TH15, $(x, y) = (5.02, 7.62)$ cm (th15r).	229
C.18	Deconvolved $f(v)$ & curve-fit at TH15, $(x, y) = (5.02, 8.89)$ cm (th15s).	230
C.19	Deconvolved $f(v)$ & curve-fit at TH15, $(x, y) = (5.02, 10.16)$ cm (th15t).	230
C.20	Deconvolved $f(v)$ & curve-fit at TH15, $(x, y) = (5.02, 11.43)$ cm (th15u).	231
C.21	Deconvolved $f(v)$ & curve-fit at TH19 w/ neutralizer, $(x, y) = (5.09, 0.00)$ cm (th19a).	232
C.22	Deconvolved $f(v)$ & curve-fit at TH19 w/ neutralizer, $(x, y) = (5.09, 1.27)$ cm (th19b).	233
C.23	Deconvolved $f(v)$ & curve-fit at TH19 w/ neutralizer, $(x, y) = (5.09, 2.54)$ cm (th19c).	233
C.24	Deconvolved $f(v)$ & curve-fit at TH19 w/ neutralizer, $(x, y) = (5.09, 3.81)$ cm (th19d).	234
C.25	Deconvolved $f(v)$ & curve-fit at TH19 w/ neutralizer, $(x, y) = (5.09, 5.08)$ cm (th19e).	234
C.26	Deconvolved $f(v)$ & curve-fit at TH19 w/ neutralizer, $(x, y) = (5.09, 6.35)$ cm (th19f).	235
C.27	Deconvolved $f(v)$ & curve-fit at TH19 w/ neutralizer, $(x, y) = (5.09, 7.62)$ cm (th19g).	235
C.28	Deconvolved $f(v)$ & curve-fit at TH15 w/ neutralizer, $(x, y) = (0.12\text{cm}, 0.00)$ cm (th15x0).	236
C.29	Deconvolved $f(v)$ & curve-fit at TH15 w/ neutralizer, $(x, y) = (0.22, 0.00)$ cm (th15x1).	237
C.30	Deconvolved $f(v)$ & curve-fit at TH15 w/ neutralizer, $(x, y) = (0.35, 0.00)$ cm (th15x2).	237
C.31	Deconvolved $f(v)$ & curve-fit at TH15 w/ neutralizer, $(x, y) = (0.411, 0.00)$ cm (th15x3).	238

C.32	Deconvolved $f(v)$ & curve-fit at TH15 w/ neutralizer, $(x, y) = (0.505, 0.00)$ cm (th15x4).	238
C.33	Deconvolved $f(v)$ & curve-fit at TH15 w/ neutralizer, $(x, y) = (0.696, 0.00)$ cm (th15x5).	239
C.34	Deconvolved $f(v)$ & curve-fit at TH15 w/ neutralizer, $(x, y) = (1.008, 0.00)$ cm (th15x6).	239
C.35	Deconvolved $f(v)$ & curve-fit at TH15 w/ neutralizer, $(x, y) = (1.394, 0.00)$ cm (th15x7).	240
C.36	Deconvolved $f(v)$ & curve-fit at TH15 w/ neutralizer, $(x, y) = (1.890, 0.00)$ cm (th15x8).	240
C.37	Deconvolved $f(v)$ & curve-fit at TH15 w/ neutralizer, $(x, y) = (2.492, 0.00)$ cm (th15x9).	241
C.38	Deconvolved $f(v)$ & curve-fit at TH15 w/ neutralizer, $(x, y) = (3.495, 0.00)$ cm (th15x10).	241
C.39	Deconvolved $f(v)$ & curve-fit at TH15 w/ neutralizer, $(x, y) = (7.008, 0.00)$ cm (th15x11).	242
C.40	Deconvolved $f(v)$ & curve-fit at TH15 w/ neutralizer, $(x, y) = (15.004, 0.00)$ cm (th15x12).	242
C.41	Deconvolved $f(v)$ & curve-fit at TH15 w/ neutralizer, $(x, y) = (15.004, 0.00)$ cm (th15x13).	243
C.42	Deconvolved $f(v)$ & curve-fit at TH15 w/ neutralizer, $(x, y) = (30.013, 0.00)$ cm (th15x14).	243
C.43	Deconvolved $f(v)$ & curve-fit at TH15 w/ neutralizer, $(x, y) = (30.013, 0.00)$ cm (th15x15).	244
C.44	Deconvolved $f(v)$ & Maxwellian curve-fit at TH19 w/ neutralizer, $(x, y) =$ $(5.10, 10.160)$ cm (th19i1).	245
C.45	Deconvolved $f(v)$ & Maxwellian curve-fit at TH19 w/ neutralizer, $(x, y) =$ $(5.10, 11.430)$ cm (th19j).	246
C.46	Deconvolved $f(v)$ & Maxwellian curve-fit at TH19 w/ neutralizer, $(x, y) =$ $(5.10, 0.000)$ cm (th19l).	246

C.47	Deconvolved $f(v)$ & Maxwellian curve-fit at TH19 w/ neutralizer, $(x, y) = (5.10, 5.080)$ cm (th19m).	247
C.48	Deconvolved $f(v)$ & Maxwellian curve-fit at TH19 w/ neutralizer, $(x, y) = (0.14, 0.254)$ cm (th19n0).	247
C.49	Deconvolved $f(v)$ & Maxwellian curve-fit at TH19 w/ neutralizer, $(x, y) = (0.14, 0.254)$ cm (th19n1).	248
C.50	Deconvolved $f(v)$ & Maxwellian curve-fit at TH19 w/ neutralizer, $(x, y) = (0.14, 1.270)$ cm (th19o).	248
C.51	Deconvolved $f(v)$ & Maxwellian curve-fit at TH19 w/ neutralizer, $(x, y) = (0.14, 2.616)$ cm (th19p).	249
C.52	Deconvolved $f(v)$ & Maxwellian curve-fit at TH19 w/ neutralizer, $(x, y) = (0.14, 3.759)$ cm (th19q).	249
C.53	Deconvolved $f(v)$ & Maxwellian curve-fit at TH19 w/ neutralizer, $(x, y) = (0.14, 5.131)$ cm (th19r0).	250
C.54	Deconvolved $f(v)$ & Maxwellian curve-fit at TH19 w/ neutralizer, $(x, y) = (0.14, 5.131)$ cm (th19r1).	250
C.55	Deconvolved $f(v)$ & Maxwellian curve-fit at TH19 w/ neutralizer, $(x, y) = (0.14, 6.299)$ cm (th19s).	251
C.56	Deconvolved $f(v)$ & Maxwellian curve-fit at TH19 w/ neutralizer, $(x, y) = (0.14, 7.671)$ cm (th19t).	251
C.57	Deconvolved $f(v)$ & Maxwellian curve-fit at TH19 w/ neutralizer, $(x, y) = (0.14, 8.839)$ cm (th19u).	252
C.58	Deconvolved $f(v)$ & Maxwellian curve-fit at TH19 w/ neutralizer, $(x, y) = (0.14, 10.185)$ cm (th19v).	252

LIST OF TABLES

Table

3.1	Symmetry properties of Fourier transforms [30].	27
4.1	Xenon isotopic abundance [67] and shift relative to ^{132}Xe [71, 72] for the $5d^4D_{7/2} - 6p^4P_{5/2}^0$ transition.	51
4.2	Hyperfine line shifts and intensities for Xe II $5d^4D_{7/2} - 6p^4P_{5/2}^0$	54
7.1	P5 operating conditions for axial-injection LIF.	101
7.2	P5 axial plume temperatures & velocities at 1.6 kW along $y = 7.37$ cm.	108
7.3	P5 axial plume temperatures & velocities at 3.0 kW along $y = 7.37$ cm.	109
7.4	P5 axial plume temperatures & velocities at 1.6 kW along $x = 0.10$ cm.	116
7.5	P5 axial plume temperatures & velocities at 3.0 kW along $x = 0.10$ cm.	116
7.6	P5 axial plume temperatures & velocities at 1.6 kW along $y = 0$ cm.	121
7.7	P5 axial plume temperatures & velocities at 3.0 kW along $y = 0$ cm.	121
7.8	P5 operating conditions for multiplex LIF.	123
7.9	Bulk velocities in the P5 plume at 3 kW.	124
7.10	P5 plume temperatures at 3 kW.	125
7.11	P5 plume temperatures & velocity: variation with analysis (3kW data at $(x, y) = (10.01, 7.37)$ cm).	126
7.12	Bulk velocities in the P5 plume at TC9.	130
7.13	P5 plume temperatures at TC9.	131

7.14	P5 plume velocities at TC 10.	138
7.15	P5 plume temperatures at TC 10.	139
7.16	P5 plume velocities at TC 1.	142
7.17	P5 plume temperatures at TC 1.	143
7.18	P5 plume velocities at TC 2.	145
7.19	P5 plume temperatures at TC 2.	146
8.1	FMT-2 operating conditions.	154
8.2	FMT plume velocities at TH15 (w/o neutralizer).	155
8.3	FMT plume temperatures at TH15 (w/o neutralizer).	155
8.4	FMT plume velocities at TH15 (w/o neutralizer).	157
8.5	FMT plume temperatures at TH15 (w/o neutralizer).	157
8.6	FMT plume velocities at TH19 (w/o neutralizer).	160
8.7	FMT plume temperatures at TH19 (w/o neutralizer).	160
8.8	FMT plume velocities at TH15 (w/ neutralizer).	162
8.9	FMT plume temperatures at TH15 (w/ neutralizer).	163
8.10	FMT plume velocities at TH19 (w/ neutralizer).	165
8.11	FMT plume temperatures at TH19 (w/ neutralizer).	166

NOMENCLATURE

VARIABLES

A	Nuclear magnetic dipole interaction constant	[MHz]
B	Nuclear electric quadrupole interaction constant	[MHz]
\mathbf{B}	Magnetic field vector	[T]
c	Light speed, 2.9979×10^8	[m/s]
e	Electron charge, 1.6022×10^{-19}	[C]
\mathbf{E}	Electric field vector	[V/m]
\mathbf{F}_e	Sum of the external forces	[N]
F	Total angular momentum quantum number	[-]
h	Planck constant, 6.6261×10^{-34}	[J·s]
h_c	Specific combustion enthalpy	[J/kg]
$i(x)$	Generic image function	[-]
$i(\nu)$	Unsaturated lineshape	[s]
$i_s(\nu)$	Saturated LIF spectrum signal	[A]
I	Nuclear spin quantum number	[-]
J	Electronic angular momentum quantum number	[-]
k	Boltzmann constant, 1.3807×10^{-23}	[J/K]
\mathbf{k}	Laser beam wave vector	[1/m]

$\hat{\mathbf{k}}$	Beamwise direction vector	[-]
m	Electron mass, 9.1094×10^{31}	[kg]
$\langle m \rangle$	Mean exhaust product mass	[kg]
\dot{m}	Mass flow rate	[kg/s]
m_0	Initial spacecraft mass	[kg]
m_1	Final spacecraft mass	[kg]
M	Ion mass	[kg]
n	Number density	[m ⁻³]
q	Particle charge	[C]
R	Spacecraft mass ratio m_0/m_1	[-]
T	Temperature	[K]
\mathbf{T}	Thrust vector	[N]
\mathcal{T}	Filter bandwidth	[s]
\mathbf{u}	Bulk velocity	[m/s]
u_e	Propellant exhaust velocity	[m/s]
$U(x)$	Potential at ionization location	[V]
\mathbf{v}	Velocity	[m/s]
$\dot{\mathbf{v}}$	Acceleration	[m/s ²]
v_k	Beamwise velocity component	[m/s]
Δv	Change in velocity	[m/s]
V	Bias voltage	[V]
V_a	Anode potential (wrt ground)	[V]
V_d	Discharge (anode-to-cathode) voltage	[V]

V_T	Anode-to-accelerator grid voltage	[V]
\hat{x}	Axial direction vector	[-]
\hat{y}	Radial direction vector	[-]
\hat{z}	Vertical direction vector	[-]
α	Axial beam angle	[rad]
α_s	Spacecraft specific power	[J/kg]
β	Lateral beam angle	[rad]
β	Saturation coefficient	[Hz/W]
γ	Ratio of specific heats	[-]
Γ	Maximum saturated LIF signal	[A]
ϵ_0	Permittivity of free space, 8.8542×10^{-12}	[F/m]
ϕ	Electric potential	[V]
ν	Frequency	[Hz]
τ	Transform-space complement to ν	[s]
ω_e	Electron cyclotron frequency	[rad/s]

OPERATORS

\otimes	Convolution operator
\oslash	Deconvolution operator
\mathcal{F}	Fourier transform
\mathcal{F}^{-1}	Inverse Fourier transform

ACRONYMNS

AIAA	American Institute of Aeronautics and Astronautics
AFRL	Air Force Rocket Laboratory
CARS	coherent Raman anti-Stokes spectroscopy
CEX	charge-exchange
CTF	Cathode Test Facility
cw	continuous-wave
DFWM	Degenerate Four-Wave Mixing
EP	Electric Propulsion
FFT	Fast Fourier Transform
FMT	Functional Model Thruster
FWHM	full width at half-maximum
GRC	NASA Glenn Research Center at Lewis Field
hfs	hyperfine structure
iedf	ion energy distribution function
IEPC	International Electric Propulsion Conference
LIF	laser-induced fluorescence
LVTF	Large Vacuum Test Facility
MBMS	Molecular Beam Mass Spectrometer
NASA	National Aeronautics and Space Administration
OAS	optical absorption spectroscopy

OES	optical emission spectroscopy
OGS	optogalvanic spectroscopy
PEPL	Plasmadynamics and Electric Propulsion Laboratory
SNR	signal-to-noise ratio
SPT	Stationary Plasma Thruster
TAL	Anode Layer Thruster
VASIMR	Variable Specific-Impulse Magnetoplasma Rocket

CHAPTER I

INTRODUCTION

Much of the joy of science is the joy of solid work done by skilled workmen. . . .
There is a great satisfaction in building good tools for other people to use. –
Freeman Dyson [1]

1.1 Problem statement

Over the past decade, electric propulsion (EP) has undergone a rapid transition from an experimental technology shunned by prudent mission planners to a flight-qualified, high-performance technology in active use on orbit. EP research has kept pace with this renaissance in spacecraft mission planning. More sophisticated computational models, higher-capacity vacuum facilities and improved diagnostics have provided a more complete understanding of the physical processes in EP devices. This understanding, in turn, has driven the design, development and characterization of new, higher-performance thrusters.

The development of plasma diagnostics is a crucial part of the EP research process. Plasma diagnostics can be roughly separated into two main classes: physical probes and optical diagnostics. Physical probes, which collect electrical currents from a surface in contact with the plasma, are easier to set up and quicker to return data than optical methods. However, the very presence of physical probes perturbs the plasma. This perturbation is, in turn, usually a function of the unperturbed plasma properties. Separating probe effects

from plasma properties can become a nonlinear (and thus difficult) inverse problem, which is rarely attempted.

Optical diagnostics, which collect light from the plasma, are slower and more difficult to set up than physical probes. They are, however, completely non-invasive. The inverse problems posed by optical diagnostics tend to be linear, and have relatively straightforward solutions.

1.1.1 Laser-induced fluorescence

Laser-induced fluorescence, or LIF, is a particularly powerful optical diagnostic, combining high sensitivity and excellent spatial resolution. In LIF, the wavelength of a narrow-linewidth tunable laser is swept through an absorption line of a plasma species, such as singly-ionized xenon (Xe II). Focusing optics direct this laser beam along a “beamwise” direction vector $\hat{\mathbf{k}} \equiv \mathbf{k}/|\mathbf{k}|$, where \mathbf{k} is the beam’s wave vector. Collection optics on another (usually perpendicular) axis sample the fluorescence emitted by absorbing particles in the interrogation volume. This interrogation volume, an ellipsoid defined by the intersecting beams, can be less than a millimeter on a side.

In species with no hyperfine structure (hfs), the LIF spectrum can be directly transformed into an excellent approximation of the beamwise velocity distribution $f(v_k)$, where $v_k \equiv \mathbf{v} \cdot \hat{\mathbf{k}}$. A direct transformation from the LIF spectrum to this velocity distribution is acceptable because the LIF spectrum in species without hfs is the convolution of two broadening functions. Doppler broadening, which has a lineshape directly proportional to the velocity distribution, is the dominant broadening function. The natural (or lifetime) broadening, a Lorentzian function caused by the finite lifetime of the upper state, is usually much narrower for warm gases than the Doppler broadening. The similarity between LIF spectra and $f(v_k)$ is good enough that LIF measurements in barium¹ [2, 3, 4] and argon

¹Though barium has hfs, the splitting is far larger than the Doppler broadening. Because the hyperfine

[5] plasmas have been reported as velocity distributions².

1.1.2 The curve-fitting analysis method

In xenon (and other species with hfs), the LIF spectrum can be modeled as the convolution of the absorbing transition's hfs with natural and Doppler broadening functions. The standard analysis method for LIF spectra at xenon transitions with known hfs, developed by Renato Cedolin in 1997 [7, 8, 9], fits the data to just such a model. Cedolin's method³ assumes that the velocity distribution is a drifting Maxwellian, which can be completely described by the bulk velocity \mathbf{u} and the temperature T . A nonlinear optimization routine varies $u_k = \mathbf{u} \cdot \hat{\mathbf{k}}$ and T until it finds an acceptable fit between the measured and modeled spectra.

Cedolin's curve-fitting method reliably returns u_k and T for the noisy spectra characteristic of EP plume LIF. In near-equilibrium plasmas, such as those found in the far-field of EP device plumes, the assumption of a drifting Maxwellian velocity distribution may be reasonable. Subsequent use of Cedolin's method by Keefer [10], Williams [11, 12], Sadeghi [6] and Hargus [14] has made curve-fitting the *de-facto* standard for xenon LIF analysis of transitions with known hfs.

1.1.3 Limitations of Cedolin's method

However, the popularity of a technique is not, by itself, an adequate measure of its utility [15]. Cedolin's method implicitly assumes that the interrogated xenon population is at equilibrium. Even in the far-field, though, interrogation along different beam paths $\hat{\mathbf{k}}$ lines do not overlap, each line can be treated as a separate transition without hfs.

²Sadeghi *et al.* [6] have incorrectly reported LIF spectra as $f(v_k)$ in xenon plasmas. Since the supporting text describes their hfs model in detail, this is clearly an oversight and not a claim of direct $f(v_k)$ measurement.

³Though Manzella developed a similar model for his 834.7 nm LIF study of the SPT-100 plume in 1994 [57], Cedolin remains the first to have accurately modeled the hfs and natural broadening of Xe II for LIF data analysis. Both methods share a common heritage in Liebeskind's Balmer- α line model [51].

returns different values of T [10, 11], which implies that Maxwell's isotropy assumption is not valid [16]. As we approach the ion creation zone, this equilibrium assumption grows increasingly unwarranted.

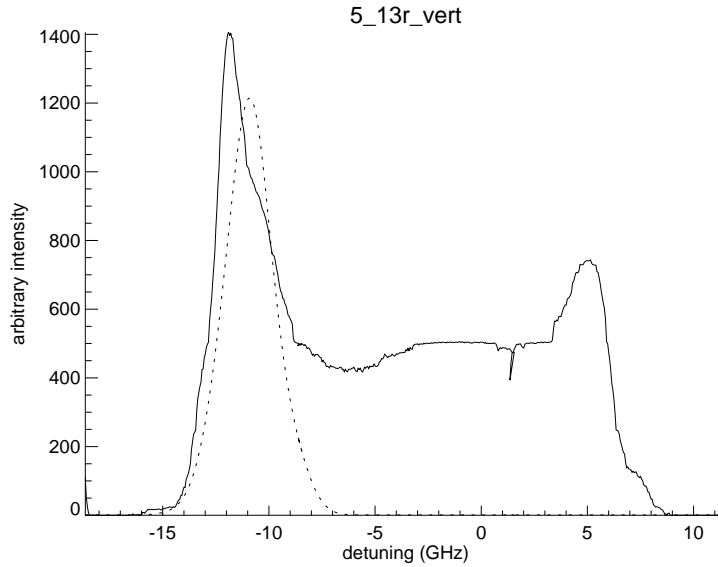


Figure 1.1: Radial LIF at P5 Hall thruster centerline. Dashed line is a curve-fit to the left peak by Cedolin's method.

Figure 1.1 shows the limitations of Cedolin's method more clearly. The solid line is a radial LIF spectrum at 605.1 nm taken on the centerline of the P5 Hall thruster, where ions streaming from the annular discharge chamber pass through from both sides with an appreciable radial velocity. This LIF spectrum suggests the presence of counterstreaming plasmas, with at least two distinct populations. The dashed line, a curve-fit to the left peak computed by Cedolin's method, shows how poorly a single Maxwellian models velocity distributions that are this complex.

Simply put, Cedolin's curve-fitting method of xenon LIF data analysis is suspect for near-field axial flows, and fails completely for counterstreaming radial flows. LIF spectra taken in these flows need a more general analysis method, preferably one that makes no assumptions about the beamwise velocity distribution.

1.2 Aim

The primary goal of this research is to develop, validate and apply a deconvolution technique that extracts velocity distribution estimates from Xe II LIF spectra at 605.1 nm. The well-established hyperfine structure and lifetime of the $5d^4 D_{7/2} - 6p^4 P_{5/2}^0$ transition provide the basis for a Gaussian-filtered, Fourier-transform deconvolution. Transforming deconvolved ion velocity distributions to an ion energy basis reproduces all Xe II features found in mass spectrometer data taken at the same location and conditions. Application of this technique to LIF spectra taken in the plume of the P5 Hall thruster and the FMT-2 ion engine provides velocity distributions that cannot be measured by probe-based methods, and reveals unexpected counterstreaming plasma phenomena in both plumes.

1.3 Organization

The remainder of this dissertation is divided into four sections: background, methods, results and discussion.

Chapters 2 through 4 lay out the background of this research. Chapter 2 presents a brief overview of the history and physical principles of electric propulsion. Chapter 3 introduces the theory of convolution and deconvolution, while chapter 4 summarizes the theory of LIF spectra in xenon. Readers who are familiar with the subject matter are encouraged to skip ahead to the next section.

Chapters 5 and 6 describe the computational and experimental methods used to create and test the deconvolution method. Chapter 5 presents the deconvolution method and describes computational studies of noise amplification and signal broadening as a function of filtering intensity. Chapter 6 details the vacuum facility, thrusters, optics and experimental procedures used in subsequent tests on electrostatic thrusters.

Chapters 7 and 8 describe the results of these tests. Chapter 7 describes multiplex

and axial-injection LIF experiments carried out in the P5 Hall thruster plume at discharge voltages of 50, 100 and 300 V. Chapter 8 describes a multiplex LIF experiment carried out in the FMT-2 ion engine plume at 1100 and 1430 V screen potential.

Chapter 9 summarizes the results of these experiments and proposes a range of subjects for future work.

CHAPTER II

ELECTRIC PROPULSION

In space, the best means of propulsion, and the one involving the least mass of ejected material, is undoubtedly the repulsion of low-speed electrons and positive metallic ions, the latter by means of an electrode. – *Robert Goddard* [17]

2.1 Historical background

At the time of its earliest mention by Goddard in 1906, electric propulsion of spacecraft was a purely theoretical concept, filling a purely theoretical need. Artificial satellites were only a remote possibility at the beginning of the twentieth century, as were the large liquid-propellant boosters needed to launch them. Though a chemical rocket's exhaust velocity is fundamentally limited by the specific heat of combustion, electrostatic repulsion has no such limitation. Goddard pointed this out in several papers in the 1920s¹, but his primary experimental concentration remained on liquid propulsion. Oberth expanded on the concept of EP in a chapter of *Wege zur Raumshiffahrt* (1929), and several theoretical studies were published from 1945 to the mid 1950s, but experimental work on EP languished until 1957 [19].

¹Goddard also obtained four patents for ion sources, which suggests he was considering experimental EP work. As E. Bright Wilson has pointed out, "A research worker in pure science who does not have at all times more problems he would like to solve than he has time and means to investigate them probably is in the wrong business." [18]

All this changed on 4 October 1957, when the Soviet Union launched the 83-kg artificial satellite *Sputnik I* into a 900-km altitude Earth orbit, followed by the 508-kg *Sputnik II* on 3 November. The launch of the 14-kg *Explorer I* on 31 January 1958 announced the United States' entry in the "Space Race." [20]

It is probably not a coincidence that experimental work on EP began in earnest about the same time. By August 1958, testing started on a ion engine model at Rocketdyne; by 1959, three more corporate teams in the United States, at least one Russian lab and the NACA Lewis Flight Laboratory (now NASA Glenn) were running ion engines in their own facilities [19]. The first academic research lab dedicated to EP problems was founded at Princeton in 1961, and the first successful in-space test of an ion engine occurred on 20 July 1964. As Robert Jahn noted in 1968, "electric thrusters thereby laid claim to a small niche in the space engine arsenal [21]."

A combination of insufficient onboard electrical power and a prudent reluctance to embrace new designs kept mission planners from expanding this niche for over 20 years. Resistojets and pulsed plasma thrusters were regularly, but infrequently, used during this era, even as research continued on far more powerful and efficient thrusters. In the early 1990s, the advent of new, high-power spacecraft architectures made EP more attractive to mission planners. At the same time, the end of the Cold War brought an influx of Russian Hall thruster technology to the West, while an aggressive new administration at NASA began to advocate the use of ion engines in interplanetary probes. Today, over 140 spacecraft use EP systems for station keeping, attitude control and orbit transfer [22], while still-higher power and efficiency units are under active development.

2.2 Advantages of electric propulsion

Jahn’s classic definition of electric propulsion is “the acceleration of gases for propulsion by electrical heating and/or by electric and magnetic body forces.” [21] The main advantage EP devices have over chemical rockets is high exhaust velocity. A chemical rocket’s combustion enthalpy h_c and the mean mass of its exhaust products $\langle m \rangle$ fundamentally limit the mean exhaust velocity to

$$u_e \leq \sqrt{2h_c/\langle m \rangle}. \quad (2.1)$$

Hydrogen burned in oxygen provides the maximum practically attainable exhaust velocity for chemical propellants, 4.6 km/s. These propellants are usually stored as cryogenic liquids, which make handling and storage difficult at best. Storable propellants, such as a 50:50 hydrazine:unsymmetrical dimethylhydrazine (N_2H_4 :UDMH) mixture burned in nitrogen tetroxide (N_2O_4), can only attain exhaust velocities of 3.3 km/s [23].

EP devices, on the other hand, can readily attain exhaust velocities from 5 km/s (for resistojets) to 110 km/s (for extremely high-voltage ion engines). Since the power source is external, EP devices can use inert, easily stored propellants.

2.2.1 The rocket equation

To illustrate the importance of high exhaust velocities, consider a rocket of mass m expelling propellant at a mass loss rate of \dot{m} and exhaust velocity (relative to the rocket) of u_e . The acceleration \dot{v} of this rocket is given by

$$m\dot{v} = \dot{m}u_e + \mathbf{F}_e \quad (2.2)$$

where \mathbf{F}_e is the sum of the external forces (such as the local gravitational force and atmospheric drag). If we define a unit vector in the direction of travel $\hat{\mathbf{x}} = \mathbf{v}/|\mathbf{v}|$ and assume

that the exhaust goes in the opposite direction, this simplifies to the one-dimensional differential equation

$$m\dot{v} = -\dot{m}u_e + F_x \quad (2.3)$$

where $F_x = \mathbf{F}_e \cdot \hat{\mathbf{x}}$ is the external force component in the direction of travel. Integrating Eqn. 2.3 over a time period $\Delta t = t_1 - t_0$ yields a relation for the change in velocity

$$\Delta v = u_e \ln \frac{m_0}{m_1} + \int_{t_0}^{t_1} F_x dt \quad (2.4)$$

where the initial mass is m_0 and the final mass is $m_1 = m_0 - \dot{m}\Delta t$. When Δt is vanishingly short (impulsive thrust) or F_x disappears (thrust perpendicular to the sum of external forces, as is the case for both burns in a Hohmann transfer), this simplifies to the *Tsiolkovsky* or *rocket equation*,

$$\Delta v = u_e \ln \frac{m_0}{m_1}. \quad (2.5)$$

For an example of how Eqn. 2.5 favors EP devices over chemical rockets, consider a geosynchronous communications satellite. Tidal forces constantly push geosynchronous satellites out of their intended equatorial plane. Without regular North-South stationkeeping (NSSK) burns, the satellite will drift out of communications lock; these burns add up over the spacecraft working lifetime to a net velocity increment of Δv . For a given mass ratio $R \equiv m_0/m_1$, the available Δv increases linearly with exhaust velocity. Thus, using Hall thrusters (typically $u_e = 24$ km/s for a 500-V discharge) rather than storable chemical propellants ($u_e = 3.3$ km/s for N_2H_4 :UDMH in N_2O_4) will allow more than seven times as many NSSK burns. In other words, a geosynchronous satellite using Hall thrusters could (barring other limits on lifetime) earn a profit seven times longer than one using storable chemical rockets.

If the designers opt instead to keep the original spacecraft lifetime, choosing Hall thrusters instead of chemical rockets will improve the mass ratio. Let R_H denote the mass

ratio for a Hall thruster design with exhaust velocity $u_H = 24$ km/s, and R_C denote the mass ratio for a chemical rocket design with exhaust velocity $u_C = 3.3$ km/s. Equation 2.5 then yields the ratio

$$\frac{R_C}{R_H} = \exp\left(\frac{\Delta v}{u_C} - \frac{\Delta v}{u_H}\right). \quad (2.6)$$

As Eqn. 2.6 shows, the EP advantage over chemical rockets increases exponentially with Δv . For a net velocity increment of $\Delta v = 2.65$ km/s, the chemical system mass ratio R_C is twice the Hall system mass ratio R_H . In this case, choosing Hall thrusters gives mission designers two attractive endpoints to their parameter space. If they opt to maintain the original launch mass, they can double the size and capability of the payload. If they opt to launch the same payload mass, they can halve the original launch mass. Though the best design will probably fall inbetween these endpoints at some break point defined by maximum launch vehicle capacity, EP devices remain a very good option for geosynchronous satellite NSSK.

2.2.2 Performance parameters

The three major performance parameters for EP devices are thrust (T), specific impulse (I_{sp}) and efficiency η . A rocket's thrust (in the absence of unbalanced pressures) is equal and opposite to the time rate of change of propellant momentum; for a constant mean exhaust velocity u_e and mass flow rate \dot{m} ,

$$\mathbf{T} \equiv -\frac{d}{dt}m\mathbf{u}_e = \dot{m}u_e\hat{\mathbf{x}}. \quad (2.7)$$

Specific impulse is a traditional measure, defined as the ratio of thrust T to propellant *weight* flow rate $\dot{w} = \dot{m}g_0$, where g_0 is the mean gravitational acceleration at sea level. Substituting Eqn. 2.7 into this definition yields the expression

$$I_{sp} = \frac{\dot{m}u_e}{\dot{m}g_0} = \frac{u_e}{g_0}. \quad (2.8)$$

For EP devices, specific impulse is experimentally determined in a vacuum facility by directly measuring thrust at a known propellant mass flow rate. In a perfect vacuum, this value would be equal to u_e/g_0 , where u_e is the mean axial velocity integrated over a plane far downstream of the thruster. In real vacuum chambers, however, entrainment of background gases increases the effective mass flow rate and decreases the mean exhaust velocity. Thus, laboratory values of I_{sp} run higher, and laboratory values of u_e run lower, than could be expected at the same operating conditions on orbit.

Thruster efficiency η is defined as the ratio of jet power

$$P_j = \frac{d}{dt} \left(\frac{1}{2} m u_e^2 \right) = \frac{1}{2} \dot{m} u_e^2 = \frac{1}{2} T u_e \quad (2.9)$$

to electrical input power P_e . Thus, for a fixed electrical power and efficiency, thrust varies linearly with exhaust velocity:

$$T = \frac{2\eta P_e}{u_e}. \quad (2.10)$$

Ion production costs, elevated ion temperatures in the plume and thruster oscillations are a few of the effects that lower thruster efficiency.

Though thrust and exhaust velocity are limited by the accelerating mechanisms in EP devices, they are not fixed values. Increasing the mass flow rate will increase T at a given u_e , while increased accelerating potentials (in electrostatic thrusters) or gas temperatures (in electrothermal thrusters) will increase u_e . However, Eqn. 2.9 points out that these increases come at the cost of increased electrical power. Typical spacecraft power supplies, such as solar panels or radioisotope generators, can be modeled as having a constant specific power α_s . In this case, the power supply mass is

$$m_p = \alpha_s P = \frac{\alpha_s T u_e}{2\eta}. \quad (2.11)$$

The total propellant mass expelled over a time Δt at a constant thrust T is inversely pro-

portional to the mean exhaust velocity,

$$\Delta m = \dot{m} \Delta t = \frac{T \Delta t}{u_e}. \quad (2.12)$$

For negligible thruster mass, the total propulsive system mass $m_T = m_p + \Delta m$ is a function of u_e . Solving $\partial m_T / \partial u_e = 0$ yields the optimum exhaust velocity at constant thrust

$$\hat{u}_e = \left(\frac{2\eta \Delta t}{\alpha_s} \right)^{1/2}. \quad (2.13)$$

Thruster lifetime is also a limiting factor in assessing thruster performance. Rearranging Eqn. 2.13 in terms of required thruster lifetime,

$$\Delta t = \frac{(\alpha_s \hat{u}_e)^2}{2\eta}; \quad (2.14)$$

thus, for a fixed thrust level, efficiency and specific power, the required thruster lifetime Δt increases with the square of the optimum exhaust velocity.

Erosion of thruster materials by the discharge is the primary limit on the lifetime of electrostatic thrusters. Avoiding the expense of conventional life tests, where the thruster is continuously operated for thousands of hours [24], is a major driver behind the development of LIF erosion diagnostics [55, 56, 12].

2.3 Electrostatic thrusters

Electric propulsion mechanisms were first divided into three canonical categories by Stuhlinger[19]:

- *Electrothermal* devices heat a propellant gas with electrical current or electromagnetic radiation. The resulting thermal energy is converted to directed kinetic energy by expansion through a nozzle. Resistojets, arcjets and cyclotron resonance thrusters (such as VASIMR) are examples of electrothermal devices.

- *Electrostatic* devices accelerate charge-carrying propellant particles in a static electric field. These devices typically use a static magnetic field that is strong enough to retard electron flow, but too weak to materially affect ion trajectories. Ion engines and Hall thrusters are examples of electrostatic thrusters.
- *Electromagnetic* devices² accelerate charge-carrying propellant particles in interacting electric and magnetic fields. Magnetic field strength in these devices is typically high enough to significantly affect both ion and electron trajectories. Examples include pulsed plasma thrusters (PPTs³), magnetoplasmadynamic (MPD) thrusters and traveling-wave accelerators.

This research used two electrostatic thrusters, the UM/AFRL P5 and the NASA Glenn FMT-2. The P5 is a 5-kW Hall thruster, while the FMT-2 is a 2.3-kW ion engine.

2.3.1 Hall thrusters

Hall thrusters create and accelerate ions through a magnetically-maintained electrostatic potential in a crossed-field discharge chamber. Unlike ion engines, the ionization and acceleration regions in a Hall thruster are closely coupled.

Figure 2.1 shows a Hall thruster schematic. Though racetrack and linear configurations exist, the standard Hall thruster design uses an annular discharge chamber. The walls of this discharge chamber are dielectric in stationary plasma thrusters (SPTs), while anode layer thrusters (TALs) use a negatively-biased metal. Inner and outer electromagnets set up a magnetic field, whose field lines are channeled by inner and outer pole pieces.

²Jahn [21] uses this category in place of Stuhlinger's *electrodynamic*, which would properly describe devices with time-varying electric and magnetic fields, such as PPTs, pulsed MPD thrusters and traveling-wave accelerators. Though the merits of both classification systems can be enjoyably debated, the question is really academic. What we are primarily interested in is *how* these devices work, *how well* they work and *how much* we can improve their performance. Questions of terminology are best left to lexicographers.

³PPTs clearly have some electrothermal nature. How much of their performance is electrodynamic is a matter of controversy.

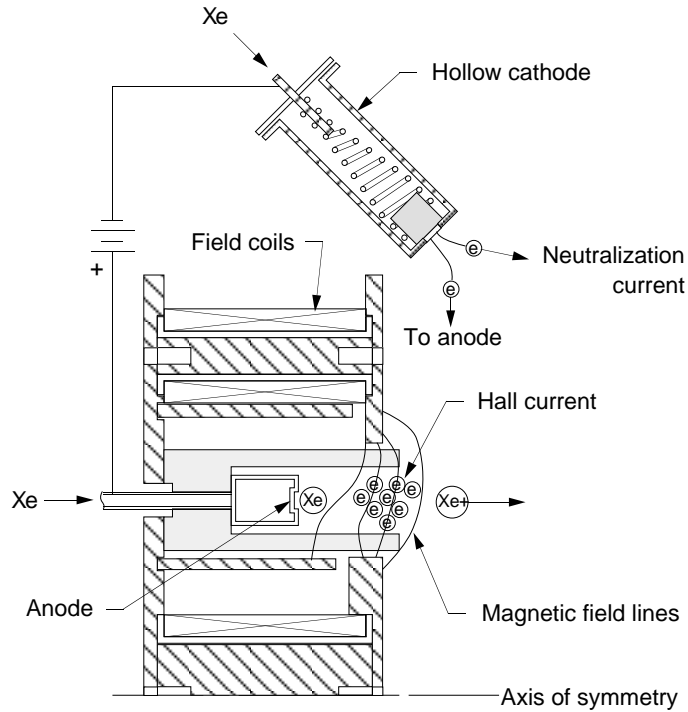


Figure 2.1: Hall thruster schematic.

Magnetic shields lining the discharge chamber exterior are often used to further shape the magnetic field lines. This creates a (mostly) radial magnetic field \mathbf{B} in the discharge chamber, whose magnitude peaks near the exit plane.

Xenon is the modern propellant of choice in Hall thrusters, though krypton and argon have also been used. A steady flow of propellant enters the thruster through the gas distributor, which also serves as the anode. Small holes, regularly spaced around the anode face in order to avoid azimuthal asymmetries, meter the propellant into the discharge chamber. A discharge voltage V_d applied between an external hollow cathode (which typically floats 10-30 V below ground) and the anode sets up an axial electric field \mathbf{E} . Electrons streaming back towards the anode under the influence of this electric field enter the region of strong magnetic field intensity and experience a crossed-field acceleration

$$\dot{\mathbf{v}}_e = -\frac{e}{m}(\mathbf{E} + \mathbf{v}_e \times \mathbf{B}). \quad (2.15)$$

The resulting motion resolves into two parts: a fast gyration (at a frequency of $\omega_e = eB/m$ radians/s) around an axis parallel to \mathbf{B} , and a slower azimuthal drift at a speed of E/B [25]. Electrons caught in this $\mathbf{E} \times \mathbf{B}$ drift create an azimuthal *Hall current*, and tend to remain in the same axial plane until perturbed by plasma turbulence, wall collisions, or collisions with other particles. The high electron density in this Hall current creates a “virtual cathode,” which restricts the majority of the anode-cathode potential drop to a relatively short region upstream of the plane of maximum radial magnetic field intensity [92]. To a first approximation, equipotential surfaces in the discharge chamber follow the magnetic field lines [86].

Elastic collisions (both electron-neutral and electron-ion) redirect the electron velocity, while maintaining the electron’s kinetic energy. Though classical kinetic theory predicts that the average elastic collision shifts the electron’s mean axial plane of about 1/3 of the Larmor radius ($r_L = v_e/\omega_e$) closer to the anode [14], non-classical effects (often labeled *anomalous* or *Bohm diffusion*) considerably increase the electron axial mobility. This increased axial mobility increases the axial electron current, which in turn decreases the overall thruster efficiency.

Electron collisions with the wall provide a major difference between SPTs and TALs. The dielectric discharge chamber wall of an SPT emits low-energy secondary electrons when struck by a high-energy primary electron. This process limits the electron temperature in the discharge chamber and extends the acceleration region. The metal wall of a TAL, however, is maintained at cathode potential, and thus reflects the majority of primary electrons. This reflection conserves electron temperature and shortens the acceleration region [26].

Inelastic collisions (both electron-neutral and electron-ion) cause both excitation and ionization. Excitation collisions have little effect on thruster performance, other than de-

creasing the mean electron energy and increasing the ionization cross-section of the excited propellant, but they do populate energy levels above the ground state. These levels include the metastable lower states used in current xenon LIF schemes, so excitation collisions take on some importance in LIF.

Ionizing collisions between electrons and thermally-effusing neutral xenon (Xe I) produce low-energy secondary electrons and singly-ionized xenon (Xe II); sufficiently energetic primary electrons colliding with Xe I can also produce doubly-ionized xenon (Xe III). Xenon ions, which are 239,000 times heavier than electrons, are not significantly affected by the magnetic field over the length of the discharge channel. The electric field, however, will accelerate an ion of mass M and charge q to an exit velocity

$$u_e = \sqrt{2q\phi(x)/M} \quad (2.16)$$

where $\phi(x)$ is the potential drop between the ionization position x and the exit plane. Since ionizing collisions occur throughout the Hall current, the resulting spread in $\phi(x)$ produces a similar irreducible spread in the ion energy distribution.

Xe II moves much more quickly than Xe I in an electric field, so the residence time of Xe II in the ionizing region is much less than the residence time for Xe I. Nonetheless, enough ionizing collisions between electrons and Xe II occur that Xe III accounts for approximately 7% of the P5 ion population. Likewise, collisions between electrons and Xe III are even less frequent, but Xe IV nonetheless makes up about 0.7% of the P5 ion population [27].

The external hollow cathode, which provides the ionizing electron current, also acts as a neutralizer. This ensures that equal ion and electron currents leave the thruster (current neutralization). Because the plasma remains electrically neutral throughout the acceleration zone, there are no space-charge limits on current or thrust density in a Hall thruster.

The current generation of Hall thrusters have typical exhaust velocities from 16 to 30 km/s, and efficiencies from 45% to 65%.

2.3.2 Ion engines

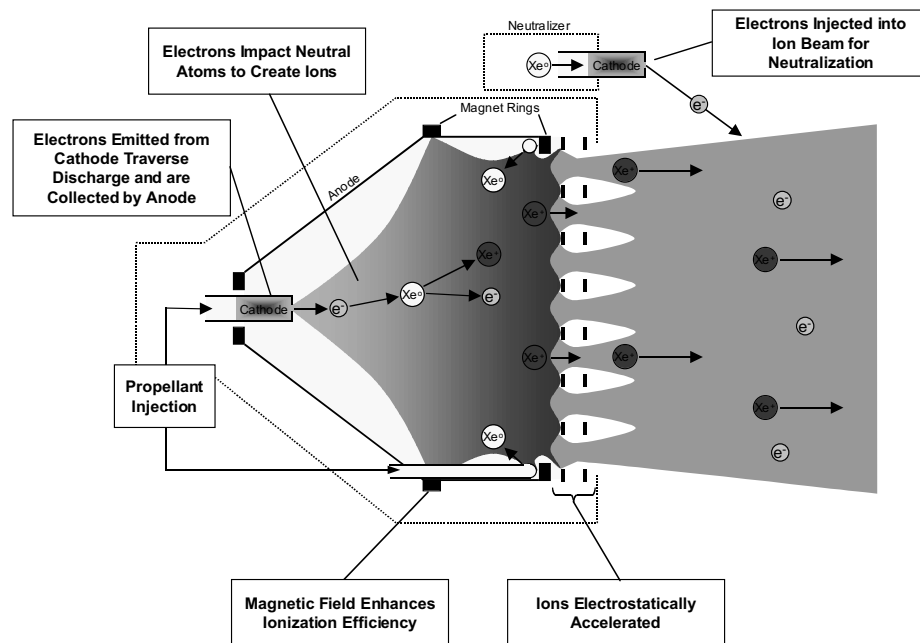


Figure 2.2: Ion engine schematic.

Ion engines focus and accelerate ions through a series of electrically-biased grids. Unlike Hall thrusters, ionization and acceleration occur in separate regions of an ion engine.

Figure 2.2 shows an ion engine schematic. A discharge voltage V_d applied between a central high-current hollow cathode and the metallic discharge chamber wall (or anode) creates a radial electric field E_d . In ion engines, V_d is decoupled from the accelerating potential, and so can be readily maintained far enough below the sum of the first and second ionization potentials to minimize the production of doubly-ionized xenon (Xe III).

The entire discharge circuit is biased at an anode voltage V_b , usually on the order of 1100 V above ground potential.

Permanent magnets placed in homopolar rings around the discharge chamber set up a ring-cusp magnetic field \mathbf{B} . At the cathode exit, the magnetic field is largely axial and low-intensity, but it becomes more radial and stronger at the poles. Primary electrons streaming outwards towards the anode under the influence of the electric field experience a Lorentz acceleration that depends on the angle between \mathbf{E} and \mathbf{B} . Where $\mathbf{E}_d \perp \mathbf{B}$, electrons streaming toward the anode will experience the same sort of azimuthal $\mathbf{E} \times \mathbf{B}$ drift found in a Hall thruster. Where $\mathbf{E}_d \parallel \mathbf{B}$, electrons with initial parallel velocity component v_{\parallel} and perpendicular velocity component v_{\perp} that fall through a potential drop ϕ towards the anode will be reflected by the magnetic mirror effect [25] if v_{\parallel}/v_{\perp} is outside a narrow loss cone, defined by

$$\frac{v_{\parallel}^2 + 2e\phi/m}{v_{\perp}^2} < \frac{|\mathbf{B}|_1}{|\mathbf{B}|_0} - 1 \quad (2.17)$$

where $|\mathbf{B}|_0$ is the magnetic field strength at the cathode and $|\mathbf{B}|_1$ is the magnetic field strength at the anode. Most electrons will experience a combination of these two effects, both of which greatly increase the effective cathode-to-anode distance and electron lifetime.

As in the Hall thruster, a steady flow of xenon passes through the discharge chamber, where high-energy electron-neutral collisions create xenon ions and secondary electrons. Ions kinetically effuse into the intergrid space, aided by the screen grid, which is kept at discharge cathode potential. At low current densities, they “see” a strong axial electric field $\mathbf{E}_b \approx V_T \hat{\mathbf{x}}/d_g$, where V_T is the anode-to-accelerator grid potential drop and d_g is the intergrid distance. As the current density increases, space-charge effects caused by the non-neutral plasma between the grids make \mathbf{E} drop to zero at the screen grid. The resulting

maximum, or *space-charge-limited* beam current [21] is

$$j_{max} = \frac{4\epsilon_0}{9} \left(\frac{2q}{M}\right)^{1/2} \frac{V_T^{3/2}}{d_g^2}. \quad (2.18)$$

Since thrust density (thrust per unit grid area) is the product of mass flow rate \dot{m} and exit velocity u_e , an ion engine's thrust density is also limited by space-charge effects.

Unlike the Hall thruster, the external hollow cathode is not required to sustain the discharge, but only assures current neutralization. Electron backstreaming into the discharge chamber is prevented by biasing the accelerator grid well below ground. The current generation of ion engines have typical exhaust velocities from 15 to 50 km/s, and efficiencies from 35% to 68%.

2.4 Kinematic compression

Electrostatic thrusters accelerate ions via conservative forces in a largely collisionless environment. This tends to axially cool the ions, in a process known as kinematic compression [81]. Ions traveling at a range of initial velocities fall through a fixed potential energy drop and accelerate to a much smaller range of final velocities. The same principle allows gravity-assisted boosting of interplanetary probes, where a small velocity change made at a high kinetic energy (periapsis) translates to a large velocity change out at a high potential energy (apoapsis or escape).

Consider an initial ion velocity distribution $f_0(v)$. Ions with initial velocity v_0 and charge-to-mass ratio q/m will be accelerated by a steady potential drop U to a final velocity

$$v_1 = \sqrt{v_0^2 + \frac{2qU}{m}} \quad (2.19)$$

as long as $v_0 \geq -\sqrt{2qU/m}$. (Otherwise, ions starting at position 0 never arrive at position 1.) Thus, the final velocity distribution $f_1(v)$ will be shifted to the right in velocity space,

giving

$$f_1(v) = \begin{cases} f_0 \left(\sqrt{v^2 - 2qU/m} \right) & , v \geq -\sqrt{2qU/m} \\ 0 & , v < -\sqrt{2qU/m}. \end{cases} \quad (2.20)$$

To illustrate how this narrows a velocity distribution, consider an ion population with an initial axial bulk velocity u_0 and velocity FWHM of Δu_0 . A steady potential drop U will accelerate ions at the FWHM points of a distribution to axial speeds of

$$u_p = \sqrt{\left(u_0 + \frac{\Delta u_0}{2}\right)^2 + \frac{2qU}{m}} \quad (2.21)$$

$$u_m = \sqrt{\left(u_0 - \frac{\Delta u_0}{2}\right)^2 + \frac{2qU}{m}} \quad (2.22)$$

The FWHM of the accelerated beam is thus

$$\Delta u_1 = u_p - u_m. \quad (2.23)$$

If the potential drop is much larger than the initial kinetic energy at either FWHM point ($2qU/m \gg [u_0 \pm \Delta u_0/2]^2$), the final axial speeds at the FWHM points become

$$\sqrt{\frac{2qU}{m}} \left(1 + \frac{m}{2qU} \left[u_0 \pm \frac{\Delta u_0}{2} \right]^2 \right)^{1/2} \approx \sqrt{\frac{2qU}{m}} \left(1 + \frac{m}{4qU} \left[u_0 \pm \frac{\Delta u_0}{2} \right]^2 \right) \quad (2.24)$$

which simplifies to the velocity FWHM ratio

$$\frac{\Delta u_1}{\Delta u_0} \approx \frac{2u_0}{\sqrt{2qU/m}}. \quad (2.25)$$

In a Maxwellian plasma, the FWHM for a given temperature T is

$$\Delta u = 2\sqrt{\frac{2 \ln 2 kT}{m}} \quad (2.26)$$

so that the ratio of the final axial temperature to the initial axial temperature is

$$\frac{T_1}{T_0} = \left(\frac{\Delta u_1}{\Delta u_0} \right)^2 \approx \frac{2mu_0^2}{qU}. \quad (2.27)$$

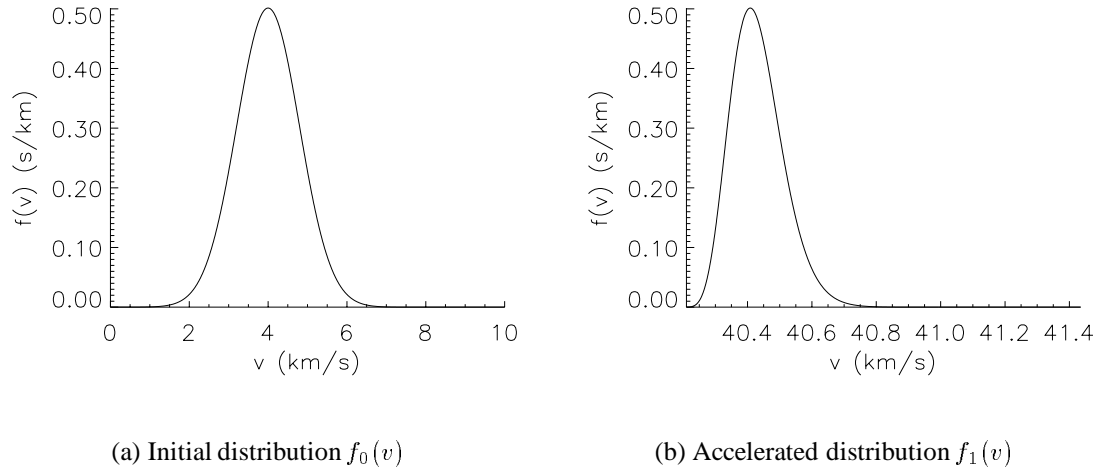


Figure 2.3: Kinematic distortion of an initially-Maxwellian distribution ($T = 10^4$ K, $u_0 = 4$ km/s) by electrostatic acceleration ($U = 1100$ V).

Kinematic compression distorts velocity distributions, as well as narrowing them. Consider the initially Maxwellian distribution ($T = 10^4$ K, $u_0 = 4$ km/s) shown in Figure 2.3(a); after electrostatic acceleration through $U = 1100$ V, the resulting distribution (shown in Figure 2.3(b)) is not only considerably narrowed, but is also asymmetric, with an extended high-velocity tail.

The above calculations only apply if the acceleration is collisionless and steady-state. Though collisionless acceleration is a reasonable assumption for electrostatic thrusters, steady-state operation is not. Hall thrusters are particularly prone to a wide variety of plasma oscillations. Some of these oscillations, such as the “breathing-mode” instability [28], cause the mean axial location of the ionization zone to vary chaotically. This oscillation, in turn, causes fluctuations in the ion velocity distribution. For time-averaged diagnostics (such as LIF), these high-frequency oscillations cause an apparent broadening in the measured ion velocity distribution.

2.5 Summary

Because of their high exhaust velocity and efficiency, Hall thrusters and ion engines are rapidly gaining favor in new spacecraft architectures. Though the basic physics underlying both devices is well-understood, much remains unknown. For instance, it is still not clear whether wall collisions or turbulence cause anomalous diffusion in Hall thrusters, or what causes the “luminous spike” observed on the Hall thruster centerline. In ion engines, the “potential hill” found immediately downstream of the discharge cathode still has multiple explanations. A better understanding of the physics of erosion, which is an active field of investigation in both devices, could lead to longer operating lifetimes.

The ability to non-invasively measure neutral and ion velocity distributions can help shed light on most, if not all, of these poorly-understood processes.

CHAPTER III

FOURIER-TRANSFORM DECONVOLUTION

Showing a Fourier transform to a physics student generally produces the same reaction as showing a crucifix to Count Dracula. – *J. F. James* [29]

In an ideal world, all measurements could be taken with infinite resolution. Images taken with an ideal camera would be clear and sharp, with none of the blurring caused by finite apertures or optical imperfections. Spectral lines would be perfect peaks, without instrument, linewidth or Doppler broadening. Langmuir probe sweeps would show every miniscule change in plasma properties from point to point, with none of the averaging caused by finite probe tips and sheath thicknesses. Even our stereo systems would faithfully reproduce the exact sounds of the original studio session, far past the limiting frequencies of the human ear.

Unfortunately, the real world is less forgiving. Finite apertures blur camera images, finite plasma temperatures blur spectra, finite tip sizes blur Langmuir sweeps, and finite frequency response blurs stereo fidelity.

Convolution is a useful way to mathematically describe these blurring, broadening and smoothing effects. The reverse process, called *deconvolution*, allows the recovery of the original, unblurred object shape from an image with a known blurring. Fourier transforms provide a simple method of carrying out this deconvolution.

3.1 Convolution

3.1.1 Definition and properties

Blurring or broadening of an object function $o(x)$ by a spread function $s(x)$ produces an image function $i(x)$. This image function can be expressed as a convolution integral $i(x)$ of the form [75]

$$i(x) = \int_{-\infty}^{\infty} s(x - x')o(x') dx'. \quad (3.1)$$

If the area under $s(x)$ is unity,

$$\int_{-\infty}^{\infty} s(x) dx = 1, \quad (3.2)$$

the spread function $s(x)$ is normalized, and Eqn. 3.1 represents a moving weighted average. If we denote convolution by the symbol \otimes , Eqn. 3.1 becomes

$$i = s \otimes o. \quad (3.3)$$

Convolution has the useful mathematical properties of commutativity,

$$a \otimes b = b \otimes a, \quad (3.4)$$

associativity,

$$a \otimes (b \otimes c) = (a \otimes b) \otimes c, \quad (3.5)$$

and distributivity with respect to addition,

$$a \otimes (b + c) = (a \otimes b) + (a \otimes c). \quad (3.6)$$

3.1.2 Fourier transforms

The Fourier transform mathematically decomposes a function into a series of frequency components whose sum is the original waveform. The Fourier transform of $f(x)$

is defined as¹

$$F(\omega) = \int_{-\infty}^{\infty} f(x) e^{-j2\pi\omega x} dx \quad (3.7)$$

while the inverse transform is

$$f(x) = \int_{-\infty}^{\infty} F(\omega) e^{j2\pi\omega x} d\omega. \quad (3.8)$$

The *function domain* x is the independent variable of the measurement space (wavelength, frequency, distance, *etc.*), while the *transform domain* ω is the independent variable of the Fourier space, given in cycles per unit of x . If we denote the forward transform by the operator \mathcal{F} and the inverse transform by the operator \mathcal{F}^{-1} , Eqn. 3.7 and 3.8 become

$$F(\omega) = \mathcal{F}[f(x)] \quad (3.9)$$

and

$$f(x) = \mathcal{F}^{-1}[F(\omega)]. \quad (3.10)$$

The forward transform \mathcal{F} maps points from the function domain to the transform domain, while the inverse transform \mathcal{F}^{-1} maps points from the transform domain to the function domain. Table 3.1 shows symmetry properties of Fourier transforms.

Fourier transforms have the useful mathematical properties of superposition

$$c_0a(x) + c_1b(x) \longleftrightarrow c_0A(\omega) + c_1B(\omega) \quad (3.11)$$

and scale similarity,

$$a(cx) \longleftrightarrow \frac{1}{|c|} A\left(\frac{\omega}{c}\right). \quad (3.12)$$

Fourier transforms also have an interesting property with respect to differentiation:

$$\frac{df(x)}{dx} \longleftrightarrow j\omega F(\omega). \quad (3.13)$$

¹I have adopted the symmetrical convention used by Bracewell [30]; asymmetrical forms are more common, but less handy.

Table 3.1: Symmetry properties of Fourier transforms [30].

function $f(x)$	transform $F(\omega)$
even	even
odd	odd
real and even	real and even
real and odd	imaginary and odd
imaginary and even	imaginary and even
complex and even	complex and even
complex and odd	complex and odd
real and asymmetrical	complex and asymmetrical
imaginary and asymmetrical	complex and asymmetrical
real even plus imaginary odd	real
real odd plus imaginary even	imaginary

Thus, differentiation increases the amplitude of high-frequency components of the original function. Since convolution is an integrating process, this property suggests that high-frequency noise will tend to cause problems with deconvolution.

In convolution and deconvolution of LIF spectra, there are three functions whose Fourier transforms are especially worth noting. The rect function, defined by

$$\text{rect}(x) = \begin{cases} 0, & |x| > 1/2, \\ 1/2, & |x| = 1/2, \\ 1, & |x| < 1/2, \end{cases} \quad (3.14)$$

is a computationally simple function often used to filter out high-frequency noise in the transform domain. The Fourier transform of $\text{rect}(x)$ is

$$\mathcal{F}[\text{rect}(x)] = \int_{-1/2}^{1/2} e^{-j\omega x} dx. \quad (3.15)$$

Using the identity $e^{-j\omega x} = \cos(\omega x) - j \sin(\omega x)$ simplifies this to

$$\mathcal{F}[\text{rect}(x)] = \frac{\sin(\pi\omega)}{\pi\omega}. \quad (3.16)$$

In terms of the function $\text{sinc}(x) = \sin(\pi x)/(\pi x)$, the mapping is

$$\text{rect}(x) \longleftrightarrow \text{sinc}(\omega). \quad (3.17)$$

The sinc function, with its distinctive “ringing” pattern, often appears in physical form. Two examples include the Fraunhofer diffraction pattern formed by light passing through a narrow slit, and a low-pass filter’s time response to an impulsive signal. Figures 3.1(a) and 3.1(b) show this Fourier transform pair.

The second function, the Gaussian distribution, is ubiquitous in physics. The most obvious example of a Gaussian in the context of this dissertation is the Maxwellian velocity distribution of an equilibrium gas or plasma, but Gaussians show up whenever there are additive random processes. The function $e^{-x^2/2}$ has the Fourier transform

$$\mathcal{F} [e^{-\pi x^2}] = \int_{-\infty}^{\infty} e^{-j2\pi\omega x - \pi x^2} dx. \quad (3.18)$$

Substituting a change of variable $z \equiv x + j\omega$ and the identity

$$\int_{-\infty}^{\infty} e^{-\pi z^2} dz = 1 \quad (3.19)$$

yields the mapping

$$e^{-\pi x^2} \longleftrightarrow e^{-\pi\omega^2}. \quad (3.20)$$

Thus, the Fourier transform of a Gaussian function is another Gaussian. Figures 3.1(c) and 3.1(d) show this Fourier transform pair.

The third function, the symmetrical exponential, is the even component of exponential decay from a steady state. The function $e^{-|x|}$ has the Fourier transform

$$\mathcal{F} [e^{-|x|}] = \int_{-\infty}^0 e^{x-j2\pi\omega x} dx + \int_0^{\infty} e^{-x-j2\pi\omega x} dx. \quad (3.21)$$

Substituting changes of variables $y = (1 - j2\pi\omega)x$ and $z = (1 + j2\pi\omega)x$ yields the mapping

$$e^{-|x|} \longleftrightarrow \frac{2}{1 + (2\pi\omega)^2}. \quad (3.22)$$

The transform of a symmetrical exponential is thus a Lorentzian distribution. Lorentzian distributions show up frequently as homogeneous broadening functions in spectroscopy.

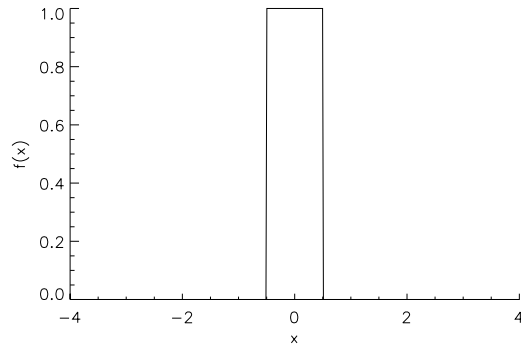
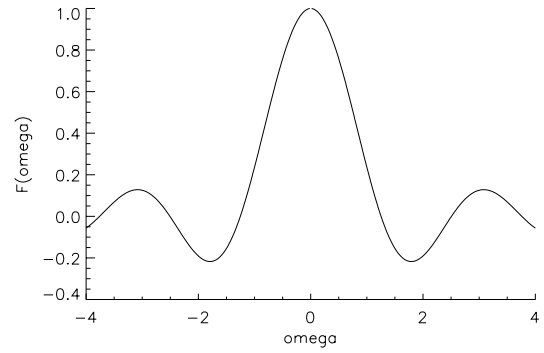
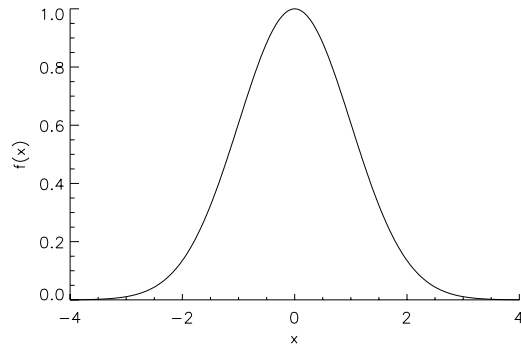
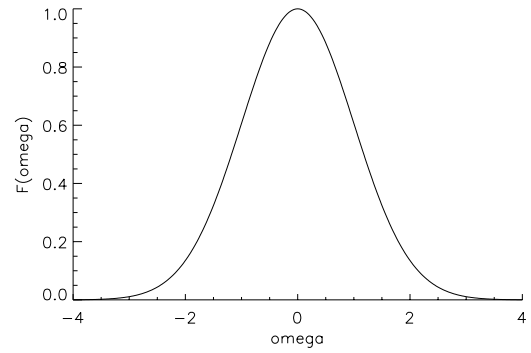
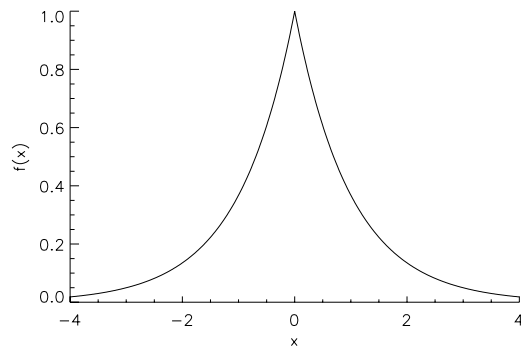
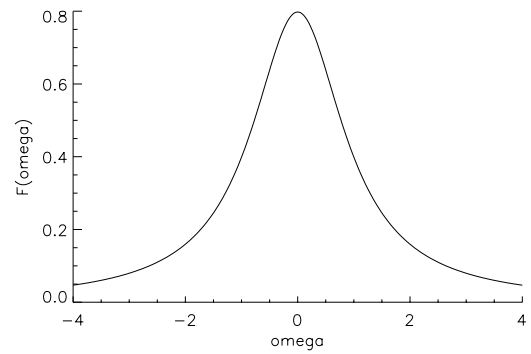
(a) $f(x) = \text{rect}(x)$ (b) $F(\omega) = \text{sinc}(\omega)$ (c) $f(x) = \exp(-\pi x^2)$ (d) $F(\omega) = \exp(-\pi \omega^2)$ (e) $f(x) = \exp(-|x|)$ (f) $F(\omega) = \frac{2}{1+(2\pi\omega)^2}$

Figure 3.1: Fourier transform pairs.

The Lorentzian of particular interest in this dissertation is the “natural” or lifetime broadening of spectral lines. Figures 3.1(e) and 3.1(f) show this Fourier transform pair.

3.1.3 Convolution theorem

Given the Fourier transforms $S(\omega) = \mathcal{F}[s(x)]$ and $O(\omega) = \mathcal{F}[o(x)]$ of the object and spread functions $o(x)$ and $s(x)$, the convolution theorem [76] states that the convolution

$$i(x) = s(x) \otimes o(x) \quad (3.23)$$

is equivalent to the product

$$I(\omega) = S(\omega)O(\omega) \quad (3.24)$$

where $I(\omega) = \mathcal{F}[i(x)]$ is the Fourier transform of $i(x)$. Thus, convolution in function space maps to multiplication in transform space,

$$s(x) \otimes o(x) \iff S(\omega)O(\omega). \quad (3.25)$$

3.2 Deconvolution

As in section 3.1.1, consider an unknown object function $o(x)$ that is blurred by a known spread function $s(x)$ to produce a measured image function $i(x)$:

$$i(x) = s(x) \otimes o(x) \quad (3.26)$$

We can define a deconvolution operator \oslash such that

$$o(x) = i(x) \oslash s(x). \quad (3.27)$$

The commutative property of convolution implies that deconvolution is also commutative,

$$s(x) = i(x) \oslash o(x). \quad (3.28)$$

Since velocity distributions tend to broaden LIF spectra, this property becomes extremely important in their deconvolution.

3.2.1 Simple inverse filter

The deconvolution approach known as *inverse filtering* [31] looks for a linear filter function $y(x)$ that will reverse the blurring caused by the spread function $s(x)$:

$$o(x) = y(x) \otimes i(x). \quad (3.29)$$

By the convolution theorem (Eqn. 3.24), the object transform is the product of the filter transform and the image transform:

$$O(\omega) = Y(\omega)I(\omega). \quad (3.30)$$

If the original convolution is perfectly described by Eqn. 3.26, the object transform is

$$O(\omega) = \frac{I(\omega)}{S(\omega)}. \quad (3.31)$$

The resulting simple inverse filter transform

$$Y_s(\omega) = \frac{1}{S(\omega)} \quad (3.32)$$

returns an object function estimate $\hat{o}_s(x)$.

This estimate is exactly the same as the object $o(x)$, as long as the image is perfectly noiseless. Unfortunately, real image functions are almost never noiseless.

In most situations, a better model of the imaging process than Eqn. 3.26 is given by

$$i(x) = s(x) \otimes o(x) + n(x) \quad (3.33)$$

where $n(x)$ is an additive, zero-mean noise function. By superposition (Eqn. 3.11) and the convolution theorem (Eqn. 3.24), the image transform is

$$I(\omega) = S(\omega)O(\omega) + N(\omega). \quad (3.34)$$

The simple inverse filter transform (Eqn. 3.32) gives an object transform estimate

$$\hat{O}_s(\omega) = Y_s(\omega)I(\omega) = O(\omega) + \frac{N(\omega)}{S(\omega)}. \quad (3.35)$$

In function space, this is equivalent to convolving the simple inverse filter $y(x)$ with the noisy image,

$$\hat{o}(x) = y_s(x) \otimes [s(x) \otimes o(x) + n(x)]. \quad (3.36)$$

Since typical spreading functions are primarily low-frequency, the spreading transform magnitude $|S(\omega)|$ goes to zero as $\omega \rightarrow \pm\infty$. Noise, on the other hand, tends to have significant high-frequency components². Thus, $|N(\omega)/S(\omega)| \rightarrow \infty$ at high values of ω , while $N(\omega)/S(\omega)$ flips from positive to negative rapidly. The combined effects strongly amplify high-frequency noise, making the simple inverse filter a poor choice for images with any noise [75].

3.2.2 Rectangular inverse filter

If the spreading function goes to zero at finite frequencies $\pm\Omega$, a classical modification of the simple linear filter is to discard all information at higher frequencies [31]. Given a rectangular inverse filter transform

$$Y_r(\omega) = \frac{\text{rect}(\omega/\Omega)}{S(\omega)}, \quad (3.37)$$

the rectangular-filtered object transform estimate is

$$\hat{O}_r(\omega) = Y_r(\omega)I(\omega) = \begin{cases} O(\omega) + [N(\omega)/S(\omega)], & |\omega| < \Omega/2 \\ 0, & |\omega| \geq \Omega/2. \end{cases} \quad (3.38)$$

In function space, this is equivalent to convolving the simple object estimate $\hat{O}_s(\omega)$ with a sinc function,

$$\hat{o}_r(x) = \Omega \text{sinc}(\Omega x) \otimes \hat{o}_s(x). \quad (3.39)$$

The resulting rectangular object estimate $\hat{o}_r(x)$ has three major drawbacks:

²*White noise*, for instance, is defined as noise of equal amplitude at all frequencies.

1. Discarding all $\omega > \Omega$ limits resolution. This is theoretically a problem, but practically speaking, estimating the bandwidth limit Ω is a matter of user judgement. Smaller values of Ω limit the noise amplification, while larger values of Ω increase the resolution.
2. Positive sidelobes of the sinc function are approximately 13% of the main peak height. The resulting “ringing” unacceptably distorts the object estimate.
3. Negative sidelobes of the sinc function are approximately 22% of the main peak height. These are especially troublesome for applications (such as deconvolving velocity distributions) where negative values are unphysical.

3.2.3 Gaussian inverse filter

The positive and negative sidelobes imposed by the rectangular inverse filter can be avoided by a Gaussian inverse filter transform of the form

$$Y_g(\omega) = \frac{\exp(-[\omega/\Omega]^2)}{S(\omega)}. \quad (3.40)$$

In function space, this is equivalent to convolving the simple object estimate $\hat{O}_s(\omega)$ with a Gaussian,

$$\hat{o}_g(x) = \frac{\Omega}{\pi} \exp(-[\Omega x]^2) \otimes \hat{o}_s(x). \quad (3.41)$$

In practice, a balance between noise amplification and resolution for the Gaussian object estimate $\hat{o}_g(x)$ is found by varying the bandwidth limit Ω . In the absence of *a priori* knowledge of the noise and object function shape, the Gaussian inverse filter is the best choice for deconvolution.

3.2.4 Wiener filter

If we have some *a priori* knowledge of power and noise trends, it is possible to tailor a linear filter for a particular set of data. Define power spectra for object and noise as the

ensemble averages

$$\phi_o(\omega) = \langle |O(\omega)|^2 \rangle \quad (3.42)$$

$$\phi_n(\omega) = \langle |N(\omega)|^2 \rangle. \quad (3.43)$$

An optimal linear inverse filter $y(x)$ produces an object estimate

$$\hat{o}(x) = y(x) \otimes [s(x) \otimes o(x) + n(x)] \quad (3.44)$$

that is closest to $o(x)$ by minimizing the ensemble mean-square error

$$\epsilon^2 = \left\langle \int_{-\infty}^{\infty} |\hat{o}(x) - o(x)|^2 dx \right\rangle. \quad (3.45)$$

Bracewell [32] and Helstrom [33] independently solved $\partial \epsilon^2 / \partial y = 0$, deriving the optimal (or Wiener³) inverse filter transform

$$Y(\omega) = \frac{S^*(\omega)\phi_o(\omega)}{|S(\omega)|^2\phi_o + \phi_n} \quad (3.46)$$

where $S^*(\omega)$ is the complex conjugate of $S(\omega)$. If the noise is additive and has a Gaussian distribution, this is an optimal filter for noise reduction, but does not undo any spreading effects.

3.2.5 Constraints

Deconvolution of a noisy image can result in an object function estimate $\hat{o}(x)$ with negative components, even when the original object function $o(x)$ has no negative components. In order to avoid nonphysical results (such as negative values of the velocity distribution), we can apply a positivity forcing function

$$p[\hat{o}(x)] = \frac{\hat{o}(x) + \sqrt{\hat{o}(x)^2 + \epsilon}}{2}, \quad (3.47)$$

³Named for Wiener's classical smoothing filter [34], designed for extracting noisy data from images without appreciable spreading [$s(x) = \delta(x)$].

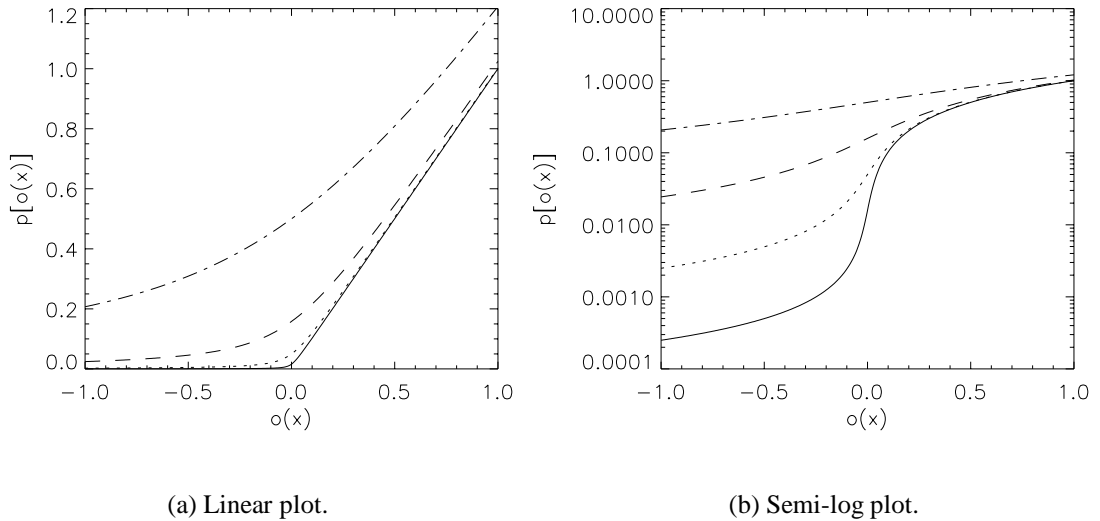


Figure 3.2: Positivity forcing function examples for $\epsilon = [10^{-3}, 10^{-2}, 10^{-1}, 10^0]$.

to the inverse filter output, where ϵ is a user-defined small positive number. Figure 3.2 shows how this function suppresses negative values of the input function $\hat{o}(x)$ while avoiding discontinuities in the output $p[\hat{o}(x)]$.

3.3 Benchmarking

In many applications (such as deconvolution of astronomical images), the spread function $s(x)$ is fairly simple. In these cases, deconvolution is a fairly transparent (though *not* simple) process, which returns an object function estimate $\hat{o}(x)$ that is a more sharply-defined version of the original image function $i(x)$.

When the spread function is complicated, deconvolution is neither simple nor transparent. Features that emerge from the deconvolution process may or may not be apparent in the original image function. Furthermore, image noise can readily produce features in $\hat{o}(x)$ that do not exist in the object function $o(x)$.

A clear benchmarking path is needed to validate the results of deconvolution with a

complicated spread function. This benchmarking should show under what conditions the deconvolution produces believable results, paying especial attention to the image signal-to-noise ratio (SNR) and noise power spectrum $\phi_n(\omega)$. The benchmarking path should be as follows:

1. Analyze sample images for input SNR and $\phi_n(\omega)$. Determine if white noise is an acceptable approximation of the image noise, or if some combination of white and $1/f$ noise (*i.e.*, “pink” noise) is needed.
2. Simulate an image function, using a typical object function and a range of input SNRs. Determine the noise amplification factor (NAF) as a function of filtering bandwidth and input SNR. From these studies, choose an optimal filtering bandwidth.
3. Simulate multiple image functions, using a range of expected object functions and reasonable SNRs; then deconvolve them, using the optimal filtering bandwidth. Compare the resulting object function estimates to the original object functions.
4. Simulate the image given by a point-source object function, $o(x) = \delta(x)$. Measure the width (FWHM) of the deconvolved object estimate as a function of filtering bandwidth.
5. Demonstrate and quantify (in terms of NAF) how well the deconvolution reproduces features broader than this FWHM, using a noiseless object function.

Unfortunately, no amount of benchmarking can completely remove the possibility that a deconvolution technique will return an object function estimate with spurious features. No frequency filter can discriminate between a signal and noise that happen to fall at the

same frequency, while the rectangular and Gaussian inverse filter methods pass all low-frequency components (both signal and noise) equally well.

The best remedy for this problem is repetition. Real object function features will show up with every repeated image, while noise will move around randomly. Spurious, but repeated, features can show up occasionally; in LIF with dye lasers, the joints between 10 GHz scan segments often produce spurious deflections in the LIF spectrum. However, reference to the original image function can usually help identify these spurious features, while shifting the x -range slightly will quickly show if a suspected feature is real or a scan joint. Most spurious features, however, will move with repetition.

In this respect, deconvolution is like a mass spectrometer, $\mathbf{E} \times \mathbf{B}$ probes, or any other instrument; it readily returns a trace that is a combination of signal and noise. Distinguishing which is which, as always, is up to the operator.

3.4 Summary

Fourier-transform deconvolution is a powerful tool for recovering an object function $o(x)$ from a distorted image $i(x)$. Since deconvolution tends to preferentially amplify high-frequency noise, deconvolution techniques require some sort of low-pass filter to improve the signal-to-noise ratio. Simple truncation of the unfiltered deconvolution in transform space, though computationally simple, corresponds to convolution with a sinc function, producing undesirable “ringing” artifacts in the object estimate $\hat{o}(x)$. A Gaussian inverse filter neatly avoids these artifacts, and returns a better estimate of the original object function. If *a priori* knowledge of the object and noise power spectra is available, a Wiener filter produces the closest possible match between the true object $o(x)$ and the estimate $\hat{o}(x)$.

CHAPTER IV

LASER-INDUCED FLUORESCENCE OF Xe II

How do you shoot a spectre through the heart, slash off its spectral head, take it by its spectral throat? – *J. Conrad* [35]

4.1 Historical background

At about the same time that EP experimental research began in earnest, lasers first emerged as a light source for optical diagnostics. Schawlow and Townes first proposed that stimulated emission of radiation could be amplified in an optical cavity in 1958¹. Maiman [38] built the first ruby laser in 1960, and Javan [39] operated a helium-neon continuous-wave (cw) laser in 1961. Practical use of lasers for spectroscopy, however, had to wait until the development of tunable lasers, which allow access to a wide range of visible and near-visible wavelengths. Pulsed dye lasers, first demonstrated in 1967, led the way to Peterson's development of the cw dye laser in 1970 [40]. Jet-stream dye circulation systems, pioneered by Runge and Rosenberg in 1972 [41], greatly improved the stability of high-power dye laser systems, and the modern, computer-controlled, narrow-linewidth traveling-wave cw ring dye laser system was well developed by the early 1980s [42].

Both pulsed and cw ring dye lasers proved especially useful in the diagnosis of flowing plasmas, such as those found in the plumes of EP devices. Older techniques, such as

¹Gould has maintained (and won in court) a prior claim on inventing the laser. Townes, however, got the Nobel Prize. Townes [36] & Taylor [37] give conflicting accounts of what happened.

optical absorption spectroscopy (OAS) and Rayleigh scattering, became much easier with these new light sources. Tunable lasers also allowed new single-point techniques, such as coherent anti-Stokes Raman scattering (CARS), degenerate four-wave mixing (DFWM), optogalvanic spectroscopy (OGS) and laser-induced fluorescence (LIF) [43].

Early use of LIF for EP concentrated on relatively high-density systems. Zimmerman and Miles [45] developed a technique for measuring hypersonic wind-tunnel velocities via helium Doppler-shifted LIF in 1980. This technique was adapted for use in hydrazine and hydrogen arcjets in the early 1990s by Erwin [46] and Liebeskind [47, 48, 49, 50, 51, 52], both of whom used hydrogen Balmer- α line LIF to measure radial profiles of axial velocity. Ruyten and Keefer [53] developed a multiplex LIF method to simultaneously measure axial and radial velocity components of an argon arcjet, using an optogalvanic cell as a stationary reference plasma.

LIF methods were quickly applied to lower-density EP systems, such as Hall thrusters and ion engines. Gaeta *et al.* pioneered the use of LIF as an erosion rate diagnostic in 1992, measuring the relative density of ground-state sputtered molybdenum (Mo I) at 390.2 nm. Both the initial proof-of-concept experiment [55] and subsequent measurements downstream of an ion engine accelerator grid [56] concentrated on density, rather than velocity. In 1994, Manzella [57] reported the first use of a diode laser to excite the 834.7 nm transition of singly-ionized xenon (Xe II), measuring axial and azimuthal velocity components in a Hall thruster plume. This transition, though easily reached with inexpensive and simple diode lasers, does not have any published values for its hyperfine structure (hfs). This unknown hfs and the laser's relatively wide linewidth prevented Manzella from making accurate temperature estimations.

Cedolin [7, 8, 9] reported Hall thruster plume LIF measurements in 1997, using a diode laser to excite the 823.2 nm transition of neutral xenon (Xe I) and a narrow-linewidth

ring dye laser to excite the 605.1 nm transition of Xe II. Both of these transitions have a well-established hfs [70, 71, 73], permitting accurate computational modeling of the absorption spectrum. Cedolin extracted the axial velocity and temperature by fitting the measured LIF spectrum to a Doppler-shifted, Doppler-broadened spectrum model.

In 1999, Keefer [10] combined Cedolin’s method with two-component multiplex LIF of Xe II at 605.1 nm to measure axial and radial velocity and temperature in an anode layer thruster (TAL) plume, while Williams *et al.* used the same line and technique to make two-component multiplex measurements in a hollow cathode discharge plume [58] and three-component multiplex measurements in the P5 Hall thruster plume [11]. Sadeghi *et al.* [6] also reported radial and axial velocities from 605.1 nm Xe II LIF surveys in a Hall thruster plume in 1999, but omitted temperature measurements, possibly because of concerns over artificial broadening of the velocity distribution by thruster oscillations.

In 2000, Hargus reported Xe I (823.2 nm) and Xe II (834.7 nm) LIF measurements of axial and radial velocities inside a Hall thruster discharge chamber [13, 14]. Dorval [60, 61] reported Xe II (834.7 nm) LIF measurements of axial velocities inside a Hall thruster, while Pollard and Beiting [59] reported three-component orthogonal measurements in a Hall thruster plume using the same line.

4.2 Xe II spectroscopy

Singly ionized xenon, Xe II, is the dominant species² in Hall thruster and ion engine plumes. Xe II has two ground states³, $5s^25p^5\ ^2P_{3/2}^0$ and $5s^25p^5\ ^2P_{1/2}$, both of which result from removal of a p -electron from the closed outer shell of the neutral (Xe I) ground state

²In terms of flux; Xe I has higher number density, but moves much more slowly.

³I use the standard notation for LS coupling throughout this dissertation, rather than the jK notation favored by Cedolin [9] and Hargus [14]. Hansen and Person [62] point out that Xe II falls in the intermediate regime, where either designation scheme suffices. Martin and Wiese [64] give an excellent on-line summary of both notation schemes.

in which fluorescence occurs on a different spectral line than the excitation. Scattered laser radiation can thus be filtered out of the collected fluorescence, removing a large dc component from the phase-locked amplifier signal.

Xe II has a number of metastable states from 11.8 to 14.8 eV above the $^2P_{3/2}^0$ ground state, as shown in Fig 4.1. Two metastable states have previously been used for Xe II LIF of EP devices. Manzella [57], Hargus [13, 14], Pollard and Beiting [59] and Dorval [60, 61] used the 834.7 nm output of a cw diode laser to excite the $5d\ ^2F_{7/2}$ metastable to the $6p\ ^2D_{5/2}^0$ radiative state, and collected fluorescence from the $6s\ ^2P_{3/2} - 6p\ ^2D_{5/2}^0$ transition at 541.9 nm. This absorption, though accessible to easily-operated diode lasers, has no published hyperfine structure constants, and thus cannot be accurately modeled.

Cedolin [7, 8, 9], Williams [11, 58, 12], Keefer [10], and Sadeghi [6] used the 605.1 nm output of a cw dye laser to excite the $5d\ ^4D_{7/2}$ metastable to the $6p\ ^4P_{5/2}^0$ radiative state, and collected fluorescence from the $6s\ ^4P_{5/2} - 6p\ ^4P_{5/2}^0$ transition at 529.2 nm. This absorption is not accessible to diode lasers, but it is the only Xe II line with a well-characterized hyperfine structure⁴.

4.3 LIF line model

As noted in Chapter 1, Xe II LIF results from the absorption, and subsequent spontaneous emission, of light energy by singly-ionized xenon. Non-resonant LIF can be modeled as a four-level system, where the subscript 0 denotes the ground state, 1 denotes the initial metastable state, 2 denotes the upper excited state, and 3 denotes the final state. The total fluorescence signal power reaching the photomultiplier tube from an interrogation

⁴Bröstrom *et al.* [73], who published the most recent nuclear-spin splitting constants for the $5d\ ^4D_{7/2}$ and $6p\ ^4P_{5/2}^0$ states, also reported nuclear-spin splitting constants for the $6p\ ^2D_{5/2}^0$ and $6p\ ^4D_{7/2}^0$ states. Unfortunately, isotopic splittings for the 553.1 nm and 547.2 nm transitions from these states to their common $5d\ ^4D_{7/2}$ metastable are not published, so these lines must remain unmodeled.

volume V can be expressed as

$$S_f = \eta_d \frac{\Omega}{4\pi} A_{23} h \nu_{23} N_2 \quad (4.2)$$

where η_d is the detection system efficiency, Ω is the collection optics solid angle, A_{23} is the spontaneous emission coefficient for the $2 \rightarrow 3$ transition, ν_{23} is the frequency of the $2 \rightarrow 3$ line and N_2 is the upper state population.

4.3.1 Two-level model

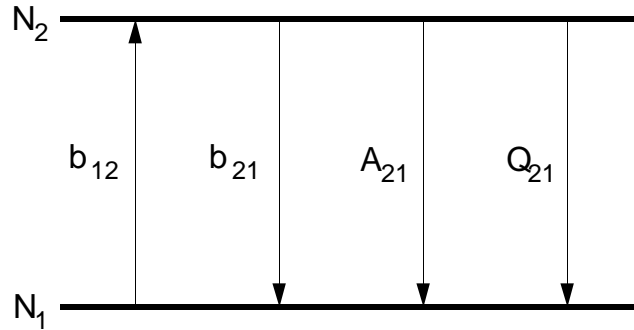


Figure 4.2: Two-level model for laser absorption, line emission and quenching.

In EP device plumes, the upper state is populated by a combination of radiative and collisional processes. Figure 4.2 shows a simple two-level model, taken by Cedolin [9] and Hargus [14] from Berg[78] and Eckbreth [79]. Though this model ignores collisional excitation to the upper state (or, for that matter, the existence of state 3), it nonetheless provides a reasonable approximation to the variation of upper state population with laser intensity. This model assumes number conservation ($N_1 + N_2 = N_1^0$, a constant), where N_1 is the lower state population. The upper state is populated by absorption alone, while the lower state is populated by spontaneous emission, stimulated emission and collisional quenching.

Absorption of laser light with intensity I_ν at a laser frequency ν causes a rate of change

for each population, given by

$$\frac{dN_1}{dt} = -b_{12}(\nu)N_1 + (b_{21}(\nu) + A_{21} + Q_{21})N_2 \quad (4.3)$$

$$\frac{dN_2}{dt} = b_{12}(\nu)N_1 - (b_{21}(\nu) + A_{21} + Q_{21})N_2 \quad (4.4)$$

where the absorption probability

$$b_{12}(\nu) = B_{12}I_\nu i(\nu)/c, \quad (4.5)$$

is a function of the absorption coefficient B_{12} , the stimulated emission probability

$$b_{21}(\nu) = B_{21}I_\nu i(\nu)/c \quad (4.6)$$

is a function of the stimulated emission coefficient B_{21} , A_{21} is the spontaneous emission coefficient and Q_{21} is the collisional quenching rate for the $2 \rightarrow 1$ transition. The unsaturated spectral lineshape $i(\nu)$, which is normalized by

$$1 = \int_{-\infty}^{\infty} i(\nu) d\nu \quad (4.7)$$

has units of time⁵, while the intensity I_ν (power per unit area) can be approximated by

$$I_\nu \approx \frac{P_L}{\pi r_b^2} \quad (4.8)$$

where P_L is the laser power delivered to the interrogation volume and r_b is the beam waist radius.

Since spontaneous emission coefficients tend to be on the order of 10^8 s^{-1} , a steady-state ($\partial/\partial t = 0$) approximation is appropriate for practical laser chopping frequencies, which tend to be on the order of kHz⁶. The steady-state upper level population is then

$$N_2 = N_1^0 \frac{B_{12}}{B_{12} + B_{21}} \frac{1}{1 + I_s(\nu)/I_\nu} \quad (4.9)$$

⁵Thus, if frequency ν is given in MHz, the corresponding lineshape $i(\nu)$ unit is μs .

⁶Vitanov *et al.* [66] point out that LIF spectra produced by extremely short-pulse lasers (of pulse duration $\tau \ll 2\pi/A_{ij}$) contain two components. Spectra taken during the pulse are power-broadened, but spectra taken after the pulse are not. Thus, high-intensity, picosecond-pulse lasers with gated CCD collection might be capable of two-dimensional LIF without either phase-locked amplification or saturation broadening.

where the two-level model's saturation intensity

$$I_s(\nu) = \frac{A_{21} + Q_{21}}{B_{12} + B_{21}} \frac{c}{i(\nu)} \quad (4.10)$$

varies inversely with the lineshape $i(\nu)$. Since the Einstein coefficients are interrelated (for upper and lower state degeneracies g_2 and g_1) by [80]

$$B_{12} = \frac{g_2}{g_1} B_{21} \quad (4.11)$$

$$B_{21} = \frac{\lambda^3}{8\pi h} A_{21}, \quad (4.12)$$

the upper state population becomes

$$N_2 = N_1^0 \left(\frac{g_2}{g_1 + g_2} \right) \frac{1}{1 + I_s(\nu)/I_\nu} \quad (4.13)$$

where the frequency-dependent saturation intensity is

$$I_s(\nu) = \frac{g_1}{g_1 + g_2} \left(1 + \frac{Q_{21}}{A_{21}} \right) \frac{8\pi h c}{\lambda^3 i(\nu)}. \quad (4.14)$$

The saturation intensity can thus be defined as the intensity at a given frequency that would equally populate equally degenerate upper and lower states. In terms of a dimensionless saturation parameter

$$S(\nu) = \frac{I_\nu}{I_s(\nu)} = \frac{g_1 + g_2}{g_1} \left(\frac{A_{21}}{A_{21} + Q_{21}} \right) \frac{\lambda^3 I_\nu}{8\pi h c} i(\nu), \quad (4.15)$$

the upper state population is

$$N_2 = N_1^0 \left(\frac{g_2}{g_1 + g_2} \right) \frac{S(\nu)}{1 + S(\nu)}. \quad (4.16)$$

Figure 4.3 shows how the upper state population (and, thus, the fluorescence intensity) saturates with increasing values of the saturation parameter.

At low laser intensity ($I_\nu \ll I_s(\nu)$), the upper state population is linear with the saturation parameter,

$$\lim_{S(\nu) \rightarrow 0} N_2 = N_1^0 \left(\frac{g_2}{g_1 + g_2} \right) S(\nu), \quad (4.17)$$

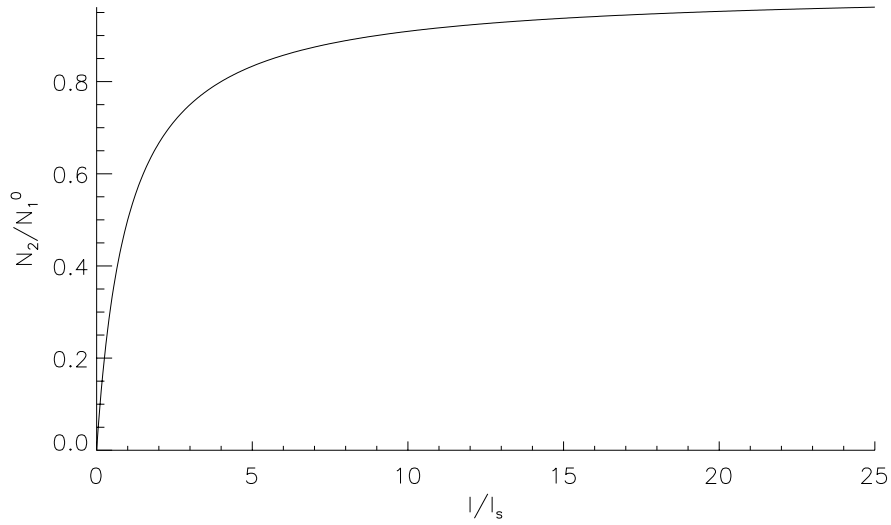


Figure 4.3: Upper state population fraction N_2/N_1^0 as a function of the dimensionless saturation parameter $S(\nu) = I_\nu/I_s(\nu)$.

and is directly proportional to the lineshape $i(\nu)$. At high laser intensity ($I_\nu \gg I_s(\nu)$), the upper state population asymptotically approaches saturation,

$$\lim_{S(\nu) \rightarrow \infty} N_2 = N_1^0 \left(\frac{g_2}{g_1 + g_2} \right). \quad (4.18)$$

Since the saturation parameter $S(\nu)$ is proportional to the lineshape $i(\nu)$, proper saturation modeling will allow lineshape (and, thus, velocity distribution) extraction from moderately saturated fluorescence signals.

If we assume that collisional quenching is negligible ($Q_{21} \rightarrow 0$), the two-level saturation intensity is no longer a function of plasma parameters:

$$I_s(\nu) = \frac{g_1}{g_2 + g_1} \frac{8\pi hc}{\lambda^3 i(\nu)}. \quad (4.19)$$

For the $5d \ ^4D_{7/2} - 6p \ ^4P_{5/2}^0$ transition at 605.1 nm, the degeneracies are $g_1 = 8$ and $g_2 = 6$, so the two-level model with negligible quenching gives a saturation intensity of

$$I_s(\nu) = \frac{32\pi}{7} \frac{hc}{\lambda^3 i(\nu)} = \frac{1.2876 \times 10^{-5} \text{ J}}{i(\nu) \text{ m}^2}. \quad (4.20)$$

4.3.2 Four-level model

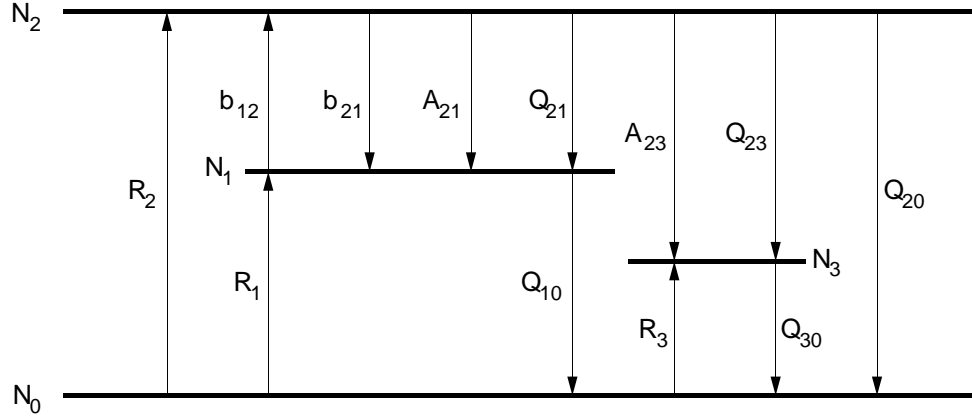


Figure 4.4: Four-level model for laser absorption, line emission, collisional excitation and quenching.

The two-level model, though useful from a conceptual standpoint, fails to account for the large “natural” fluorescence found in an EP plume. Natural, or collisionally-excited, fluorescence overwhelms LIF in EP plasmas; even when narrow-bandwidth filters (such as a monochromator) block all but the fluorescence line, and the steady-state natural fluorescence is rejected by the lock-in amplifier, up to 100 dB of phase-locked amplification is still needed to boost the LIF signal-to-noise ratio to a usable level.

In order to better understand saturation in non-resonant LIF, consider the four-level system shown in Fig. 4.4. Collisional excitation from the ground state population N_0 pumps the first metastable lower-state population N_1 at a rate R_1 , the excited upper-state population N_2 at a rate R_2 , and the final metastable state population N_3 at a rate R_3 . Absorption of laser light with spectral irradiance I_ν at a laser frequency ν further pumps the excited state population N_2 , while spontaneous emission and collisional quenching depopulate each state.

Assuming that fluorescence intensity is much lower than the laser intensity, so that

stimulated emission only depopulates the excited state (N_2), the rate equations are

$$\frac{dN_1}{dt} = R_1 - (b_{12}(\nu) + Q_{10}) N_1 + (b_{21}(\nu) + R_{21}) N_2 \quad (4.21)$$

$$\frac{dN_2}{dt} = R_2 + b_{12}(\nu) N_1 - (b_{21}(\nu) + R_{21} + R_{23} + Q_{20}) N_2 \quad (4.22)$$

$$\frac{dN_3}{dt} = R_3 + R_{23} N_2 - Q_{30} N_3 \quad (4.23)$$

where the absorption probability is

$$b_{12}(\nu) = B_{12} I_\nu i(\nu)/c, \quad (4.24)$$

the stimulated emission probability is

$$b_{21}(\nu) = B_{21} I_\nu i(\nu)/c \quad (4.25)$$

and $R_{ij} = A_{ij} + Q_{ij}$ for each $i \rightarrow j$ transition. Each population can be, in turn, divided into collisionally-excited (N_i^0) and LIF (N_i') components

$$N_1 = N_1^0 + N_1' \quad (4.26)$$

$$N_2 = N_2^0 + N_2' \quad (4.27)$$

$$N_3 = N_3^0 + N_3' \quad (4.28)$$

so that (in the steady-state approximation),

$$0 = R_1 - (b_{12}(\nu) + Q_{10}) (N_1^0 + N_1') + (b_{21}(\nu) + R_{21}) (N_2^0 + N_2') \quad (4.29)$$

$$0 = R_2 + b_{12}(\nu) (N_1^0 + N_1') - (b_{21}(\nu) + R_{21} + R_{23} + Q_{20}) (N_2^0 + N_2') \quad (4.30)$$

$$0 = R_3 + R_{23} (N_2^0 + N_2') - Q_{30} (N_3^0 + N_3'). \quad (4.31)$$

Setting the laser spectral intensity to zero yields the collisionally-excited component equations

$$0 = R_1 - Q_{10} N_1^0 + (b_{21}(\nu) + R_{21}) N_2^0, \quad (4.32)$$

$$0 = R_2 + b_{12}(\nu) N_1^0 - (b_{21}(\nu) + R_{21} + R_{23} + Q_{20}) N_2^0, \text{ and} \quad (4.33)$$

$$0 = R_3 + R_{23} N_2^0 - Q_{30} N_3^0. \quad (4.34)$$

Substituting these back into the full steady-state equations yields (after some algebra) the laser-induced excited-state population

$$N_2' = \frac{Q_{10}}{R_{23} + Q_{20} + (g_1/g_2)Q_{10}} \left(N_1^0 - \frac{g_1}{g_2} N_2^0 \right) \frac{S(\nu)}{1 + S(\nu)} \quad (4.35)$$

where the frequency-dependent saturation parameter is now

$$S(\nu) = \frac{R_{23} + Q_{20} + (g_1/g_2)Q_{10}}{R_{21} + R_{23} + Q_{20}} \left(\frac{A_{21}}{Q_{10}} \right) \frac{\lambda^3}{8\pi h c} i(\nu). \quad (4.36)$$

Again, the saturation parameter $S(\nu)$ is directly proportional to the lineshape $i(\nu)$.

4.3.3 Line shape

As noted in Chapter 1, the normalized absorption spectrum lineshape measured in unsaturated xenon LIF is the convolution of three functions,

$$i(\nu) = h(\nu) \otimes l(\nu) \otimes d(\nu). \quad (4.37)$$

The first function, the hyperfine splitting $h(\nu)$, can be modeled as a series of nineteen Dirac delta functions,

$$h(\nu) = \sum_{i=1}^{19} p_i \delta(\nu - \nu_i), \quad (4.38)$$

where ν_i is the i^{th} hyperfine line center and p_i is the i^{th} hyperfine line intensity. The second function, the natural broadening $l(\nu)$, can be modeled as a Lorentzian distribution whose width is determined by the line's spontaneous transition probability A_{ij} . The third function, the combined Doppler shift and broadening $d(\nu)$, can be directly transformed from the beamwise velocity distribution $f(v_k)$ of the metastable state population.

4.4 Hyperfine structure at 605.1 nm

Multiplet splitting caused by coupling between the electron-spin angular momentum S with the orbital angular momentum L produces the *fine structure* in a species' spectrum

[9]. Each fine-structure level within a multiplet has a unique total electronic angular momentum $\mathbf{J} = \mathbf{S} + \mathbf{L}$. However, closer examination of a line resulting from the transition between two fine-structure levels in a complex species such as xenon shows that the line is even more finely split. This splitting is the result of the species' *hyperfine structure* [63].

Hyperfine structure consists of two components. The first component, known as *isotopic splitting*, is caused by the mass and nuclear volume differences between isotopes in the sample. The second component, known as *nuclear-spin splitting*, is caused by the coupling between the nuclear spin \mathbf{I} and the total electronic angular momentum \mathbf{J} .

4.4.1 Isotopic splitting

There are nine stable isotopes of xenon, seven of which have natural abundances greater than one percent. Each of these isotopes causes a slightly different transition energy E_{ij} . This energy difference is referred to as isotopic splitting.

Isotopic splitting has its origin in two effects, the *mass effect* and the *volume effect* [65]. The mass effect results from movement of the nucleus, and is primarily relevant to light elements ($Z < 30$). For heavy elements ($Z > 60$), the volume effect predominates. For a medium-weight element like xenon, both effects contribute to isotopic splitting.

The mass effect is conventionally separated into two additive components. The first component, called the normal mass shift, represents the contribution of the reduced mass of the electron in the atomic system. The second component, the specific mass shift, arises from interactions between outer electron momenta. Modeling the specific mass shift requires complicated many-body atomic structure calculations.

The volume effect is conventionally modeled as the product of two factors. The first factor, called the field shift, is proportional to the change in the total electron density at the nucleus when the atom undergoes the atomic transition. The second factor, called

the nuclear parameter, represents the change in the mean-square nuclear charge radius between isotopes.

Table 4.1 presents naturally-occurring xenon isotopic abundances and shifts for the $5d^4D_{7/2} - 6p^4P_{5/2}^0$ transition taken from the fast ion-beam LIF surveys of Bingham *et al.* [71] and Borghs *et al.* [72].

Table 4.1: Xenon isotopic abundance [67] and shift relative to ^{132}Xe [71, 72] for the $5d^4D_{7/2} - 6p^4P_{5/2}^0$ transition.

Mass (amu)	124	126	128	129	130	131	132	134	136
Abundance (%)	0.0096	0.009	1.92	26.4	4.1	21.1	26.9	10.4	8.9
Shift (MHz)	336.6	252.4	172.0	113.7	83.6	16.7	0.0	-75.8	-140.9

4.4.2 Nuclear-spin splitting

Seven of the nine stable isotopes of xenon have even atomic mass, resulting in no nuclear spin I . The two isotopes with an odd atomic mass, however, have non-zero nuclear spin quantum numbers I . The lighter isotope, ^{129}Xe , has $I = 1/2$, while ^{131}Xe has $I = 3/2$. These non-zero nuclear spins cause nuclear-spin splitting of the atomic energy levels. This nuclear-spin splitting is considerably broader than the isotopic splitting, and provides most of the $5d^4D_{7/2} - 6p^4P_{5/2}^0$ line's characteristic shape.

The total angular momentum $\mathbf{F} = \mathbf{I} + \mathbf{J}$ takes quantum number values

$$F = I + J, I + J - 1, \dots, |I - J| \quad (4.39)$$

where J is the total electronic angular momentum quantum number [68]. The extra term energy due to nuclear-spin splitting is given by [65]

$$E_{nss} = A \frac{C}{2} + BD, \quad (4.40)$$

where A is the nuclear magnetic dipole interaction constant, B is the nuclear electric

quadrupole interaction constant, and the terms

$$C = F(F + 1) - I(I + 1) - J(J + 1) \quad (4.41)$$

and

$$D = \frac{(3C/4)(C + 1) - I(I + 1)J(J + 1)}{2I(2I - 1)J(2J - 1)} \quad (4.42)$$

contain the nuclear spin-orbit interactions. This model uses Bröstrom's nuclear-spin structure constants for the Xe II $5d^4D_{7/2}$ and $6p^4P_{5/2}^0$ energy levels [73].

The transition rule for nuclear-spin splitting is $\Delta F \equiv F - F' = [0, \pm 1]$, where F is the upper and F' is the lower state's total angular momentum quantum number. (The zero-zero transition is forbidden, $F = 0 \not\rightarrow F' = 0$.) Figure 4.5 shows the fine structure and nuclear-spin splitting for the $5d^4D_{7/2} - 6p^4P_{5/2}^0$ line.

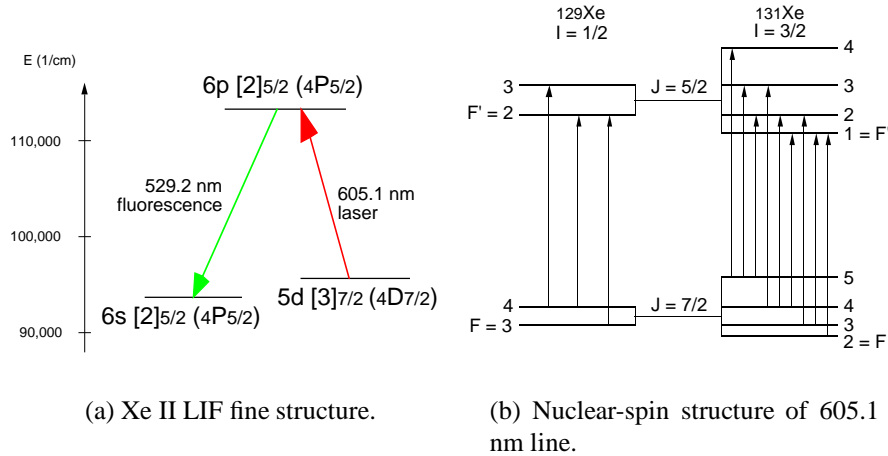


Figure 4.5: Fine and hyperfine structure of Xe II LIF.

4.4.3 Hyperfine line intensity

The relative intensity of each nuclear-spin split component is given for a $J \rightarrow J - 1$ transition by [69]

$$I(F \rightarrow F - 1) \propto \frac{P(F)P(F - 1)}{F} \quad (4.43)$$

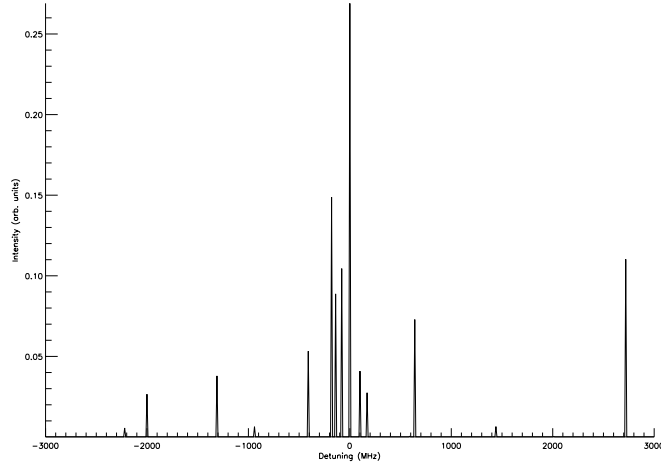


Figure 4.6: Hyperfine splitting $h(\nu)$ for the Xe II $5d^4 D_{7/2} - 6p^4 P_{5/2}^0$ line.

$$I(F \rightarrow F) \propto \frac{(2F + 1)}{F(F + 1)} P(F)Q(F) \quad (4.44)$$

$$I(F - 1 \rightarrow F) \propto \frac{Q(F)Q(F - 1)}{F} \quad (4.45)$$

where $P(F) = (F + J)(F + J + 1) - I(I + 1)$ and $Q(F) = I(I + 1) - (F - J)(F - J + 1)$.

For the isotopes with even mass numbers (i.e., without nuclear-spin splitting), the line intensity p_j is linearly proportional to the naturally-occurring abundance for each isotope. The line intensities of ^{129}Xe and ^{131}Xe are linearly proportional to the product of the isotopic abundance and the relative intensity of the nuclear-spin split components.

Table 4.2 and Fig. 4.6 present hyperfine line intensities p_i and line centers ν_i (relative to ν_o , the line center for ^{132}Xe) for the 605.1 nm absorption hyperfine splitting model of Eqn. 4.38.

4.5 Line broadening

4.5.1 Natural broadening

The probability per unit time that an atom at state i will decay to state j is given by the spontaneous emission coefficient A_{ij} . The total spontaneous transition probability per

Table 4.2: Hyperfine line shifts and intensities for Xe II $5d^4D_{7/2} - 6p^4P_{5/2}^0$.

line	mass		shift		intensity
	M (amu)	F (-)	F' (-)	$\nu_i - \nu_o$ (MHz)	p_i (-)
0	124	-	-	336.6	0.000096
1	126	-	-	252.4	0.000090
2	128	-	-	172.0	0.019200
3	129	3	2	2718.3	0.110167
4	129	3	3	-2194.8	0.005508
5	129	4	3	-182.5	0.148725
6	130	-	-	83.6	0.040800
7	131	2	1	-2000.4	0.026475
8	131	2	2	-938.5	0.006304
9	131	2	3	566.9	0.000315
10	131	3	2	-1335.2	0.037821
11	131	3	3	170.2	0.008273
12	131	3	4	2014.1	0.000236
13	131	4	3	-406.1	0.053186
14	131	4	4	1437.8	0.006382
15	131	5	4	641.3	0.072806
16	132	-	-	0.0	0.268900
17	134	-	-	-75.8	0.104400
18	136	-	-	-140.9	0.088700

unit time for an atom at state i decaying to N levels with energies below E_i is

$$A_i = \sum_{j=1}^N A_{ij}. \quad (4.46)$$

Defining $\tau_i = 1/A_i$, the mean lifetime of state i is

$$\bar{t} = \frac{\int_0^\infty t e^{-t/\tau} dt}{\int_0^\infty e^{-t/\tau} dt}. \quad (4.47)$$

Likewise, the lifetime variance is

$$(\Delta t)^2 = \frac{\int_0^\infty (t - \tau)^2 e^{-t/\tau} dt}{\int_0^\infty e^{-t/\tau} dt} = \tau^2. \quad (4.48)$$

so the lifetime uncertainty is also τ [65].

The Heisenberg uncertainty relation, though usually stated in terms of linear momentum and position uncertainty, can also be stated in terms of energy and time uncertainty

as

$$\Delta E \Delta t \geq \frac{h}{4\pi} \quad (4.49)$$

where h is Planck's constant. Since $E = h\nu$ for a photon, the “natural” linewidth of a state with lifetime uncertainty τ is

$$\Delta\nu = \frac{1}{2\pi\tau}. \quad (4.50)$$

Each $i \rightarrow j$ transition thus has an irreducible homogeneous broadening. The resulting lineshape can be deduced by modeling the resulting wave packet as an exponentially damped wave with frequency ν_o :

$$E(t) = E_0 \exp\left(-2\pi\left[\frac{1}{2\tau} + i\nu_o\right]t\right). \quad (4.51)$$

The Fourier transform of this wave packet's amplitude [65] is

$$A(\nu) = \frac{E_0}{\sqrt{2\pi}} \frac{-1}{i2\pi(\nu_o - \nu) - 1/2\tau} \quad (4.52)$$

whose normalized intensity spectrum is the Lorentzian lineshape [77]

$$l(\nu) = \frac{\Delta\nu_n}{2\pi} \frac{1}{(\nu - \nu_o)^2 + (\Delta\nu_n/2)^2} \quad (4.53)$$

where ν_o is the line center, $\Delta\nu_n = A_i/(2\pi)$ is the natural linewidth, and

$$\int_{-\infty}^{\infty} l(\nu) d\nu = 1. \quad (4.54)$$

The LIF spectrum from a perfectly cold stationary plasma, where the velocity distribution $f(\mathbf{v}) = \delta(\mathbf{v})$, can be described by the convolution

$$c(\nu) = h(\nu) \otimes l(\nu) \quad (4.55)$$

for species with hyperfine structure. Figure 4.7 shows the “cold-plasma spectrum” for the $5d^4D_{7/2} - 6p^4P_{5/2}^0$ line, which forms the computational kernel for the Xe II velocity distribution deconvolution method.

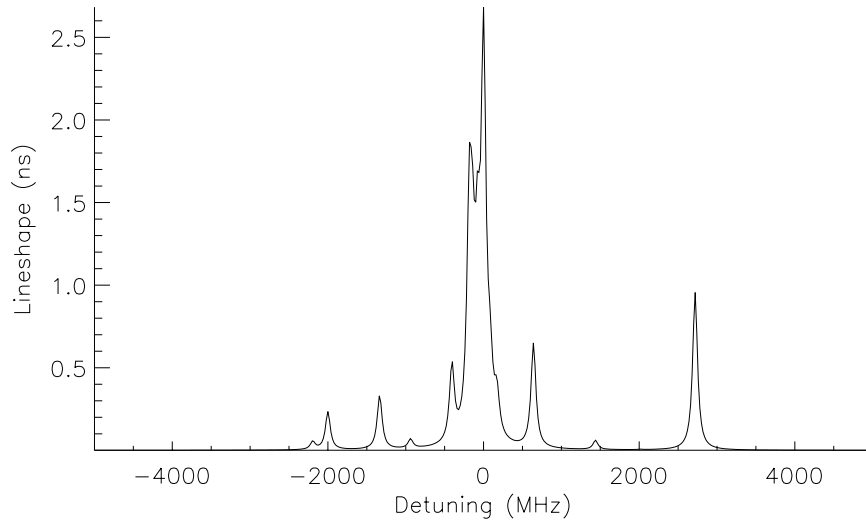


Figure 4.7: Cold-plasma spectrum $c(\nu)$ for the Xe II $5d^4 D_{7/2} - 6p^4 P_{5/2}^0$ line.

4.5.2 Doppler shift and broadening

Consider a light source with vacuum wavelength λ_o and frequency $\nu_o = c/\lambda_o$. An observer who is stationary with respect to the light source will see light at the same frequency ν . An observer moving towards the light source will see a bluer (*i.e.*, higher-frequency) light than the stationary viewer, while an observer moving away from the light source will see a redder (*i.e.*, lower-frequency) light.

In LIF, this Doppler effect appears as a shift in the resonant frequency ν_o as the laser is scanned over a very short frequency range. The change in photon frequency $\Delta\nu = \nu - \nu_o$ for a particle with velocity \mathbf{v} passing through a light beam of wave vector \mathbf{k} is

$$\Delta\nu = -\frac{\mathbf{k} \cdot \mathbf{v}}{2\pi}. \quad (4.56)$$

Given a beamwise velocity component

$$v_k = \mathbf{v} \cdot \hat{\mathbf{k}}, \quad (4.57)$$

Eqn. 4.56 gives the beamwise velocity-to-frequency transformations

$$\nu = \left(1 - \frac{v_k}{c}\right) \nu_0 \quad (4.58)$$

$$v_k = \left(1 - \frac{\nu}{\nu_0}\right) c. \quad (4.59)$$

A swarm of particles with a normalized velocity distribution $f(\mathbf{v})$ will also “see” the frequency of incoming photons shifted by the relative velocity of the particle in the direction of the photon. The resulting Doppler lineshape will be shifted by the beamwise bulk velocity $u_k = \langle \mathbf{v} \cdot \hat{\mathbf{k}} \rangle$ and broadened by the thermal width of the distribution. The generalized Doppler lineshape, when properly normalized so that

$$\int_{-\infty}^{\infty} d(\nu) d\nu = 1, \quad (4.60)$$

is given by

$$d(\nu) = \frac{c}{\nu_0} f\left(\left[1 - \frac{\nu}{\nu_0}\right] c\right). \quad (4.61)$$

When $f(v)$ is a one-dimensional stationary Maxwellian of the form

$$f_m(v) = \left(\frac{M}{2\pi kT}\right)^{1/2} \exp\left(-\frac{Mv^2}{2kT}\right), \quad (4.62)$$

Eqn. 4.61 takes the familiar form [77]

$$d_m(\nu) = \frac{c}{\nu_0} \left(\frac{M}{2\pi kT}\right)^{1/2} \exp\left(-\frac{Mc^2}{2kT} \left[\frac{\nu - \nu_0}{\nu_0}\right]^2\right). \quad (4.63)$$

The LIF spectrum from a warm plasma, where the velocity distribution $f(\mathbf{v}) \neq \delta(\mathbf{v})$, can be described by the convolution

$$w(\nu) = c(\nu) \otimes d(\nu)$$

for species with hyperfine structure. Figure 4.8 shows the “warm-plasma spectrum” for a stationary Xe II plasma with a translational temperature of 600 K.

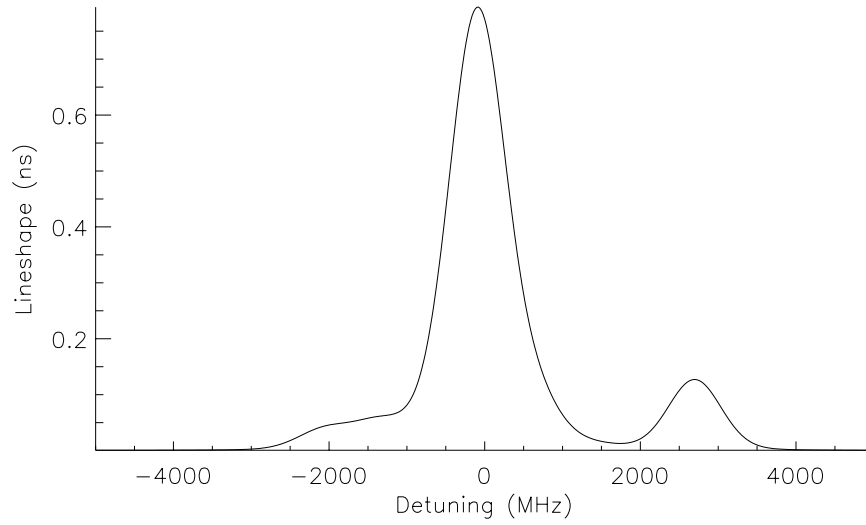


Figure 4.8: Warm-plasma spectrum $w(\nu)$ for the Xe II $5d^4 D_{7/2} - 6p^4 P_{5/2}^0$ line, $T = 600$ K.

4.5.3 Saturation broadening

A third type of line broadening results from line saturation. This effect, which is traditionally called “saturation broadening,” is caused by the nonlinear response of the upper state population to high values of the dimensionless saturation parameter $S(\nu)$. The traditional method of modeling saturation broadening given by Demtröder [43] and Yariv [44] multiplies the linewidth of a homogeneous (*i.e.*, Lorentzian) transition by a constant term,

$$\Delta\nu_s = \Delta\nu_n \sqrt{1 + I_\nu/I_s}. \quad (4.64)$$

In this case, the saturation intensity I_s is not typically considered a frequency-dependent value, but is single-valued. The resulting Lorentzian lineshape of the form

$$l(\nu) = \frac{\Delta\nu_s}{2\pi} \frac{1}{(\nu - \nu_o)^2 + (\Delta\nu_s/2)^2} \quad (4.65)$$

is then convolved with the Doppler broadening and hyperfine structure to create the simulated absorption spectrum.

This traditional approach tends to obscure the underlying distortion effect of saturation, and instead treats saturation broadening as yet another homogeneous broadening mechanism, such as pressure broadening. In fact, the traditional label of “saturation broadening” is misleading. Unlike natural or Doppler broadening, saturation broadening does not reflect inherent properties of either the transition or the velocity distribution. Saturation is really a *distortion*, akin to the nonlinear acoustic response of an overloaded speaker system, which systematically decreases the peak system response amplitude.

Appendix A presents a simple, algebraic transformation that can replace this traditional line-broadening approach to saturation. Unfortunately, I developed this method fairly recently, and did not collect the necessary second scan at each location to apply it to the data reported in this dissertation.

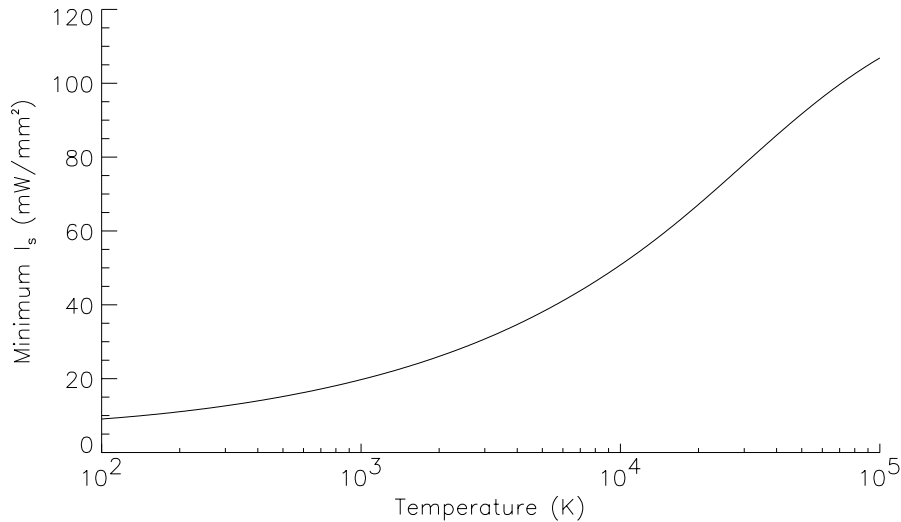


Figure 4.9: Minimum saturation intensity $I_s(\nu)$ as a function of temperature for the simple two-level model of Eqn. 4.20.

There are, however, enough data to determine whether or not the LIF spectra collected in these experiments are saturated, according to the simple two-level model⁷ of Eqn. 4.20.

⁷Recall that this model ignores transitions from state 2 to state 3; therefore, it overestimates the upper state population, and so underestimates the saturation intensity.

Figure 4.9 shows the saturation intensity corresponding to the maximum value of $i(\nu)$ for Maxwellian plasmas with temperatures from 10^2 to 10^5 K. Previous investigations [82] have shown that typical ion temperatures in the Hall thruster plume are around 0.5 eV, which corresponds to a minimum $I_s(\nu)$ of 40.5 mW/mm^2 . An optical loss survey carried out between axial-injection LIF experiments on the P5 showed that 350 mW of dye laser output was attenuated by the beamhandling system to 58 mW at the interrogation volume.

Assuming a beam waist area of approximately 1 mm^2 , the corresponding maximum saturation parameter (using the two-level model) for axial-injection LIF is $S(\nu) = 1.4$. Multiplex LIF, which splits the laser into three beams of approximately equal power, will have saturation parameters approximately one-third as large. In both cases, the LIF spectra are lightly saturated, even using the conservative predictions of the two-level model; therefore, it is reasonable to treat the LIF spectrum $i_s(\nu)$ as linearly proportional to the unsaturated lineshape $i(\nu)$.

4.6 Summary

The absorption spectrum recorded in Xe II LIF can be generalized as the combination of two effects: convolution and saturation.

The unsaturated spectral lineshape $i_s(\nu)$ is the convolution of the hyperfine structure, natural broadening and Doppler broadening of the absorbing transition. Since isotopic shifts and nuclear-spin structure constants for Xe II are currently known only for the $5d^4 D_{7/2} - 6p^4 P_{5/2}^0$ line at 605.1 nm, this is the only line with a known hyperfine structure.

Convolving the hyperfine structure $h(\nu)$ with the natural broadening $l(\nu)$ simulates the LIF spectrum of a perfectly cold, stationary plasma. Convolving the “cold-plasma” spectrum

$$c(\nu) = h(\nu) \otimes l(\nu)$$

with the Doppler broadening $d(\nu)$ simulates the LIF spectrum of a warm, moving plasma,

$$w(\nu) = c(\nu) \otimes d(\nu).$$

If the simulated ion velocity distribution $f(v)$ used to calculate $d(\nu)$ matches the true beamwise ion velocity distribution $f(v_k)$, this “warm-plasma” spectrum $w(\nu)$ is a good match to the unsaturated LIF spectrum $i(\nu)$.

Finally, for a given transition and set of plasma parameters, the saturated LIF spectrum $i_s(\nu)$ can be predicted by a simple algebraic transformation from the unsaturated LIF spectrum $i(\nu)$. For the small maximum values of the saturation parameter $S(\nu)$ seen in these experiments, $i(\nu)$ is approximately linearly proportional to $i_s(\nu)$.

CHAPTER V

COMPUTATIONAL METHODS

And *then!* Oh, the noise! Oh, the Noise! Noise! Noise! Noise!
That's one thing he hated! The NOISE! NOISE! NOISE! NOISE!
– *T. S. Geisel* [83]

Extracting the beamwise¹ velocity distribution $f(v_k)$ from an LIF spectrum $i_s(\nu)$ requires two steps: *desaturation* and *deconvolution*.

Desaturation removes the effects of saturation broadening from the LIF spectrum $i_s(\nu)$ with a simple computational transformation. Unfortunately, this transformation (detailed in Appendix A) requires a fuller data set than collected in these experiments. Section 4.5.3 shows that it is reasonable to assume that the LIF spectra lie within the linear section of the saturation curve, so that $i(\nu)$ is linearly proportional to $i_s(\nu)$.

Deconvolution separates the unsaturated lineshape $i(\nu)$ into its constituents, the cold-plasma spectrum $c(\nu)$ and the Doppler broadening function estimate $\hat{d}(\nu)$. The simple transformation of Eqn. 4.56 and 4.61 then yields an estimate $\hat{f}(v_k)$ of the beamwise velocity distribution $f(v_k)$.

In the absence of noise, these processes are exact, so that $\hat{i}(\nu) = i(\nu)$ and $\hat{f}(v_k) = f(v_k)$. The presence of noise, however, inevitably distorts the estimates. This distortion can be effectively separated into two effects: noise amplification and broadening.

¹“Beamwise” means parallel to the laser beam direction vector $\hat{\mathbf{k}} = \mathbf{k}/|\mathbf{k}|$.

As noted in section 3.3, we need to characterize the noise properties of sample LIF spectra in order to properly estimate of the effects of noise on the deconvolution. Section 5.1 presents an analysis of these noise properties for ensemble averages of typical reference cell and P5 plume LIF spectra. (FMT-2 plume LIF spectra were, at best, only repeated once, giving no ensemble large enough to extract any useful noise property statistics.) Section 5.2 then demonstrates how three candidate deconvolution methods deal with noise amplification and broadening.

5.1 Noise analysis of LIF spectra

5.1.1 Reference cell

The reference cell used in these experiments is a Hamamatsu L2783-42 XeNe-Mo hollow-cathode optogalvanic cell. The relatively cool, steady discharge obtained in this cell provides a repeatable source of xenon ions with zero bulk velocity and good optical access.

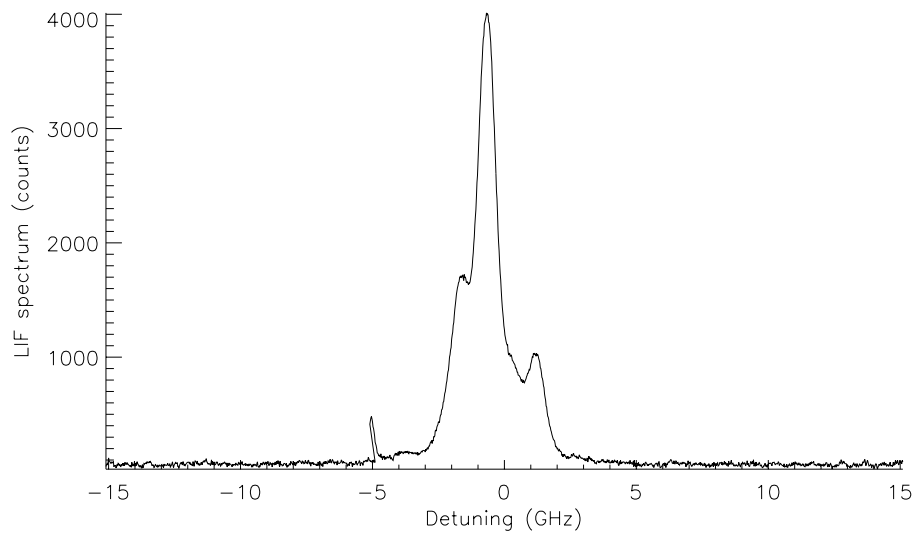
Figure 5.1(a) shows the ensemble average

$$\langle i_s(\nu) \rangle \equiv \frac{1}{N} \sum_{k=1}^N [i_s(\nu)]_k \quad (5.1)$$

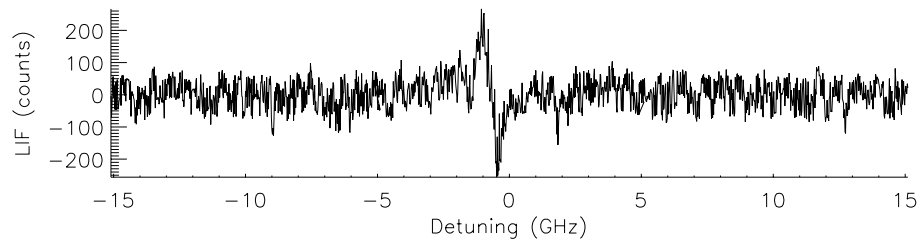
of twelve ($N = 12$) 30-GHz LIF scans of the reference cell, taken at a scan rate of 60 s per 10-GHz scan segment. The dye laser output power during these scans ranged from 327 to 340 mW, of which approximately 8% goes through the reference cell. The abscissa of this plot is in counts of the 12-bit Autoscan analog-to-digital (A-D) converter, which records the Stanford SRS850 lock-in output (at 50 nA full scale with a 300 ms time constant). The 500-count peak at a detuning of -5 GHz is the result of an imperfect joint between 10-GHz scan segments, as noted in section 3.3.

Figure 5.1(b) shows the residual

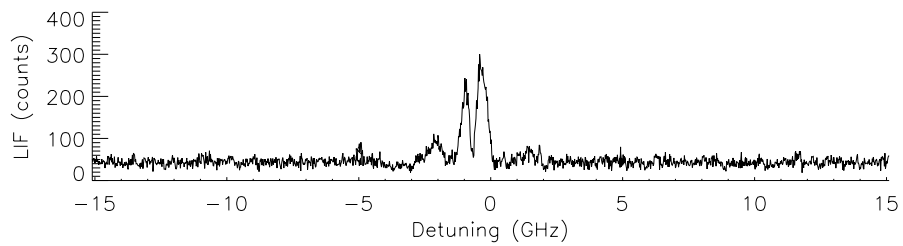
$$[e(\nu)]_k = [i_s(\nu)]_k - \langle i_s(\nu) \rangle \quad (5.2)$$



(a) Ensemble average, $\langle i_s(\nu) \rangle$.



(b) Sample residual, $e(\nu) = i_s(\nu) - \langle i_s(\nu) \rangle$.



(c) Ensemble standard deviation, $\sigma_n(\nu)$.

Figure 5.1: Reference cell LIF spectra.

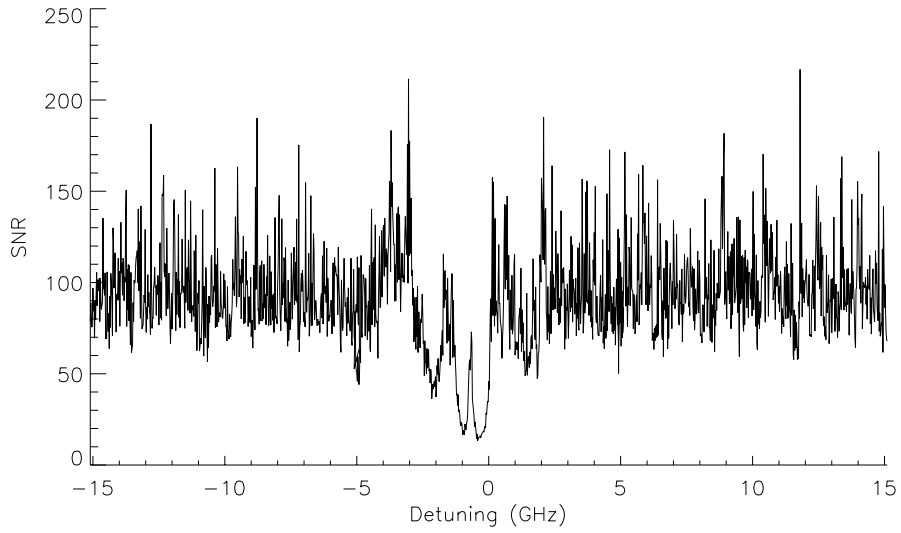


Figure 5.2: Signal-to-noise ratio for reference cell LIF spectra.

for a sample scan, while Fig. 5.1(c) shows the ensemble standard deviation

$$\sigma(\nu) = \left(\frac{1}{N-1} \sum_{k=1}^N [e^2(\nu)]_k \right)^{1/2} \quad (5.3)$$

where $N = 12$ is the number of independent scans. Figure 5.2 shows the signal-to-noise ratio, defined by

$$\text{SNR}(\nu) \equiv \frac{\max\langle i_s(\nu) \rangle}{\sigma(\nu)}, \quad (5.4)$$

for the ensemble. The mean value of $\text{SNR}(\nu)$ is 91.1 for this set of 30-GHz scans; longer scans tend to have higher SNRs (mean $\text{SNR}(\nu) = 117$ for a set of nine 50-GHz scans), while shorter scans have lower SNRs. This trend is readily explained by the higher standard deviation values near the line center.

Figure 5.3 shows the noise power spectrum

$$\phi_n(\tau) \equiv \langle |N(\tau)|^2 \rangle \quad (5.5)$$

where $N(\tau)$ is the Fourier transform of the residual $e(\nu)$. The dashed line shows a reason-

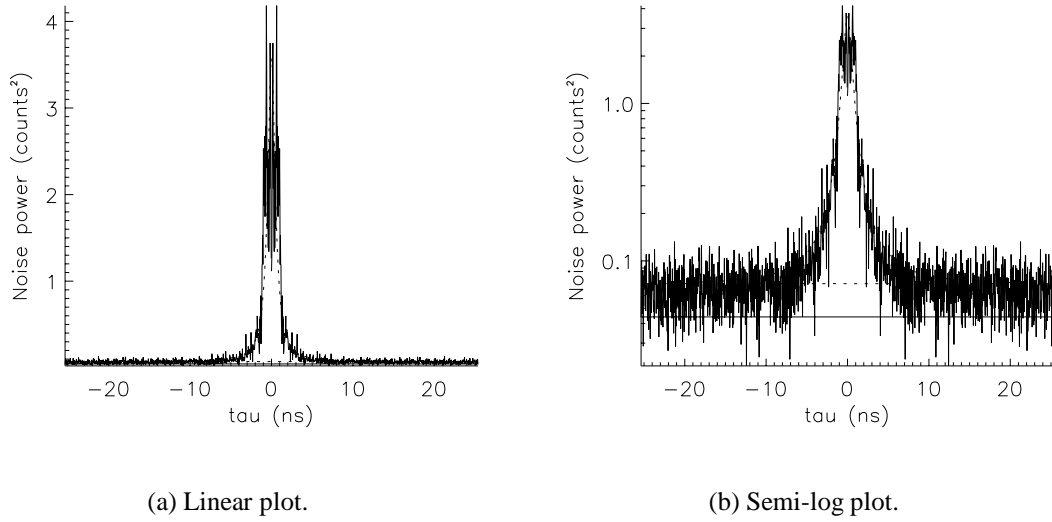


Figure 5.3: Noise power $\phi_n(\tau)$ for reference cell LIF spectra.

able fit to this noise power spectrum, given by the Lorentzian-over-background curve

$$\hat{\phi}_n(\tau) = \phi_w + \frac{\phi_L}{1 + (\tau/\tau_0)^2} \quad (5.6)$$

where $\phi_w = 0.07 \text{ counts}^2$ is the white-noise background, $\phi_L = 3.50 \text{ counts}^2$ is the Lorentzian amplitude and $\tau_0 = 0.55 \text{ ns}$ is the Lorentzian half-width.

If we only consider points on the wings of the LIF spectrum (where $i_s(\nu) \rightarrow 0$), the resulting noise power spectrum shows no structure; *i.e.*, white noise predominates in the wings of the LIF spectrum. Repeated tests with 50-GHz scans give the same result. This suggests that the low-frequency noise shown in Fig. 5.3 reflects laser-plasma interactions, and is not caused by any of the following:

1. natural fluorescence at 529 nm that happens to be at the same frequency and phase as the chopped laser beam;
2. scattered laser light that is not blocked by the monochromator and interference filter;
3. broadband noise from the PMT that is not rejected by the lock-in amplifier;

4. Johnson noise in the coaxial cables linking the lock-in amplifier output to the Autoscan A-D converter; and
5. least-significant-digit error in the Autoscan A-D conversion process.

Low-frequency variations in laser power or reference cell discharge current may be the source of this noise component.

5.1.2 P5 plume

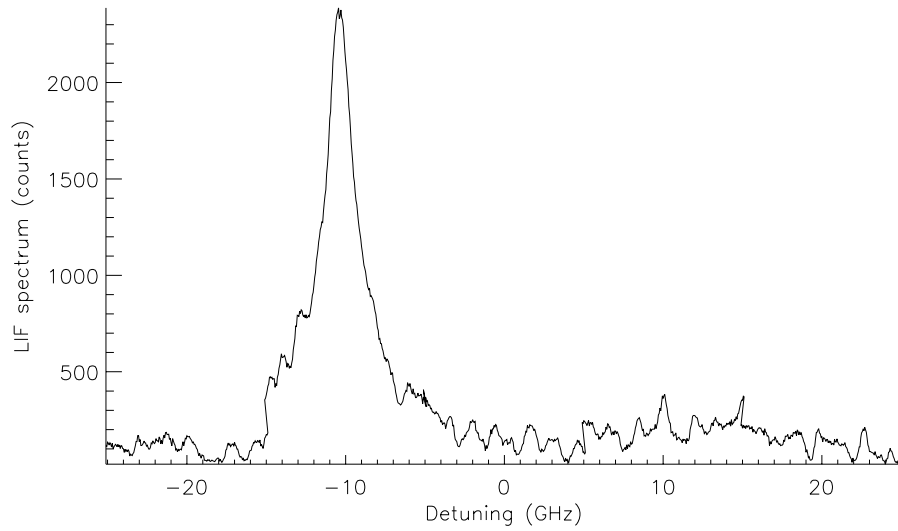
Figure 5.4 shows the ensemble average $\langle i_s(\nu) \rangle$, sample residual $e(\nu)$ and ensemble standard deviation $\sigma_n(\nu)$ for a set of seven 50-GHz LIF scans taken 10 cm downstream of the P5 discharge channel centerline at a scan rate of 60 s per 10-GHz scan segment. The dye laser output power during these scans ranged from 432 to 440 mW, of which approximately 17% is directed into the interrogation volume. As before, the abscissa of this plot is in counts of the 12-bit Autoscan analog-to-digital (A-D) converter, which records the Stanford SRS810 lock-in output (at 500 pA full scale with a 1 s time constant).

Figure 5.5 shows the signal-to-noise ratio for the ensemble. The mean value of $\text{SNR}(\nu)$ is 18.6 for this set of 50-GHz scans; this is artificially low, since scans with higher mean SNRs were only taken once, and thus cannot be ensemble averaged. Nonetheless, this provides a useful lower bound for what (in terms of SNR) constitutes an acceptable LIF scan. Clearly, if the noise statistics are Gaussian, N repeated scans (or equivalently longer scan times) will improve the SNR by a factor of \sqrt{N} .

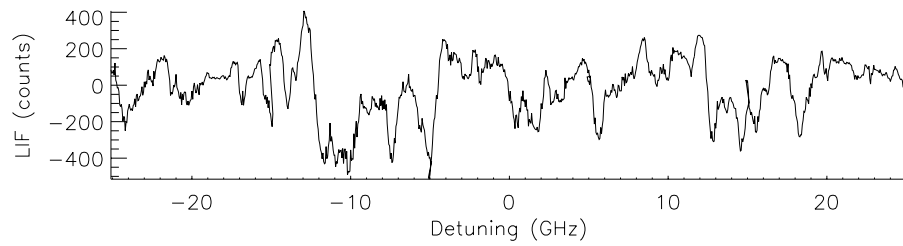
Figure 5.6 shows the noise power spectrum for the ensemble. The dashed line shows a reasonable fit to this noise power spectrum, given by the Gaussian-over-background curve

$$\hat{\phi}_n(\tau) = \phi_w + \phi_L \exp\left(-\left[\frac{\tau}{\tau_0}\right]^2\right) \quad (5.7)$$

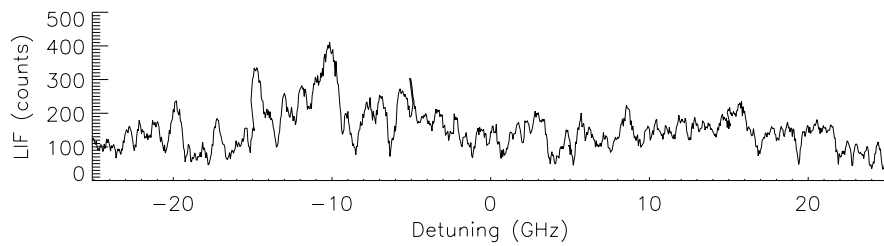
where $\phi_w = 0.038 \text{ counts}^2$ is the white-noise background, $\phi_L = 40 \text{ counts}^2$ is the Lorentzian amplitude and $\tau_0 = 0.60 \text{ ns}$ is the Gaussian $1/e$ width.



(a) Ensemble average, $\langle i_s(\nu) \rangle$.



(b) Sample residual, $e(\nu) = i_s(\nu) - \langle i_s(\nu) \rangle$.



(c) Ensemble standard deviation, $\sigma_n(\nu)$.

Figure 5.4: P5 LIF spectra, 10 cm downstream of discharge channel, 1.6 kW.

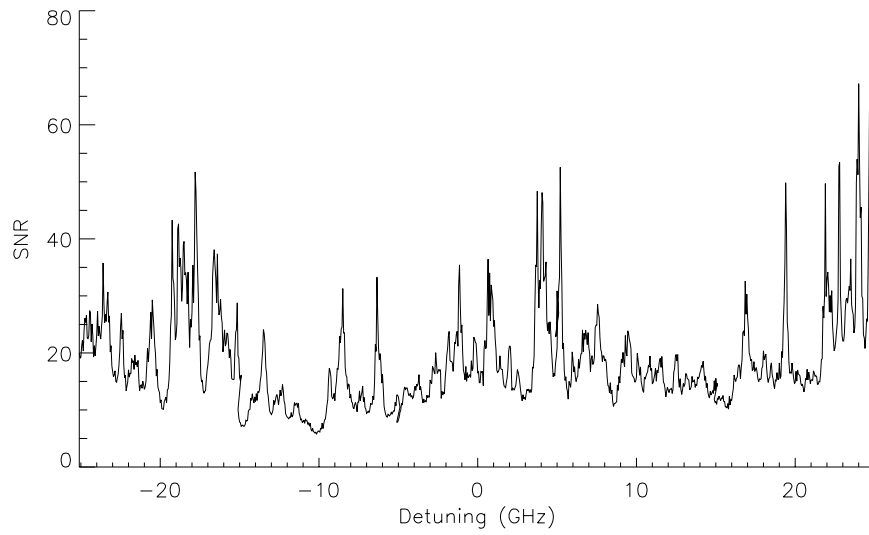
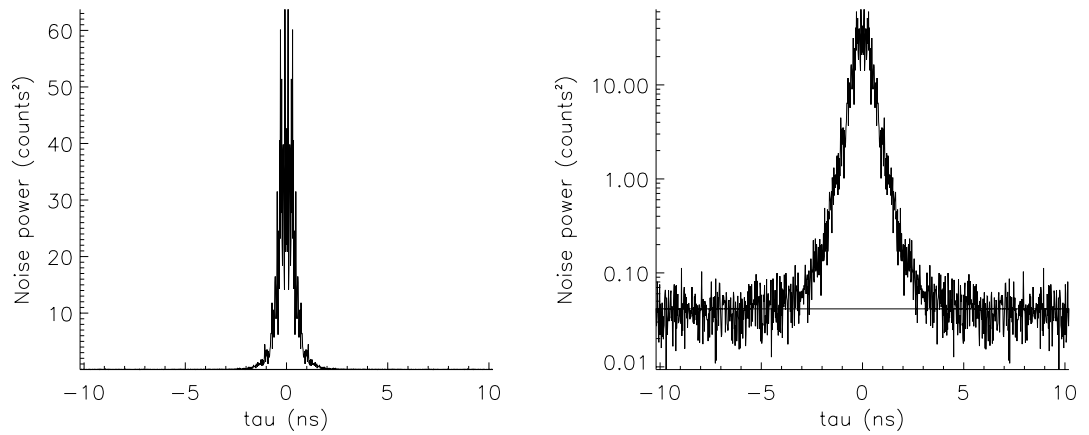


Figure 5.5: Signal-to-noise ratio for P5 LIF spectra.



(a) Linear plot.

(b) Semi-log plot.

Figure 5.6: Noise power $\phi_n(\tau)$ for P5 LIF spectra.

5.2 Deconvolution

The unsaturated LIF spectrum of a warm plasma can be modeled by

$$i(\nu) = c(\nu) \otimes d(\nu) + n(\nu) \quad (5.8)$$

where $c(\nu)$ is the “cold-plasma” spectrum and $n(\nu)$ is a noise function. It then follows that deconvolving the measured LIF spectrum $i(\nu)$ with the cold-plasma spectrum $c(\nu)$ will return an estimate of the Doppler broadening,

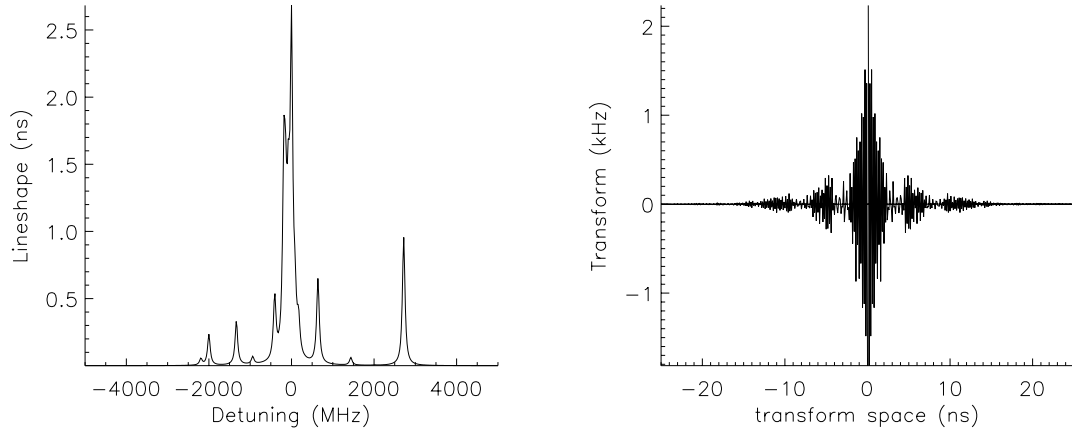
$$\hat{d}(\nu) = i(\nu) \oslash c(\nu) \quad (5.9)$$

which can be converted to a beamwise velocity distribution estimate by the transformation

$$\hat{f}(v_k) = \frac{1}{\lambda_o} \hat{d} \left(\left[1 - \frac{v_k}{c} \right] \nu_o \right) \quad (5.10)$$

where λ_o is the line center wavelength.

5.2.1 Simple inverse filter



(a) Spectrum, $c(\nu)$

(b) Transform, $C(\tau)$

Figure 5.7: Cold-plasma spectrum and transform (computational kernel).

Direct application of the simple inverse filter (Eqn. 3.32) works quite well for extremely low-noise LIF spectra. In this case, the image transform

$$I(\tau) = \int_{-\infty}^{\infty} i(\nu) e^{-j2\pi\tau\nu} d\nu \quad (5.11)$$

maps the frequency-space image function $i(\nu)$ to a corresponding function $I(\tau)$ in a transformed time-space. Likewise, the “spread function” transform

$$C(\tau) = \int_{-\infty}^{\infty} c(\nu)e^{-j2\pi\tau\nu} d\nu \quad (5.12)$$

maps the cold-plasma spectrum $c(\nu)$ to a corresponding function $C(\tau)$ in a transformed time-space, as shown in Fig. 5.7. The object transform estimate

$$\hat{D}(\tau) = \int_{-\infty}^{\infty} d(\nu)e^{-j2\pi\tau\nu} d\nu \quad (5.13)$$

is then given by

$$\hat{D}_s(\tau) = Y_s(\tau)I(\tau) \quad (5.14)$$

where the simple inverse filter transform is

$$Y_s(\tau) = \frac{1}{C(\tau)}, \quad (5.15)$$

while an inverse Fourier transform returns the Doppler broadening function estimate

$$\hat{d}_s(\nu) = \int_{-\infty}^{\infty} \hat{D}_s(\tau)e^{j2\pi\tau\nu} d\tau. \quad (5.16)$$

Figure 5.8 shows velocity distribution estimates for steadily decreasing signal-to-noise values. This technique’s fidelity rapidly diminishes from the nearly-perfect Gaussian reproduced at $\text{SNR} = 10^5$, through light background noise at $\text{SNR} = 10^4$, to the barely-distinguishable signal at $\text{SNR} = 10^3$. At $\text{SNR} = 10^2$, the velocity distribution is completely buried in the noise.

As with desaturation, we can define a frequency-dependant fractional noise power

$$P_n(\nu) = \left[\frac{n(\nu)}{\max |i(\nu)|} \right]^2 \quad (5.17)$$

and a fractional estimation error

$$P_e(\nu) = \left[\frac{\hat{d}(\nu) - d(\nu)}{\max |d(\nu)|} \right]^2, \quad (5.18)$$

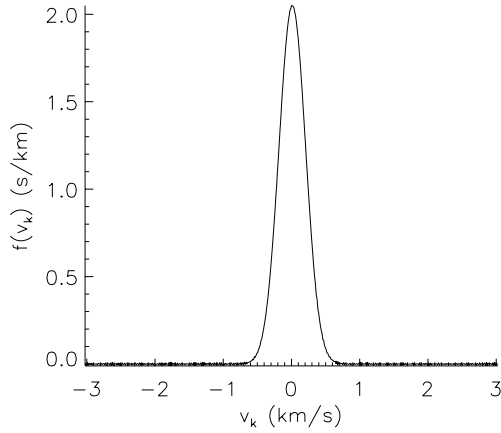
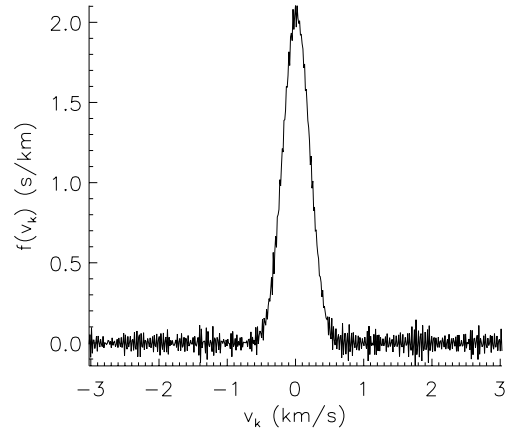
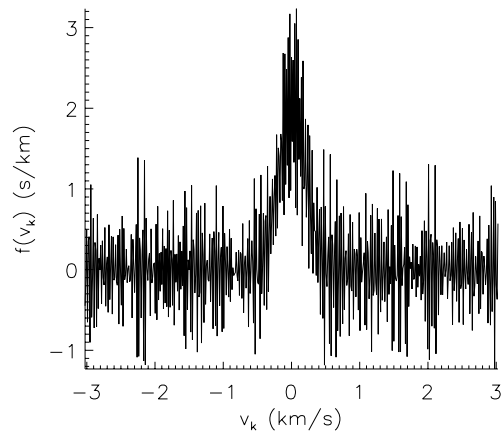
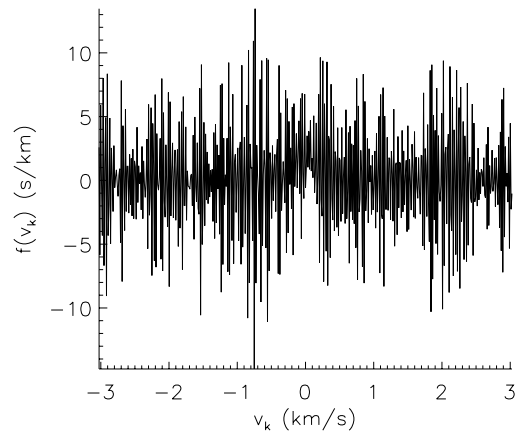
(a) Input SNR = 10^5 (b) Input SNR = 10^4 (c) Input SNR = 10^3 (d) Input SNR = 10^2

Figure 5.8: Velocity distribution estimate $\hat{f}(v_k)$ for warm-plasma (600 K) spectrum, deconvolved by the simple inverse filter.

so that the integrated noise amplification factor is given by Eqn. A.31.

Figure 5.9, a plot of computed NAF versus input signal-to-noise ratio (SNR), uniformly shows NAF values above 10^5 . Multiple repetitions of this plot show that variations in these NAF values are driven by small variations in the error function, rather than by differences in SNR.

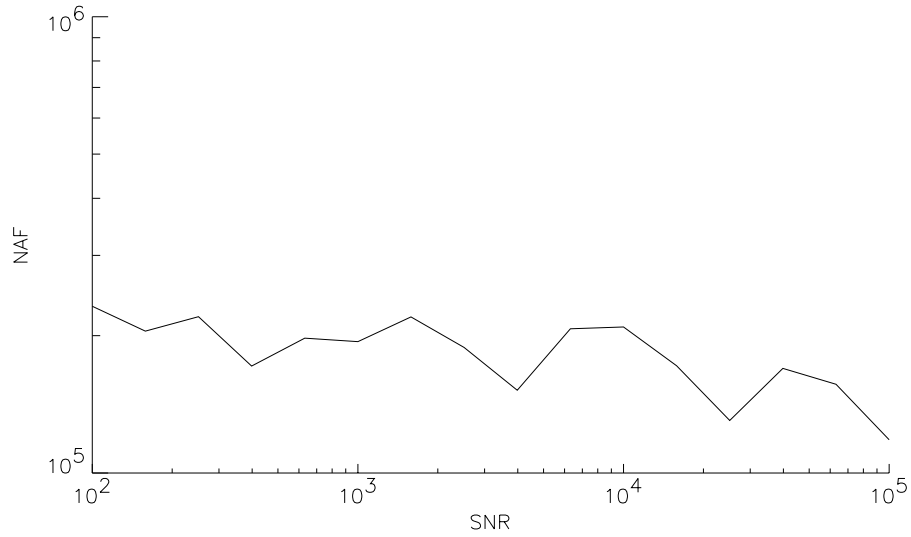


Figure 5.9: Noise amplification factor as a function of signal-to-noise ratio for simple inverse filter deconvolution of a warm-plasma (600 K) spectrum.

5.2.2 Rectangular inverse filter

Since most of the information encoded in the cold-plasma transform $C(\tau)$ lies near the center of the transform space (*i.e.*, near $\tau = 0$), the rectangular inverse filter is a classical choice for deconvolving lineshapes with signal-to-noise ratios that are less than 10^4 . In this scheme, the object transform estimate is

$$\hat{D}_r(\tau) = Y_r(\tau)I(\tau) \quad (5.19)$$

where the filter transform is

$$Y_r(\tau) = \frac{\text{rect}(\tau/\mathcal{T})}{C(\tau)}. \quad (5.20)$$

In function space, this is equivalent to convolving the simple object estimate $\hat{d}_s(\nu)$ with a scale-similar (see Eqn. 3.12) sinc function,

$$\hat{d}_g(\nu) = \mathcal{T} \text{sinc}(\mathcal{T}\nu) \otimes \hat{d}_s(\nu). \quad (5.21)$$

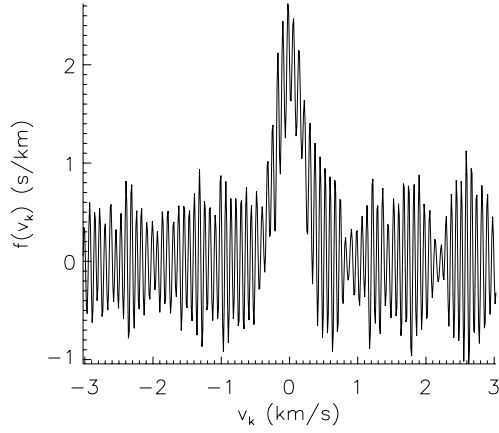
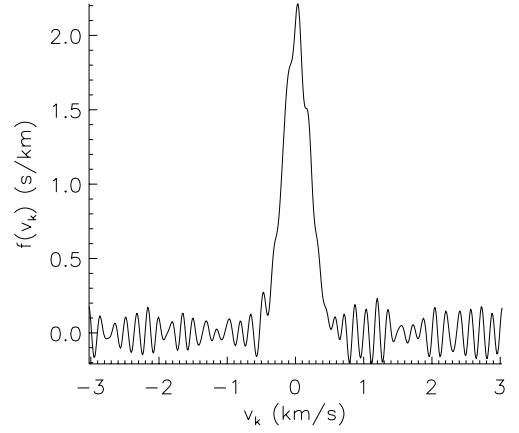
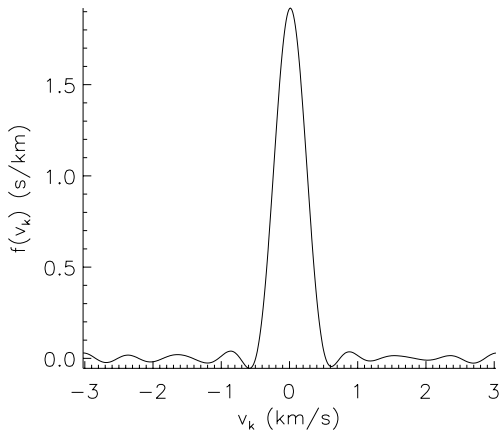
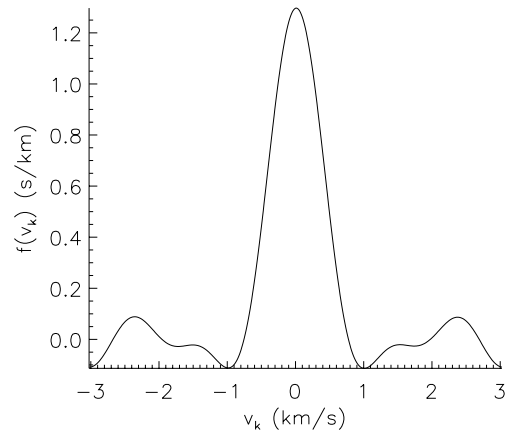
(a) Bandwidth $\mathcal{T} = 20$ ns(b) Bandwidth $\mathcal{T} = 10$ ns(c) Bandwidth $\mathcal{T} = 2$ ns(d) Bandwidth $\mathcal{T} = 1$ ns

Figure 5.10: Velocity distribution estimate $\hat{f}(v_k)$ for warm-plasma (600 K) spectrum, SNR = 100, deconvolved by the rectangular inverse filter.

Clearly, as \mathcal{T} increases², the rectangular inverse filter transform converges to the simple inverse filter transform,

$$\lim_{\mathcal{T} \rightarrow \infty} Y_r(\tau) = \frac{1}{C(\tau)}, \quad (5.22)$$

²For these 10-GHz simulations, $\mathcal{T} \geq 50$ ns is equivalent to $\mathcal{T} \rightarrow \infty$.

while decreasing values of \mathcal{T} discard increasing amounts of high-frequency noise and information.

Figure 5.10 shows how velocity distribution estimates made by this technique respond to decreasing values of the bandwidth limit \mathcal{T} at a $\text{SNR} = 100$. High-frequency noise steadily diminishes with \mathcal{T} , but lower-frequency ringing effects not only persist, but increase with decreasing \mathcal{T} . As noted in Chapter 3, the rect function and the sinc function are a Fourier transform pair; therefore, multiplication with a rect function in transform space is equivalent to convolution with a sinc function in function space. The low-frequency ringing effects are thus artifacts of the filtering function, and will only increase with decreasing bandwidth. Furthermore, broadening caused by the rectangular filter (indicated by decreasing maximum values of $f(v_k)$) becomes increasingly apparent at small bandwidth values ($\mathcal{T} \leq 2$ ms).

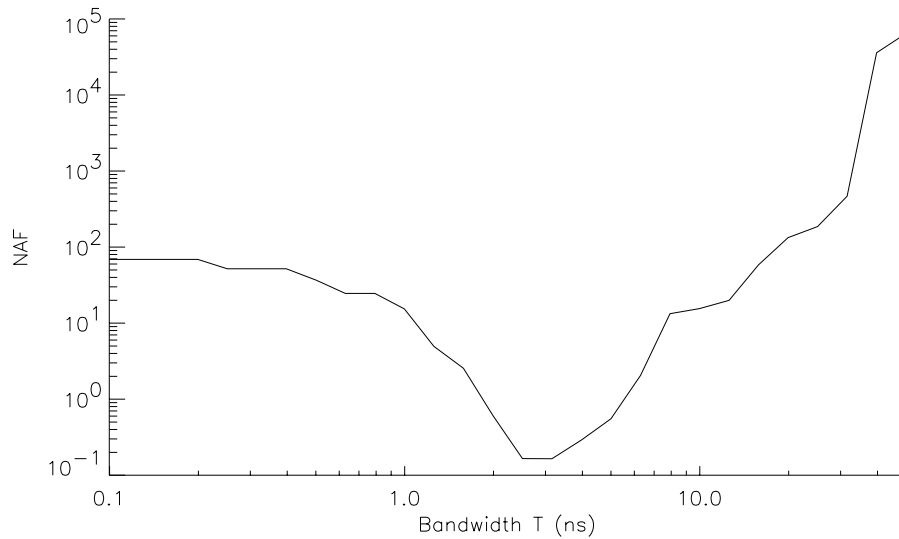


Figure 5.11: Noise amplification factor as a function of filter bandwidth for rectangular inverse filter transform deconvolution of a warm-plasma (600 K) spectrum, $\text{SNR} = 33$.

Figure 5.11 plots noise amplification factors computed by Eqn. A.31 for the rectangular inverse filter as a function of bandwidth \mathcal{T} . Since the high-bandwidth limit of this

scheme is the simple inverse filter, it is not surprising that the NAF is on the order of 10^5 at $\mathcal{T} > 50$ ns. NAF steadily decreases with bandwidth, reaching a minimum in the range $2 < \mathcal{T} < 4$ ns, but then increases as sinc function sidelobes grow in importance.

In order to characterize the broadening effects of an inversion technique, Ruf [84] suggests using a Dirac delta function as the input. When deconvolving velocity distributions from LIF spectra, this is equivalent to using the cold-plasma spectrum $c(\nu)$ as the image function. In the absence of noise, this gives a cold-plasma object transform of

$$[D_r(\tau)]_c \equiv \frac{\text{rect}(\tau/\mathcal{T})}{C(\tau)} C(\tau) = \text{rect}\left(\frac{\tau}{\mathcal{T}}\right). \quad (5.23)$$

The equivalent cold-plasma object function is

$$[d_r(\nu)]_c = \mathcal{T} \text{sinc}(\mathcal{T}\nu). \quad (5.24)$$

The full width half maximum (FWHM) $\Delta\nu_b$ of this object function characterizes the inherent broadening of the rectangular inverse filter. Though this filter broadening takes the form of a sinc function, approximating it with a Maxwellian of equal FWHM lets us assign an equivalent broadening “temperature” [65]

$$T_b = \frac{1}{8 \ln 2} \left(\frac{\Delta\nu_b}{\nu_o}\right)^2 \frac{Mc^2}{k} = \left(\frac{\Delta\nu_b}{\nu_o}\right)^2 T^* \quad (5.25)$$

for a known $\Delta\nu_b$, where

$$T^* = \frac{1}{8 \ln 2} \left(\frac{Mc^2}{k}\right) = 2.5592 \times 10^{14} \text{ K} = 2.2054 \times 10^{10} \text{ eV}. \quad (5.26)$$

The variance of the convolution of two functions is equal to the sum of the variances for the two functions [75]. Since a Gaussian of the form $g(x) = \exp(-x^2/[2\sigma^2])$ has a variance of σ^2 [65], a Maxwellian distribution (e.g., Eqn. 4.62) has a variance of $v_{\text{th}}^2 = kT/m$. If we can assume that a velocity distribution is Maxwellian, this means that the

apparent temperature T_o of a deconvolved velocity distribution is the sum of the actual ion temperature T and an equivalent broadening “temperature” T_b ,

$$T_o = T + T_b. \quad (5.27)$$

Therefore, knowing the broadening $\Delta\nu_b$ caused by the bandwidth \mathcal{T} for a given deconvolution scheme lets us predict the actual ion temperature T from a measurement of the filter-broadened deconvolution’s apparent temperature T_o .

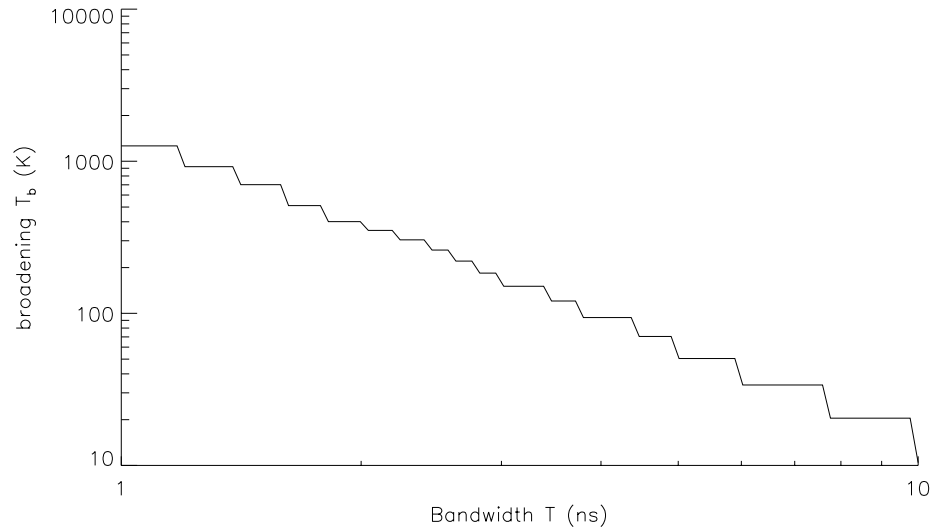


Figure 5.12: Line broadening as a function of filter bandwidth for the rectangular inverse filter.

Figure 5.12 shows how T_b increases with decreasing bandwidth over a range $1 \leq \mathcal{T} \leq 10$ ns for the rectangular inverse filter. Unfortunately, attempting to use this information to deconvolve the actual (unbroadened) ion velocity distribution $f(v_k)$ from the filter-broadened ion velocity distribution estimate $\hat{f}(v_k)$ is doomed to failure, as it simply recreates the simple inverse filter deconvolution, with noise amplification factors in the 10^4 to 10^5 range. Any filtered deconvolution has to have some computational broadening, and the best we can do at any filtering level is to characterize that broadening.

5.2.3 Gaussian inverse filter

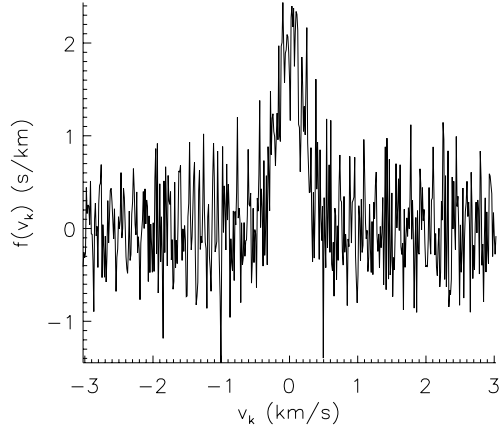
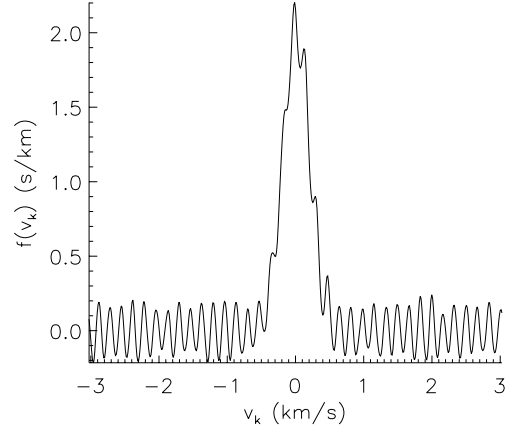
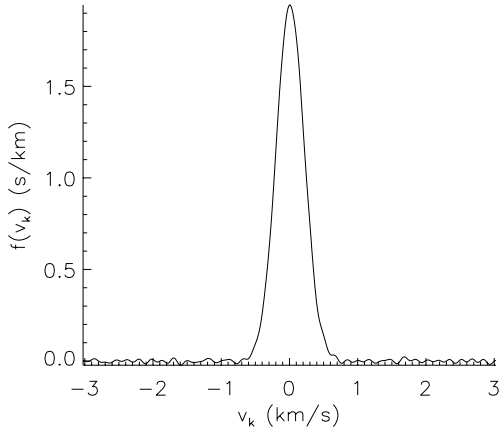
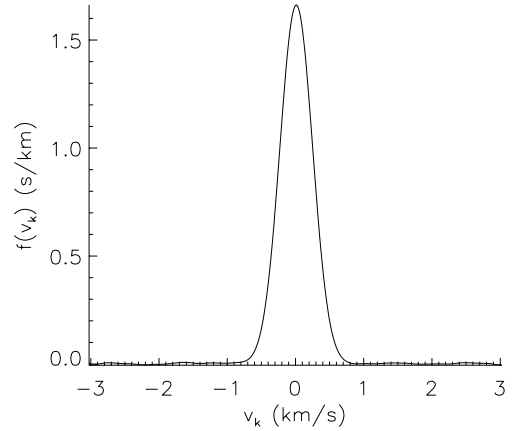
(a) Bandwidth $\mathcal{T} = 12$ ns(b) Bandwidth $\mathcal{T} = 4$ ns(c) Bandwidth $\mathcal{T} = 2$ ns(d) Bandwidth $\mathcal{T} = 1$ ns

Figure 5.13: Velocity distribution estimate $\hat{f}(v_k)$ for warm-plasma (600 K) spectrum, SNR = 100, deconvolved by the Gaussian inverse filter transform.

As noted in Chapter 3, the positive and negative sidelobes imposed by the rectangular inverse filter can be avoided by a Gaussian inverse filter transform

$$Y_g(\tau) = \frac{\exp(-[\tau/\mathcal{T}]^2)}{C(\tau)} \quad (5.28)$$

so that the object transform estimate is

$$\hat{D}_g(\tau) = Y_r(\tau)I(\tau). \quad (5.29)$$

In function space, this is equivalent to convolving the simple object estimate $\hat{d}_s(\nu)$ with a Gaussian,

$$\hat{d}_g(\nu) = \pi\mathcal{T}^2 \exp\left(-[\pi\mathcal{T}\nu]^2\right) \otimes \hat{d}_s(\nu). \quad (5.30)$$

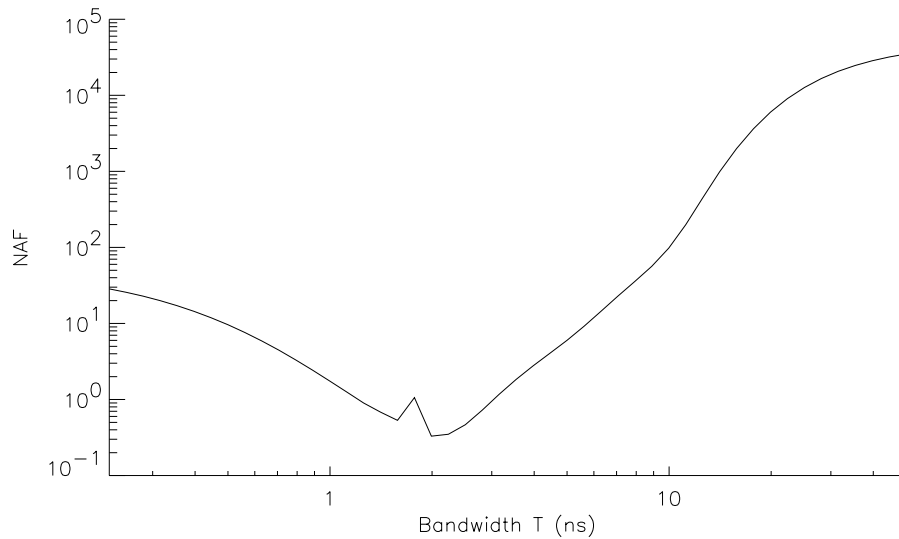


Figure 5.14: Noise amplification factor as a function of filter bandwidth for Gaussian inverse filter transform deconvolution of a warm-plasma (600 K) spectrum, SNR = 33.

Figure 5.13 shows how velocity distribution estimates made by the Gaussian inverse filter respond to decreasing values of the bandwidth at a SNR = 100, while Fig. 5.14 plots noise amplification factors computed by Eqn. A.31 as a function of \mathcal{T} . Unlike the rectangular inverse filter, the Gaussian inverse filter exhibits no low-frequency ringing. High-frequency noise dominates NAF at high values of \mathcal{T} , but steadily drops to negligible amounts around $\mathcal{T} = 3$ ns. At this point, broadening effects start to take over, causing the NAF to rise again below $\mathcal{T} = 2$ ns.

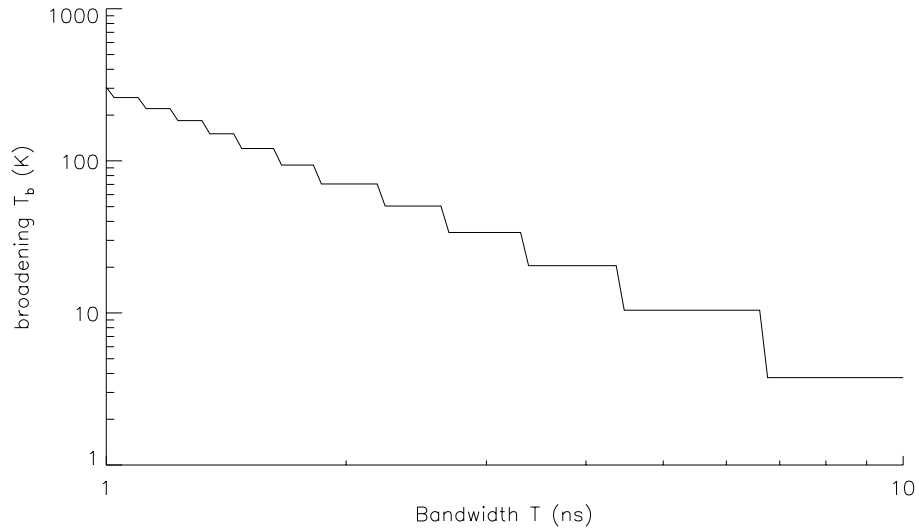


Figure 5.15: Line broadening as a function of filter bandwidth for the Gaussian inverse filter.

As before, we can characterize broadening effects for the Gaussian inverse filter by using a Dirac delta function as the input velocity distribution. The resulting cold-plasma object transform is

$$[D_g(\nu)]_c \equiv \frac{\exp(-[\tau/\mathcal{T}]^2)}{C(\tau)} C(\tau) = \exp\left(-\left[\frac{\tau}{\mathcal{T}}\right]^2\right) \quad (5.31)$$

while the equivalent cold-plasma object function is

$$[d_g(\nu)]_c = \pi \mathcal{T}^2 \exp\left(-[\pi \mathcal{T} \nu]^2\right). \quad (5.32)$$

Figure 5.15 shows how T_b increases with decreasing bandwidth over a range $1 \leq \mathcal{T} \leq 10$ ns for the Gaussian inverse filter.

5.3 Summary

Both desaturation and deconvolution have proven to be useful, within certain limits, for increasing the amount of information we can extract from LIF spectra.

Desaturation requires two LIF scans: one taken at low power (and, presumably, low saturation parameters), and one taken at high power (presumably with a better SNR). Noise

amplification mainly occurs at the spectral peaks, and remains acceptable for saturation levels below $\beta P_L = 10^4$ MHz for the normal range of signal-to-noise ratios ($50 < \text{SNR} < 100$).

Simple inverse filter deconvolution, though free from filter broadening, amplifies noise so badly that it is only usable at unrealistically low signal-to-noise ratios (SNR) In the absence of *a priori* knowledge of the object and noise power spectra, a Gaussian inverse filter with a bandwidth $\mathcal{T} = 2$ ns appears to be the best choice for velocity distribution deconvolution. The resulting filter-broadening adds an additional 70 K to the apparent temperature of a Maxwellian plasma.

CHAPTER VI

EXPERIMENTAL APPARATUS AND METHODS

And there's a dreadful law there — it was made by mistake, but there it is — that if any one asks for machinery they have to have it and keep on using it. — *E. Nesbit* [85]

The computational techniques developed in the previous chapter are intended to extract velocity distributions from Xe II LIF spectra taken in the plumes of two electrostatic thrusters. Acquiring these spectra requires a certain amount of experimental equipment, both standard and custom, such as a vacuum facility, thrusters, lasers, beam-handling and LIF-collection optics, and data-collection electronics.

This chapter describes the equipment used in these experiments, with a particular emphasis on the design, installation, and alignment of custom optical systems for LIF experiments.

6.1 Facility

Both thrusters were tested in the Large Vacuum Tank Facility (LVTF) at PEPL. This is a $\phi 6$ m x 9 m, stainless-clad cylindrical tank with domed end caps. A $\phi 1.5$ m access hatch in the south end allows routine entry for personnel and small equipment, while the entire north end cap can be removed for the occasional larger piece of equipment. Five 61 cm x 183 cm (24 in. x 72 in.) graphite panels are attached by a hinge mechanism to the

north end cap, providing an adjustable 1.8 x 2.2 m beam dump which protects the north viewing window and suppresses back sputtering caused by the ion beam.

During operation, two pairs of 400 cfm mechanical pumps (backed by a single 2000 cfm Roots blower per pair) rough the chamber to approximately 60 mTorr. At this point, the mechanical pumping system is sealed and turned off, and the cryopumps take over. Though the mechanical pumps can take the chamber below 10 mTorr, the higher minimum roughing pressure suppresses chamber contamination by oil backstreaming.

Seven CVI Model TM-1200 Re-Entrant Cryopumps, each protected from radiant heat transfer (from the room-temperature chamber walls) by a liquid nitrogen-cooled baffle, provide high vacuum. Since each cryopump can pump 35,000 l/s of xenon, the combined pumping speed of all seven cryopumps is 240,000 l/s, providing an ultimate base pressure of 2.5×10^{-7} Torr. For routine operation at moderate mass-flow rates, only four of the seven available pumps operate, providing a combined xenon pumping speed of 140,000 l/s.

Each thruster is supplied by a separate propellant flow system. The P5 propellant flow (to the anode and cathode) is controlled by two MKS Model 1100 Flow Controllers, calibrated by the pressure rise rate in a known volume to a total mass flow uncertainty of less than 1% [86]. The FMT-2 propellant flow (to the discharge cathode, discharge chamber and neutralizer) is manually controlled by needle valves and monitored by three Teledyne Hastings NALL-100G flowmeters, calibrated by a bubble flow meter to an accuracy within NASA specifications [12].

Two hot-cathode gauges monitor the chamber pressure at high vacuum. The older gauge, a Varian model 571 with a HPS model 919 Hot Cathode Controller, is mounted on a valved extension to the west wall of the chamber. The newer gauge, a Varian model UHV-24 nude gauge with a Varian UHV senTorr Vacuum Gauge Controller, is mounted

inside the chamber along the west wall, as was calibrated on nitrogen as a complete system (gauge, cable and controller) by the manufacturer. The indicated pressure P_i for both gauges is corrected for xenon by the equation

$$P = \frac{P_i - P_b}{2.87} + P_b \quad (6.1)$$

where P_b is the base pressure [87].

Both thrusters were mounted on thruster station 2. This is an axially-adjustable work platform spanning the LVTF centerline, which supports a custom positioning system developed by New England Affiliated Technologies (NEAT). This system consists of a 1.8 m (6 ft) linear stage in the radial (east-west) direction, mounted on a 0.9 m (3 ft) linear stage in the axial (north-south). Though we mounted a rotational stage on the probe table for axial-injection testing, laser problems terminated tests before we could use it. Both lateral stages are PC-controlled by a custom LabView VI, with locational resolution on the order of 0.25 mm.

6.2 Thrusters

As previously noted (in section 2.3.1), we carried out Xe II LIF experiments on two electrostatic thrusters, the UM/AFRL P-5 Hall thruster and the NASA Glenn FMT-2 ion engine.

6.2.1 UM/AFRL P5 Hall thruster

Figure 6.1 shows the P5, a 5-kW Hall thruster developed for basic thruster physics research at PEPL in cooperation with the Air Force Rocket Laboratory. Haas and Gulczinski [88] demonstrated that the P5 shows performance levels and operating conditions consistent with thrusters under commercial development. The P5 can be divided into four

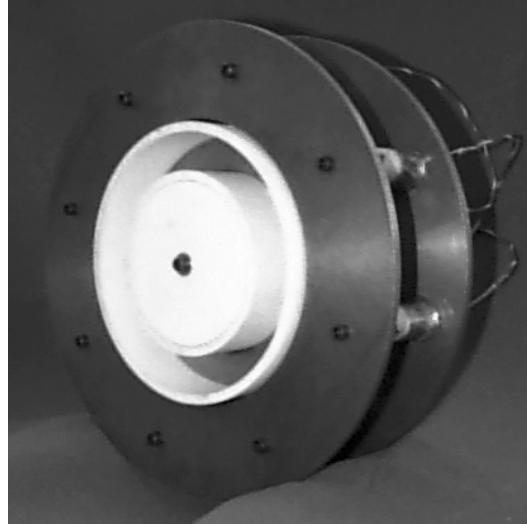


Figure 6.1: Photograph of the P5 Hall thruster.

major components: the magnetic circuit, discharge chamber, anode/gas distributor, and the neutralizer.

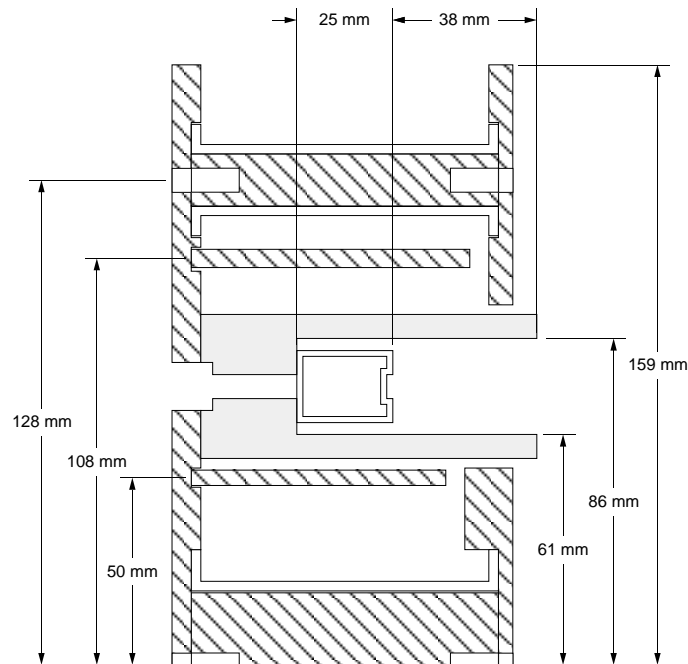


Figure 6.2: Dimensioned half-section of the P5 Hall thruster.

The magnetic circuit consists of eight outer electromagnets, one inner electromagnet, three pole pieces (rear, outer front and inner front), and two magnetic screens. The

pole pieces, screens and electromagnet cores are turned from machinable cast iron, while the electromagnet bobbins are martensitic (*i.e.*, magnetic) 430F stainless steel. The magnet wire wound on these bobbins is 18 AWG nickel-coated copper, with a double layer of fiberglass insulation; the inner core has 240 windings, while each outer core has 120 windings [86]. Figure 6.2 shows a half-section of this magnetic circuit.

The P5 discharge chamber is an $\phi 185$ mm x 88.9 mm cylinder of 50/50 boron nitride/silica ceramic (Carborundum's M26 grade). A $\phi 109$ mm hole bored through its center allows the chamber to fit over the inner magnetic screen, while a 25.4 mm wide, 38.1 mm deep channel centered on $\phi 170$ mm forms the interior chamber walls [86].

The anode/gas distributor assembly sits at the upstream end of the discharge chamber. This assembly is a 25 mm deep, 19 mm wide weldment, made of austenitic (*i.e.*, nonmagnetic) 324 stainless steel. Xenon entering the gas distributor feeds through 72 x $\phi 0.8$ mm holes into 36 evenly-spaced blind troughs in the anode face.

The neutralizer is a $\phi 25$ mm x 104 mm hollow cathode built by the Moscow Aviation Institute. A tungsten spring inside the molybdenum neutralizer body presses a lanthanum hexaboride (LaB_6) pellet against a tantalum washer. Electrical current passing through this spring to the cathode body heats the LaB_6 pellet until thermionic emission initiates a steady, self-sustaining discharge. Though the neutralizer is normally mounted directly above the thruster centerline, we moved it to a position roughly 45 degrees from vertical for these tests to avoid interference with the LIF optics.

One custom and four standard laboratory power supplies power the P5. A Kepco ATE36-30M provides current to the cathode heater, while a custom high-voltage ignition supply ignites the cathode discharge. A Kikusui PAD 55-10L drives the inner electromagnet circuit, while a Sorensen DCS 33-33 drives the eight outer electromagnets in series. A Sorensen DCR 600-16T, electrically isolated by a low-pass filter (1.3Ω equivalent re-

sistance in series with the discharge current and a $95 \mu\text{F}$ capacitor in parallel), powers the main discharge.

6.2.2 NASA FMT-2 ion engine



Figure 6.3: Photograph of the FMT-2 ion thruster.

Figure 6.3 shows the FMT-2 ion thruster, one of the two 2.3-kW functional model thrusters (FMTs) developed as immediate predecessors to the engineering model (EMT) NSTAR thrusters. The EMT thrusters are the principal ground test versions of the NASA Solar Electric Propulsion Technology Application Readiness (NSTAR) $\phi 30$ cm ion engine, which was successfully used as the primary propulsion for the Deep Space 1 (DS-1) probe. Unlike the EMT, the FMT makes extensive use of 1100 grade (*i.e.*, soft) aluminum for components with low thermal loads or erosion rates. The discharge cathode and ion optics are identical to those used in the EMTs and flight thrusters (FTs).

The FMT-2 was assembled and modified at NASA GRC specifically for use at PEPL. These modifications include the addition of windows to the discharge chamber wall and plasma screen, allowing optical access for internal LIF studies [12]. Three 102 mm x 32

mm x 3 mm quartz windows are mounted in the top, bottom and right-hand side (looking downstream) of the discharge chamber wall, with the discharge cathode exit plane passing roughly just upstream of the window centers. Though the EMT and FT plasma screens are conformal, the FMT plasma screen is cylindrical, facilitating window placement. Two 127 mm x 45 mm x 1.5 mm quartz windows are mounted in the top and bottom of the plasma screen, while a 127 mm x 76 mm x 1.5 mm window on the plasma screen side reduces vignetting of the LIF signal.

The discharge and overall engine performance of the FMT at PEPL has been nearly identical to that of the flight engine over the entire throttling range of the NSTAR thruster.

6.3 Beam-injection schemes

We used two laser beam-injection schemes in these experiments. The first, which I call the “off-axis multiplex” technique, focuses two to four beams through a single lens; this technique allows simultaneous LIF measurement along multiple beam direction vectors, at the cost of increased velocity uncertainty. The second, which I call the “axial-injection” technique, sends a single, focused beam upstream towards the thruster exit plane; this technique has much smaller velocity uncertainties, but only collects one velocity component at a time.

6.3.1 Off-axis multiplex

In the original multiplex technique developed by Keefer *et al.* [53], a large focusing lens is placed so its optical axis is perpendicular to the thruster axis. Two parallel beams, which are chopped at different frequencies to aid phase-locked amplification, are directed to the lens. One beam, which passes through the center of the lens, is called the “radial” beam; the other, which enters the lens upstream of its center, is called the “axial” beam. Both beams are focused by the lens, meeting at the LIF interrogation point. A collection

lens, placed so its optical axis is perpendicular to both the thruster and focusing lens axes, sends LIF from both beams through a monochromator to a photomultiplier tube (PMT). The resulting current signal is passed to the lock-in amplifiers, which separate out each beam's LIF signal.

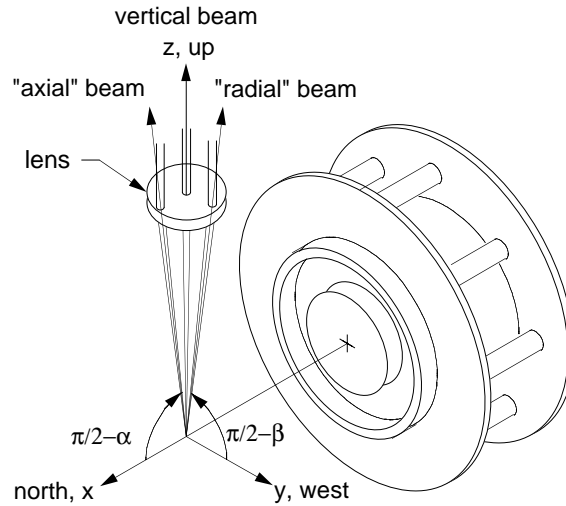


Figure 6.4: Beam and thruster orthogonal axes for the off-axis multiplex technique.

Fig. 6.4 shows the beam propagation axes relative to the thruster for the three-beam multiplex technique perfected by Williams *et al.* [11, 12, 58]. In this variant, the focusing lens axis is pointed downward, so that the center beam is “vertical” (rather than “radial”), with a direction vector \hat{v} . The “off-axial” beam enters downstream of the lens center, emerging at an angle α from the vertical beam along a beam direction vector \hat{a} , on a plane parallel to the thruster axis. Finally, the third (or “off-radial”) beam enters to one side of the lens center, emerging at an angle β from the vertical beam along a beam direction vector \hat{r} , on a plane perpendicular to the thruster axis.

Decomposed onto a set of axes orthogonal to the thruster, the beam direction vectors are

$$\hat{v} = -\hat{z} \quad (6.2)$$

$$\hat{\mathbf{a}} = -\sin \alpha \hat{\mathbf{x}} - \cos \alpha \hat{\mathbf{z}} \quad (6.3)$$

$$\hat{\mathbf{r}} = -\sin \beta \hat{\mathbf{y}} - \cos \beta \hat{\mathbf{z}}. \quad (6.4)$$

Thus, the beamwise bulk velocity components u_v , u_a and u_r (measured by the Doppler shift relative to a stationary reference plasma) can be readily transformed to thruster coordinates by

$$u_x = -\frac{u_a + u_v \cos \alpha}{\sin \alpha} \quad (6.5)$$

$$u_y = -\frac{u_r + u_v \cos \beta}{\sin \beta} \quad (6.6)$$

$$u_z = -u_v \quad (6.7)$$

Unfortunately, the small laser beam convergence angles needed to avoid vignetting can cause significant errors in the above transformation. Consider an off-axial velocity uncertainty of Δu_a ; even in the absence of angular uncertainty or vertical velocity uncertainty, the true axial (x -component) uncertainty is $\Delta u_x = \Delta u_a / \sin \alpha$. Furthermore, the proportional axial velocity uncertainty with respect to angular error is

$$\frac{1}{u_x} \frac{\partial u_x}{\partial \alpha} = \frac{u_z}{u_x} - \cot \alpha. \quad (6.8)$$

Thus, both velocity errors and angular errors diverge rapidly at small angles. For instance, at $\alpha = 10^\circ$, independent 2% random errors in u_z and u_a , combined with a 2% bias in angular measurement, result in a 20% error in the calculated axial velocity u_x .

Transforming the beamwise temperatures to axes orthogonal to the thruster is less straightforward, as it requires two major assumptions. The first assumption, that the orthogonal velocity distribution projections

$$f_x(v_x) = \int_{-\infty}^{\infty} \int_{-\infty}^{\infty} f(\mathbf{v}) dv_y dv_z \quad (6.9)$$

$$f_y(v_y) = \int_{-\infty}^{\infty} \int_{-\infty}^{\infty} f(\mathbf{v}) dv_x dv_z \quad (6.10)$$

$$f_z(v_z) = \int_{-\infty}^{\infty} \int_{-\infty}^{\infty} f(\mathbf{v}) dv_y dv_x \quad (6.11)$$

are drifting Maxwellians, is implicit in the term “temperature,” and is a reasonable way to quickly summarize the distribution in terms of bulk velocity and temperature components. The second assumption, that the velocity distributions along the orthogonal axes are statistically independent (*i.e.*, $f(\mathbf{v}) = f_x(v_x)f_y(v_y)f_z(v_z)$), is less supportable; any tilting of the two-dimensional velocity distribution contours with respect to the thruster axes makes this second assumption invalid. However, we currently have no reason to suppose that this assumption is not valid in electrostatic thruster plumes.

If we make this simplifying assumption, we can model the two-dimensional contours of $f_{xz}(v_x, v_z)$ and $f_{xy}(v_x, v_y)$ as untilted ellipses in velocity space. Since the velocity FWHM of a Maxwellian is

$$\text{FWHM} = \sqrt{8 \ln 2 \frac{kT}{M}}, \quad (6.12)$$

this untilted ellipse model implies that the off-axial temperature T_a , the axial temperature T_x and the vertical temperature T_v are related by

$$\cos^2 \alpha + \left(\frac{T_v}{T_x}\right)^2 \sin^2 \alpha = \left(\frac{T_v}{T_a}\right)^2. \quad (6.13)$$

Solving for the axial temperature yields

$$T_x = T_v \left[\frac{(T_v/T_a)^2 - 1}{\cos^2 \alpha} + 1 \right]^{-1/2} \quad (6.14)$$

for $\alpha \neq 0$ and $T_v/T_a > \sin \alpha$. By the same train of logic, the radial (*i.e.*, y -component) temperature is

$$T_y = T_v \left[\frac{(T_v/T_r)^2 - 1}{\cos^2 \beta} + 1 \right]^{-1/2} \quad (6.15)$$

for $\beta \neq 0$ and $T_v/T_r > \sin \beta$.

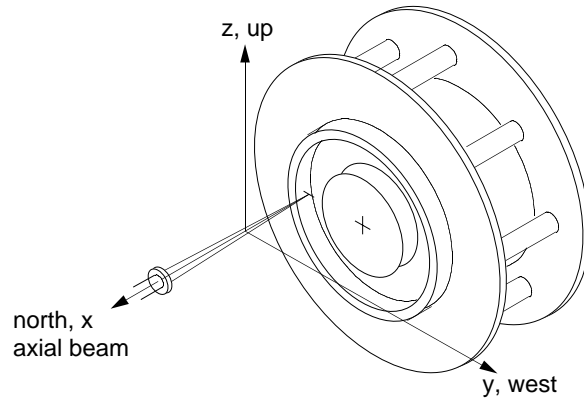


Figure 6.5: Beam and thruster orthogonal axes for the off-axis multiplex technique.

6.3.2 Axial-injection

The axial-injection setup illustrated in Fig. 6.5 avoids the problems inherent in the off-axis multiplex setup by direct measurement of the axial velocity distribution

$$f_x(v_x) = \int_{-\infty}^{\infty} \int_{-\infty}^{\infty} f(\mathbf{v}) dv_y dv_z. \quad (6.16)$$

As in the off-axis multiplex technique, a collection lens, placed so its optical axis is perpendicular to the thruster axis, sends LIF from the interrogation volume through a monochromator to a PMT. Since LIF is isotropic, this collection axis can be shifted to best suit the experiment; however, the interrogation volume is defined by the intersection of the laser beam waist and the magnified monochromator slit image at the collection lens focus. This volume is minimized when the axes are perpendicular, improving the spatial resolution of the LIF measurements.

6.4 External optics

6.4.1 Laser

The laser system used in these experiments is a Coherent 899-29 Autoscan ring dye laser. This PC-controlled system has a nominal linewidth of 500 kHz, tuning repeatability

of 50 MHz and a scanning range of over 100 GHz (in 10 GHz segments). PC-controlled scanning and data collection are synchronized by the Autoscan software.

Pumping for this dye laser is provided by an Innova R-series argon-ion laser, with a nominal broadband power rating of 25 W. With the intercavity assembly (ICA) removed, the dye laser can generate up to 2 W of tunable broadband light using Rhodamine-6G dye at 605 nm. With the ICA installed, the same system can provide anywhere from 300 to 450 mW of narrow-linewidth light at 605.1 nm.

6.4.2 Beam-handling

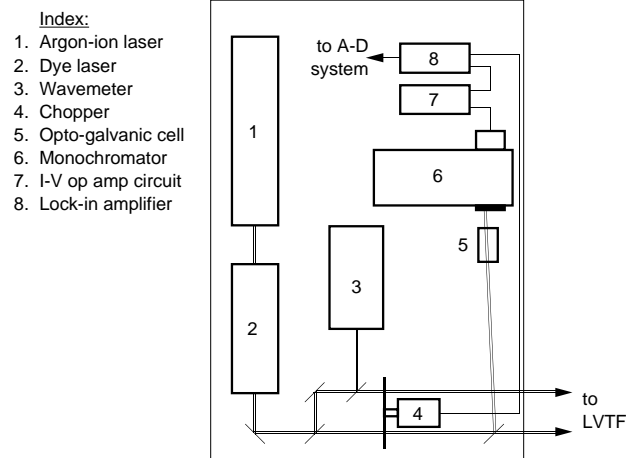


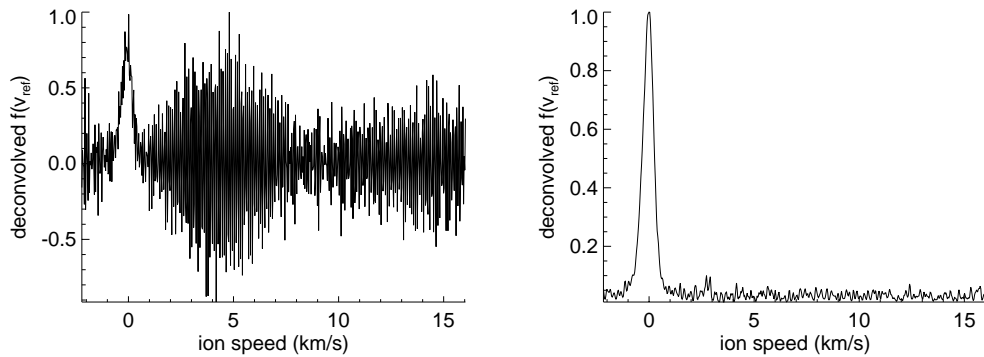
Figure 6.6: Laser division and modulation.

Fig. 6.6 shows a schematic of the optical table contents, which include the laser system, wavemeter, choppers and beamsplitting optics. A controlled atmosphere/low-dust enclosure (usually referred to as the laser room) protects these from the rest of the lab¹. A high-reflecting $\phi 25$ mm mirror directs the laser beam into the conditioning optics. The first optic in this train is a 25 mm x 25 mm x 1.6 mm quartz slide, which sends a sampling beam to a Burleigh WA1000 wavemeter with a 0.1 pm resolution and a 1.0 pm accuracy between 400 nm and 1 μm .

¹And *vice versa*.

Axial-injection LIF only sends one laser beam into the LVTF. Off-axis multiplex LIF, on the other hand, splits the laser output into three beams with two 25 mm x 25 mm x 1.6 mm parallel-plate beamsplitters. Small high-reflecting mirrors on kinematic mounts send these beams down the LVTF beam tube, while micrometer stages holding the kinematic mounts allow fine adjustment of the distance between parallel beams.

Since the large natural fluorescence at 529 nm would otherwise drown out the LIF signal, we chop the laser beam to permit phase-lock amplification of the LIF signal. For axial-injection LIF, the beam passes through a Stanford SR541 two-frequency optical chopper powered by a Stanford SR540 chopper controller. For off-axis multiplex LIF, two beams pass through one chopper, while the third passes through another chopper. The frequencies of all three beams must be kept well away from harmonics of the other beams; otherwise, aliasing within the lock-in amplifiers can cause cross-talk between LIF signals.



(a) Simple inverse filter deconvolution.

(b) Gaussian inverse filter deconvolution.

Figure 6.7: Typical velocity distribution estimate $\hat{f}(v)$ from stationary plasma in a xenon opto-galvanic cell .

Another 25 mm quartz slide downstream of the chopper sends a sampling beam through the center of a Hamamatsu L2783-42 XeNe-Mo hollow-cathode optogalvanic cell filled with a Xe-Ne gas mixture [12]. A 250 V discharge across this optogalvanic cell gives a

strong Xe II LIF signal, collected by a Chromex 500is monochromator with a Hamamatsu 928 photo-multiplier tube (PMT). An equivalent optogalvanic signal can be detected in the AC voltage drop across the cell's ballast resistor. Deconvolution of either signal, as shown in Fig. 6.7(b), provides a stationary reference for the distributions extracted from plume LIF.

Two $\phi 100$ mm protected silver mirrors in a periscope configuration (with the upfold mirror on the optical table and the downfold mirror on the LVTF window waterline) send the primary beams out of the laser room, down the beam tube and into the LVTF. The sole purpose of this beam tube is to minimize the chance that somebody will look directly into the laser. Absorbent material lining the beam tube walls reduces internal reflections, and helps absorb reflections from the LVTF windows.

6.5 LVTF optics

6.5.1 Off-axis multiplex

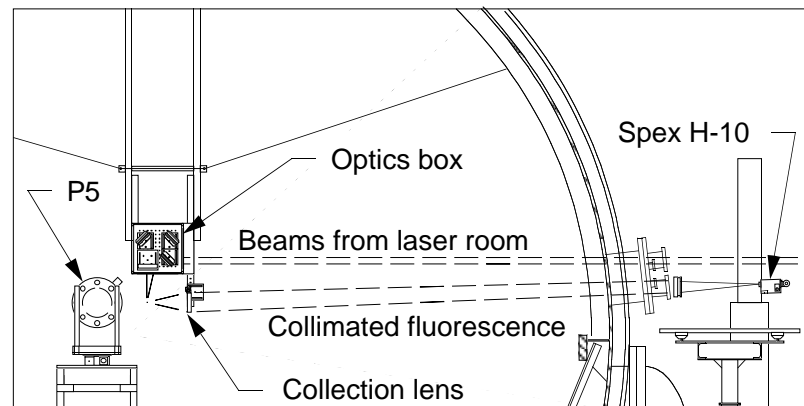


Figure 6.8: Multiplex laser beam delivery and fluorescence collection optics schematic, looking upstream (north) from behind thruster.

Figure 6.8 shows the LVTF beam handling setup for the off-axis multiplex technique. The LVTF optics box is a 318 mm x 394 mm x 220 mm graphite-lidded enclosure with anti-reflection (AR) coated windows, which protect its contents from sputtering deposition

and erosion. This enclosure contains three square 100 mm mirrors on kinematic mounts, used to direct all three incoming beams through a focusing lens. Small adjustments of the $\phi 100$ mm upfold and downfold mirrors in the laser room steer the vertical beam to the center of the focusing lens. This lens focuses all three beams to sub-millimeter beam waists at the interrogation volume. During testing, this point remains fixed in space. To take LIF spectra at different points in the plume, we translate the thruster around the interrogation volume.

We use a small level during setup to ensure that the upper surface of this lens is level, and then temporarily place a second-surface mirror atop the focusing lens mount during setup and realignment. Small adjustments of the square 100 mm mirrors steer the retroreflected spots back to the laser room, ensuring that the vertical beam is plumb. When the retroreflected beam spots on the laser room upfold mirror overlay the original beam spots, the beams are also parallel. We measure beam spacing by replacing the retroreflection mirror with a gridded card, photographing the beam spots, and measuring the distances between spot centers in Photoshop; the standard deviation of multiple measurements provides an estimate of beam angle uncertainty.

Each thruster has a small wire or pin, added to facilitate laser alignment. The P5 carries a $\phi 1$ mm steel pin, centered on the downstream face of the thruster, while the FMT has a $\phi 0.2$ mm tungsten wire loop attached to the forward edge of the side plasma screen window. Two separate AR windows protect the $\phi 100$ mm, $f/2.5$ collection lens. After placing the laser focal volume on the alignment feature, we adjust the collection lens, sending a collimated² beam of scattered light through the LVTF window. During experiments, the collected fluorescence follows the same path.

Between experiments, we bring the LVTF up to atmospheric pressure, inspect all in-

²Or slightly focusing, in order to avoid vignetting by the LVTF exit window.

chamber optics, and clean or replace AR windows as necessary. We then confirm thruster continuity, realign the optics and evacuate the LVTF.

6.5.2 Axial-injection

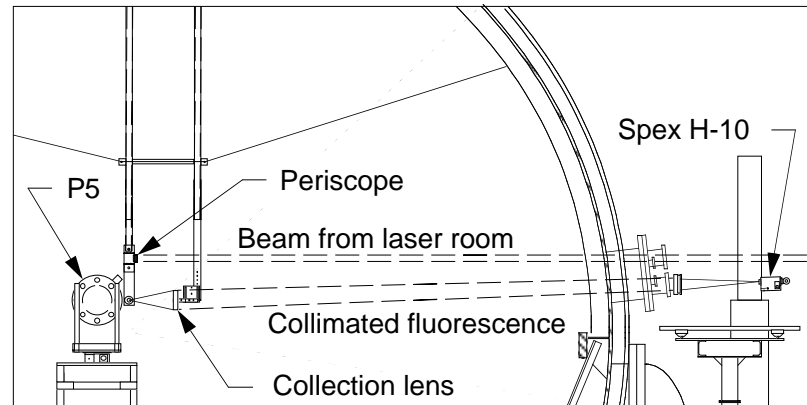


Figure 6.9: Axial-injection and LIF collection optics, looking upstream (north) from behind thruster.

Figure 6.9 shows the LVTF beam handling setup for the axial-injection technique. A three-prism periscope system, shown in Fig. 6.10, sends the beam through a focusing telescope parallel to the thruster axis, reducing the beam diameter (which grows to approximately 2.0 cm over the 12 m path length) to less than 1 mm at the interrogation. As before, we move the thruster around a fixed interrogation point, and not *vice versa*.

An enclosure with anti-reflection (AR) coated windows protects the beam-turning prisms and focusing telescope from sputtering deposition and erosion. A focus tube between the telescope elements provides axial adjustment of the laser focus.

We have not yet carried out any axial-injection experiments with the FMT-2. For the P5 axial-injection experiments, we replaced the P5's center alignment pin with a $\phi 1$ mm steel T-pin, also centered on the downstream face of the thruster. After placing the laser focal volume on the pin head, we adjust the $\phi 100$ mm, $f/2.5$ collection lens, sending a collimated beam of scattered light through the LVTF window.

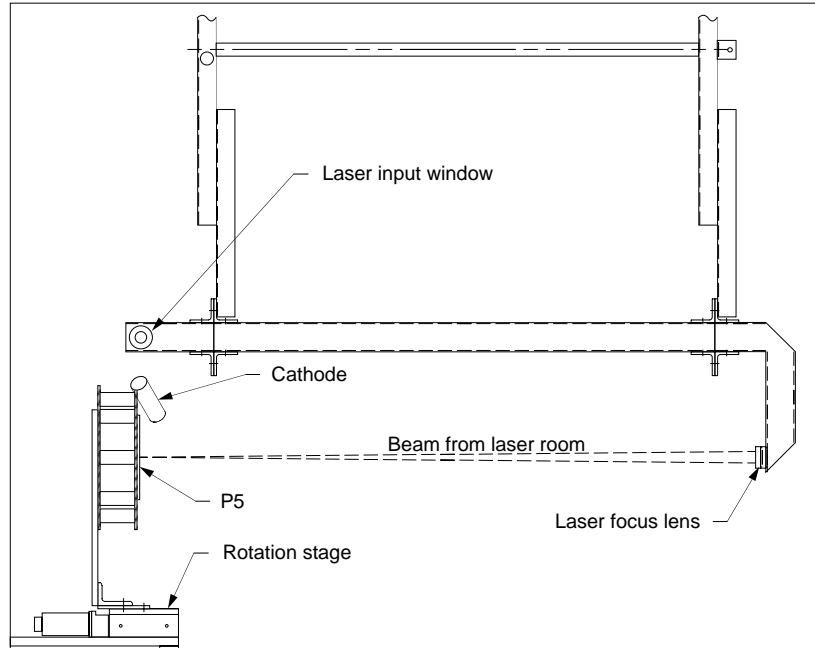


Figure 6.10: Axial-injection periscope, looking west.

The laser focal point inevitably shifts during chamber evacuation. By orienting the T-pin so that its head's long axis is vertical, we can recover alignment of the laser and collection train focal points by lateral translation of the thruster and vertical translation of the H10 monochromator.

6.6 LIF collection

The collimated fluorescence from the thruster plume is focused by a $\phi 100$ mm, $f/5$ lens onto a Spex H-10 monochromator with a Hamamatsu 928 PMT. This monochromator acts as a linewidth filter centered on the 529 nm fluorescence line. By holding a second-surface mirror flat against the monochromator entrance slits, we can use retroreflection of scattered light from the alignment pin to determine if the monochromator is aligned with the collection optics axis. Micrometer-driven rotation stages allow fine tilt and pan adjustment of the monochromator body.

We sometimes use an interference filter, centered on 530 nm with a 10 nm bandwidth,

to further reduce the natural fluorescence and LIF from other emission lines. Stanford SR810 and SR850 DSP lock-in amplifiers, using a 1-second time constant, isolate the fluorescence components of these signals.

The Coherent 899-29 laser's Autoscan software collects and matches laser wavelength to the corresponding lock-in output. A scan rate of 60 s/10 GHz has proven to be sufficiently slow to ensure a reasonable signal-to-noise ratio in most cases. For noisier signals, we collect several scans at the same scan rate, pass them through a Chauvenet's criterion [90] rejection filter, and average them into a single, smoother scan.

CHAPTER VII

P5 PLUME LIF

This chapter presents data obtained in two series of P5 plume LIF experiments, using the computational and experimental tools described in Chapters 5 and 6. Section 7.1 presents axial velocity distributions deconvolved from axial-injection LIF spectra, along with axial bulk velocity and temperature components derived from a Maxwellian curve-fit to the velocity distribution. Section 7.2 presents beamwise velocity distributions deconvolved from off-axis multiplex LIF spectra, along with three-component bulk velocities and temperatures extrapolated from Maxwellian curve-fits. In Section 7.3, I discuss some of the findings from these experiments.

7.1 Axial-injection LIF of P5 plume

We took three sets of axial-injection LIF spectra at 1.6 kW and 3.0 kW operating conditions. The first was an axial sweep from 50 cm to 0.05 cm downstream of the thruster exit plane along the P5 discharge channel axis (7.37 cm outboard of the thruster axis). The second was a 2 cm lateral sweep across the discharge channel, 1 mm downstream of the thruster exit plane. The third was an axial sweep from 5 cm to 50 cm downstream of the thruster exit plane along the thruster centerline. Figure 7.1 shows the coordinate grid used to specify data collection locations.

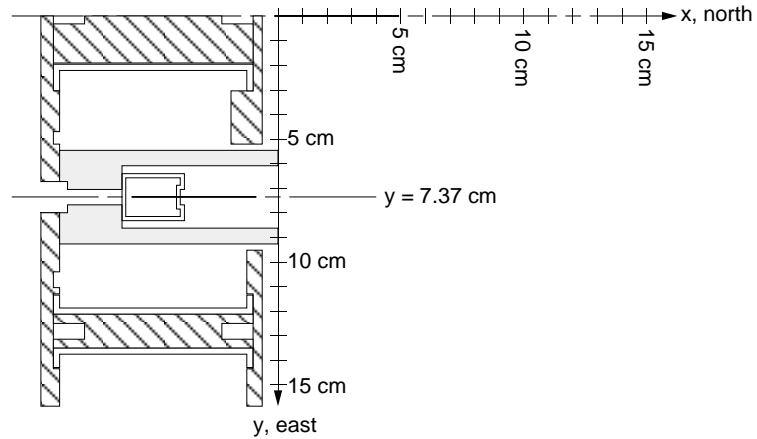


Figure 7.1: Coordinate grid for P5 LIF experiments, looking down.

With the exception of Fig. 7.12, each data point reported here is a single scan, taken at a rate of 60 s per 10-GHz segment, using a lock-in time constant of 1 second. Table 7.1 gives the thruster operating conditions¹ used in these experiments.

Table 7.1: P5 operating conditions for axial-injection LIF.

		1.6 kW	3.0 kW	units
Discharge voltage	V_d	300.1	300.1	V
Anode potential	V_a	277.0	271.9	V
Cathode potential	V_c	-23.1	-28.2	V
Discharge current	I_d	5.30	10.40	A
Anode flow rate	\dot{m}_a	61.0	114.0	sccm
Cathode flow rate	\dot{m}_c	6.00	6.00	sccm
Facility pressure	P	5.5	12.	μ Torr

Discharge voltage was held constant within the power supply measurement precision during each test. The anode and cathode flow rate settings also remained constant. The run-to-run variation of discharge current was less than 10%, while the day-to-day variation of cathode floating potential was less than 2%.

¹Cathode and anode potentials are relative to facility ground potential; facility pressures are corrected for xenon.

7.1.1 Axial sweep along discharge centerline

Figures 7.2 through 7.11 show representative axial velocity distributions taken downstream of the discharge channel. The solid line is the deconvolved distribution, while the dashed line is a Maxwellian curve-fit to a user-defined area within the major peak.

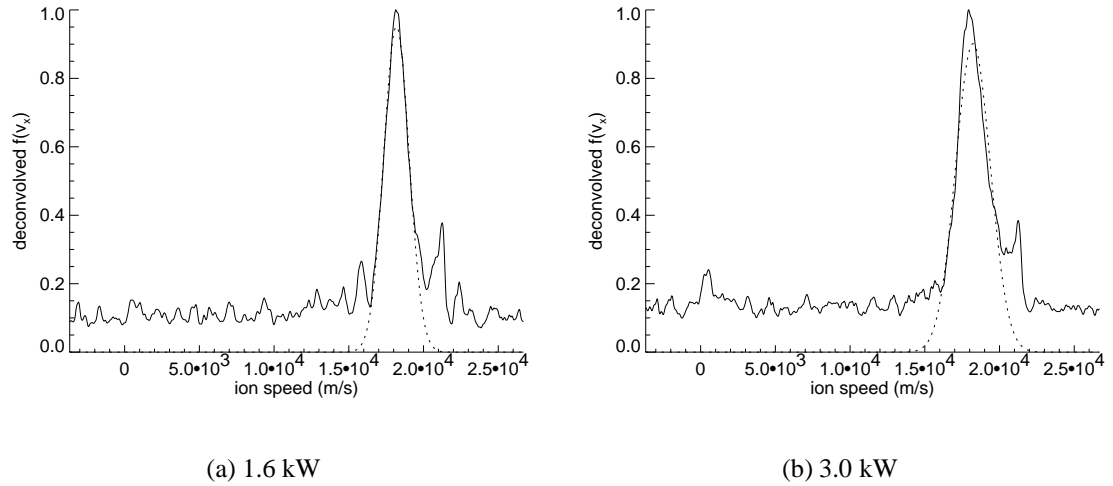


Figure 7.2: Deconvolved $f(v_x)$ (solid) & curve-fit (dashed) at $(x, y) = (50, 7.37)$ cm.

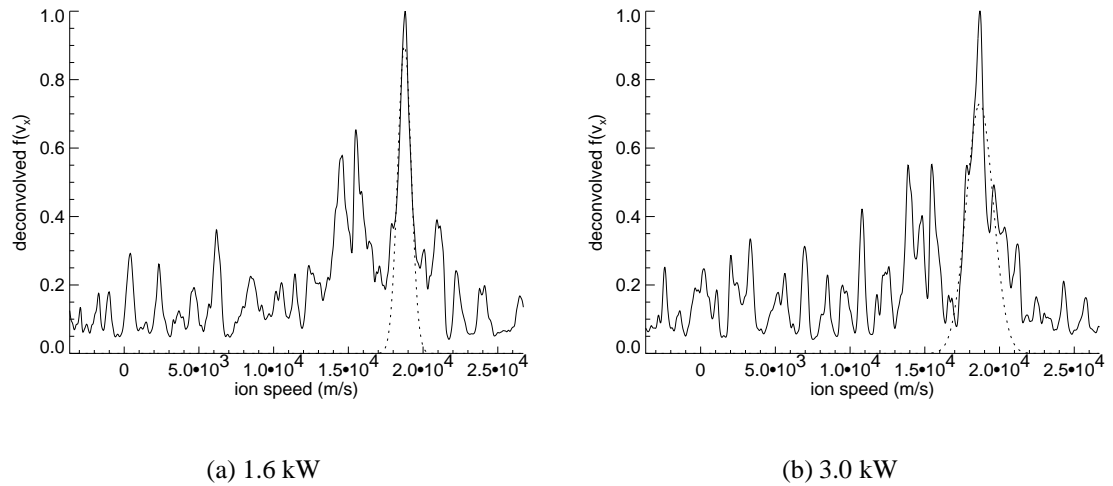


Figure 7.3: Deconvolved $f(v_x)$ (solid) & curve-fit (dashed) at $(x, y) = (20, 7.37)$ cm.

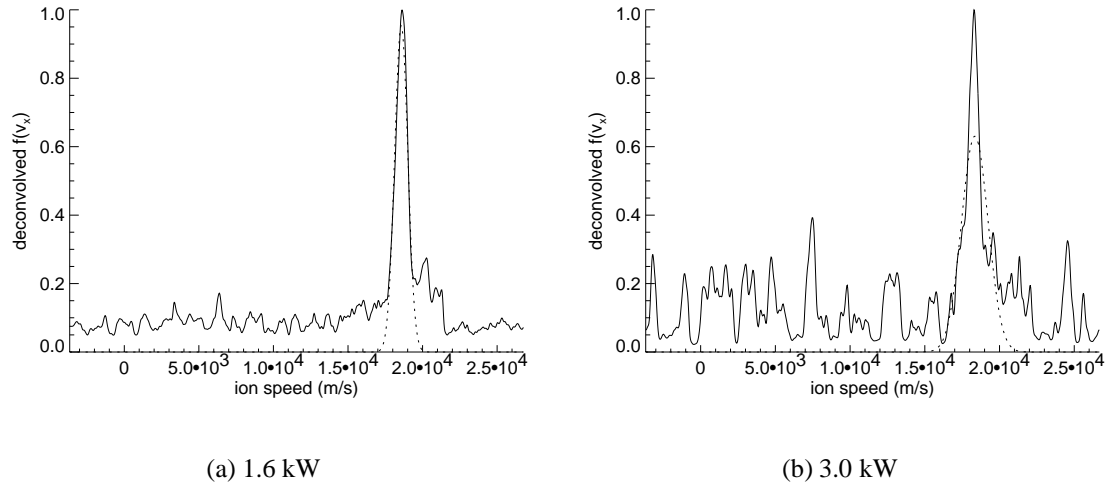


Figure 7.4: Deconvolved $f(v_x)$ (solid) & curve-fit (dashed) at $(x, y) = (10, 7.37)$ cm.

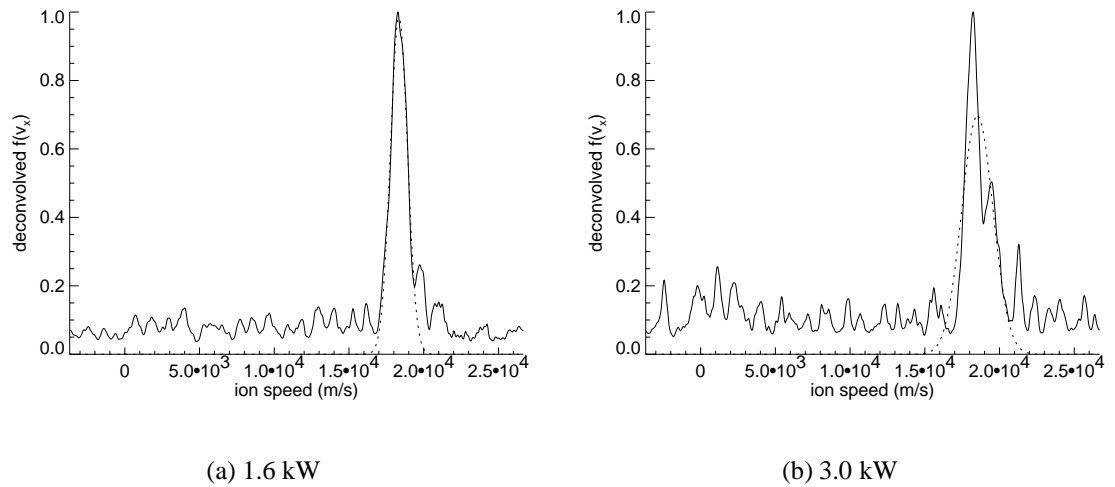


Figure 7.5: Deconvolved $f(v_x)$ (solid) & curve-fit (dashed) at $(x, y) = (5.0, 7.37)$ cm.

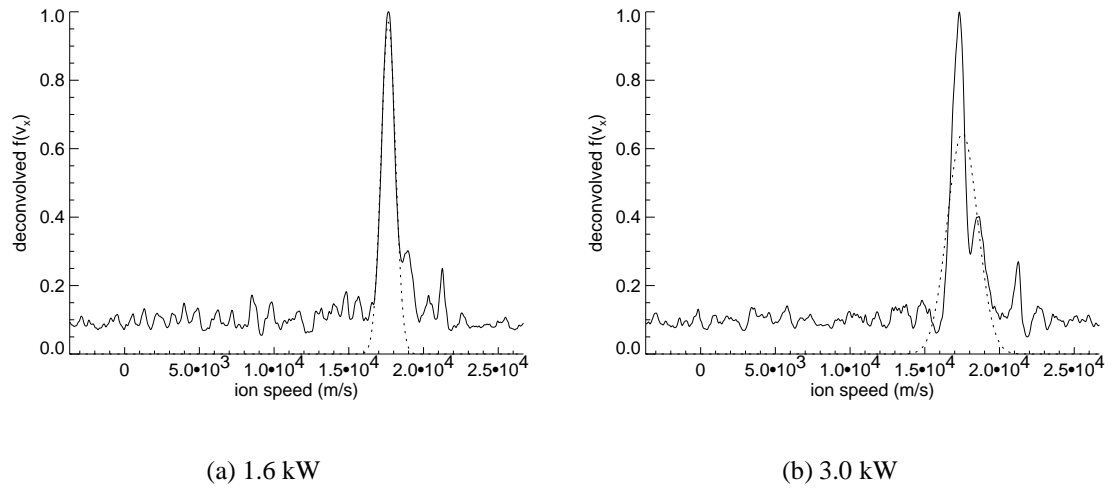


Figure 7.6: Deconvolved $f(v_x)$ (solid) & curve-fit (dashed) at $(x, y) = (2.0, 7.37)$ cm.

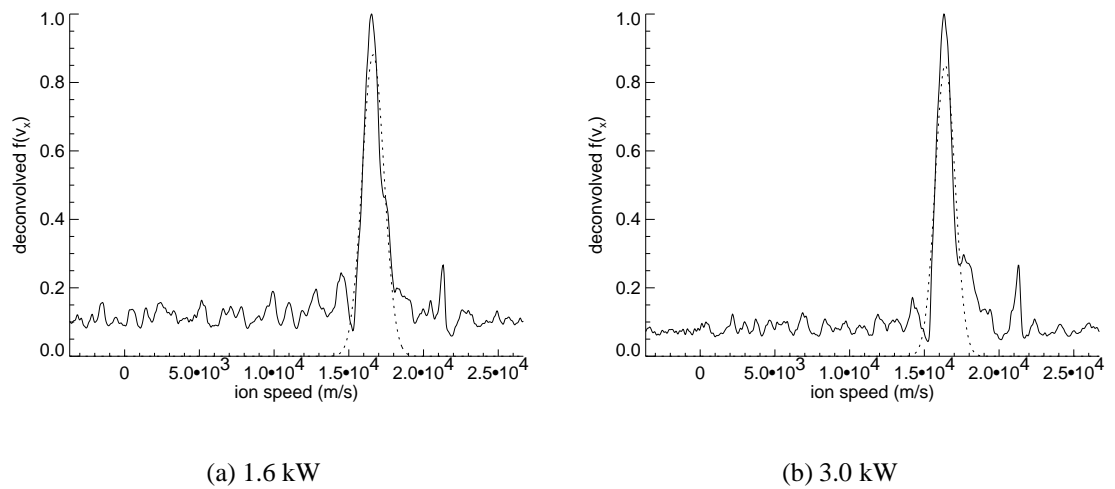


Figure 7.7: Deconvolved $f(v_x)$ (solid) & curve-fit (dashed) at $(x, y) = (1.0, 7.37)$ cm.

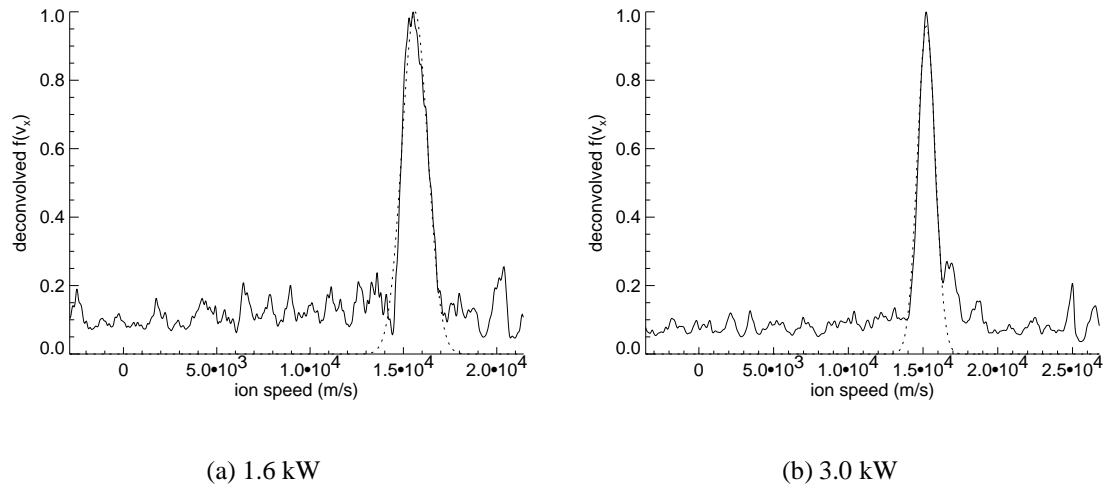


Figure 7.8: Deconvolved $f(v_x)$ (solid) & curve-fit (dashed) at $(x, y) = (0.5, 7.37)$ cm.

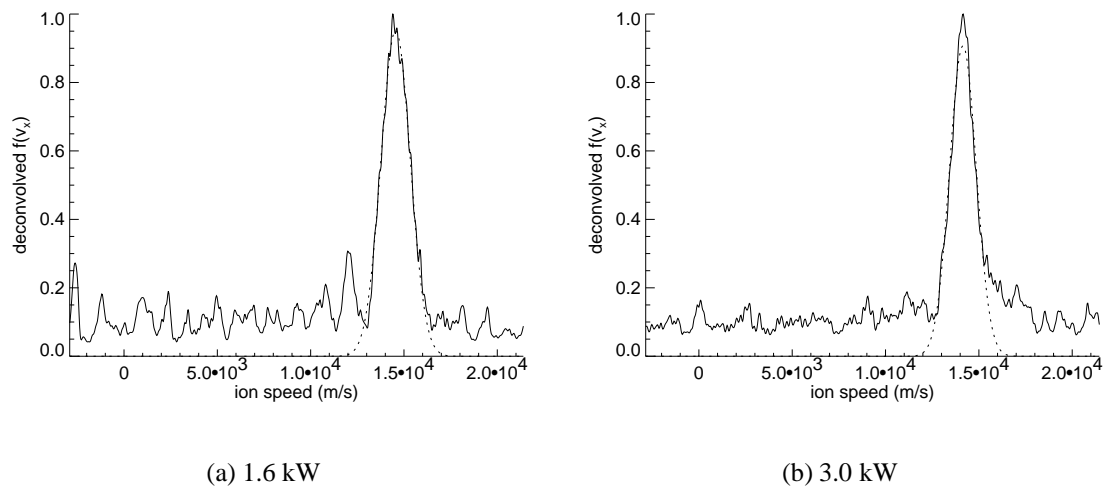


Figure 7.9: Deconvolved $f(v_x)$ (solid) & curve-fit (dashed) at $(x, y) = (0.2, 7.37)$ cm.

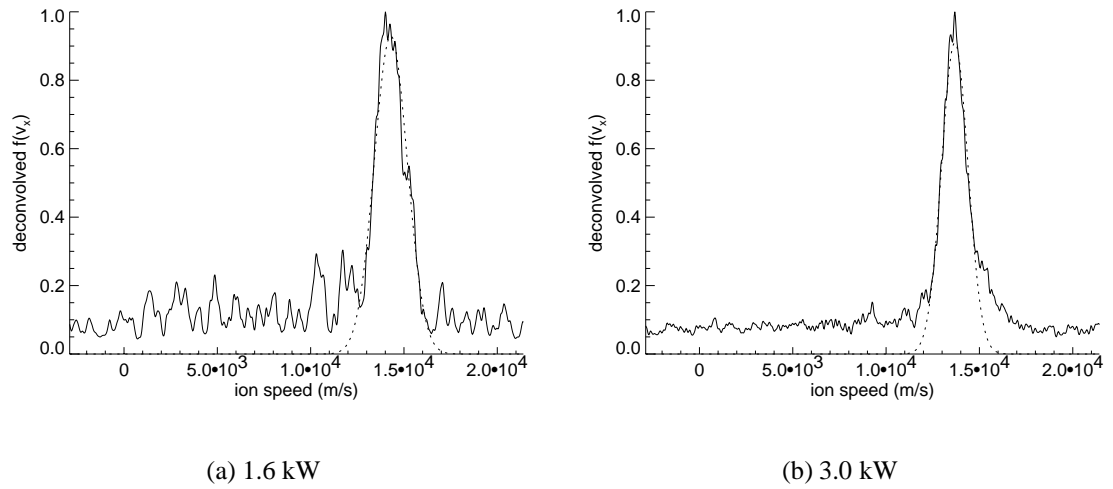


Figure 7.10: Deconvolved $f(v_x)$ (solid) & curve-fit (dashed) at $(x, y) = (0.1, 7.37)$ cm.

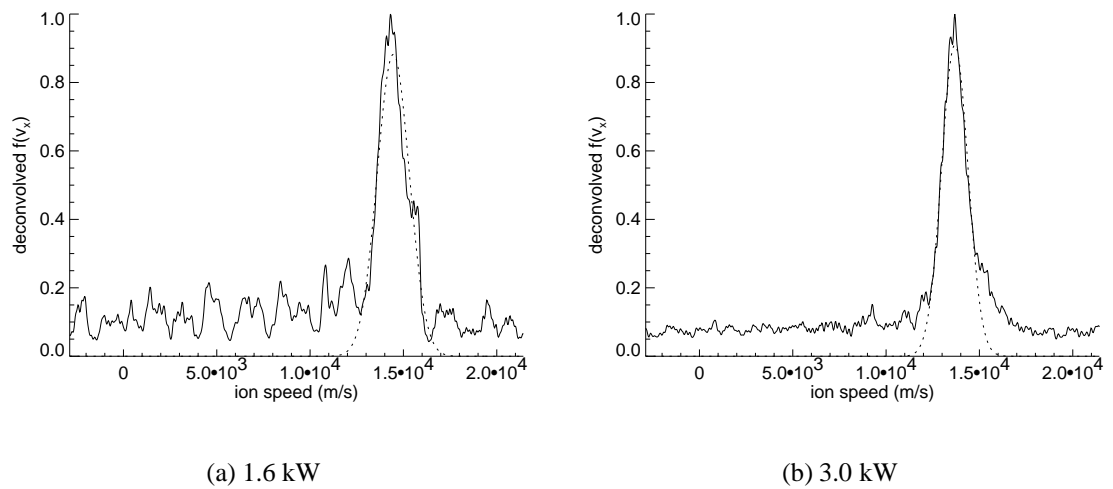


Figure 7.11: Deconvolved $f(v_x)$ (solid) & curve-fit (dashed) at $(x, y) = (0.05, 7.37)$ cm.

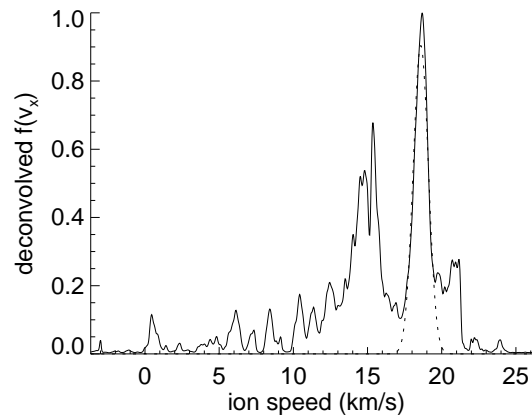


Figure 7.12: Averaged, twin-peaked distribution at 1.6 kW, $(x, y) = (20., 7.37)$ cm.

Repeat runs and extended laser frequency sweeps failed to pick up significant secondary populations in all but one case, shown in Fig. 7.12. Chauvenet-filtered averaging of four successive LIF spectra at this point ensures that this peak is not random noise.

Tables 7.2 and 7.3 contain values from Maxwellian curve-fits to the major peak of these distributions.

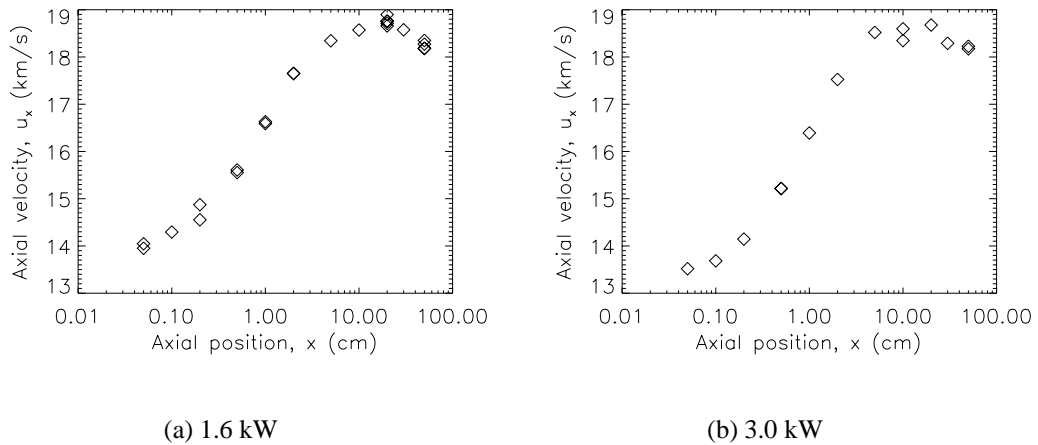


Figure 7.13: Axial ion velocity vs. axial position along P5 discharge centerline ($y = 7.37$ cm).

Figure 7.13 shows the axial variation of ion axial velocity along the P5 discharge channel axis, 7.37 cm outboard of the thruster axis. The axial velocity precision error [90]

Table 7.2: P5 axial plume temperatures & velocities at 1.6 kW along $y = 7.37$ cm.

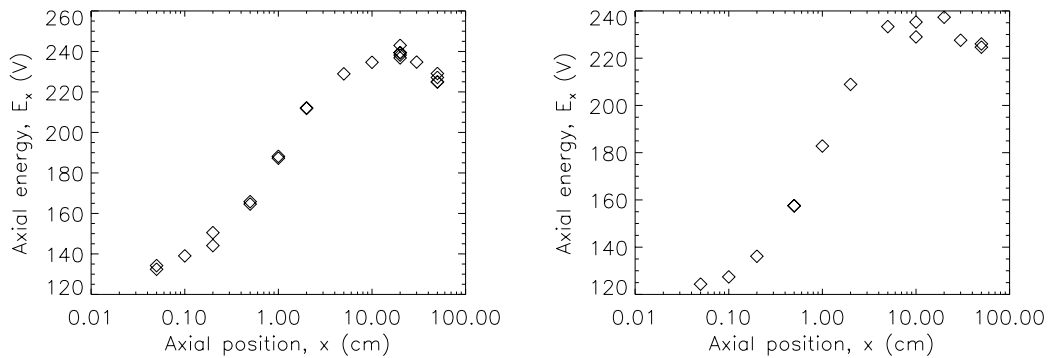
File name	Axial position x (cm)	Radial position y (cm)	Axial speed u_x (m/s)	Axial temp. T_x (eV)
15hwf	10.000	7.366	18571.	0.2666
15hwg	5.000	7.366	18344.	0.4481
16hwa	50.000	7.366	18179.	0.7101
16hwa1	50.000	7.366	18350.	0.9818
16hwa2	50.000	7.366	18272.	0.8417
16hwa3	50.000	7.366	18186.	0.9888
16hwb0	20.000	7.366	18755.	0.2795
16hwb1	20.000	7.366	18657.	0.7006
16hwb2	20.000	7.366	18897.	0.3130
16hwb3	20.000	7.366	18761.	0.3604
16hwb4	20.000	7.366	18710.	0.4445
16hwc	2.000	7.366	17646.	0.3144
16hwc1	2.000	7.366	17657.	0.5491
16hwd0	1.000	7.366	16631.	0.7273
16hwd1	1.000	7.366	16591.	0.4052
16hwe0	0.500	7.366	15554.	0.9515
16hwe1	0.500	7.366	15610.	0.6519
16hwf0	0.200	7.366	14873.	0.9109
16hwf1	0.200	7.366	14553.	0.8365
16hwg	0.100	7.366	14295.	1.0645
16hwh0	0.050	7.366	14046.	0.7593
16hwh1	0.050	7.366	13952.	0.8562
16hwt	30.000	7.366	18576.	0.5758

is less than 0.5% at 1.6 kW, and less than 1.0% at 3.0 kW. At 20 cm downstream of the exit plane, axial velocity hits a maximum of 18.7 km/s at 1.6 kW. Figure 7.12 shows how a significant secondary population with a velocity of 15.0 km/s occurs at this point. The axial velocity at 3.0 kW also reached its maximum (18.7 km/s) at $x = 20$ cm, but no secondary population appears in the velocity distribution there.

Figure 7.14 shows the same data in terms of axial energy. At 1.6 kW, axial energy rises from 133 V at $x = 5$ mm to 239 V at $x = 20$ cm, while it rises from 124 V to 237 V over the same range at 3.0 kW. Measurements at $x = 35$ cm and $x = 50$ cm show a slight

Table 7.3: P5 axial plume temperatures & velocities at 3.0 kW along $y = 7.37$ cm.

File name	Axial position x (cm)	Radial position y (cm)	Axial speed u_x (m/s)	Axial temp. T_x (eV)
30hwa	30.000	7.366	18290.	2.2194
30hwb0	50.000	7.366	18227.	1.8284
30hwb1	50.000	7.366	18172.	1.5476
30hwc	20.000	7.366	18677.	1.0972
30hwd0	10.000	7.366	18596.	1.8877
30hwd1	10.000	7.366	18347.	1.0727
30hwe	5.000	7.366	18520.	1.4961
30hwf	2.000	7.366	17524.	1.3963
30hwg	1.000	7.366	16392.	0.5960
30hwh0	0.500	7.366	15214.	1.5524
30hwh1	0.500	7.366	15219.	0.4884
30hwi	0.200	7.366	14146.	0.6956
30hwj	0.100	7.366	13685.	0.7590
30hwk	0.050	7.366	13519.	0.7431



(a) 1.6 kW operating condition.

(b) 3.0 kW operating condition.

Figure 7.14: Axial ion energy vs. axial position along P5 discharge centerline ($y = 7.37$ cm).

deceleration, so that by $x = 50$ cm, the axial energy drops to 227 V at 1.6 kW and 225 V at 3.0 kW.

Figure 7.15 shows the variation of ion axial temperature along the P5 discharge channel axis. The temperature trend at 1.6 kW roughly mirrors the velocity trend; *i.e.*, the

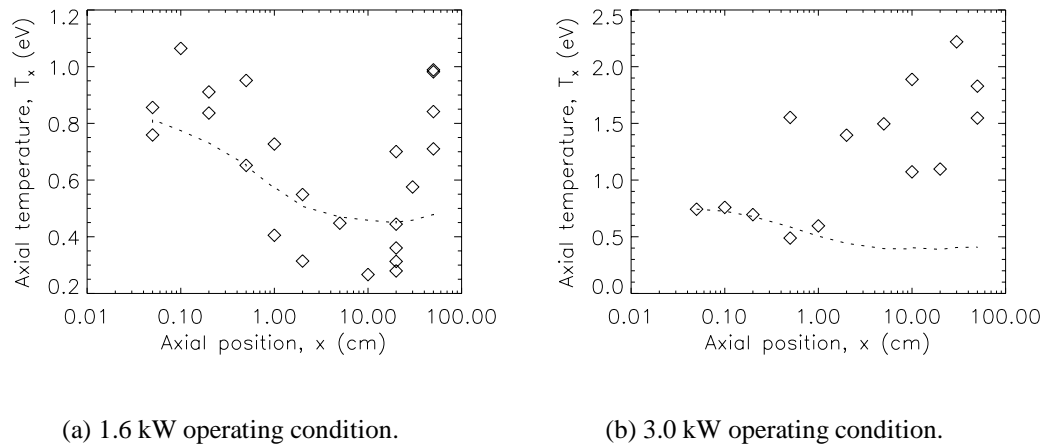


Figure 7.15: Axial ion temperature vs. axial position along P5 discharge centerline ($y = 7.37$ cm). Dashed line shows predicted kinematic compression.

minimum temperature (0.42 eV) is at the point of maximum velocity, while the temperature maxima are at the beginning (0.80 eV) and end (0.88 eV) of the sweep. This roughly follows the kinematic compression trend predicted by Eqn. 2.27. The temperature trend at 3.0 kW is more difficult to follow, but appears to be more-or-less linear with $\ln(x)$, rising from 0.74 eV near the exit plane to 1.68 eV at the end of the sweep. The predicted kinematic compression, if at all applicable, fails to appear past $x = 1.0$ cm. The axial temperature precision error is considerably higher than the velocity precision error, with most points lying within a 20% uncertainty band at 1.6 kW and a 40% uncertainty band at 3.0 kW.

7.1.2 Lateral sweep across discharge

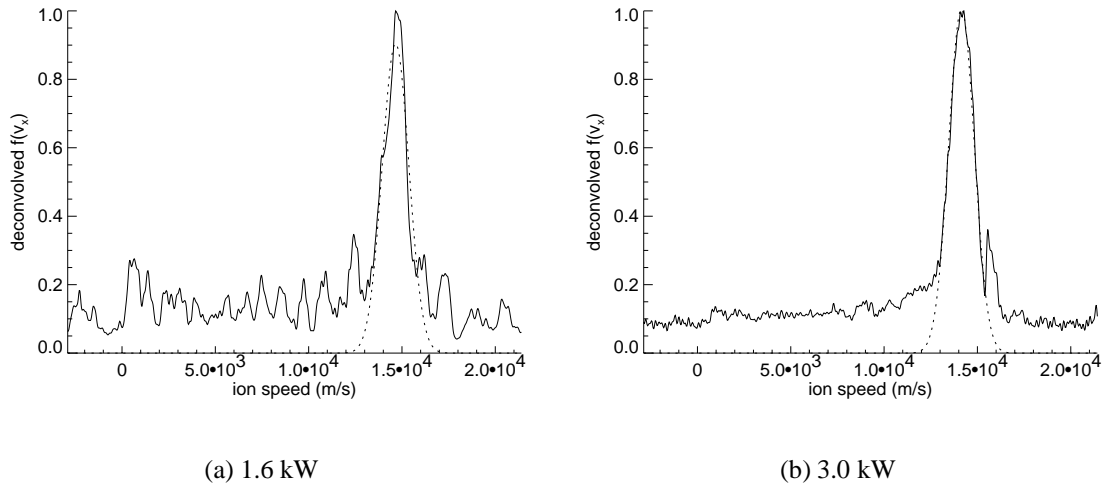


Figure 7.16: Deconvolved $f(v_x)$ (solid) & curve-fit (dashed) at $(x, y) = (0.1, 6.37)$ cm.

Figures 7.16 through 7.24 show axial velocity distributions taken on a lateral sweep 1 mm downstream of the discharge channel. As before, the solid line is the deconvolved distribution, while the dashed line is a Maxwellian curve-fit to a user-defined area within the major peak.

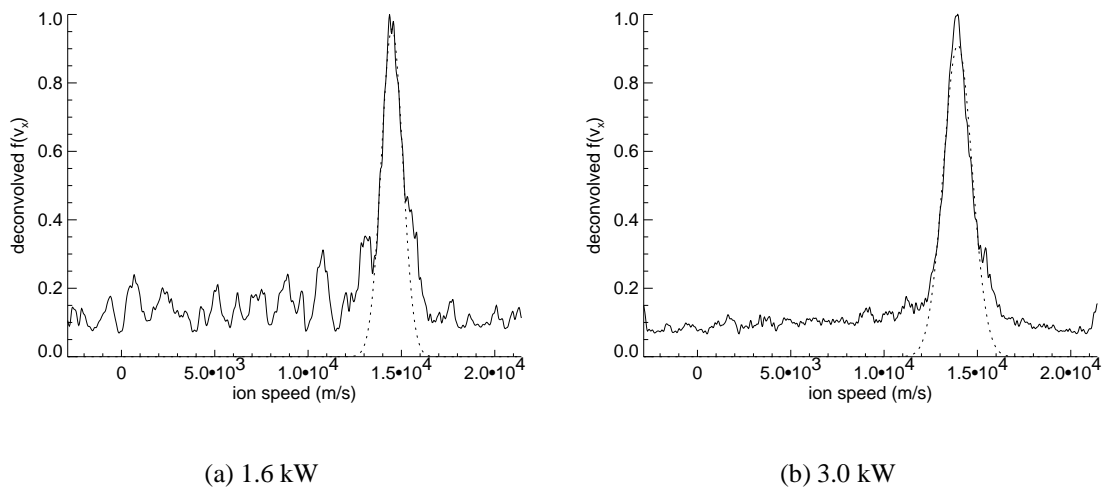


Figure 7.17: Deconvolved $f(v_x)$ (solid) & curve-fit (dashed) at $(x, y) = (0.1, 6.62)$ cm.

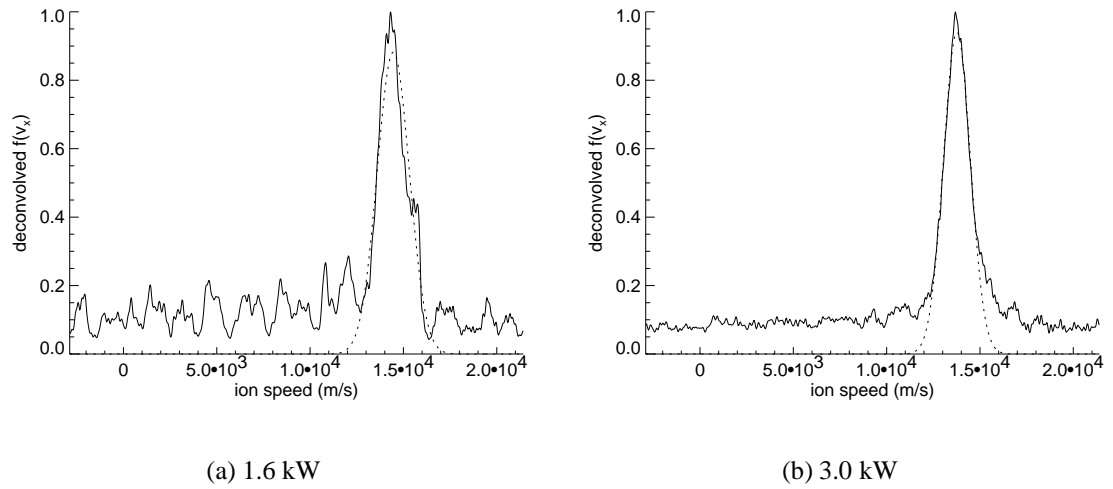


Figure 7.18: Deconvolved $f(v_x)$ (solid) & curve-fit (dashed) at $(x, y) = (0.1, 6.87)$ cm.

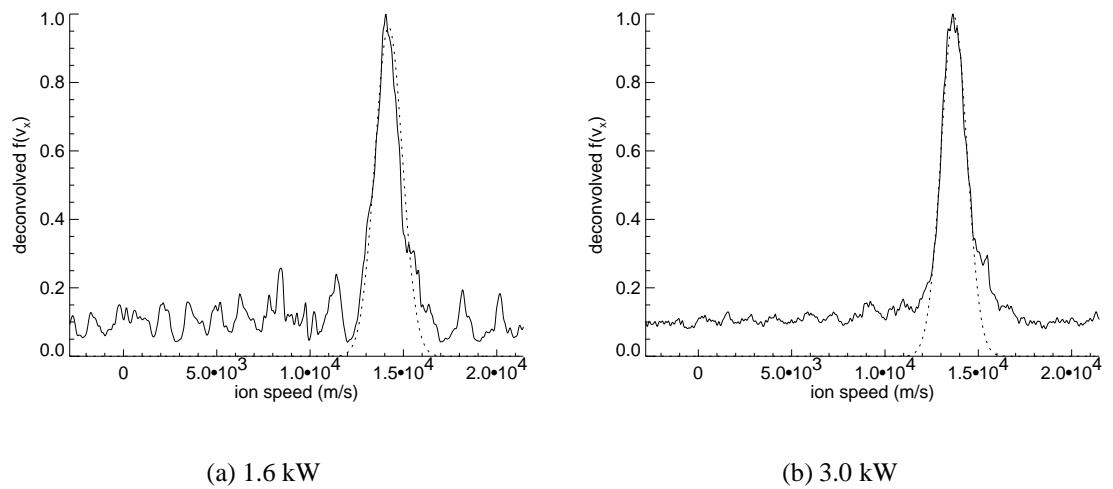


Figure 7.19: Deconvolved $f(v_x)$ (solid) & curve-fit (dashed) at $(x, y) = (0.1, 7.12)$ cm.

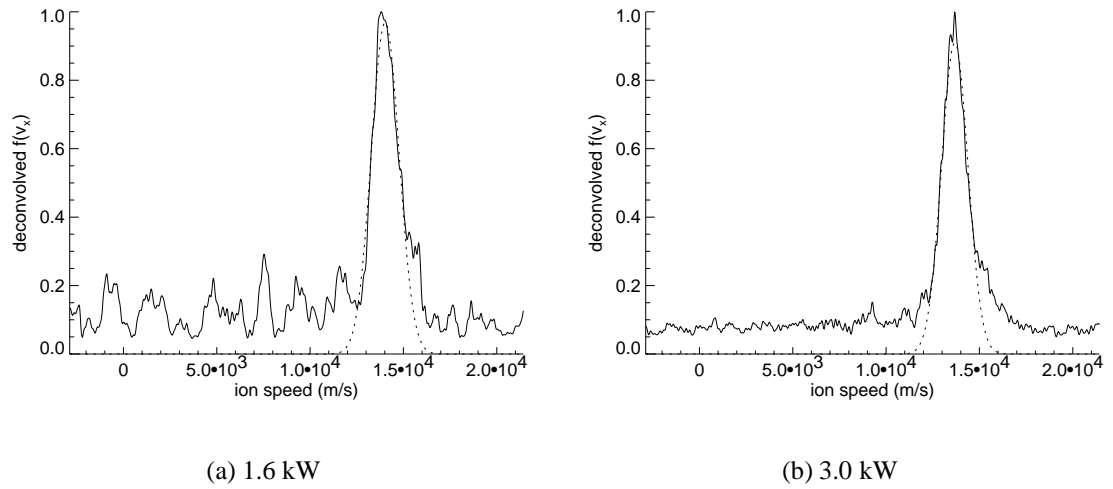


Figure 7.20: Deconvolved $f(v_x)$ (solid) & curve-fit (dashed) at $(x, y) = (0.1, 7.37)$ cm.

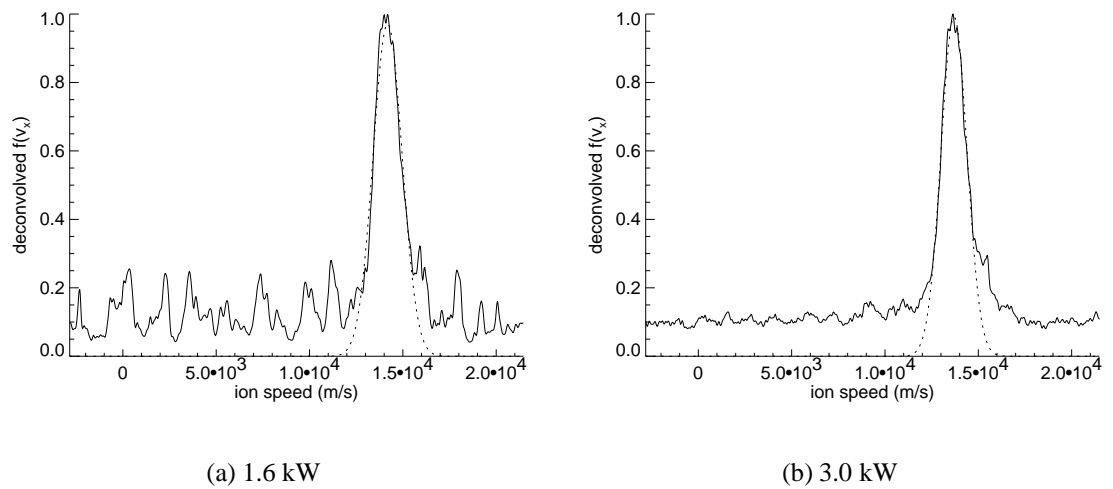


Figure 7.21: Deconvolved $f(v_x)$ (solid) & curve-fit (dashed) at $(x, y) = (0.1, 7.62)$ cm.

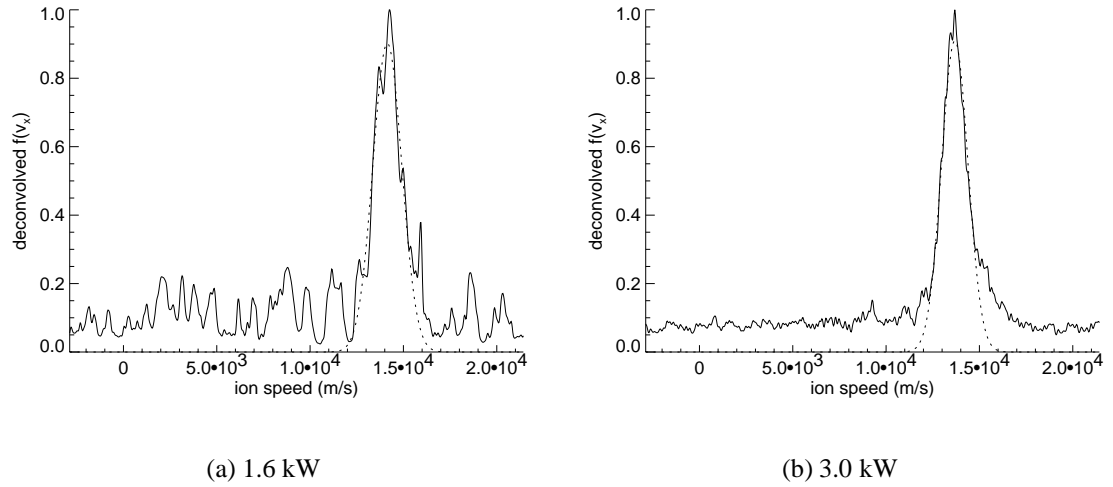


Figure 7.22: Deconvolved $f(v_x)$ (solid) & curve-fit (dashed) at $(x, y) = (0.1, 7.87)$ cm.

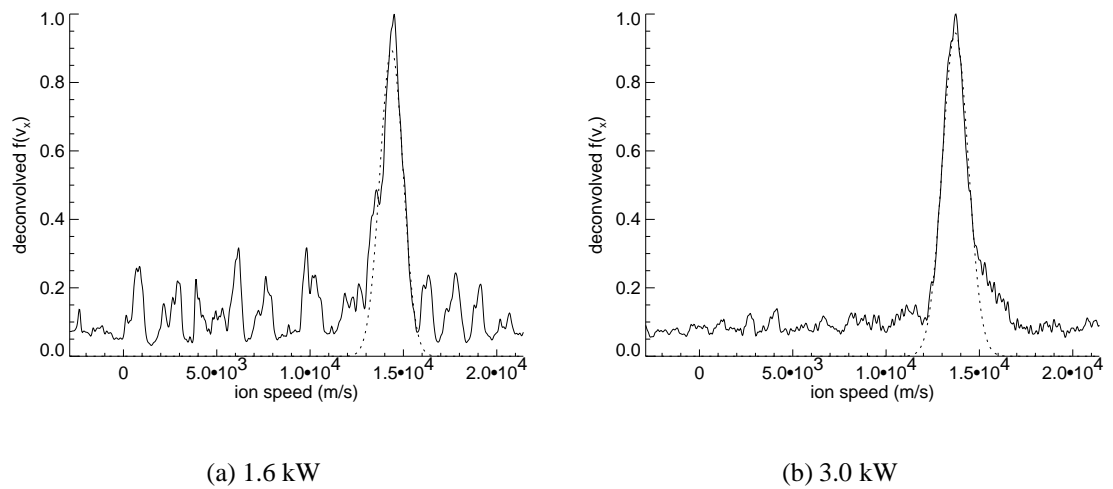


Figure 7.23: Deconvolved $f(v_x)$ (solid) & curve-fit (dashed) at $(x, y) = (0.1, 8.12)$ cm.

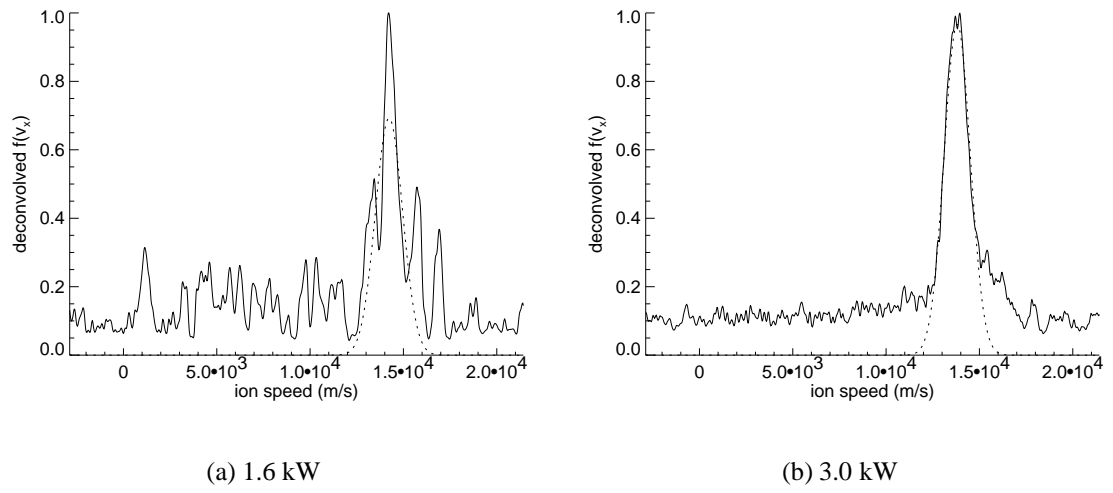


Figure 7.24: Deconvolved $f(v_x)$ (solid) & curve-fit (dashed) at $(x, y) = (0.1, 8.37)$ cm.

Tables 7.4 and 7.5 contain values from Maxwellian curve-fits to the major peak of these distributions.

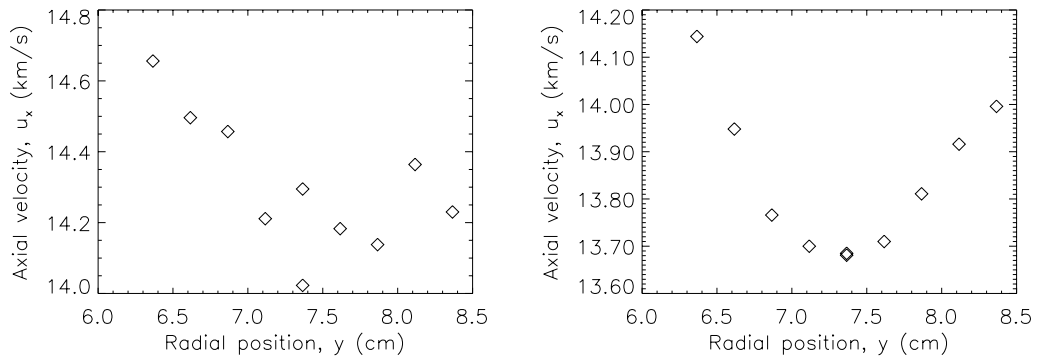
Table 7.4: P5 axial plume temperatures & velocities at 1.6 kW along $x = 0.10$ cm.

File name	Axial position x (cm)	Radial position y (cm)	Axial speed u_x (m/s)	Axial temp. T_x (eV)
16hwg	0.100	7.366	14295.	1.0645
16hwi	0.100	6.366	14656.	0.6947
16hwj	0.100	6.616	14496.	0.4449
16hwk	0.100	6.866	14457.	1.0074
16hwl	0.100	7.116	14211.	0.7395
16hwm	0.100	7.366	14023.	0.7567
16hwn	0.100	7.616	14183.	0.8211
16hwo	0.100	7.866	14138.	0.8162
16hwp	0.100	8.116	14364.	0.5231
16hwq	0.100	8.366	14230.	0.7244

Table 7.5: P5 axial plume temperatures & velocities at 3.0 kW along $x = 0.10$ cm.

File name	Axial position x (cm)	Radial position y (cm)	Axial speed u_x (m/s)	Axial temp. T_x (eV)
30hwj	0.100	7.366	13685.	0.7590
30hwl	0.100	6.366	14144.	0.6452
30hwm	0.100	6.616	13948.	0.8081
30hwn	0.100	6.866	13766.	0.7108
30hwo	0.100	7.116	13700.	0.6590
30hwp	0.100	7.366	13681.	0.6826
30hwq	0.100	7.616	13710.	0.6559
30hwr	0.100	7.866	13811.	0.6695
30hws	0.100	8.116	13916.	0.7121
30hwt	0.100	8.366	13996.	0.4832

Figure 7.25 shows the lateral variation of ion axial velocity along a plane 1 mm downstream of the P5 discharge channel axis. At both operating conditions, the minimum velocity is along the discharge channel centerline, with higher axial velocities at both edges of the discharge. The lateral profile at 1.6 kW ranges from 14.2 km/s to 14.7 km/s, with a



(a) 1.6 kW operating condition.

(b) 3.0 kW operating condition.

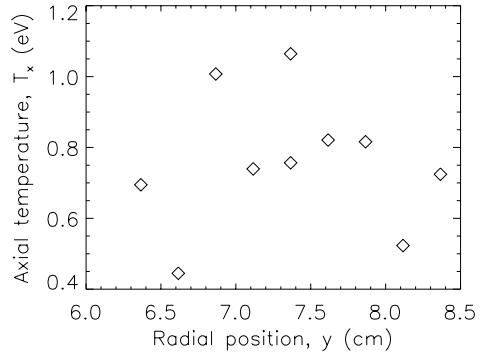
Figure 7.25: Axial ion velocity vs. lateral position 1 mm downstream of P5 discharge ($x = 0.1$ cm).

precision error within 1.5%. The lateral profile at 3.0 kW is an unusually smooth, nearly parabolic curve from 13.7 km/s to 14.1 km/s, with precision error well below 0.02%.

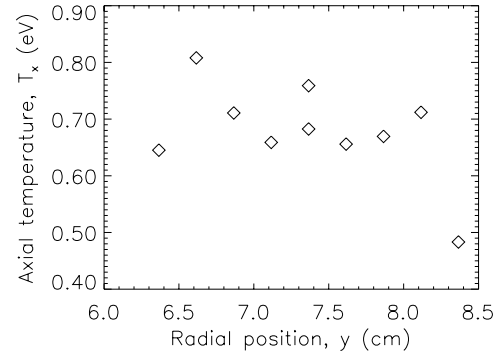
Figure 7.26 shows the variation of ion axial temperature along a plane 1 mm downstream of the P5 discharge channel axis. No clear trend is visible in the 1.6 kW data, while the 3.0 kW trend is largely flat around 0.72 eV.

7.1.3 Axial sweep along thruster centerline

Figures 7.27 through 7.31 show axial velocity distributions taken along the thruster centerline. Again, the solid line is the deconvolved distribution, while the dashed line is a Maxwellian curve-fit to a user-defined area within the major peak.

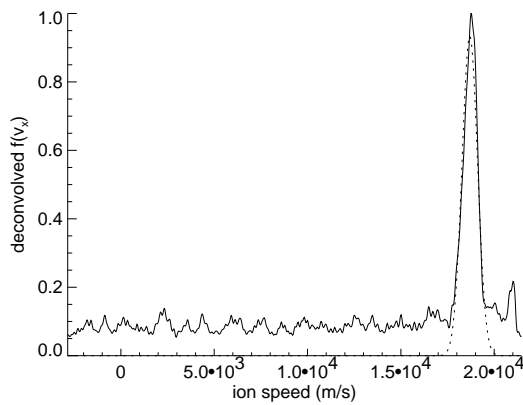


(a) 1.6 kW operating condition.

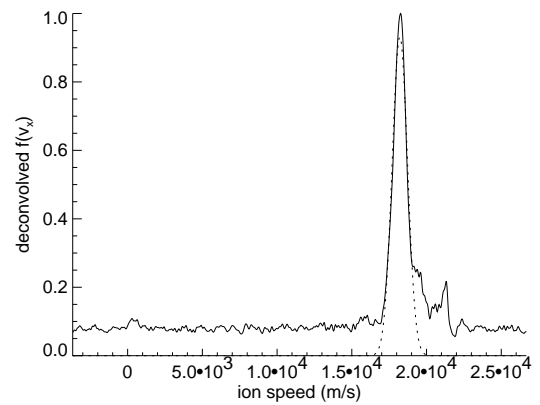


(b) 3.0 kW operating condition.

Figure 7.26: Axial ion temperature vs. lateral position 1 mm downstream of P5 discharge ($x = 0.1$ cm).



(a) 1.6 kW



(b) 3.0 kW

Figure 7.27: Deconvolved $f(v_x)$ (solid) & curve-fit (dashed) at $(x, y) = (50, 0)$ cm.

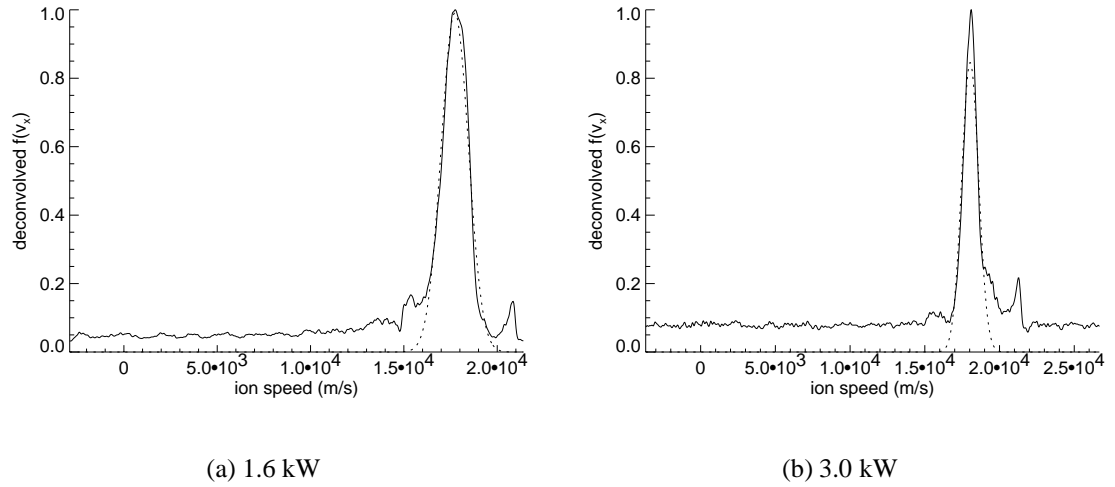


Figure 7.28: Deconvolved $f(v_x)$ (solid) & curve-fit (dashed) at $(x, y) = (40, 0)$ cm.

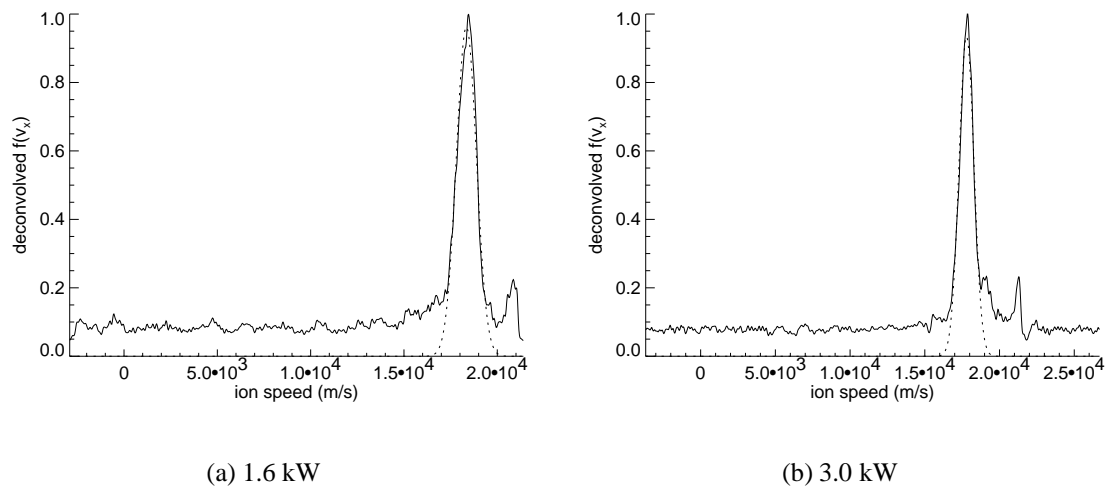


Figure 7.29: Deconvolved $f(v_x)$ (solid) & curve-fit (dashed) at $(x, y) = (30, 0)$ cm.

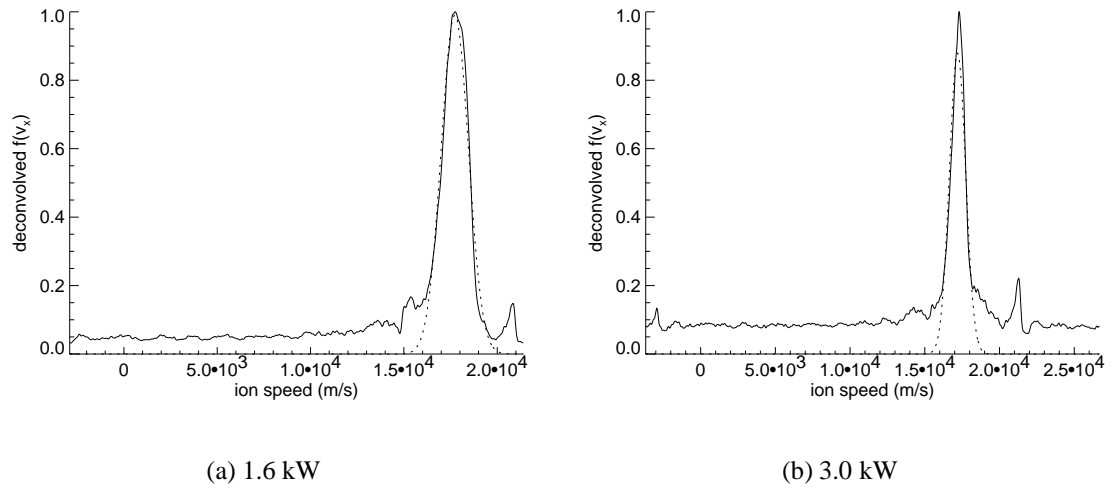


Figure 7.30: Deconvolved $f(v_x)$ (solid) & curve-fit (dashed) at $(x, y) = (20, 0)$ cm.

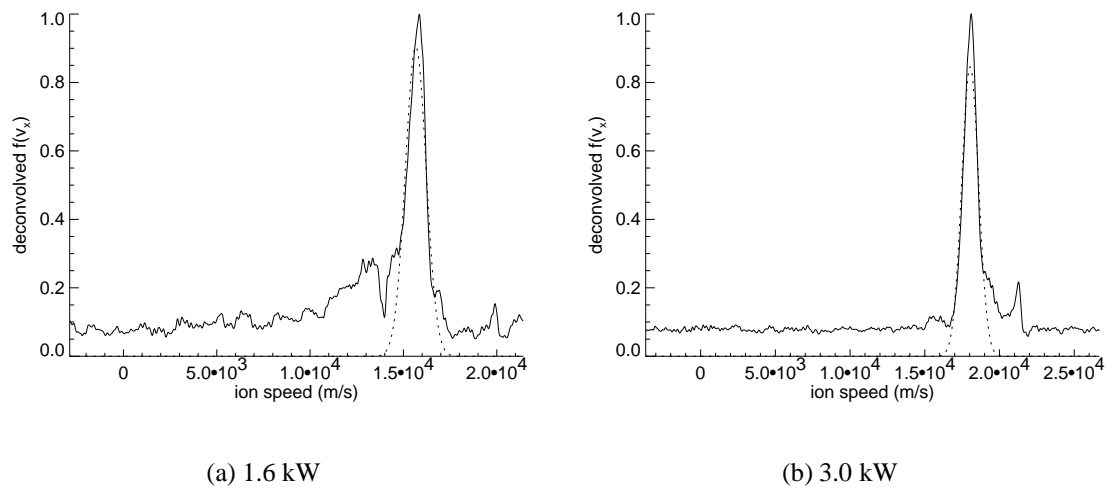


Figure 7.31: Deconvolved $f(v_x)$ (solid) & curve-fit (dashed) at $(x, y) = (10, 0)$ cm.

Tables 7.6 and 7.7 contain values from Maxwellian curve-fits to the major peak of these distributions.

Table 7.6: P5 axial plume temperatures & velocities at 1.6 kW along $y = 0$ cm.

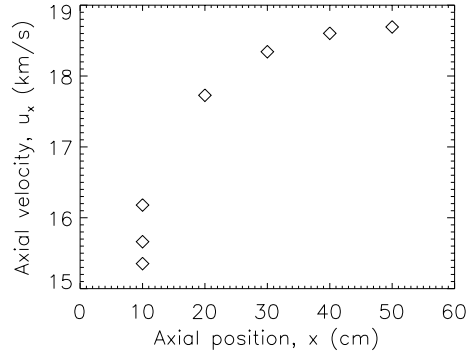
File name	Axial position x (cm)	Radial position y (cm)	Axial speed u_x (m/s)	Axial temp. T_x (eV)
16hwr0	10.000	0.000	15353.	1.7253
16hwr1	10.000	0.000	15662.	0.4207
16hws0	5.000	0.000	10324.	15.9219
15hwa	10.000	0.000	16180.	2.7319
15hwb	20.000	0.000	17729.	0.7256
15hwc	30.000	0.000	18343.	0.3936
15hwd	40.000	0.000	18603.	0.2714
15hwe	50.000	0.000	18693.	0.2351

Table 7.7: P5 axial plume temperatures & velocities at 3.0 kW along $y = 0$ cm.

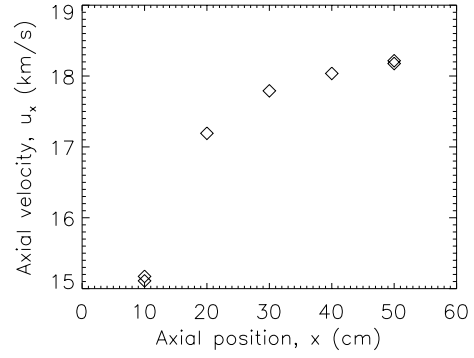
File name	Axial position x (cm)	Radial position y (cm)	Axial speed u_x (m/s)	Axial temp. T_x (eV)
30hwu	50.000	0.000	18176.	0.3241
30hwu1	50.000	0.000	18216.	0.3579
30hwv	40.000	0.000	18037.	0.4326
30hww	30.000	0.000	17791.	0.3378
30hwx	20.000	0.000	17192.	0.4055
30hwy0	10.000	0.000	15110.	1.3727
30hwy1	10.000	0.000	15173.	0.6588

Figure 7.32 shows the axial variation of ion axial velocity along the thruster axis. Here, the velocity increases monotonically with distance.

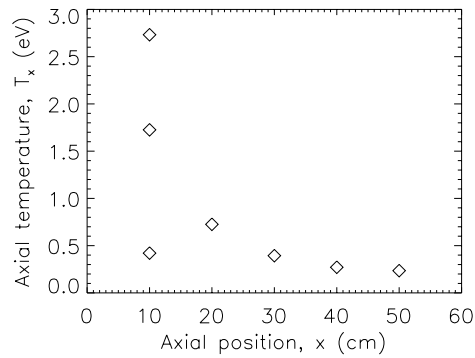
Figure 7.33 shows the variation of ion axial temperature along the P5 discharge channel axis.



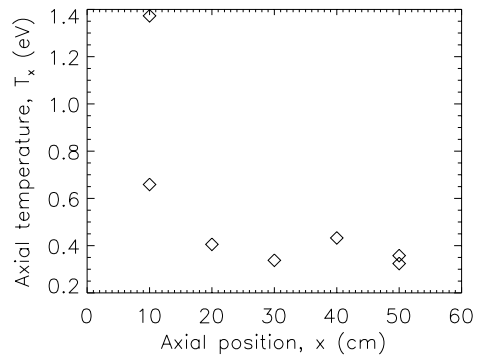
(a) 1.6 kW operating condition.



(b) 3.0 kW operating condition.

Figure 7.32: Axial ion velocity vs. axial position along P5 centerline ($y = 0$ cm).

(a) 1.6 kW operating condition.



(b) 3.0 kW operating condition.

Figure 7.33: Axial ion temperature vs. axial position along P5 centerline ($y = 0$ cm).

7.2 Multiplex LIF of P5 plume

These off-axis multiplex LIF experiments were part of a series of electrodynamic tether experiments carried out by Gilchrist *et al.* [89]. We took off-axis multiplex LIF spectra at five operating conditions: the standard 3.0 kW condition, and four operating conditions specifically chosen for ionospheric simulation (TC 9, TC 10, TC 1 and TC 2).

Each data point reported here is the Chauvenet-filtered average of seven scans, taken at a rate of 60 s per 10-GHz segment; we used a lock-in time constant of 1 second for each P5 spectrum. We used a Princeton Applied Research model 121 lock-in amplifier for the reference cell signal; its 3 second time constant gives the same effect as a 1 second time constant on the Stanford lock-ins. Post-calibration runs allowed us to determine how much this time constant difference shifts the relative peak location, and adjust the deconvolution routine output accordingly.

Table 7.8 gives the thruster operating conditions used in these experiments.

Table 7.8: P5 operating conditions for multiplex LIF.

	3.0 kW	TC 9	TC 10	TC 1	TC 2	units
Discharge voltage V_d	300.1	150.1	100.0	100.0	100.0	V
Anode potential V_a	271.9	125.9	77.2	78.7	79.9	V
Cathode potential V_c	-28.2	-24.2	-22.8	-21.3	-20.1	V
Discharge current I_d	10.40	11.20	12.70	5.46	4.22	A
Anode flow rate \dot{m}_a	114.0	108.6	111.6	61.5	48.0	sccm
Cathode flow rate \dot{m}_c	6.00	6.00	6.00	6.00	6.00	sccm
Facility pressure P	8.9	8.5	8.5	5.2	4.2	μ Torr

Discharge voltage was held constant within the power supply measurement precision during each test. The anode and cathode flow rate settings also remained constant. The run-to-run variation of discharge current was less than 10%, while the day-to-day variation of cathode floating potential was less than 2%.

7.2.1 3 kW condition

The first P5 operating condition was the standard 3.0 kW discharge (300 V, 10.4 A). As our initial plan was to keep the maximum number of test conditions under 50 points, we only took 5 data points at 3.0 kW, primarily as a check that the LIF system was operating properly.

Figures B.1 through B.5 show off-axial, off-radial and vertical velocity distributions taken downstream of the discharge channel and on the thruster centerline. (The first sub-figure shows the stationary plasma velocity distribution from the optogalvanic cell.) The solid line is the deconvolved distribution, while the dashed line is a Maxwellian curve-fit to a user-defined area within the major peak. Velocity distributions taken along the thruster centerline (3kwa and 3kwe) show the prominent two-peak structure characteristic of counterflowing plasmas. Distributions taken downstream of the discharge channel show a more conventional, single-peak structure, which can be readily fit to a Maxwellian distribution.

Table 7.9 gives bulk velocities, while Table 7.10 gives temperatures, for these locations. Distributions with two peaks are reported twice, with one velocity and temperature for each peak.

Table 7.9: Bulk velocities in the P5 plume at 3 kW.

File name	Axial position x (cm)	Radial position y (cm)	Peak flow direction	Axial speed u_x (m/s)	Radial speed u_y (m/s)	Vertical speed u_z (m/s)
3kwa	10.01	0.000	up	14137	-1142.8	8447.0
3kwa	10.01	0.000	down	15207	-746.2	-7375.4
3kwb	10.01	6.366	–	19888	-953.6	-135.0
3kwc	10.01	7.366	–	20122	768.3	-149.1
3kwd	10.01	8.366	–	19971	2284.5	-124.5
3kwe	50.02	0.000	up	19274	145.9	1715.5
3kwe	50.02	0.000	down	20639	-571.3	-1893.9

Table 7.11 shows how repeated runs through the analysis code change the reported

values. This variation is caused by the need to manually choose curve-fitting endpoints.

Figure 7.34 shows the radial variation of ion axial velocity and energy 10.01 cm downstream of the P5 exit plane. The maximum value of u_x along this plane is at the discharge channel centerline, which is odd; axial-injection LIF measurements (Fig. 7.25) indicate that the minimum value of u_x along a plane 1 mm downstream of the P5 exit is also at the discharge channel centerline.

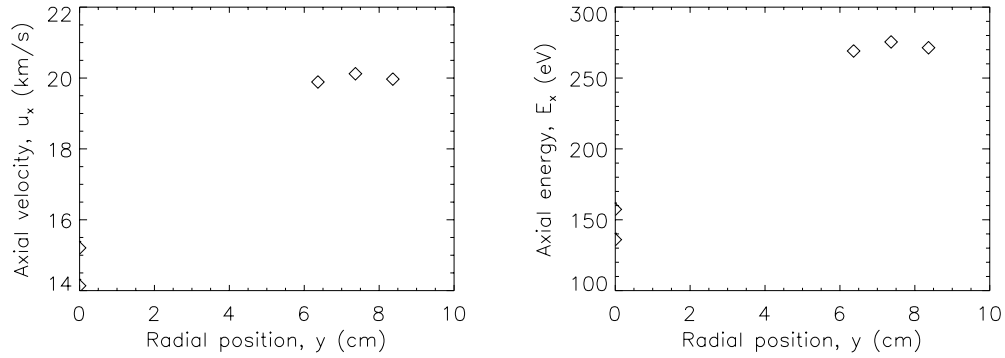


Figure 7.34: Axial ion velocity & energy vs. radial position at $x = 10.01$ cm for 3kW.

Figure 7.35 shows the radial variation of ion radial and vertical velocity along the same axial plane. The radial velocity pattern follows expected patterns of beam divergence, with inward flow at the inner edge of the discharge channel and outward flow at the outer edge;

Table 7.10: P5 plume temperatures at 3 kW.

File name	Axial position x (cm)	Radial position y (cm)	Peak flow direction	Axial temp T_x (eV)	Radial temp T_y (eV)	Vertical temp T_z (eV)
3kwa	10.01	0.000	up	2.6900	4.6924	5.5495
3kwa	10.01	0.000	down	3.1224	5.7856	7.0978
3kwb	10.01	6.366	–	0.7180	0.7207	0.7221
3kwc	10.01	7.366	–	0.4776	0.5933	0.6494
3kwd	10.01	8.366	–	0.3906	0.5680	0.5686
3kwe	50.02	0.000	up	0.3021	0.3033	0.3041
3kwe	50.02	0.000	down	0.4534	0.4507	0.4539

Table 7.11: P5 plume temperatures & velocity: variation with analysis (3kW data at $(x, y) = (10.01, 7.37)$ cm).

Trial	Axial speed u_x (m/s)	Radial speed u_y (m/s)	Vertical speed u_z (m/s)	Axial temp. T_x (eV)	Radial temp. T_y (eV)	Vertical temp. T_z (eV)
0	20122	768.3	-149.1	0.4776	0.5933	0.6494
1	20124	825.4	-138.2	0.4831	0.6021	0.6704
2	20065	719.7	-143.4	0.5046	0.6729	0.6863
3	20086	864.1	-138.4	0.5187	0.6420	0.6434
4	20181	693.1	-154.0	0.5560	0.5849	0.7212
μ	20116	774.1	-144.6	0.5080	0.6190	0.6741
σ	44.23	71.21	6.882	0.0315	0.0372	0.0314

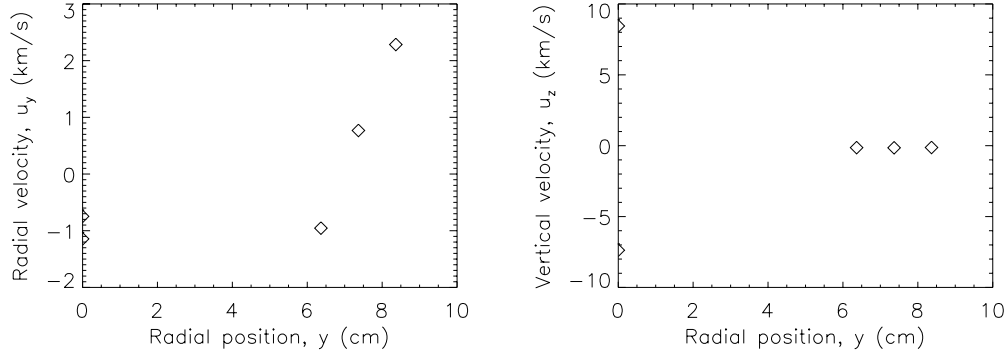


Figure 7.35: Radial & vertical ion velocity vs. radial position at $x = 10.01$ cm for 3kW.

however, the positive value of u_y on the discharge channel centerline clearly shows that assuming a purely axial ion trajectory along the centerline is unrealistic. Thus, the apparent “deceleration zone” shown in Fig. 7.13 could be more properly termed a zone of slowly decreasing axial velocity, as it is unclear if any ions are actually decelerating in that zone.

Figure 7.36 shows the radial variation of all three temperature components 10.01 cm downstream of the P5 exit plane. Axial temperatures are consistently lower than radial or vertical temperatures, which again lends support to the kinematic compression hypothesis. The highest temperatures occur in both peaks of the thruster centerline distribution, with ion temperatures tending to drop with increasing distance from the thruster centerline.

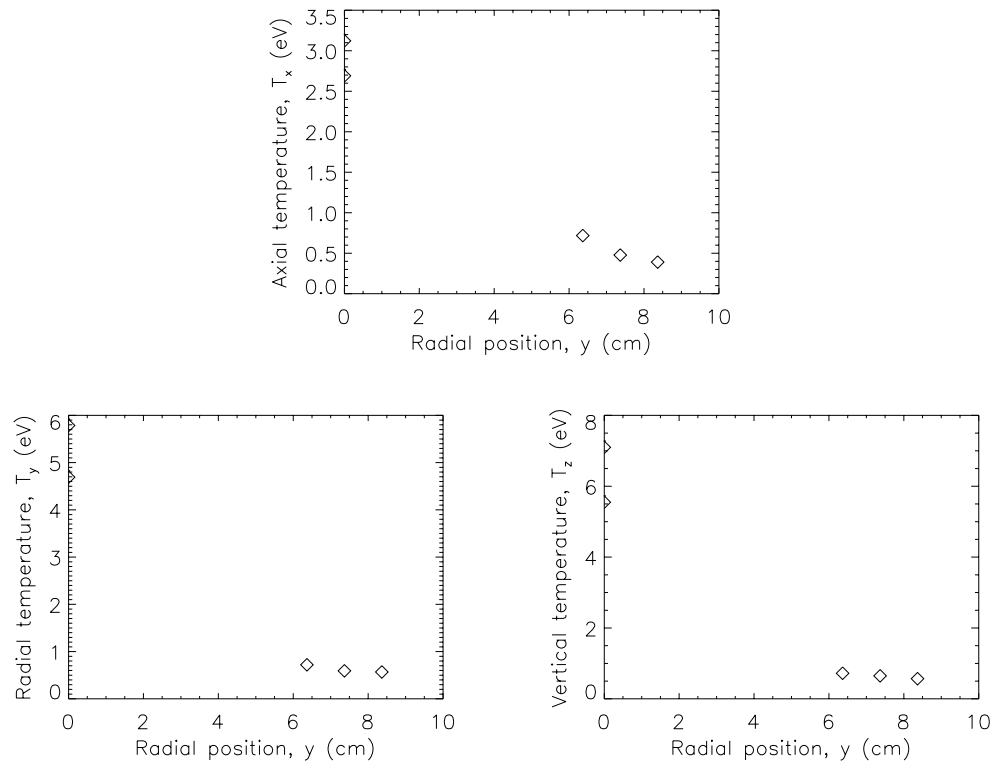


Figure 7.36: Axial, radial and vertical temperatures vs. radial position at $x = 10.01$ cm for 3kW.

7.2.2 Test condition 9

Test condition 9 (TC9) was the second P5 operating condition. Since the specified data collection points were spaced radially around the thruster centerline, all velocity distributions were again two-peaked.

Figures B.6 through B.26 show off-axial, off-radial and vertical velocity distributions taken 50, 63 and 75 cm downstream of the P5 exit plane. Again, the solid line is the deconvolved distribution, while the dashed line is a Maxwellian curve-fit to one of the peaks. Tables 7.12 and 7.13 contain bulk velocities and temperatures from these curve-fits.

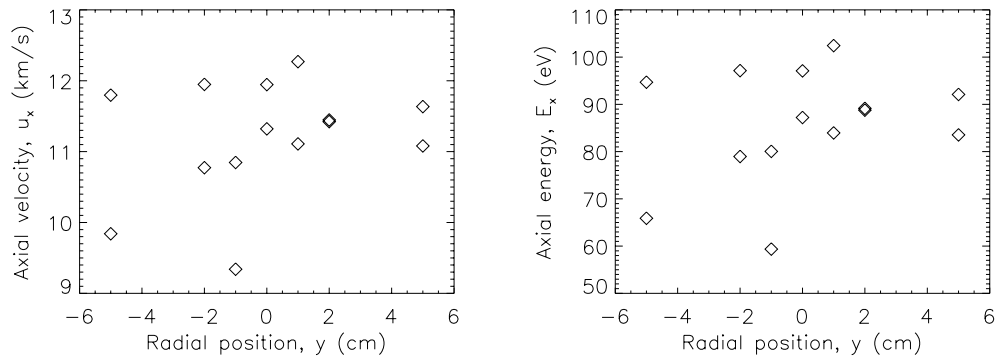


Figure 7.37: Axial ion velocity & energy vs. radial position at $x = 50.02$ cm for TC9.

Figures 7.37, 7.38 and 7.39 show the radial variation of axial velocity and energy 50 cm, 63 cm and 75 cm downstream of the P5 exit plane. Trends are difficult to determine, as the axial velocity spread between peaks of a distribution is usually larger than the difference between average axial velocities at different radial locations. This spread is largest at $y = -5$ cm at all three axial planes, while the spread is relatively small at $y = 5$ cm.

No noticeable trends stand out in the other plots of velocity and temperature as a function of radial location.

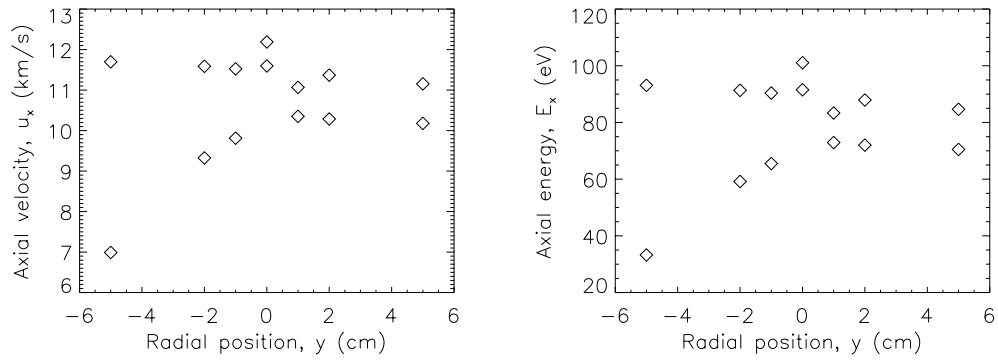


Figure 7.38: Axial ion velocity & energy vs. radial position at $x = 63.14$ cm for TC9.

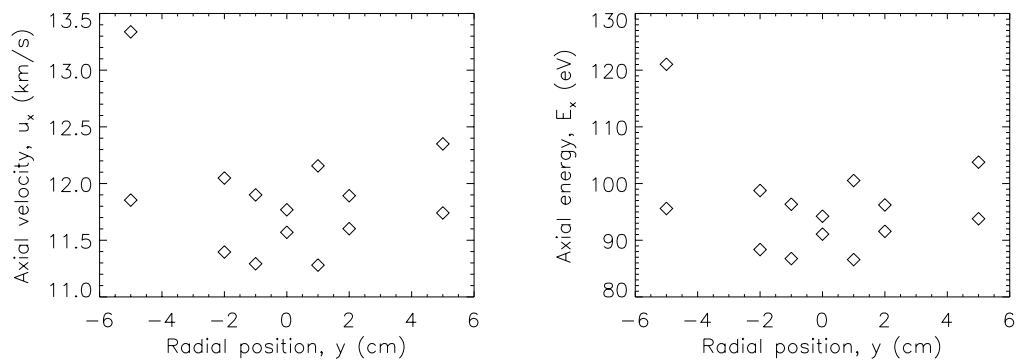


Figure 7.39: Axial ion velocity & energy vs. radial position at $x = 75.00$ cm for TC9.

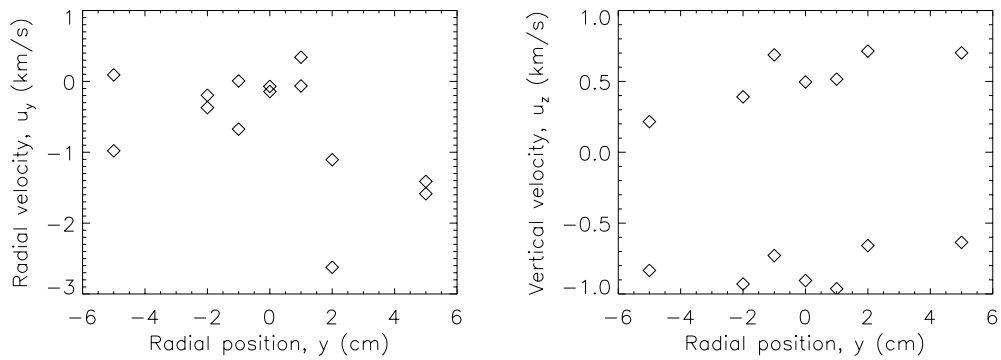


Figure 7.40: Radial & vertical ion velocity vs. radial position at $x = 50.02$ cm for TC9.

Table 7.12: Bulk velocities in the P5 plume at TC9.

File name	Axial position	Radial position	Peak flow direction	Axial speed	Radial speed	Vertical speed
	x (cm)	y (cm)		u_x (m/s)	u_y (m/s)	u_z (m/s)
tc9a	50.02	0.000	up	11322	-142.6	496.4
tc9a	50.02	0.000	down	11946	-70.8	-904.6
tc9b	50.02	-1.000	up	9341	6.1	687.0
tc9b	50.02	-1.000	down	10847	-673.3	-728.7
tc9c	50.02	1.000	up	11109	-63.6	516.0
tc9c	50.02	1.000	down	12270	341.4	-962.7
tc9d	50.02	2.000	up	11447	-1104.9	714.0
tc9d	50.02	2.000	down	11423	-2623.4	-658.6
tc9e	50.02	-2.000	up	10773	-370.6	391.3
tc9e	50.02	-2.000	down	11949	-195.1	-929.5
tc9f	50.02	-5.000	up	9841	-979.3	216.5
tc9f	50.02	-5.000	down	11797	91.7	-833.3
tc9g	50.02	5.000	up	11081	-1411.1	701.6
tc9g	50.02	5.000	down	11635	-1585.4	-635.5
tc9h	63.14	0.000	up	11598	570.8	512.7
tc9h	63.14	0.000	down	12189	1097.0	-517.8
tc9i	63.14	-1.000	up	9812	723.1	772.7
tc9i	63.14	-1.000	down	11525	528.5	-482.3
tc9j	63.14	1.000	up	10353	192.6	697.0
tc9j	63.14	1.000	down	11067	273.0	-490.0
tc9k	63.14	2.000	up	10287	217.9	754.2
tc9k	63.14	2.000	down	11369	6.1	-444.6
tc9l	63.14	-2.000	up	9326	1163.1	694.5
tc9l	63.14	-2.000	down	11587	742.0	-532.0
tc9m	63.14	-5.000	up	6991	1512.2	690.5
tc9m	63.14	-5.000	down	11698	1669.7	-482.6
tc9n	63.14	5.000	up	10178	-367.2	741.8
tc9n	63.14	5.000	down	11155	-640.2	-342.8
tc9o	75.00	0.000	up	11570	590.0	430.9
tc9o	75.00	0.000	down	11769	-288.9	-307.6
tc9p	75.00	1.000	up	11281	665.2	435.3
tc9p	75.00	1.000	down	12156	176.0	-354.4
tc9q	75.00	-1.000	up	11293	528.5	406.9
tc9q	75.00	-1.000	down	11900	86.8	-331.3
tc9r	75.00	-2.000	up	11396	-247.6	362.0
tc9r	75.00	-2.000	down	12049	17.8	-427.9
tc9s	75.00	2.000	up	11602	379.9	471.2
tc9s	75.00	2.000	down	11893	-304.0	-355.8
tc9t	75.00	5.000	up	11741	-294.5	482.8
tc9t	75.00	5.000	down	12350	-1876.5	-336.1
tc9u	75.00	-5.000	up	13338	-332.3	-58.2
tc9u	75.00	-5.000	down	11854	1221.4	-395.0

Table 7.13: P5 plume temperatures at TC9.

File name	Axial position x (cm)	Radial position y (cm)	Peak flow direction	Axial temp T_x (eV)	Radial temp T_y (eV)	Vertical temp T_z (eV)
tc9a	50.02	0.000	up	0.3866	0.3879	0.3892
tc9a	50.02	0.000	down	0.2875	0.3920	0.3943
tc9b	50.02	-1.000	up	0.3439	0.2480	0.3478
tc9b	50.02	-1.000	down	0.2104	0.5158	0.5190
tc9c	50.02	1.000	up	0.3404	0.2978	0.3429
tc9c	50.02	1.000	down	0.4335	0.4134	0.4351
tc9d	50.02	2.000	up	0.3268	0.3269	0.3281
tc9d	50.02	2.000	down	0.3473	0.3929	0.3963
tc9e	50.02	-2.000	up	0.4154	0.3240	0.4194
tc9e	50.02	-2.000	down	0.3588	0.3571	0.3596
tc9f	50.02	-5.000	up	0.5072	0.4232	0.5123
tc9f	50.02	-5.000	down	0.4207	0.4184	0.4211
tc9g	50.02	5.000	up	0.3629	0.3637	0.3657
tc9g	50.02	5.000	down	0.3977	0.4516	0.4518
tc9h	63.14	0.000	up	0.2651	0.2672	0.2681
tc9h	63.14	0.000	down	0.2591	0.3075	0.3082
tc9i	63.14	-1.000	up	0.2016	0.2033	0.2040
tc9i	63.14	-1.000	down	0.1990	0.4013	0.4023
tc9j	63.14	1.000	up	0.1946	0.1965	0.1968
tc9j	63.14	1.000	down	0.2049	0.4313	0.4319
tc9k	63.14	2.000	up	0.1914	0.1932	0.1936
tc9k	63.14	2.000	down	0.2475	0.4081	0.4092
tc9l	63.14	-2.000	up	0.2356	0.2372	0.2385
tc9l	63.14	-2.000	down	0.3434	0.3573	0.3585
tc9m	63.14	-5.000	up	0.2822	0.2845	0.2859
tc9m	63.14	-5.000	down	0.2718	0.3751	0.3764
tc9n	63.14	5.000	up	0.1713	0.1729	0.1733
tc9n	63.14	5.000	down	0.3162	0.4175	0.4189
tc9o	75.00	0.000	up	0.2492	0.2492	0.2505
tc9o	75.00	0.000	down	0.2222	0.3157	0.3169
tc9p	75.00	1.000	up	0.3197	0.3205	0.3219
tc9p	75.00	1.000	down	0.3078	0.3080	0.3082
tc9q	75.00	-1.000	up	0.3389	0.3408	0.3413
tc9q	75.00	-1.000	down	0.2681	0.3258	0.3267
tc9r	75.00	-2.000	up	0.2807	0.2822	0.2822
tc9r	75.00	-2.000	down	0.2002	0.2092	0.2102
tc9s	75.00	2.000	up	0.2661	0.2665	0.2676
tc9s	75.00	2.000	down	0.2008	0.2836	0.2841
tc9t	75.00	5.000	up	0.2518	0.2521	0.2531
tc9t	75.00	5.000	down	0.2827	0.2819	0.2833
tc9u	75.00	-5.000	up	0.3926	0.3671	0.7391
tc9u	75.00	-5.000	down	0.2519	0.3290	0.3300

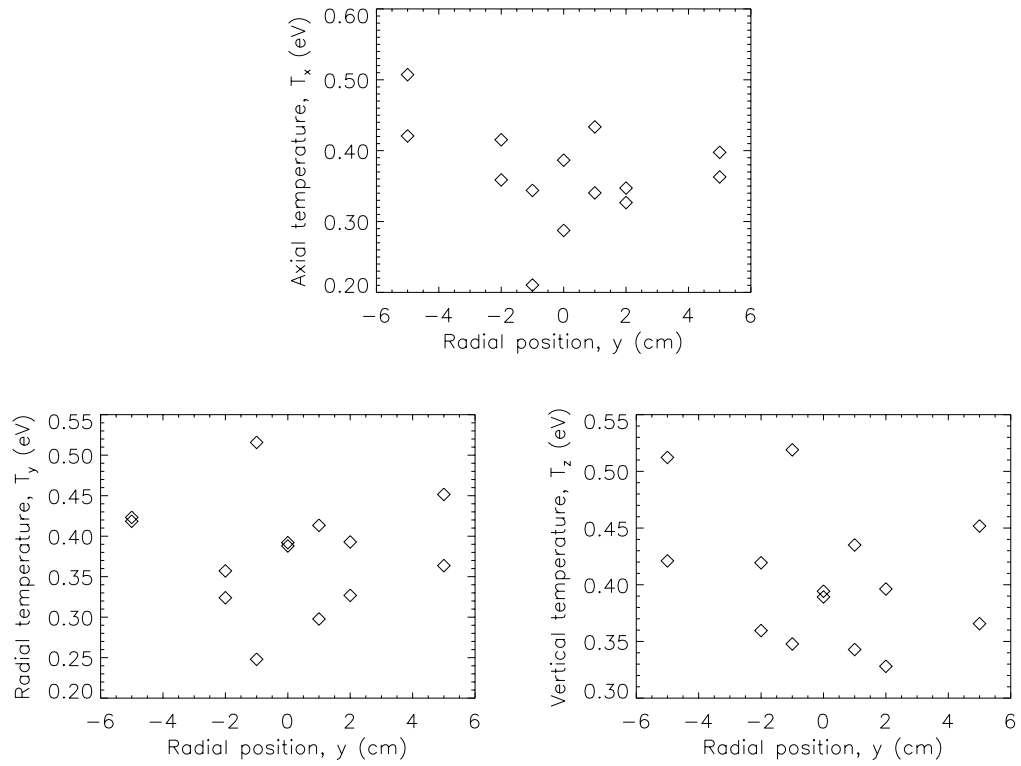


Figure 7.41: Axial, radial and vertical temperatures vs. radial position at $x = 50.02$ cm for TC9.

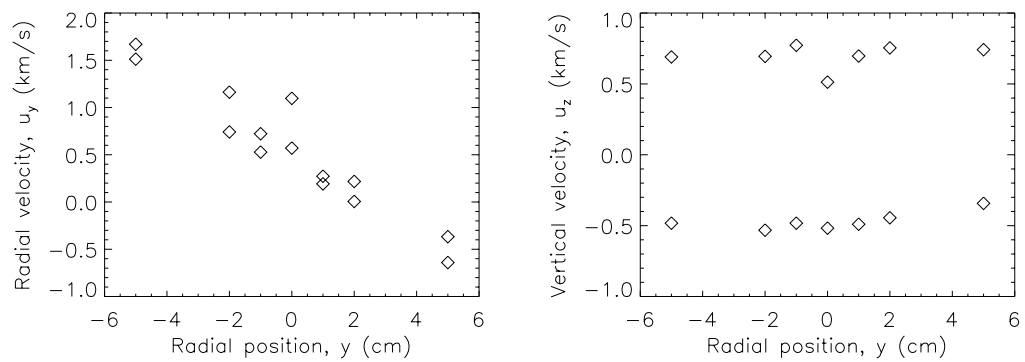


Figure 7.42: Radial & vertical ion velocity vs. radial position at $x = 63.14$ cm for TC9.

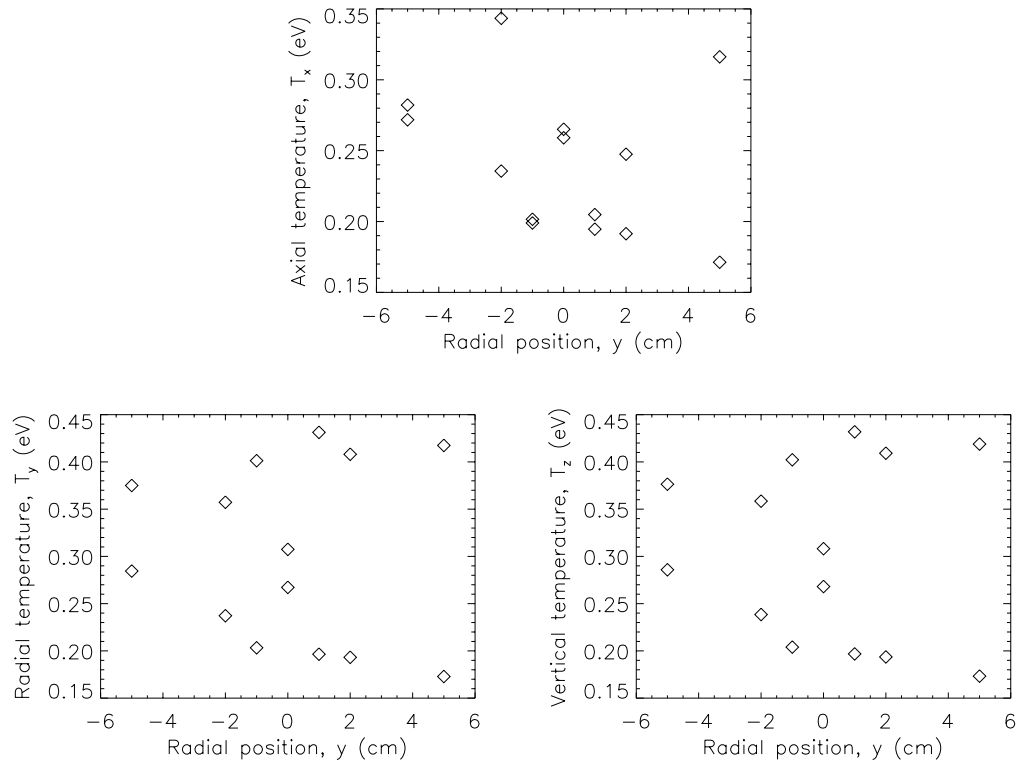


Figure 7.43: Axial, radial and vertical temperatures vs. radial position at $x = 63.14$ cm for TC9.

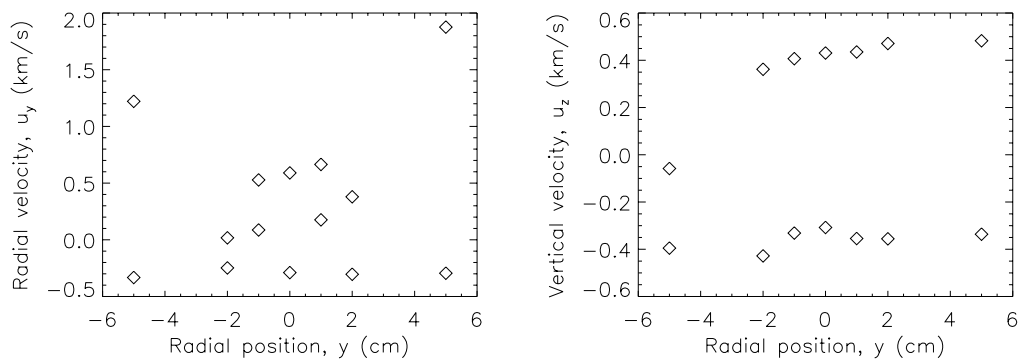


Figure 7.44: Radial & vertical ion velocity vs. radial position at $x = 75.00$ cm for TC9.

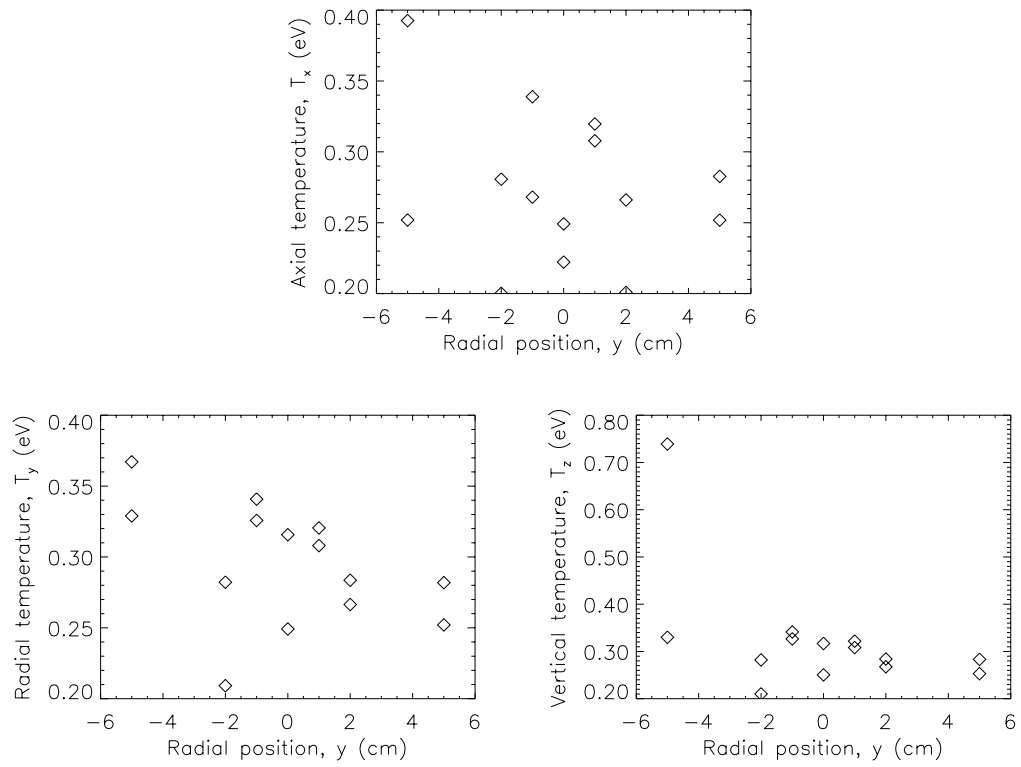


Figure 7.45: Axial, radial and vertical temperatures vs. radial position at $x = 75.00$ cm for TC9.

7.2.3 Test condition 10

Test condition 10 (TC 10) was the third P5 operating condition. Again, the specified data collection points were spaced radially around the thruster centerline. However, the characteristic two-peaked structure previously noted is not apparent up in these velocity distributions. Though the lower discharge voltage and greater axial distance might have allowed enough time for the two distributions to merge, this is probably similar to the optical resolution problem caused by overlapping point source images; beyond a certain closest approach (the Taylor and Rayleigh criteria [93]), it is impossible to distinguish the individual images from one another.

Figures B.6 through B.40 show off-axial, radial and vertical velocity distributions taken 63 cm and 75 cm downstream of the P5 exit plane. Again, the solid line is the deconvolved distribution, while the dashed line is a Maxwellian curve-fit.

Tables 7.14 and 7.15 contain values from Maxwellian curve-fits to the resulting single peak.

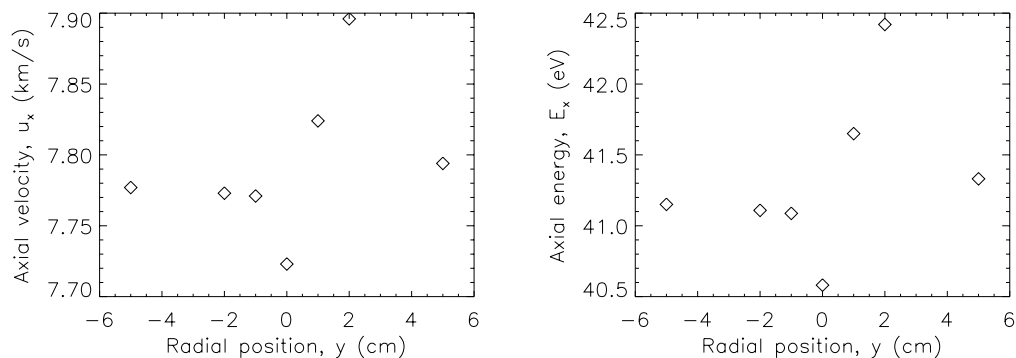


Figure 7.46: Axial ion velocity & energy vs. radial position at $x = 63.14$ cm for TC 10.

Figures 7.46 and 7.47 show what little radial variation there is in axial ion velocity and energy 63 and 75 cm downstream of the P5 exit plane. Variations appear to be random, and fall within a ± 100 m/s band around 7.80 km/s at 63 cm and 7.85 km/s at 75 cm. Any

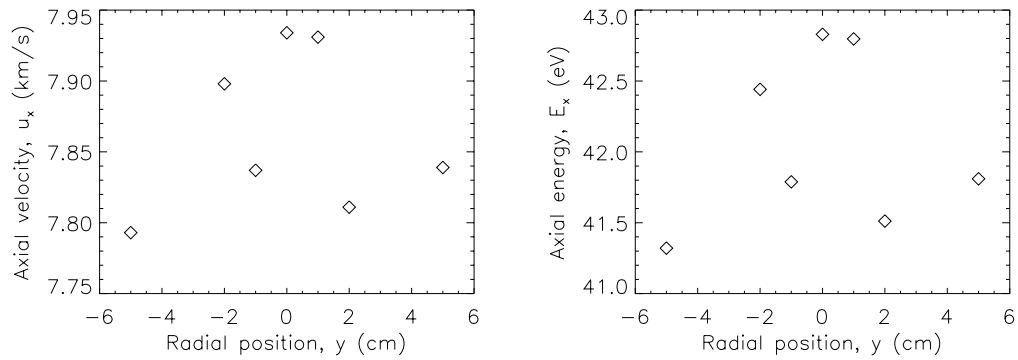


Figure 7.47: Axial ion velocity & energy vs. radial position at $x = 75.00$ cm for TC 10.

acceleration at these distances is unlikely, and the increased axial velocity probably stems from the decreasing angle between the thruster centerline and the discharge channel as axial distance increases.

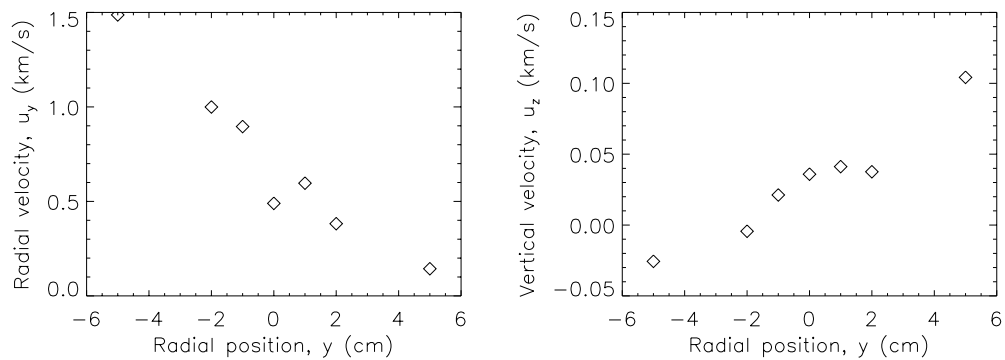


Figure 7.48: Radial & vertical ion velocity vs. radial position at $x = 63.14$ cm for TC 10.

Figures 7.48 and 7.49 show more appreciable radial variations in radial and vertical velocity. All radial velocities are positive, suggesting that the thruster axis is misaligned with the plane formed by the off-axis and vertical beams; on the thruster centerline, $u_y = 490$ m/s at 63 cm and $u_y = 1033$ m/s at 75 cm. The expected beam divergence, with u_y rising linearly with y , is overlaid on this effect. Similarly, vertical velocities are predominantly positive, suggesting a much milder misalignment of the vertical beam with a plane perpendicular to the thruster centerline. Overlaid on this effect is a mild (90 m/s, end-to-end)

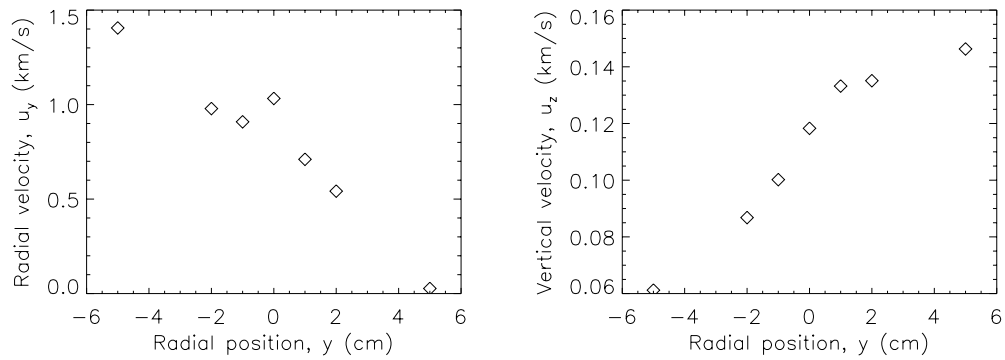


Figure 7.49: Radial & vertical ion velocity vs. radial position at $x = 75.00$ cm for TC 10.

but clear linear variation of vertical velocity, or “swirl,” in the counter-clockwise direction (looking downstream). Manzella [57] reported a similar swirl in the SPT-100 plume.

Figures 7.50 and 7.51 show the radial variation of axial, radial and vertical temperatures 63 cm and 75 cm downstream of the P5 exit plane. Though there is no noticeable radial trend, axial temperatures tend to be slightly lower than vertical and radial temperatures. All three temperatures at a point are very close to one another, suggesting that the plume is nearing thermal equilibrium in the far-field.

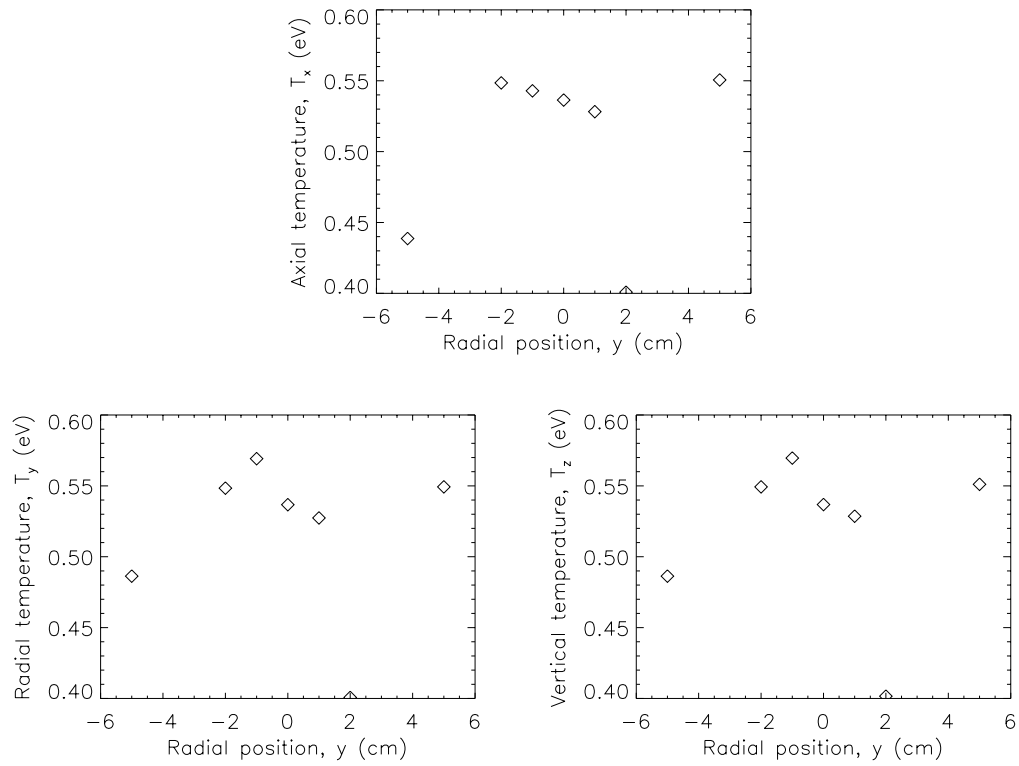


Figure 7.50: Axial, radial and vertical temperatures vs. radial position at $x = 63.14$ cm for TC 10.

Table 7.14: P5 plume velocities at TC 10.

File name	Axial position	Radial position	Axial speed	Radial speed	Vertical speed
	x (cm)	y (cm)	u_x (m/s)	u_y (m/s)	
tc10a	63.14	0.000	7723.	489.8	35.9
tc10b	63.14	-1.000	7771.	896.3	21.2
tc10c	63.14	1.000	7824.	596.6	41.2
tc10d	63.14	2.000	7896.	382.2	37.6
tc10e	63.14	-2.000	7773.	999.7	-4.4
tc10f	63.14	-5.000	7777.	1486.9	-25.6
tc10g	63.14	5.000	7794.	143.8	104.2
tc10h	75.00	0.000	7934.	1032.7	118.3
tc10i	75.00	1.000	7931.	710.6	133.2
tc10j	75.00	-1.000	7837.	908.8	100.2
tc10k	75.00	-2.000	7898.	979.1	86.8
tc10l	75.00	2.000	7811.	542.1	135.1
tc10m	75.00	5.000	7839.	27.1	146.3
tc10n	75.00	-5.000	7793.	1405.6	61.2

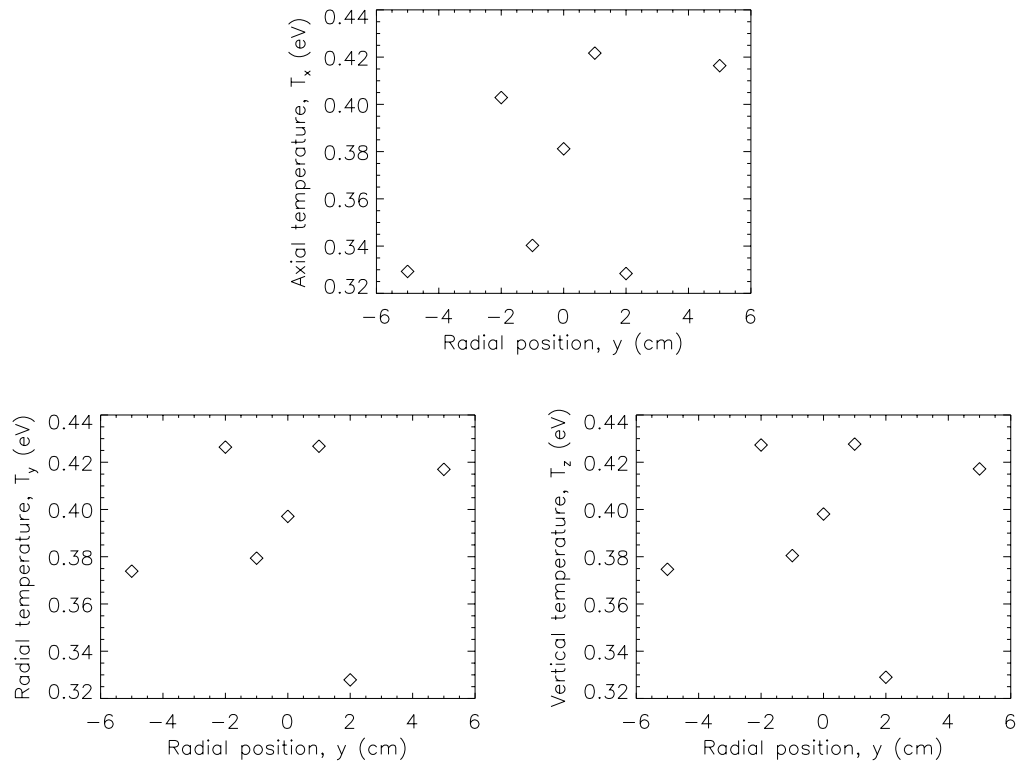


Figure 7.51: Axial, radial and vertical temperatures vs. radial position at $x = 75.00$ cm for TC 10.

Table 7.15: P5 plume temperatures at TC 10.

File name	Axial position x (cm)	Radial position y (cm)	Axial temp. T_x (eV)	Radial temp. T_y (eV)	Vertical temp. T_z (eV)
tc10a	63.14	0.000	0.5364	0.5367	0.5368
tc10b	63.14	-1.000	0.5429	0.5692	0.5696
tc10c	63.14	1.000	0.5282	0.5274	0.5286
tc10d	63.14	2.000	0.4008	0.4007	0.4016
tc10e	63.14	-2.000	0.5485	0.5484	0.5493
tc10f	63.14	-5.000	0.4387	0.4863	0.4863
tc10g	63.14	5.000	0.5506	0.5493	0.5511
tc10h	75.00	0.000	0.3812	0.3971	0.3981
tc10i	75.00	1.000	0.4217	0.4268	0.4277
tc10j	75.00	-1.000	0.3403	0.3794	0.3805
tc10k	75.00	-2.000	0.4029	0.4264	0.4273
tc10l	75.00	2.000	0.3284	0.3279	0.3290
tc10m	75.00	5.000	0.4164	0.4170	0.4172
tc10n	75.00	-5.000	0.3293	0.3739	0.3747

7.2.4 Test condition 1

Test condition 1 (TC 1) was the fourth P5 operating condition. As before, the counterflowing populations had sufficiently merged that a single-peaked distribution can be fit to the data.

Figures B.41 through B.51 show off-axial, radial and vertical velocity distributions taken 63 cm downstream of the P5 exit plane. Again, the solid line is the deconvolved distribution, while the dashed line is a Maxwellian curve-fit.

Tables 7.16 and 7.17 contain values from Maxwellian curve-fits to the deconvolved velocity distributions.

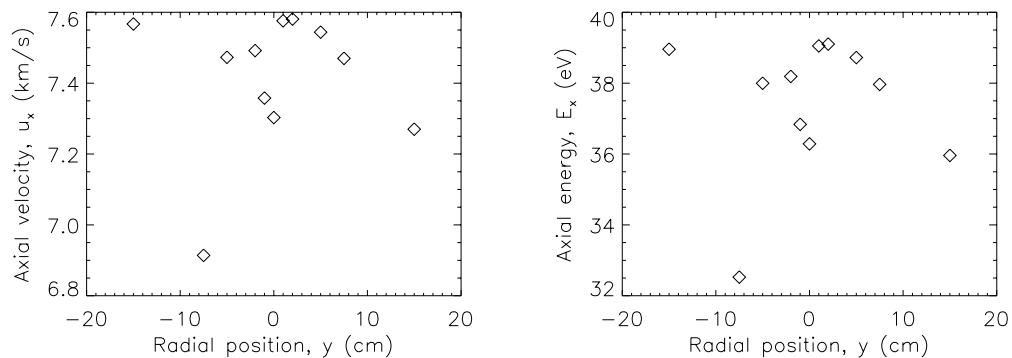


Figure 7.52: Axial ion velocity & energy vs. radial position at $x = 63.14$ cm for TC 1.

Figure 7.52 shows the radial variation in axial ion velocity and energy 63 cm downstream of the P5 exit plane. No radial trend is apparent; with one exception, all values of u_x fall within a ± 100 m/s band around 7.4 km/s.

Figure 7.53 shows more appreciable radial variations in radial and vertical velocity. As at TC 10, radial velocities are mostly positive, suggesting that the thruster axis is misaligned with the plane formed by the off-axis and vertical beams; on the thruster centerline, $u_y = 1080$ m/s. The expected beam divergence, with u_y rising linearly with y , is again overlaid on this effect. Again, vertical velocities are predominantly positive, suggesting (as

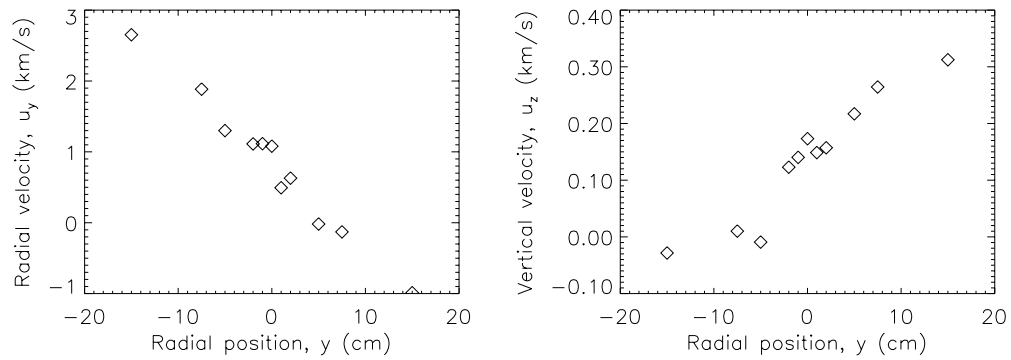


Figure 7.53: Radial & vertical ion velocity vs. radial position at $x = 63.14$ cm for TC 1.

before) a much milder misalignment of the vertical beam relative to the thruster centerline. Overlaid on this effect is a slightly stronger (340 m/s, end-to-end) but clear linear variation of vertical velocity, or “swirl,” in the counter-clockwise direction (looking downstream).

Figure 7.54 shows the radial variation of axial, radial and vertical temperatures 63 cm downstream of the P5 exit plane. As at TC 10, there is no noticeable radial trend, but axial temperatures tend to be slightly lower than vertical and radial temperatures.

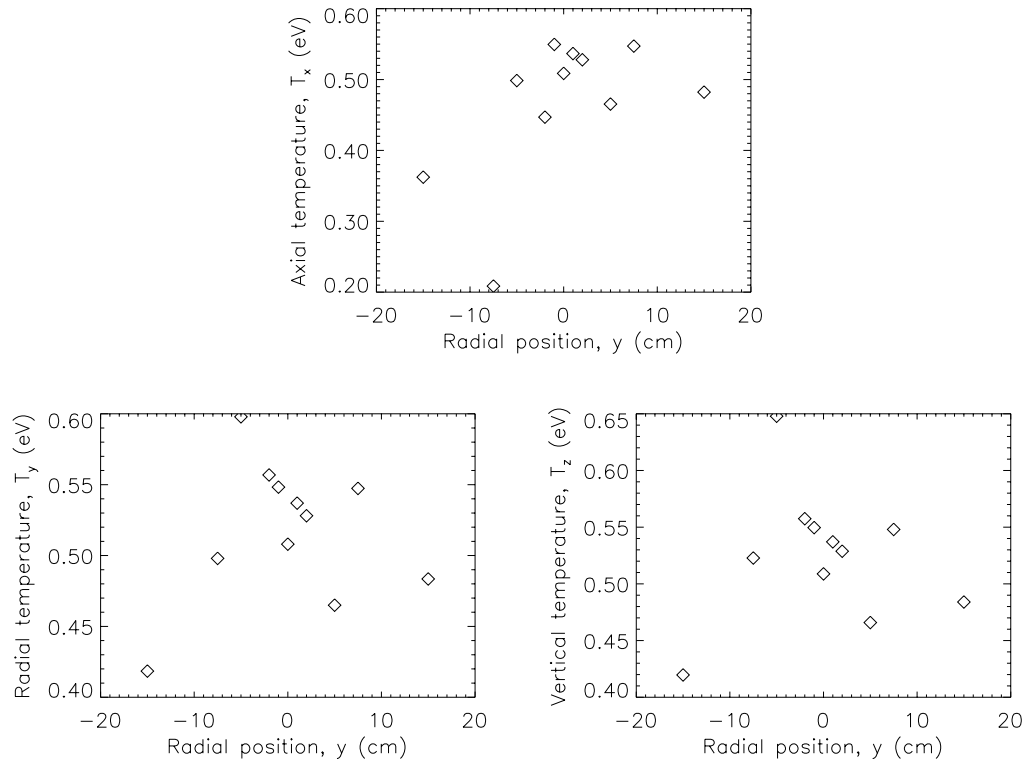


Figure 7.54: Axial, radial and vertical temperatures vs. radial position at $x = 63.14$ cm for TC 1.

Table 7.16: P5 plume velocities at TC 1.

File name	Axial position x (cm)	Radial position y (cm)	Axial speed u_x (m/s)	Radial speed u_y (m/s)	Vertical speed
tc01a	63.14	0.000	7303.	1080.0	173.3
tc01b	63.14	1.000	7576.	494.0	148.7
tc01c	63.14	-1.000	7358.	1115.8	140.3
tc01d	63.14	-2.000	7492.	1112.6	123.0
tc01e	63.14	2.000	7581.	629.2	157.3
tc01f	63.14	5.000	7544.	-18.0	217.1
tc01g	63.14	-5.000	7473.	1299.9	-9.1
tc01h	63.14	15.000	7270.	-988.2	312.4
tc01i	63.14	-15.000	7567.	2652.3	-28.3
tc01j	63.14	-7.500	6914.	1884.9	10.2
tc01k	63.14	7.500	7470.	-129.1	264.4

Table 7.17: P5 plume temperatures at TC 1.

File name	Axial position x (cm)	Radial position y (cm)	Axial temp. T_x (eV)	Radial temp. T_y (eV)	Vertical temp. T_z (eV)
tc01a	63.14	0.000	0.5087	0.5080	0.5088
tc01b	63.14	1.000	0.5367	0.5370	0.5371
tc01c	63.14	-1.000	0.5496	0.5483	0.5496
tc01d	63.14	-2.000	0.4470	0.5569	0.5575
tc01e	63.14	2.000	0.5279	0.5281	0.5288
tc01f	63.14	5.000	0.4654	0.4650	0.4659
tc01g	63.14	-5.000	0.4986	0.5979	0.6479
tc01h	63.14	15.000	0.4823	0.4835	0.4840
tc01i	63.14	-15.000	0.3623	0.4185	0.4197
tc01j	63.14	-7.500	0.2086	0.4980	0.5228
tc01k	63.14	7.500	0.5472	0.5474	0.5480

7.2.5 Test condition 2

Test condition 2 (TC 2) was the fifth P5 operating condition. As before, the counterflowing populations had sufficiently merged that a single-peaked distribution fits the data.

Figures B.52 through B.56 show off-axial, radial and vertical velocity distributions taken 63 cm downstream of the P5 exit plane. Again, the solid line is the deconvolved distribution, while the dashed line is a Maxwellian curve-fit.

Tables 7.18 and 7.19 contain values from Maxwellian curve-fits to the deconvolved velocity distributions.

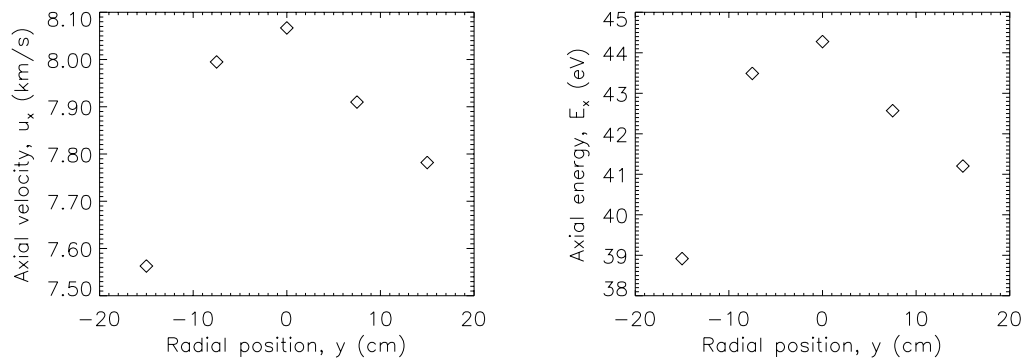


Figure 7.55: Axial ion velocity & energy vs. radial position at $x = 63.14$ cm for TC 2.

Figure 7.55 shows the radial variation in axial ion velocity and energy 63 cm downstream of the P5 exit plane. The maximum axial velocity (8.07 km/s) falls on the thruster centerline, with a vaguely parabolic decrease in axial velocity with increasing distance from the centerline.

Figure 7.56 shows the same radial variations in radial and vertical velocity noted for TC 10 and TC 01. Mostly-positive radial velocities suggest that the thruster axis is tilted to the east; on the thruster centerline, $u_y = 863$ m/s. The linear increase of u_y with rising y implies beam divergence. Uniformly-positive vertical velocities suggest that the thruster

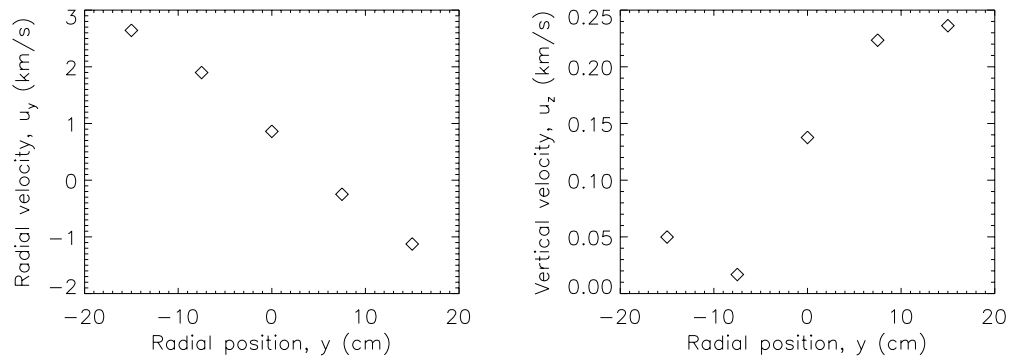


Figure 7.56: Radial & vertical ion velocity vs. radial position at $x = 63.14$ cm for TC 2.

axis is tipped upwards, while the linear variation of vertical velocity implies a counter-clockwise “swirl.”

Table 7.18: P5 plume velocities at TC 2.

File name	Axial position x (cm)	Radial position y (cm)	Axial speed u_x (m/s)	Radial speed u_y (m/s)	Vertical speed u_z (m/s)
tc02a	63.14	0.000	8067.	862.5	137.7
tc02b	63.14	7.500	7910.	-247.1	223.5
tc02c	63.14	-7.500	7995.	1899.0	16.8
tc02d	63.14	-15.000	7563.	2642.9	49.9
tc02e	63.14	15.000	7782.	-1124.4	236.3

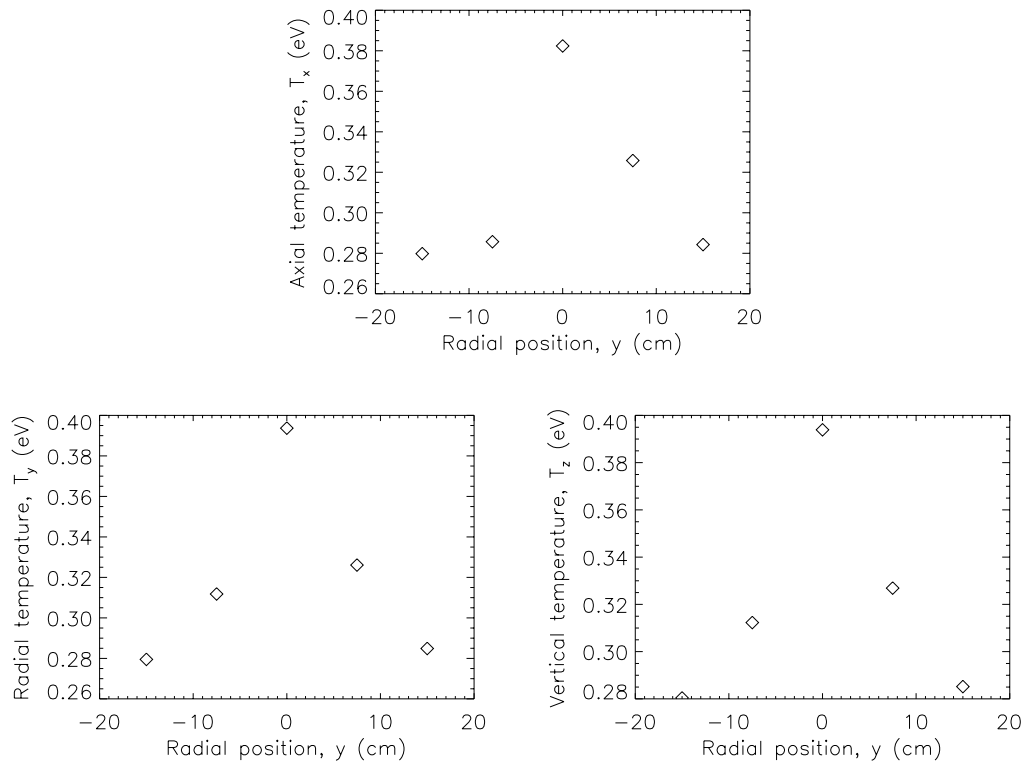


Figure 7.57: Axial, radial and vertical temperatures vs. radial position at $x = 63.14$ cm for TC 2.

Table 7.19: P5 plume temperatures at TC 2.

File name	Axial position x (cm)	Radial position y (cm)	Axial temp. T_x (eV)	Radial temp. T_y (eV)	Vertical temp. T_z (eV)
tc02a	63.14	0.000	0.3824	0.3937	0.3939
tc02b	63.14	7.500	0.3258	0.3261	0.3269
tc02c	63.14	-7.500	0.2857	0.3118	0.3123
tc02d	63.14	-15.000	0.2798	0.2795	0.2804
tc02e	63.14	15.000	0.2843	0.2849	0.2852

7.3 Discussion

Previous multiplex LIF measurements of the P5 plume reported by Williams *et al.* [11] indicate axial ion velocities at $x = 10$ cm on the discharge chamber centerline of 16.0 km/s at 1.6 kW and 17.0 km/s at 3.0 kW. A check run at 3.0 kW during multiplex LIF measurements of the P5 plume returned an axial ion velocity at the same location of 20.12 km/s. These values neatly straddle the speed measured by axial-injection LIF, while the $\pm 16\%$ error band implied by the multiplex values is within the 20% uncertainty caused by a stackup of 2% uncertainties in angle and bulk velocity (see Eqn. 6.8).

Haas [88] reported a P5 specific impulse of 1580 s at 1.6 kW and 1670 s at 3.0 kW. Adjusted for the ratio of anode flow rate to total flow rate, this corresponds to expected axial velocities of 17.0 km/s at 1.6 kW and 17.2 km/s at 3.0 kW. These values are 9.2% and 7.9% lower than the maximum axial velocities measured by direct-injection LIF, but match the axial velocity in the region 1 to 2 cm downstream of the thruster exit plane.

Williams *et al.* [11] noted a 90 V increase in axial ion energy downstream of the P5 discharge. The “near-field” range covered in that study, however, stopped 10 cm downstream of the exit plane, missing the point of maximum velocity and the subsequent deceleration. Subsequent plasma potential measurements by Haas [86] showed an 85 V drop in plasma potential from $x = 0$ to $x = 10$ cm at 1.6 kW, which is 16% less than the 101 V increase in ion axial energy we measured over the same range. Though the inherently intrusive nature of probe-based diagnostics might account for the 16 V difference in results, a more sophisticated hypothesis is that ions arriving at an interrogation point on the discharge channel centerline do not originate on that same centerline. Multiplex LIF measurements at 3.0 kW support this hypothesis; we measured a radial velocity of $u_y = (774 \pm 71)$ m/s along the discharge channel centerline at $x = 10.01$ cm. Future

lateral-injection LIF of the P5 plume will further test this hypothesis.

Cedolin [7] also noted increasing axial velocity downstream of the Stanford 260 W Hall thruster discharge, as well as a “levelling off” around 3.0 cm downstream; unfortunately, this study also failed to note any deceleration in the remaining 1.0 cm of the survey. The loss of axial velocity downstream of $x = 20$ cm is probably not caused by ion-neutral collisions; the mean free path (MFP) for Xe II - Xe I elastic collisions at these conditions is almost 30 m, while the Xe II - Xe I charge exchange (CEX) MFP is 11 m. Ion-ion elastic collisions, with a MFP of 60 cm, are a more likely cause of the perceived velocity loss. The sudden departure of the axial temperature profile from the predicted kinematic compression trend at $x = 20$ cm lends credence to the collisional hypothesis. Future lateral sweeps at this location, and possibly testing at lower base pressures, will shed more light on this effect.

Figure 7.58 shows reconstructions of the two-dimensional velocity distribution $f(v_x, v_z)$ at 3.0 kW, directly downstream of the P5 centerline at $x = 10$ cm and $x = 50$ cm. These reconstructions are based on an assumption of statistical independence of the axial and vertical distributions,

$$f(v_x, v_z) = f_x(v_x)f_z(v_z) \quad (7.1)$$

where the axial distribution $f_x(v_x)$ is taken from the axial-injection data and the vertical distribution $f_z(v_z)$ is taken from the off-axis multiplex data at 3.0 kW.

The $x = 10$ cm reconstruction in Figure 7.58 shows counterflowing plasmas with a mean axial velocity of 15.2 km/s. The upward-flowing peak is at a vertical velocity of 8.5 km/s, while the downward-flowing peak is at a vertical velocity of -7.4 km/s. A significant portion of the distribution is spread out between the two peaks; $f(v_x, v_z)$ is 38% of its maximum value at the saddle point, $(v_x, v_z) = (15.2, -2.6)$ km/s. The vertical asymmetry in the distribution is slight, and may reflect a slight misalignment of the vertical beam with

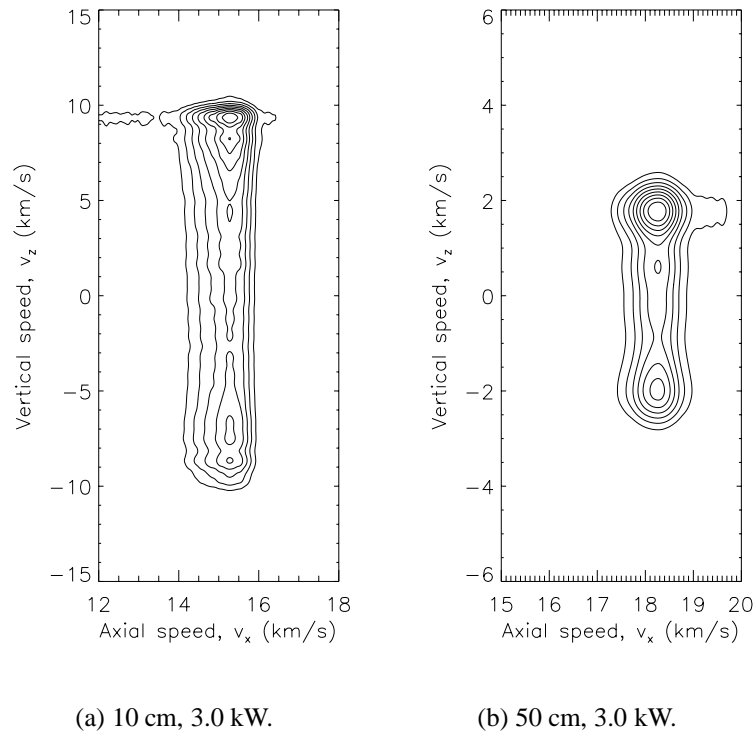


Figure 7.58: Two-dimensional velocity distribution $f(v_x, v_z)$ downstream of P5 centerline, normalized so $f \leq 1.0$. Contour lines are at $f = [0.1, 0.2, \dots 0.9]$.

the z -axis.

The $x = 50$ cm reconstruction in Figure 7.58 shows counterflowing plasmas with a mean axial velocity of 18.2 km/s. The upward-flowing peak is at a vertical velocity of 1.8 km/s, while the downward-flowing peak is at a vertical velocity of -2.0 km/s. A significant portion of the distribution remains spread out between the two peaks, with $f(v_x, v_z) = 43\%$ of the maximum at the saddle point, $(v_x, v_z) = (18.2, -0.9)$ km/s. As before, the upwards population is slightly larger, which tends to confirm a slight misalignment of the vertical beam with the z -axis.

The centerline velocity distribution peaks shown in Fig. 7.58 are consistent with collisionless expansion from an annular discharge. Electric field effects downstream of the exit plane are not negligible; not only do the bulk velocity vectors fail to line up on position

vectors from the discharge, but the velocity magnitude of the peaks rises from 17.1 km/s at 10 cm to 18.3 km/s at 50 cm. The portion of the distribution between peaks, which I will call the “mixing population,” is especially interesting, as ions with very low vertical velocity magnitudes cannot follow a straight line from the discharge to the centerline. Though the centerline distributions are likely to be two-stream unstable, it is unclear if this instability is responsible for the mixing population. Future lateral LIF sweeps, combined with ion trajectory simulations, will help explain this portion of the distribution.

By converting velocity distributions deconvolved from LIF spectra to energy space, we can compare our data to existing mass spectrometer data. Figure VII.59(a) shows a Molecular Beam Mass Spectrometer (MBMS) energy spectrum taken by Gulczinski [91] 10 cm downstream of the discharge channel centerline at 1.6 kW. The MBMS primary peak occurs at an ion energy per unit charge of 260 V, while a second, broader peak occurring at 350 V (approximately 4/3 of the primary peak energy) is a Xe IV population caused by the Xe V - Xe I CEX collision

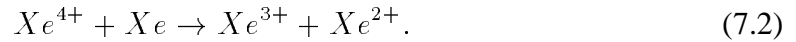


Figure VII.59(b) shows an ion energy distribution (iedf), transformed from the deconvolved velocity distribution at the same location by the relation

$$g(E_x) = \sqrt{\frac{2E_x}{m^3}} f(v). \quad (7.3)$$

The LIF primary peak occurs at 235 V, with a second, broader peak centered at 270 V. The primary peak widths are quite similar, as should be expected when the axes are properly transformed between velocity and energy space. Both distributions also have a pronounced low-energy tail. The 25 V difference between the primary peak energies may be explained by the 15 V plasma potential measured by Haas [86]; ions falling from this potential into

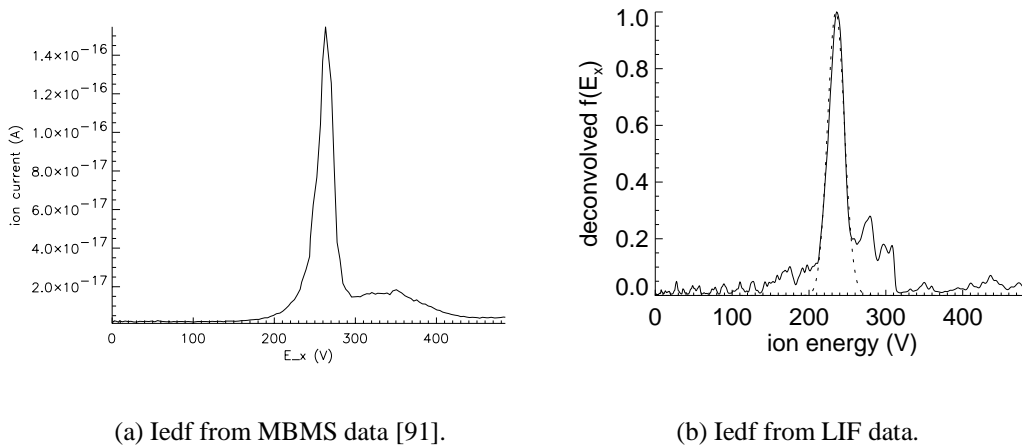


Figure 7.59: Ion energy distributions at 1.6 kW, $(x, y) = (10., 7.37)$ cm.

a parallel-plate energy analyzer with grounded entry and exit slits will indicate a higher energy than LIF. Since our LIF scheme can only detect Xe II, the LIF secondary peak is not a Xe V - Xe I CEX population, as the only Xe II peaks from CEX distributions occur at integral multiples of the primary peak energy [92]. Since the ion-ion MFP at these conditions is 60 cm, Xe III - Xe II elastic collisions are the most likely explanation for the LIF secondary peak.

7.4 Summary

We performed two sets of Xe II LIF experiments in the plume of the P5 Hall thruster: axial-injection experiments from 0.05 to 50 cm downstream of the exit plane, and off-axis multiplex experiments from 10 to 75 cm downstream of the exit plane.

The deconvolution of axial-injection LIF spectra has proved to be a viable diagnostic technique for Hall thruster plumes. Repeated measurements of axial velocity agree within 2%, while axial temperatures agree within a 40% error band. Multiplex LIF measurements of axial velocity differ from previously-published multiplex measurements by 18%, but both values bracket the axial-injection LIF results. This bracketing falls within predicted

error bands for multiplex LIF, showing both the accuracy of axial-injection LIF and the large error bands inherent in multiplex LIF.

Energy distributions transformed from axial-injection LIF deconvolutions compare well with MBMS energy distributions at the same location. The primary peaks have nearly identical widths, while the peak location shift was commensurate with the floating potential at the measurement location.

We found that an acceleration region extends 20 cm downstream of the P5 exit plane, followed by a region of slowly decreasing axial velocity. Axial temperatures during 1.6 kW operation tend to decrease with increasing axial velocity and increase with decreasing axial velocity, supporting the hypothesis of kinematic compression. No such effect was observed during 3.0 kW operation, where a collisionless model may be less reasonable.

CHAPTER VIII

FMT-2 PLUME LIF

This chapter presents data obtained in two off-axis multiplex Xe II LIF experiments downstream of the FMT-2 accelerator grid, using the computational and experimental tools described in Chapters 5 and 6. Radial sweeps at 1 mm and 50 mm downstream of the screen grid provided data at 12.7 mm (0.5 in.) intervals from the thruster centerline, until the signal degraded at $y = 11.4$ cm (4.5", for TH19) to $y = 12.7$ cm (5.0 in, for TH15). Axial sweeps on the centerline provided data from 1 mm to 30 cm downstream of the accelerator grid.

8.1 Multiplex LIF of FMT plume

Table 8.1 gives the thruster operating conditions used in these experiments. Power supply limits and thruster instabilities kept us from reaching the full TH19 screen potential (1500 V). The neutralizer failed to light for the first run, but worked for the second run.

All the following analyses fit a single Maxwellian to each of the three beamwise velocity distributions returned by the multiplex deconvolution code `fmt_lif.pro`. This fit ignores the characteristic multi-peaked structure of the distributions, and returns unrealistically high translational temperatures. Future studies of this phenomenon might profit from considering each peak separately. Bulk velocity components, however, should re-

Table 8.1: FMT-2 operating conditions.

		TH 15 (run 1)	TH 19 (run 1)	TH 15 (run 2)	TH19 (run 2)	units
Discharge voltage	V_b	25.56	25.00	25.38	24.86	V
Discharge current	I_d	12.88	13.08	12.60	12.16	A
Beam current	I_b	1.75	1.78	1.74	1.79	A
Accelerator potential	V_a	-180.0	-241.1	-180.0	-245.0	V
Screen potential	V_s	1100	1429	1102	1325	V
Main flow rate	\dot{m}_m	22.6	22.6	22.6	22.6	sccm
Discharge cathode flow rate	\dot{m}_c	3.80	4.20	3.80	4.20	sccm
Neutralizer cathode flow rate	\dot{m}_n	0.00	0.00	3.00	3.20	sccm
Facility pressure	P	2.9	2.9	2.9	2.9	μ Torr

main reasonably unaffected by the single Maxwellian curve-fit.

8.1.1 TH15 without neutralizer

The first set of measurements was a radial sweep approximately 1.4 mm downstream of the FMT-2 accelerator grid at the TH15 operating point. Though the neutralizer did not light this time, we continued without a working neutralizer.

The ion current immediately downstream of the accelerator grid is very highly concentrated into beamlets that pass through the grid apertures. Because of this concentrated ion current density, we had to hunt around the initial target radius in order to find a spot with enough ion density to provide a strong, clean LIF signal. This shows up in the somewhat irregular pattern of radial locations probed in this test. Tables 8.2 and 8.3 give bulk velocities and temperatures for these locations.

Figure 8.1 shows the radial variation of ion axial velocity and energy along a plane 1.40 mm downstream of the FMT-2 accelerator grid at TH15. Reasonable values for the ion axial energy E_x lie between the screen potential V_s and the total voltage $V_T \equiv V_s - V_a$; at the first-run TH15 condition, $V_s = 1100$ V and $V_T = 1280$ V. Three points (th15b, th15e and th15h) lie outside this range, but the mean axial velocity (42.3 km/s) remains

Table 8.2: FMT plume velocities at TH15 (w/o neutralizer).

File name	Axial position x (cm)	Radial position y (cm)	Axial speed u_x (m/s)	Radial speed u_y (m/s)	Vertical speed u_z (m/s)
th15a	0.140	0.000	41979.	2907.4	1114.1
th15b	0.140	1.372	43964.	4374.6	1084.6
th15c	0.140	2.540	41129.	6116.4	1179.8
th15d	0.140	3.912	42128.	5866.1	1039.1
th15e	0.140	5.080	43507.	5446.2	869.6
th15f	0.140	6.452	42029.	6087.5	812.6
th15g	0.140	7.772	41358.	7568.8	922.1
th15h	0.140	8.992	43901.	6871.1	1152.4
th15i	0.140	10.160	40054.	9039.8	1577.2
th15j	0.140	11.557	42980.	5918.5	1429.2

Table 8.3: FMT plume temperatures at TH15 (w/o neutralizer).

File name	Axial position x (cm)	Radial position y (cm)	Axial temp. T_x (eV)	Radial temp. T_y (eV)	Vertical temp. T_z (eV)
th15a	0.140	0.000	4.6481	4.7019	6.4550
th15b	0.140	1.372	1.7869	5.4320	5.7419
th15c	0.140	2.540	5.6788	4.9676	6.8335
th15d	0.140	3.912	6.5601	6.7098	7.7489
th15e	0.140	5.080	6.9438	6.6895	6.9534
th15f	0.140	6.452	6.7881	6.7929	6.7962
th15g	0.140	7.772	7.6151	7.6588	7.6733
th15h	0.140	8.992	11.4978	11.4951	11.5120
th15i	0.140	10.160	9.9839	7.7550	12.9075
th15j	0.140	11.557	7.7321	5.6103	18.2718
th15k	0.140	12.751	1.1577	1.1118	4.0635
th15k2	0.140	12.751	9.5198	0.0538	13.5784

reasonable, and the maximum velocity error is within 4% of the mean.

Figure 8.2 shows the radial variation of ion radial and vertical velocity along the same plane. Radial velocity tends to increase linearly with radial position, with a centerline radial velocity of 2.91 km/s that suggests the thruster axis is pointed slightly (3.9°) eastward. The vertical velocity is uniformly positive, with a mean value (1.12 km/s) that

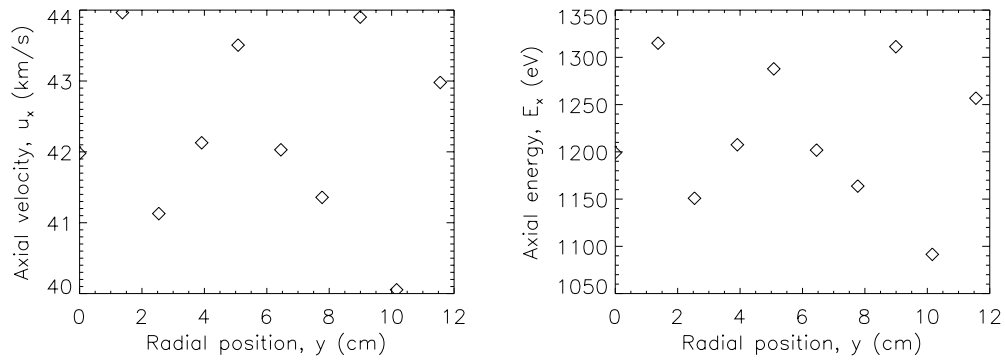


Figure 8.1: Axial ion velocity & energy vs. radial position at $x = 0.140$ cm for unneutralized TH15.

suggests the thruster is tilted slightly (1.5°) upwards. The next set of measurements was a radial sweep approximately 5.0 cm downstream of the FMT grid at the TH15 operating point, again without a working neutralizer. The beamlets apparently diverge enough by 5.0 cm to make the current density much more nearly uniform; this allowed more regular spacing of the radial sweep positions.

Tables 8.4 and 8.5 give bulk velocities and temperatures for these locations.

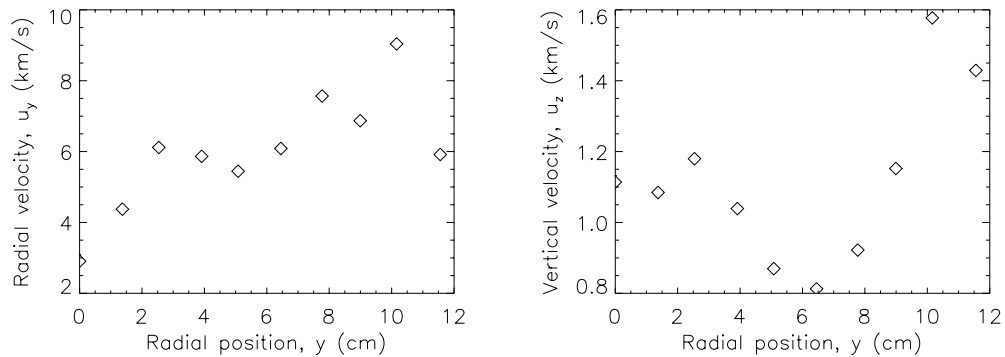


Figure 8.2: Radial & vertical ion velocity vs. radial position at $x = 0.140$ cm for unneutralized TH15.

Table 8.4: FMT plume velocities at TH15 (w/o neutralizer).

File name	Axial position	Radial position	Axial speed	Radial speed	Vertical speed
	x (cm)	y (cm)	u_x (m/s)	u_y (m/s)	u_z (m/s)
th15l	5.017	0.000	40937.	4103.5	1036.5
th15m	5.017	1.270	40630.	4866.2	1071.4
th15n	5.017	2.540	41349.	4258.1	986.6
th15o	5.017	3.810	40891.	5095.3	1009.2
th15p	5.017	5.080	41308.	5502.7	947.8
th15q	5.017	6.350	41102.	5563.1	930.4
th15r	5.017	7.620	41122.	6080.7	932.0
th15s	5.017	8.890	41404.	6783.4	1025.5
th15t	5.017	10.160	41409.	7191.6	1127.7
th15u	5.017	11.430	41407.	7855.6	1160.9

Table 8.5: FMT plume temperatures at TH15 (w/o neutralizer).

File name	Axial position	Radial position	Axial temp.	Radial temp.	Vertical temp.
	x (cm)	y (cm)	T_x (eV)	T_y (eV)	T_z (eV)
th15l	5.017	0.000	7.6159	7.8698	8.3600
th15m	5.017	1.270	6.3924	7.8915	7.9003
th15n	5.017	2.540	6.6437	8.4240	9.4889
th15o	5.017	3.810	6.1572	8.8944	8.8976
th15p	5.017	5.080	7.5894	9.1914	9.2022
th15q	5.017	6.350	7.2259	8.4091	9.1259
th15r	5.017	7.620	7.4234	8.9190	8.9328
th15s	5.017	8.890	7.4931	9.0076	9.0241
th15t	5.017	10.160	9.6141	9.5987	9.6200
th15u	5.017	11.430	11.3383	11.8263	11.8274

Figure 8.3 shows the radial variation of ion axial velocity and energy along a plane 5.017 cm downstream of the FMT-2 accelerator grid at TH15. All ion axial energies lie in the range $V_s \leq E_x \leq V_T$ at this plane, with a mean axial velocity of 41.2 km/s and a maximum velocity error within 1.3% of the mean.

Figure 8.4 shows the radial variation of ion radial and vertical velocity along the same plane. Again, radial velocity tends to increase linearly with radial position, with a cen-

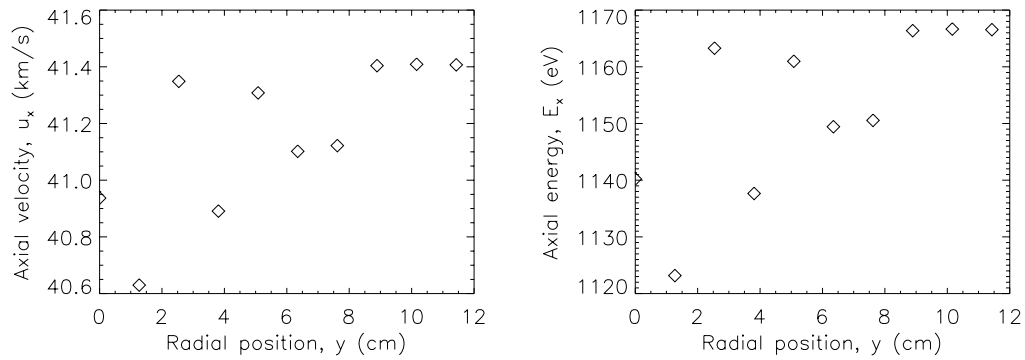


Figure 8.3: Axial ion velocity & energy vs. radial position at $x = 5.017$ cm for unneutralized TH15.

terline radial velocity that suggests the thruster axis is pointed a little more sharply (5.7°) eastward and a maximum beam divergence of 5.1° at the outermost radius. Likewise, the vertical velocity is again uniformly positive, with a mean value (1.02 km/s) that suggests the thruster is tilted slightly (1.4°) upwards.

8.1.2 TH19 without neutralizer

The next set of measurements was a radial sweep 5.09 cm downstream of the FMT-2 accelerator grid at the TH19 operating point. The neutralizer was still not working for this set of tests.

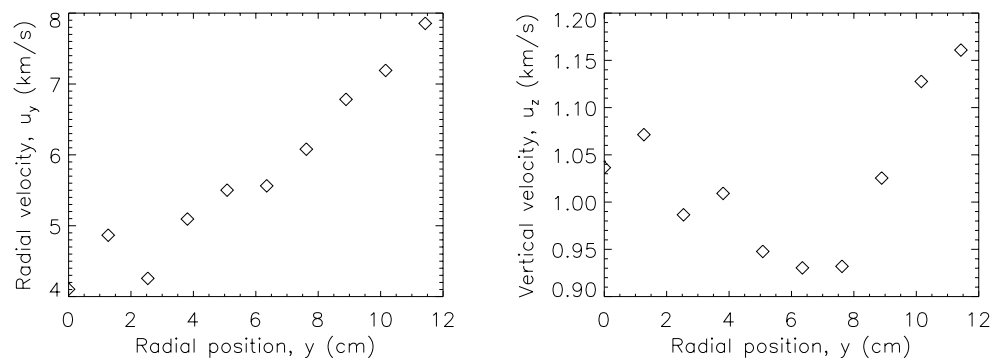


Figure 8.4: Radial & vertical ion velocity vs. radial position at $x = 5.017$ cm for unneutralized TH15.

Continual recycling¹, apparently caused by cyclic thermal expansion and sagging of the FMT's soft aluminum body, made continued operation at TH19 increasingly impractical; it also made steady LIF measurement very difficult. Continued operation at the full-voltage TH19 condition (1430 V screen potential) would have required the removal and disassembly of the FMT in order to space the grids another 0.8 to 1.6 mm away from the anode. We opted instead to finish this test, vent the LVTF and fix the neutralizer; we ran subsequent TH19 tests at a slightly lower-voltage version of TH19 (1350 V screen potential), retaining the 1.75 A beam current.

Tables 8.6 and 8.7 give bulk velocities and temperatures 5.09 cm downstream of the accelerator grid.

¹An automatic response of the FMT-2 power supply, designed to clear shorts between the screen and acceleration grid [12].

Table 8.6: FMT plume velocities at TH19 (w/o neutralizer).

File name	Axial position	Radial position	Axial speed	Radial speed	Vertical speed
	x (cm)	y (cm)	u_x (m/s)	u_y (m/s)	
th19a	5.090	0.000	46931.	5386.6	1112.3
th19b	5.090	1.270	47450.	4823.4	1032.6
th19c	5.090	2.540	46834.	5591.4	1115.0
th19d	5.090	3.810	46692.	5462.3	1072.0
th19e	5.090	5.080	47038.	7179.9	1028.1
th19f	5.090	6.350	47292.	6637.9	979.4
th19g	5.090	7.620	50401.	8234.6	1130.9

Table 8.7: FMT plume temperatures at TH19 (w/o neutralizer).

File name	Axial position	Radial position	Axial temp.	Radial temp.	Vertical temp.
	x (cm)	y (cm)	T_x (eV)	T_y (eV)	T_z (eV)
th19a	5.090	0.000	10.5359	11.2157	11.2248
th19b	5.090	1.270	9.7908	11.8212	13.2675
th19c	5.090	2.540	9.9730	10.7864	11.9577
th19d	5.090	3.810	12.1001	13.9633	13.9661
th19e	5.090	5.080	12.7983	13.0387	13.0474
th19f	5.090	6.350	14.0237	15.9576	15.9839
th19g	5.090	7.620	14.8087	14.8838	14.9224

Figure 8.5 shows the radial variation of ion axial velocity and energy along a plane 5.090 cm downstream of the FMT-2 accelerator grid at TH19. Screen potential at this condition is 1429 V, while the total voltage is 1670 V. Ion axial energies for all but one point lie in the range $V_s \leq E_x \leq V_T$ at this condition, with a mean axial velocity of 47.5 km/s and a maximum velocity error within 6.1% of the mean.

Figure 8.6 shows the radial variation of ion radial and vertical velocity along the same plane. Once again, radial velocity tends to increase linearly with radial position, with a centerline radial velocity that suggests the thruster axis is pointed still more sharply (6.5°) eastward and a maximum beam divergence of 3.3° at the outermost radius. Likewise, the

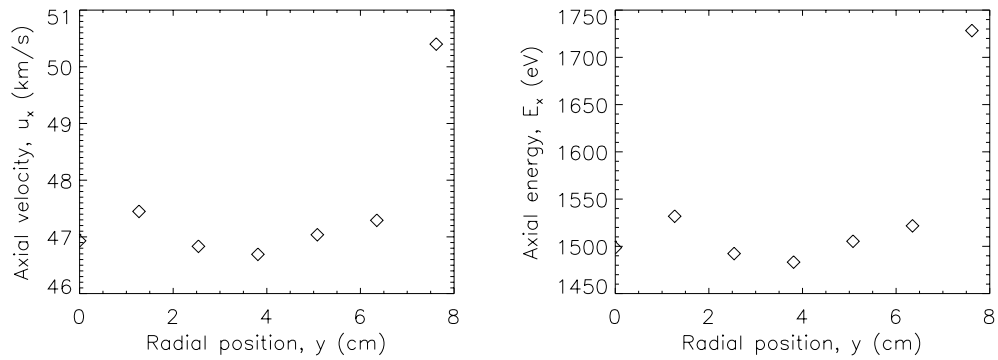


Figure 8.5: Axial ion velocity & energy vs. radial position at $x = 5.090$ cm for unneutralized TH19.

vertical velocity is again uniformly positive, with a mean value (1.07 km/s) that suggests the thruster is tilted slightly (1.3°) upwards.

8.1.3 TH15 with neutralizer

After completing the unneutralized TH19 runs, we shut down the thruster, vented the chamber, and inspected the neutralizer. Though we found no obvious electrical or mechanical problems, we made slight adjustments to the connections while checking continuity. We then evacuated the chamber and conditioned the cathodes per NASA specifications [12].

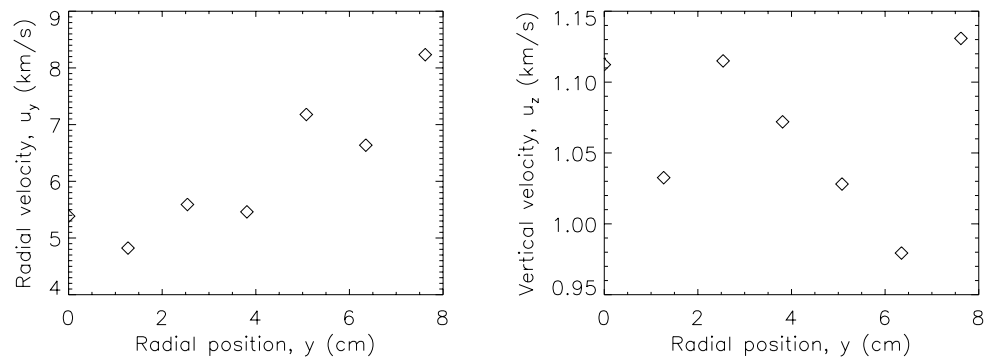


Figure 8.6: Radial & vertical ion velocity vs. radial position at $x = 5.090$ cm for unneutralized TH19.

The next set of measurements was an axial sweep on the FMT grid centerline at the TH15 operating point. This time, the neutralizer struck a discharge, and subsequent tests had a working neutralizer. Tables 8.8 and 8.9 give bulk velocities and temperatures for these locations.

Table 8.8: FMT plume velocities at TH15 (w/ neutralizer).

File name	Axial position	Radial position	Axial speed	Radial speed	Vertical speed
	x (cm)	y (cm)	u_x (m/s)	u_y (m/s)	u_z (m/s)
th15x0	0.117	0.000	41969.	3917.7	223.7
th15x1	0.224	0.000	41319.	3497.6	293.2
th15x2	0.351	0.000	41332.	3891.9	354.5
th15x3	0.411	0.000	41776.	3976.9	240.0
th15x4	0.505	0.000	41197.	4275.3	358.5
th15x5	0.696	0.000	41764.	4191.2	375.0
th15x6	1.008	0.000	41385.	3894.5	353.6
th15x7	1.394	0.000	41017.	3206.2	358.5
th15x8	1.890	0.000	41354.	3546.8	345.1
th15x9	2.492	0.000	40921.	3581.0	369.0
th15x10	3.495	0.000	41600.	2987.0	341.4
th15x11	7.008	0.000	41261.	2678.4	252.8
th15x12	15.004	0.000	41036.	3415.9	250.6
th15x13	15.004	0.000	39132.	4456.3	480.4
th15x14	30.013	0.000	40560.	3509.8	133.7
th15x15	30.013	0.000	41038.	3363.9	203.4

Table 8.9: FMT plume temperatures at TH15 (w/ neutralizer).

File name	Axial position x (cm)	Radial position y (cm)	Axial temp. T_x (eV)	Radial temp. T_y (eV)	Vertical temp. T_z (eV)
th15x0	0.117	0.000	4.4008	5.0490	6.2101
th15x1	0.224	0.000	4.9739	3.8419	5.7430
th15x2	0.351	0.000	4.3995	3.9274	5.7994
th15x3	0.411	0.000	4.8760	4.2337	4.8821
th15x4	0.505	0.000	4.5253	4.4164	4.5868
th15x5	0.696	0.000	5.0961	4.6589	5.1161
th15x6	1.008	0.000	5.2126	4.4516	5.6099
th15x7	1.394	0.000	5.6173	5.6016	5.6443
th15x8	1.890	0.000	5.8302	4.3927	7.2956
th15x9	2.492	0.000	6.2494	4.6561	6.2646
th15x10	3.495	0.000	5.1385	4.8104	5.1642
th15x11	7.008	0.000	4.9718	4.9860	4.9863
th15x12	15.004	0.000	4.6119	4.6247	4.6257
th15x13	15.004	0.000	5.7973	5.7974	5.8163
th15x14	30.013	0.000	4.0476	4.0547	4.0585
th15x15	30.013	0.000	5.3006	6.4169	6.4238

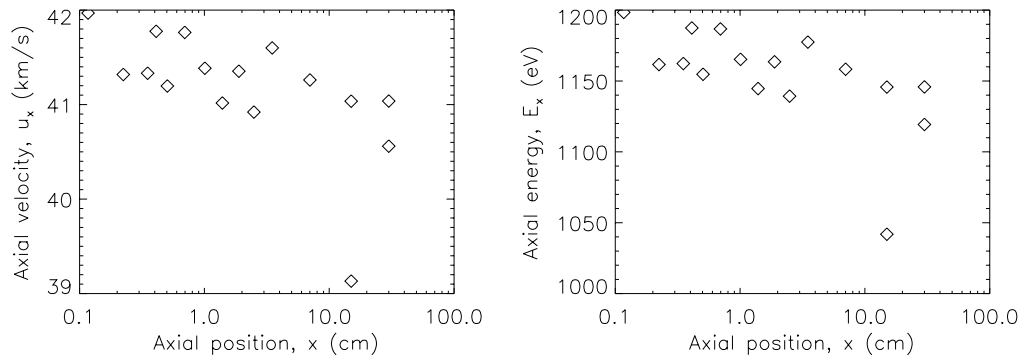


Figure 8.7: Axial ion velocity & energy vs. axial position at $y = 0.000$ cm for neutralized TH15.

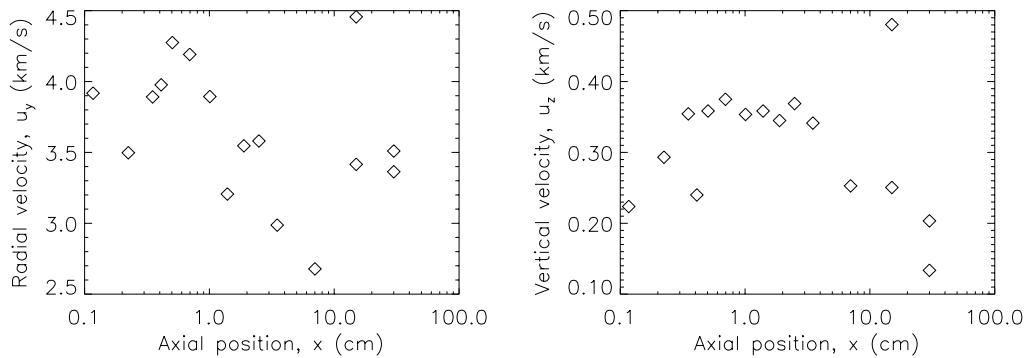


Figure 8.8: Radial & vertical ion velocity vs. axial position at $y = 0.000$ cm for neutralized TH15.

Figure 8.7 shows the radial variation of ion axial velocity and energy along the FMT-2 centerline at TH15. Screen potential at this condition is 1102 V, while the total voltage is 1282 V. Ion axial energies for all but one point lie in the range $V_s \leq E_x \leq V_T$ at this condition, with a mean axial velocity of 41.2 km/s and a maximum velocity error within 5.0% of the mean. Both axial velocity and energy fall off with axial distance more-or-less linearly with $\ln(x)$.

Figure 8.8 shows the radial variation of ion radial and vertical velocity along the same centerline. Both radial and vertical velocities are uniformly positive. The mean centerline radial velocity (3.66 km/s) suggests a 5.1° eastward misalignment of the thruster axis,

while the mean vertical velocity (0.31 km/s) suggests a mere 0.43° upwards tilt.

8.1.4 TH19 with neutralizer

The next-to-last set of measurements was a radial sweep 5.09 cm downstream of the FMT-2 accelerator grid at the reduced-voltage (1350 V screen potential) TH19 operating point. The neutralizer continued to work through this test.

Tables 8.10 and 8.11 give bulk velocities and temperatures 5.10 cm and 1.42 mm downstream of the accelerator grid.

Table 8.10: FMT plume velocities at TH19 (w/ neutralizer).

File name	Axial position	Radial position	Axial speed	Radial speed	Vertical speed
	x (cm)	y (cm)	u_x (m/s)	u_y (m/s)	u_z (m/s)
th19i1	5.100	10.160	44331.	9402.9	624.8
th19j	5.100	11.430	41706.	9571.3	280.7
th19l	5.100	0.000	45743.	3690.4	543.9
th19m	5.100	5.080	49137.	-6552.3	-236.1
th19n0	0.142	0.254	48779.	-6536.6	-232.4
th19n1	0.142	0.254	48774.	-6388.6	-265.1
th19o	0.142	1.270	45750.	4333.7	583.5
th19p	0.142	2.616	45927.	5280.8	544.8
th19q	0.142	3.759	46540.	4605.1	431.5
th19r0	0.142	5.131	46989.	5693.0	374.3
th19r1	0.142	5.131	44987.	5640.6	475.2
th19s	0.142	6.299	45391.	6305.2	339.0
th19t	0.142	7.671	44396.	7071.8	603.2
th19u	0.142	8.839	45636.	8467.6	699.4
th19v	0.142	10.185	44500.	8679.7	754.5

Figure 8.9 shows the radial variation of ion axial velocity and energy 5.10 cm downstream of the FMT-2 accelerator grid at TH19. Screen potential at this condition is 1325 V, while the total voltage is 1570 V. Ion axial energies overlap both sides of the range $V_s \leq E_x \leq V_T$ at this condition. A quick look at Fig. C.44 through C.45 shows why the ion energy spread is so large: these velocity distributions are extremely noisy, making any

Table 8.11: FMT plume temperatures at TH19 (w/ neutralizer).

File name	Axial position x (cm)	Radial position y (cm)	Axial temp. T_x (eV)	Radial temp. T_y (eV)	Vertical temp. T_z (eV)
th19i1	5.100	10.160	15.2141	18.9139	18.9287
th19j	5.100	11.430	24.7254	27.8528	28.6320
th19l	5.100	0.000	8.3202	8.3318	8.3319
th19m	5.100	5.080	7.7495	7.7829	7.7931
th19n0	0.142	0.254	7.5943	7.6150	7.6289
th19n1	0.142	0.254	6.8230	4.3201	9.6573
th19o	0.142	1.270	7.7372	7.7518	7.7649
th19p	0.142	2.616	7.5074	8.3492	9.2234
th19q	0.142	3.759	9.4159	7.6512	10.0491
th19r0	0.142	5.131	10.4670	7.7503	10.5392
th19r1	0.142	5.131	7.8390	11.8272	11.8465
th19s	0.142	6.299	10.4834	10.5073	10.5075
th19t	0.142	7.671	10.3681	11.7911	12.5935
th19u	0.142	8.839	16.3555	15.7706	16.7405
th19v	0.142	10.185	22.4414	17.2702	22.5338

bulk velocity predictions highly suspect. Figure 8.10 shows similarly suspect ion radial and vertical velocity trends.

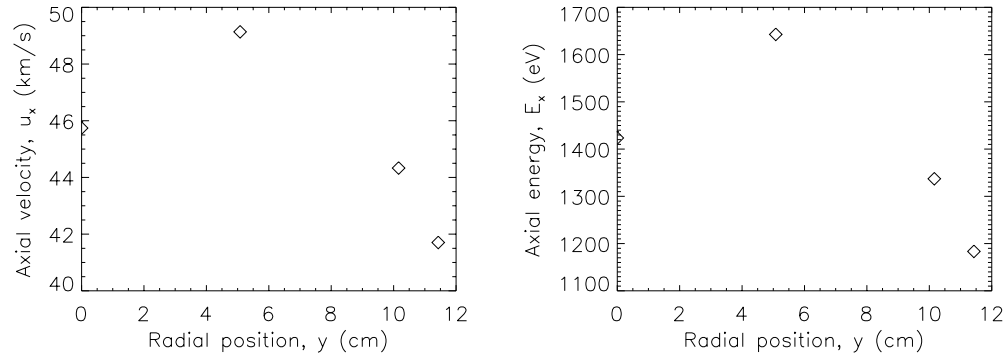


Figure 8.9: Axial ion velocity & energy vs. radial position at $x = 5.100$ cm for neutralized TH19.

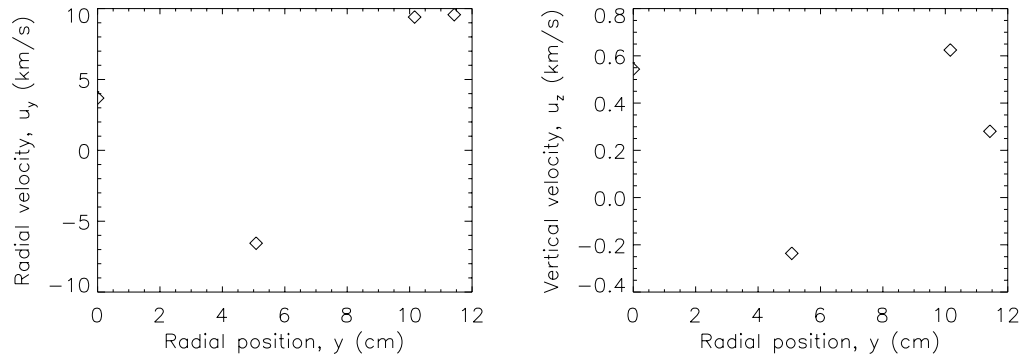


Figure 8.10: Radial & vertical ion velocity vs. radial position at $x = 5.100$ cm for neutralized TH19.

Figure 8.11 shows the radial variation of ion axial velocity and energy 1.42 mm downstream of the FMT-2 accelerator grid at TH19. Only one point is outside the expected $V_s \leq E_x \leq V_T$ range; the mean axial velocity is 46.2 km/s, and the maximum velocity error is within 3.9% of the mean.

Figure 8.12 shows the radial variation of ion radial and vertical velocity along the same plane. Except for one point on the centerline, radial velocity tends to increase linearly with radial position, while vertical velocity shows no clear trend.

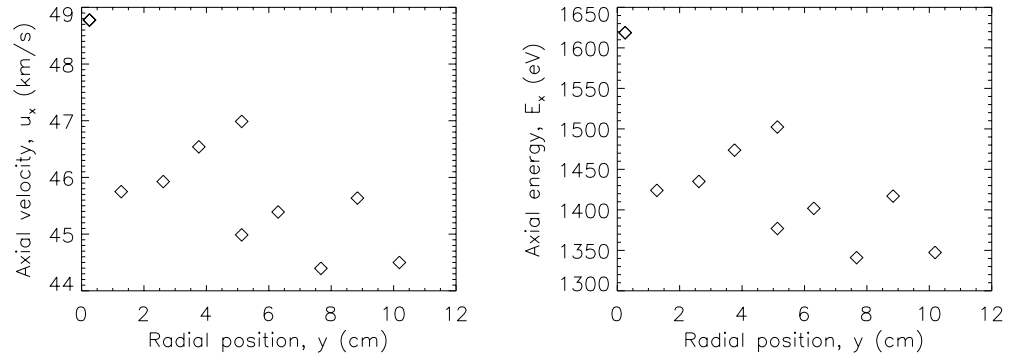


Figure 8.11: Axial ion velocity & energy vs. radial position at $x = 0.142$ cm for neutralized TH19.

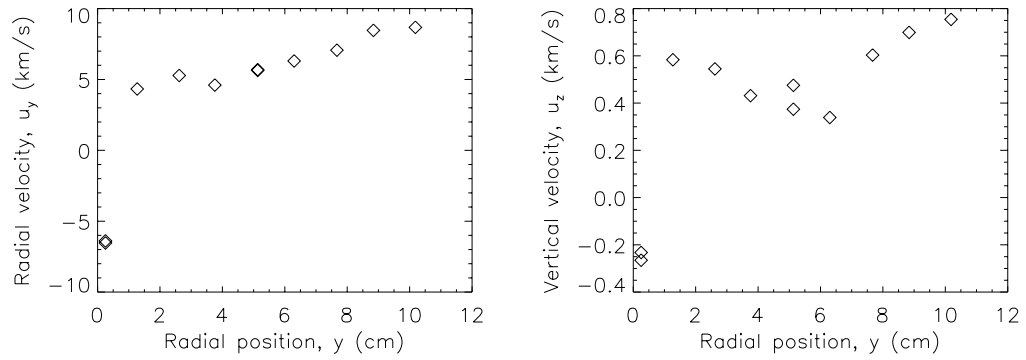


Figure 8.12: Radial & vertical ion velocity vs. radial position at $x = 0.142$ cm for neutralized TH19.

8.2 Summary

This study is, to the best of my knowledge, the first set of Xe II LIF velocimetry measurements made downstream of an ion thruster. The highly-concentrated nature of the beamlets immediately downstream of the accelerator grid makes extreme near-field LIF at a regular series of radial positions difficult; getting a good overlap between the interrogation volume and a beamlet requires a bit of searching around the desired values. The LIF spectrums' signal-to-noise ratios (SNRs) quickly diminish with increasing radial distance, but the overall beam is so well collimated that the SNR is still quite good at the translation table's limit of axial travel.

CHAPTER IX

CONCLUSIONS AND FUTURE WORK

It is a wise man who knows when to abandon a research or field of research. – *E. Bright Wilson* [18]

In this dissertation, I have developed and validated a deconvolution technique for extracting velocity distributions from Xe II LIF spectra at 605.1 nm. Application of this technique to LIF measurements of Hall thruster and ion engine plumes has provided velocity distributions that cannot be measured by conventional probe-based methods, and has revealed some unexpected plasma phenomena in these plumes.

9.1 Deconvolution

Three candidate Fourier-transform deconvolution methods were considered. Simple inverse filter deconvolution works admirably for almost-noiseless LIF spectra, with no filter broadening of the original velocity distribution, but preferentially amplifies noise to an unacceptable degree. Rectangular inverse filter deconvolution attenuates noise, is computationally simple and gives the user a great deal of control over filtering bandwidth, but induces low-frequency ringing artifacts at small filter bandwidths. Gaussian inverse filter deconvolution has all the advantages of the rectangular inverse filter without ringing, and is clearly the best of the three methods.

The velocity distributions returned by Gaussian inverse filtered deconvolution of LIF spectra show excellent agreement with distributions taken with probe-based instruments. When transformed into an ion energy distribution (iedf), an LIF deconvolution taken downstream of the P5 Hall thruster exit plane reproduced most of the features of an iedf measured with a mass spectrometer (MBMS) at the same point. The primary peaks of both distributions are nearly identical. Differences in the two iedfs also support the believability of the deconvolved distribution. Features found in the MBMS distribution that do not show up in the Xe II LIF distribution are caused by other species, while the energy difference between primary peaks is commensurate with the plasma potential at the measurement location.

9.2 P5 Hall thruster

Off-axis multiplex and axial-injection LIF experiments in the P5 Hall thruster plume returned a mix of expected and unexpected results. Repeated measurements of axial velocity by axial-injection LIF agree within 2%, while axial temperatures agree within a 40% error band. Multiplex LIF measurements of axial velocity differ from previously-published multiplex measurements by 18%, but both values bracket the axial-injection LIF results.

We found that an acceleration region extends 20 cm downstream of the P5 exit plane, followed by a zone of decreasing axial velocity. Though the acceleration zone downstream of a Hall thruster has been reported before, the deceleration region we noted has not. Axial temperatures during 1.6 kW operation tend to decrease with increasing axial velocity and increase with decreasing axial velocity, supporting the hypothesis of kinematic compression.

Vertical velocity distributions taken at the P5 centerline showed unexpected counter-

streaming plasma phenomena. A significant portion of the velocity distribution has near-zero radial velocity; this “mixing population” can only occur if some sort of interaction between particles has occurred. Since mean flow path calculations indicate that the flow is largely collisionless, some sort of collisionless interaction (such as two-stream instability) may explain the presence of this population.

9.3 FMT-2 ion engine

Off-axis multiplex LIF experiments in the FMT-2 ion engine plume also returned a mix of expected and unexpected results.

The highly-concentrated nature of the beamlets immediately downstream of the accelerator grid makes extreme near-field LIF difficult. The signal-to-noise ratio rapidly diminishes as the interrogation point nears the edge of the grid, but remains quite strong out to the axial limits of the table along the centerline.

9.4 Future work

Every research project seems to generate a cascade of subordinate questions and projects. Some of these can be profitably pursued in the course of the main project, but many more have to be let go (or shelved for another day) if the project is ever to be finished. Some unexplored avenues suggested by this dissertation are as follows:

1. Improved desaturation techniques. Though the direct computational desaturation of highly-saturated transitions¹ ($\max S(\nu) > 5$) produces unacceptable noise amplification (see section 5.1.2), smoothing techniques might extend desaturation techniques to higher saturation levels. The classic Wiener filter [34], in particular, war-

¹Check value!

rants further investigation. This might make a good project for a computationally-oriented undergraduate.

2. Improved filtering methods for deconvolution. Optimal filters, such as the so-called Wiener filter invented by Bracewell [32] and Helstrom [33] or Frieden's sharpness-constrained filter [31], could improve the fidelity of this dissertation's velocity distribution extraction method. Much more modeling, however, needs to be done to determine how well these methods respond to unexpected object functions. Again, a good project for a computationally-oriented undergraduate.
3. Radial-injection LIF in the P5 plume. Previous attempts to carry this out by rotating the thruster toward the collection optics failed when the collection optics cover plate was quickly etched into unusability. A better method would be to keep the P5 pointed north, as in the axial-injection experiments, and bring the laser in from the east.
4. More axial-injection LIF measurements of the P5 plume. When done in conjunction with direct radial-injection measurements, this would provide vector plots of mean ion velocities in the plume, and shed some light on the apparent deceleration zone starting 20 cm from the thruster exit plane.
5. Internal P5 LIF. This can be done without modifying the P5 by simply placing a single mirror in the collection optics train. Since LIF is isotropic, the collection axis can be placed anywhere on a line-of-sight with the thruster interior, though the interrogation volume will grow as the angle between the laser beam and the collection axis moves out of square. Rotating the P5 slightly should allow off-axis measurement of mean radial velocities, which could be quite useful in future erosion studies.

6. Orthogonal 3-component plume LIF. Beitung and Pollard [94] recently reported a 3-beam LIF system that avoids the angular error problems inherent in off-axis multiplex LIF. Independent beam trains direct each focused beam along orthogonal axes to a common interrogation volume. Keeping alignment during chamber evacuation could be a problem, but this technique would combine the advantages of the off-axis multiplex and axial-injection techniques.
7. Tomographic measurement of the two-dimensional velocity distribution in the P5 plume. This may only be of academic interest, but knowing how the principal axes of $f(v_x, v_r)$ are oriented with respect to the P5 geometry might shed some light on future computational models.
8. Detailed investigation of the luminous cone structure downstream of the P5 inner pole. Beal's collisionless shock hypothesis [95] seems reasonable, but the data currently available neither prove nor disprove the hypothesis. Computational modeling of two-stream instability growth would be useful to see if the measured radial distributions along the thruster centerline match predictions. Also, fine-grid LIF measurements and Langmuir probe sweeps have a good chance of catching the mean velocity drop and ion density jump at the expected shock.
9. Axial-injection LIF measurements of the FMT plume. We still have no indication of Xe III - Xe II CEX from the current crop of LIF measurements; axial-injection LIF should permit that. Kinematic compression effects should be prevalent, simplifying the task somewhat.
10. Expansion of the deconvolution method to other LIF lines, especially the 834.7 nm line. Since the hyperfine structure for this line is not characterized, we cannot create a computational kernel. My first attempt to remedy this by LIF of a kinematically-

compressed beam has failed, but I plan to try again after the defence. I am also working on a concurrent attack on the problem, using intermodulated optogalvanic spectroscopy (IMOG) to isolate the hyperfine lines.

APPENDICES

APPENDIX A

Saturation and desaturation of LIF spectra

As noted in Chapter 1, Xe II LIF results from the absorption, and subsequent spontaneous emission, of light energy by singly-ionized xenon. Non-resonant LIF can be modeled as a four-level system, where the subscript 0 denotes the ground state, 1 denotes the initial metastable state, 2 denotes the upper excited state, and 3 denotes the final state. The total fluorescence signal power reaching the photomultiplier tube from an interrogation volume V can be expressed as

$$S_f = \eta_d \frac{\Omega}{4\pi} A_{23} h \nu_{23} N_2 \quad (\text{A.1})$$

where η_d is the detection system efficiency, Ω is the collection optics solid angle, A_{23} is the spontaneous emission coefficient for the $2 \rightarrow 3$ transition, ν_{23} is the frequency of the $2 \rightarrow 3$ line and N_2 is the upper state population.

A.1 Saturation

A.1.1 Empirical model

Both the two-level and four-level models suffer from the same set of problems. Though degeneracies and spontaneous emission coefficients are readily available for most Xe II transitions, collisional quenching rates are not. Also, measuring the lineshape (in order to compute the laser's spectral intensity distribution) for a narrow-bandwidth laser is not

trivial. Measuring the beam waist diameter is, by comparison, relatively easy, but still requires fairly precise aperture measurements.

A simpler, empirical approach to describing the saturation behavior of a transition can resolve these problems. Though laser spectral intensity is difficult to measure, the laser power P_L is not. In both the two-level and four-level models, the dimensionless saturation parameter $S(\nu, P_L)$ varies linearly with the laser power P_L and the unsaturated lineshape $i(\nu)$, so that

$$S(\nu, P_L) = \beta P_L i(\nu) \quad (\text{A.2})$$

where the saturation coefficient β , a constant for a given transition and set of plasma parameters, has units of frequency over power. Likewise, the saturated LIF signal can be expressed by

$$i_s(\nu, P_L) = \Gamma \frac{S(\nu, P_L)}{1 + S(\nu, P_L)} = \Gamma \frac{\beta P_L i(\nu)}{1 + \beta P_L i(\nu)}. \quad (\text{A.3})$$

where Γ , which represents the maximum (*i.e.*, fully saturated) possible value of $i_s(\nu)$, is again a constant for a given transition and set of plasma parameters, with units of LIF signal power.

The saturation curve constants β and Γ in Eqn. A.3 can be determined by two LIF spectra¹, taken at different laser powers P_0 and P_1 . Consider two LIF signal measurements made at the same frequency ν :

$$i_0 \equiv i_s(\nu, P_0) = \Gamma \frac{\beta P_0 i(\nu)}{1 + \beta P_0 i(\nu)}, \text{ and} \quad (\text{A.4})$$

$$i_1 \equiv i_s(\nu, P_1) = \Gamma \frac{\beta P_1 i(\nu)}{1 + \beta P_1 i(\nu)}. \quad (\text{A.5})$$

The ratio of these two measurements is

$$\frac{i_1}{i_0} = \frac{P_1}{P_0} \left[\frac{1 + \beta P_0 i(\nu)}{1 + \beta P_1 i(\nu)} \right], \quad (\text{A.6})$$

¹The third point needed to define a curve is the origin; no laser power, no LIF signal.

which (after some algebraic manipulation) yields the product

$$\beta i(\nu) = \frac{1}{P_0} \left[\frac{P_0/P_1 - i_0/i_1}{i_0/i_1 - 1} \right] = \frac{1}{P_1} \left[\frac{P_1/P_0 - i_1/i_0}{i_1/i_0 - 1} \right]. \quad (\text{A.7})$$

where both β and $i(\nu)$ are unknown. Since $i(\nu)$ is normalized,

$$\int_{-\infty}^{\infty} \beta i(\nu) d\nu = \beta \int_{-\infty}^{\infty} i(\nu) d\nu = \beta \quad (\text{A.8})$$

so that

$$\beta = \int_{-\infty}^{\infty} \frac{d\nu}{P_0} \left[\frac{P_0/P_1 - i_0/i_1}{i_0/i_1 - 1} \right] = \int_{-\infty}^{\infty} \frac{d\nu}{P_1} \left[\frac{P_1/P_0 - i_1/i_0}{i_1/i_0 - 1} \right] \quad (\text{A.9})$$

where $i_0 = i_s(\nu, P_0)$ and $i_1 = i_s(\nu, P_1)$ are the only functions of frequency. As a practical matter, restricting the integration domain to the center of the LIF spectrum (where $i_s(\nu)$ is much greater than the noise amplitude) will avoid noise amplification problems. Using this approach,

$$\beta = R \int_{\nu_0}^{\nu_1} \frac{d\nu}{P_0} \left[\frac{P_0/P_1 - i_0/i_1}{i_0/i_1 - 1} \right] = R \int_{\nu_0}^{\nu_1} \frac{d\nu}{P_1} \left[\frac{P_1/P_0 - i_1/i_0}{i_1/i_0 - 1} \right] \quad (\text{A.10})$$

where the scaling factor

$$R = \frac{\int_{-\infty}^{\infty} i(\nu) d\nu}{\int_{\nu_0}^{\nu_1} i(\nu) d\nu} \approx \frac{\int_{-\infty}^{\infty} i_s(\nu) d\nu}{\int_{\nu_0}^{\nu_1} i_s(\nu) d\nu} \quad (\text{A.11})$$

allows for the restricted range of integration.

Rearranging Eqn. A.3 yields the maximum LIF signal strength

$$\Gamma = \left[\frac{1 + \beta P_L i(\nu)}{\beta P_L i(\nu)} \right] i_s(\nu) \quad (\text{A.12})$$

in terms of the (still-unknown) unsaturated lineshape $i(\nu)$. Since Γ is a constant, this applies to both power levels:

$$\Gamma = \left[\frac{1 + \beta P_0 i(\nu)}{\beta P_0 i(\nu)} \right] i_0 = \left[\frac{1 + \beta P_1 i(\nu)}{\beta P_1 i(\nu)} \right] i_1. \quad (\text{A.13})$$

Solving for the lineshape,

$$i(\nu) = \frac{1}{\beta} \left[\frac{i_1 - i_0}{P_0 i_0 - P_1 i_1} \right] \quad (\text{A.14})$$

which can be substituted into Eqn. A.12. The resulting maximum LIF signal strength is

$$\Gamma = i_1 \left[1 + \frac{(P_0/P_1)i_0 - i_1}{i_1 - i_0} \right] = i_0 \left[1 + \frac{i_0 - (P_1/P_0)i_1}{i_1 - i_0} \right]. \quad (\text{A.15})$$

Again, integration over a restricted domain reduces the effects of noise, while reducing noise amplification problems in the wings of the LIF spectrum:

$$(\nu_1 - \nu_0)\Gamma = i_1 \int_{\nu_0}^{\nu_1} \left[1 + \frac{(P_0/P_1)i_0 - i_1}{i_1 - i_0} \right] d\nu = i_0 \int_{\nu_0}^{\nu_1} \left[1 + \frac{i_0 - (P_1/P_0)i_1}{i_1 - i_0} \right] d\nu. \quad (\text{A.16})$$

Thus, two LIF measurements $i_s(\nu)$ at differing laser powers (P_L) will determine the saturation curve coefficients β and Γ at a given set of plasma parameters. This curve, in turn, indicates how much saturation perturbs the measured LIF signal.

A.1.2 Saturation broadening

A third type of line broadening results from line saturation. This effect, which is traditionally called “saturation broadening,” is caused by the nonlinear response of the upper state population to high values of the dimensionless saturation parameter $S(\nu)$. The traditional method of modeling saturation broadening given by Demtröder [43] and Yariv [44] multiplies the linewidth of a homogeneous (*i.e.*, Lorentzian) transition by a constant term,

$$\Delta\nu_s = \Delta\nu_n \sqrt{1 + I_\nu/I_s}. \quad (\text{A.17})$$

In this case, the saturation intensity I_s is not typically considered a frequency-dependent value, but is single-valued. The resulting Lorentzian lineshape of the form

$$l(\nu) = \frac{\Delta\nu_s}{2\pi} \frac{1}{(\nu - \nu_0)^2 + (\Delta\nu_s/2)^2} \quad (\text{A.18})$$

is then convolved with the Doppler broadening and hyperfine structure to create the simulated absorption spectrum.

This traditional approach tends to obscure the underlying distortion effect of saturation, and instead treats saturation broadening as yet another homogeneous broadening mechanism, such as pressure broadening. In fact, the traditional label of “saturation broadening” is misleading. Unlike natural or Doppler broadening, saturation broadening does not reflect inherent properties of either the transition or the velocity distribution. Saturation is really a *distortion*, akin to the nonlinear acoustic response of an overloaded speaker system, which systematically decreases the peak system response amplitude.

A simple, algebraic transformation can replace this traditional line-broadening approach to saturation. As I have shown in section A.1.1, the saturation parameter is linearly proportional to the laser power P_L and the unsaturated lineshape $i(\nu)$. Therefore, the saturation curve shown in Figure A.1 applies to changes in lineshape as well as laser power. Given the empirical saturation coefficients β and Γ , the saturated LIF spectrum $i_s(\nu)$ can be predicted for any laser power P_L and unsaturated lineshape $i(\nu)$ by the transformation

$$i_s(\nu, P_L) = \Gamma \frac{\beta P_L i(\nu)}{1 + \beta P_L i(\nu)}. \quad (\text{A.19})$$

Out at the edges of the LIF spectrum, the lineshape approaches zero, so the LIF signal remains linear with lineshape. At high laser intensities, though, the upper state population approaches saturation near the line center. The resulting nonlinearity diminishes the LIF signal at the unsaturated lineshape’s peaks.

Figure A.1 shows how this nonlinearity changes the original, unsaturated lineshape for the warm-plasma spectrum of Fig. 4.8. At low saturation levels ($\beta P_L = 10^2$ MHz, corresponding to a maximum saturation parameter of 0.08), the LIF spectrum’s normalized lineshape is essentially indistinguishable from the unsaturated lineshape. As the laser power increases, though, two effects become apparent. Both of the main peaks become broader, as expected; but the secondary peak height begins to increase with respect to the

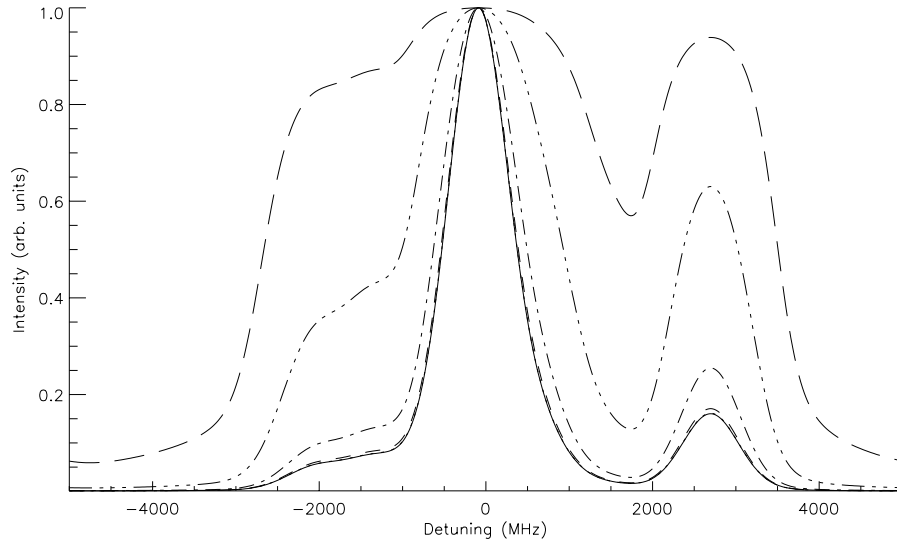


Figure A.1: Unsaturated (solid curve) and saturation-broadened warm-plasma spectra (dashed curves for βP_L values of $10^0, 10^1, 10^2, 10^3, 10^4$ and 10^5 MHz) for the Xe II $5d^4 D_{7/2} - 6p^4 P_{5/2}^0$ line, $T = 600$ K.

primary peak height. At $\beta P_L = 10^3$ MHz (where $\max[S(\nu)] = 0.79$), the broadening effect is barely noticeable, but the secondary peak height increases considerably (from 17% to 28% of the primary peak height). At $\beta P_L = 10^4$ MHz (where $\max[S(\nu)] = 7.92$), both effects become obvious, with the secondary peak climbing to 66% of the primary peak height. Finally, at $\beta P_L = 10^5$ MHz (where $\max[S(\nu)] = 79.2$, the LIF spectrum distortion is so great that the primary peak is visibly flattened, while the secondary peak rises to 94% of the primary peak height.

A.2 Desaturation

Extracting the beamwise² velocity distribution $f(v_k)$ from an LIF spectrum $i_s(\nu)$ requires two steps: *desaturation* and *deconvolution*.

Desaturation removes the effects of saturation broadening from the LIF spectrum $i_s(\nu)$ with a simple computational transformation. Unfortunately, this transformation (detailed

²“Beamwise” means parallel to the laser beam direction vector $\hat{\mathbf{k}} = \mathbf{k}/|\mathbf{k}|$.

in Appendix A) requires a fuller data set than collected in these experiments. Section 4.5.3 shows that it is reasonable to assume that the LIF spectra lie within the linear section of the saturation curve, so that $i(\nu)$ is linearly proportional to $i_s(\nu)$.

Deconvolution separates the unsaturated lineshape $i(\nu)$ into its constituents, the cold-plasma spectrum $c(\nu)$ and the Doppler broadening function estimate $\hat{d}(\nu)$. The simple transformation of Eqn. 4.56 and 4.61 then yields an estimate $\hat{f}(v_k)$ of the beamwise velocity distribution $f(v_k)$.

In the absence of noise, these processes are exact, so that $\hat{i}(\nu) = i(\nu)$ and $\hat{f}(v_k) = f(v_k)$. The presence of noise, however, inevitably distorts the estimates. This distortion can be effectively separated into two effects: noise amplification and broadening.

As noted in section 3.3, we need to characterize the noise properties of sample LIF spectra in order to properly estimate of the effects of noise on the deconvolution. Section 5.1 presents an analysis of these noise properties for ensemble averages of typical reference cell and P5 plume LIF spectra. (FMT-2 plume LIF spectra were, at best, only repeated once, giving no ensemble large enough to extract any useful noise property statistics.) Section 5.2 then demonstrates how three candidate deconvolution methods deal with noise amplification and broadening.

A.2.1 Method

The empirical approach of section A.1.1 shows how two saturated LIF spectra $i_s(\nu, P_L)$ at known laser powers P_L can provide the saturation coefficients β and Γ for a given transition and set of plasma parameters. In terms of the saturation parameter $S(\nu)$, the saturated LIF spectrum is (in the absence of noise)

$$i_s(\nu, P_L) = \Gamma \frac{S(\nu)}{1 + S(\nu)}, \quad (\text{A.20})$$

which can be rearranged to give

$$S(\nu, P_L) = \frac{i_s(\nu)}{\Gamma - i_s(\nu)}. \quad (\text{A.21})$$

Recalling the definition of β and letting $i(\nu)$ denote the unsaturated lineshape,

$$S(\nu) = \beta P_L i(\nu) = \frac{i_s(\nu)}{\Gamma - i_s(\nu)} \quad (\text{A.22})$$

so that the normalized, unsaturated lineshape at a given laser power P_L is

$$i(\nu) = \frac{1}{\beta P_L} \left[\frac{i_s(\nu)}{\Gamma - i_s(\nu)} \right]. \quad (\text{A.23})$$

A.2.2 Noise amplification

The above transformation works perfectly for noiseless spectra. Unfortunately, real LIF spectra are rarely noiseless. A better model for noisy, power-broadened spectra is given by

$$i_s(\nu, P_L) = \Gamma \frac{S(\nu)}{1 + S(\nu)} + n_s(\nu) \quad (\text{A.24})$$

which can be rearranged as above to give a lineshape estimate

$$\hat{i}(\nu) = \frac{1}{\beta P_L} \left[\frac{i_s(\nu) - n_s(\nu)}{\Gamma - i_s(\nu) - n_s(\nu)} \right]. \quad (\text{A.25})$$

At low saturation levels, Eqn. A.25 gives

$$\lim_{i_s(\nu) \rightarrow 0} \hat{i}(\nu) = \frac{1}{\beta P_L} \left[\frac{i_s(\nu) - n_s(\nu)}{\Gamma - n_s(\nu)} \right] \approx \frac{i_s(\nu) - n_s(\nu)}{\beta P_L \Gamma} \quad (\text{A.26})$$

since $\Gamma \gg n_s(\nu)$ for reasonable noise levels³. Figure A.2 shows how desaturation of a lightly-saturated transition ($\beta P_L = 10^3$ MHz, where $\max[S(\nu)] = 0.79$) evenly and minimally amplifies the original noise component, a Gaussian-distributed random function with a signal-to-noise ratio

$$\text{SNR} \equiv \frac{\max |i_s(\nu)|}{\sigma_n} \quad (\text{A.27})$$

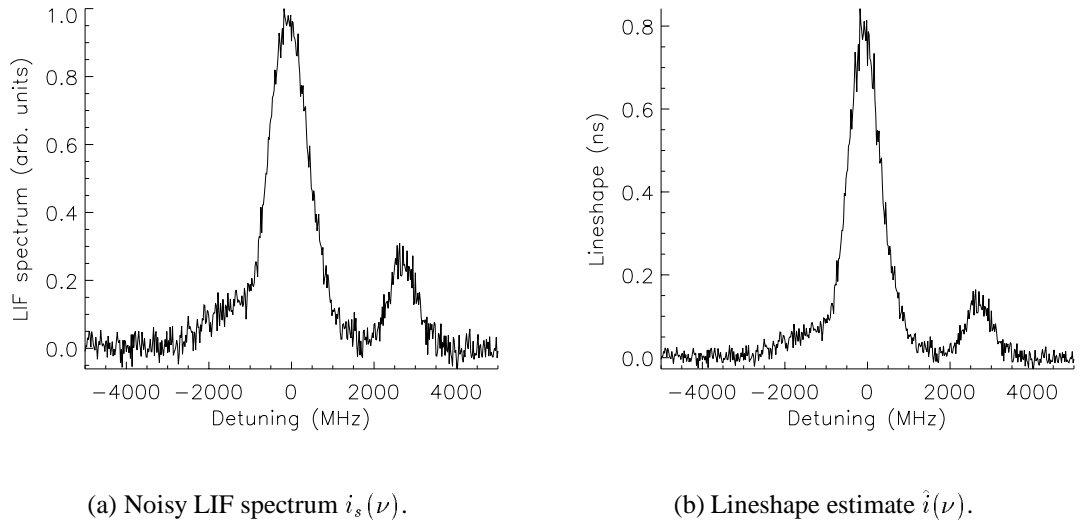


Figure A.2: Desaturation example for lightly-saturated ($\beta P_L = 10^3$ MHz) warm-plasma (600 K) spectrum with SNR = 33.

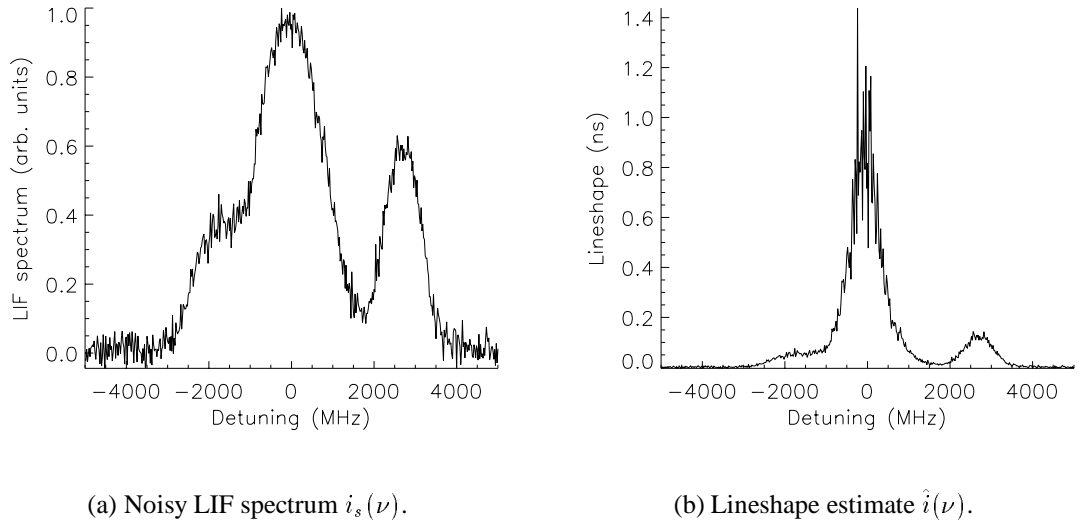


Figure A.3: Desaturation example for moderately-saturated ($\beta P_L = 10^4$ MHz) warm-plasma (600 K) spectrum SNR = 33.

where σ_n is the standard deviation of $n_s(\nu)$.

At higher saturation levels, where $\Gamma \gg i_s(\nu) + n_s(\nu)$, desaturation begins to pref-

³If the noise amplitude rivals the maximum possible LIF signal, the experimental apparatus needs either adjustment or redesign!

entially amplify noise near the line center. Figure A.3 shows how desaturation begins to fail for a moderately-saturated transition ($\beta P_L = 10^4$ MHz, where $\max[S(\nu)] = 7.92$) with $\text{SNR} = 33$.

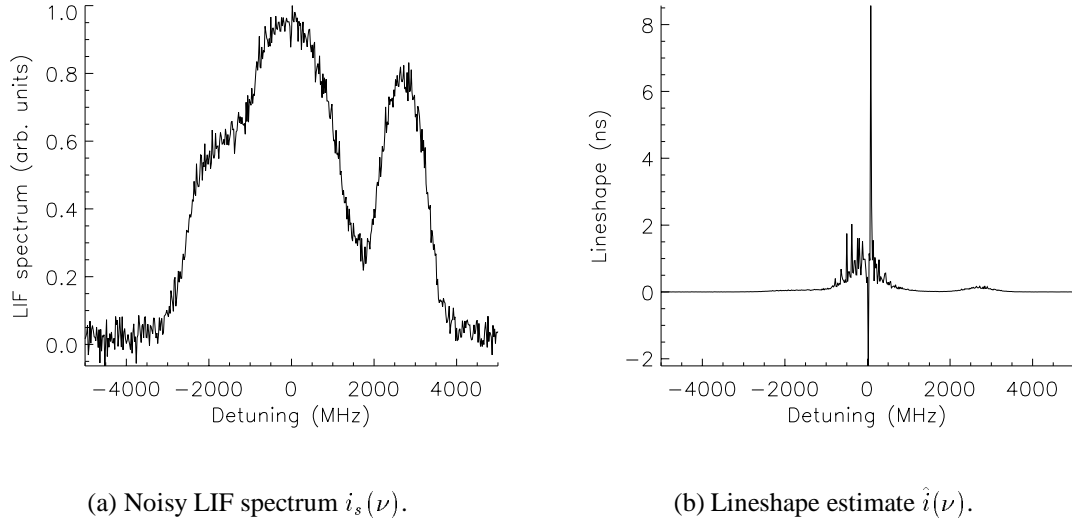


Figure A.4: Desaturation example for heavily-saturated ($\beta P_L = 3 \times 10^4$ MHz) warm-plasma (600 K) spectrum with $\text{SNR} = 33$.

At the highest saturation levels, the saturated LIF signal $i_s(\nu)$ approaches Γ , so that

$$\lim_{i_s(\nu) \rightarrow \infty} \hat{i}(\nu) = \frac{1}{\beta P_L} \left[1 - \frac{\Gamma}{n_s(\nu)} \right]. \quad (\text{A.28})$$

Clearly, each time the noise $n_s(\nu)$ drops to zero at this limit, the desaturated signal estimate $\hat{i}(\nu) \rightarrow -\infty$. Figure A.4 shows how poorly desaturation works for a heavily-saturated transition ($\beta P_L = 3 \times 10^4$ MHz, where $\max[S(\nu)] = 23.8$) with $\text{SNR} = 33$. Smoothing techniques might reduce the amplified noise to an acceptable level, but the present unsmoothed desaturation technique becomes unusable at these high saturation levels.

Given a frequency-dependant fractional noise power

$$P_n(\nu) = \left[\frac{n_s(\nu)}{\max |i_s(\nu)|} \right]^2 \quad (\text{A.29})$$

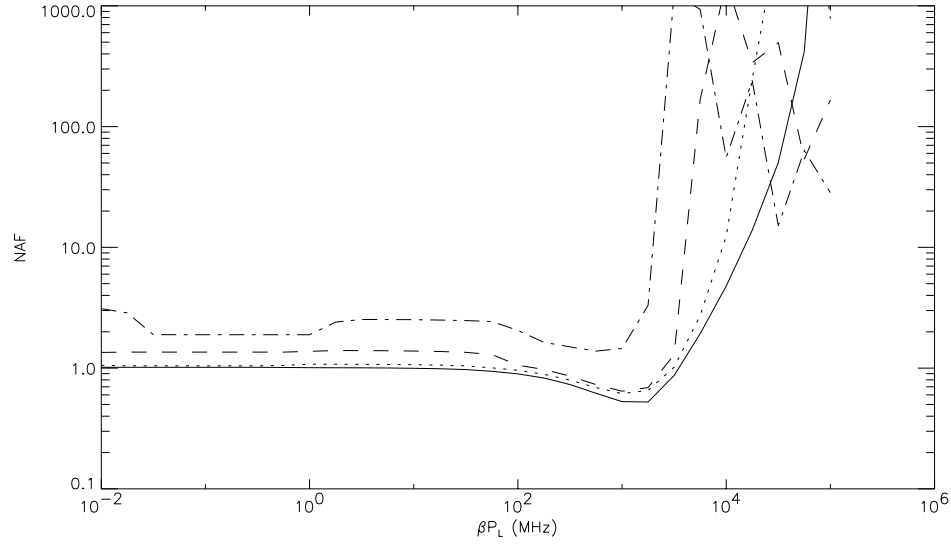


Figure A.5: Desaturation noise amplification factor as a function of saturation βP_L for SNR = 100 (solid curve), 33, 10 and 3.3 (dashed curves).

and a fractional estimation error

$$P_e(\nu) = \left[\frac{\hat{i}(\nu) - i(\nu)}{\max |i(\nu)|} \right]^2, \quad (\text{A.30})$$

we can define a noise amplification factor (integrated over the detuning range $\Delta\nu = \nu_1 - \nu_0$) of

$$\text{NAF} = \int_{\nu_0}^{\nu_1} P_e(\nu) d\nu \bigg/ \int_{\nu_0}^{\nu_1} P_n(\nu) d\nu. \quad (\text{A.31})$$

Figure A.5 shows how the desaturation technique's noise amplification factor (NAF) varies with saturation level (βP_L) for noise amplitudes of 1, 3, 10 and 30%. In all cases, the NAF remains fairly constant for $\beta P_L < 10^3$. In the regime $10^3 < \beta P_L < 10^4$, the NAF curve reaches a break point, after which it quickly climbs to unacceptable levels. The curves for higher initial noise amplitudes, to no great surprise, reach this break point well before lower-noise curves, and diverge more quickly after the break point.

APPENDIX B

P5 multiplex LIF: deconvolved velocity distributions

B.1 Standard 3-kW

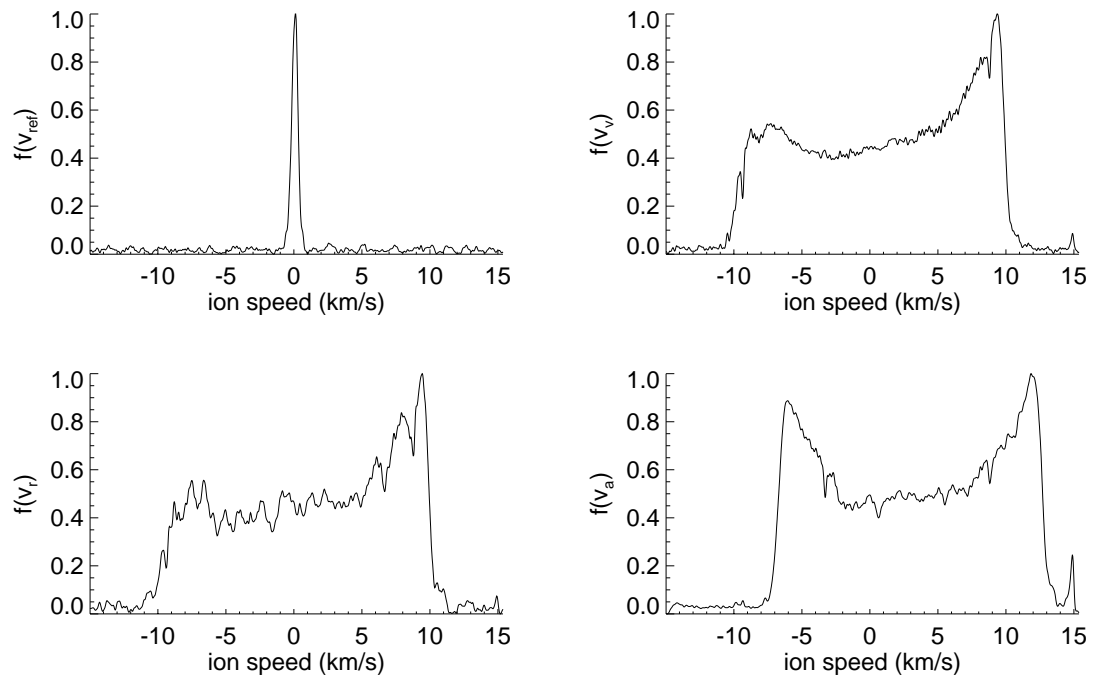


Figure B.1: Deconvolved $f(v_k)$ & curve-fit at 3 kW, $(x, y) = (10.01, 0.00)$ cm (3kwa).

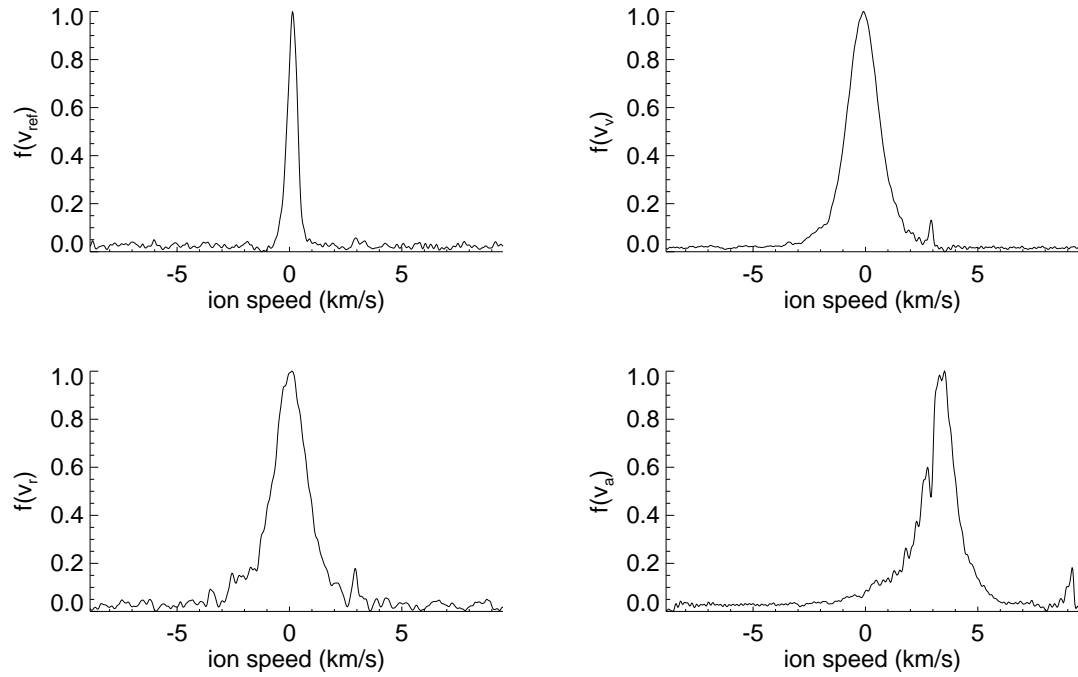


Figure B.2: Deconvolved $f(v_k)$ & curve-fit at 3 kW, $(x, y) = (10.01, 6.37)$ cm (3kwb).

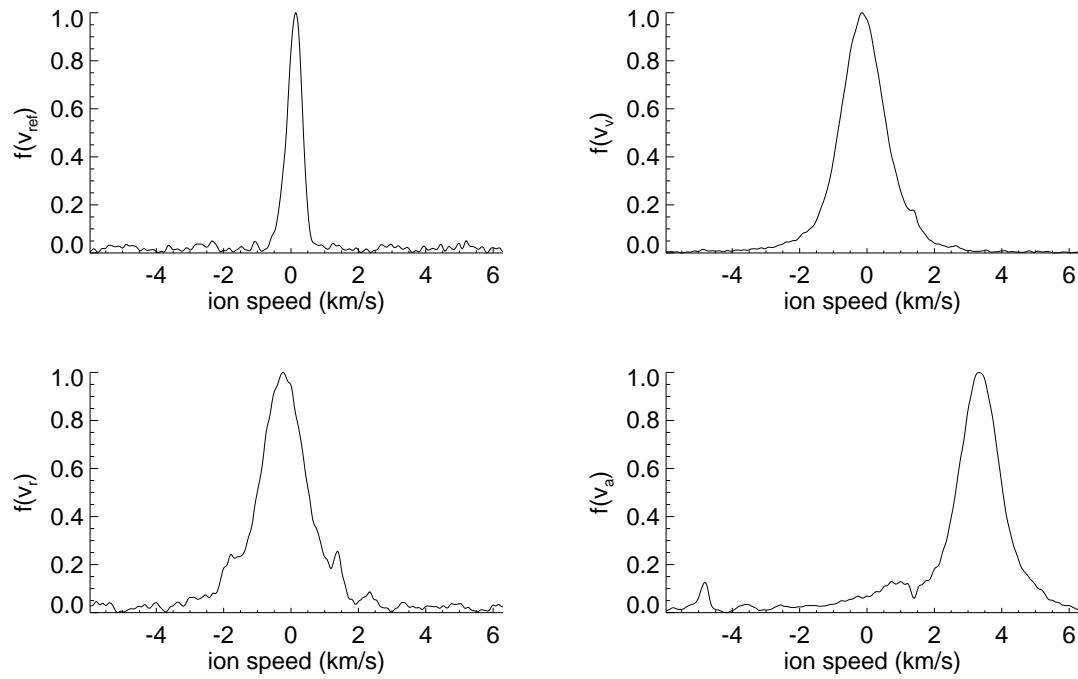


Figure B.3: Deconvolved $f(v_k)$ & curve-fit at 3 kW, $(x, y) = (10.01, 7.37)$ cm (3kwc).

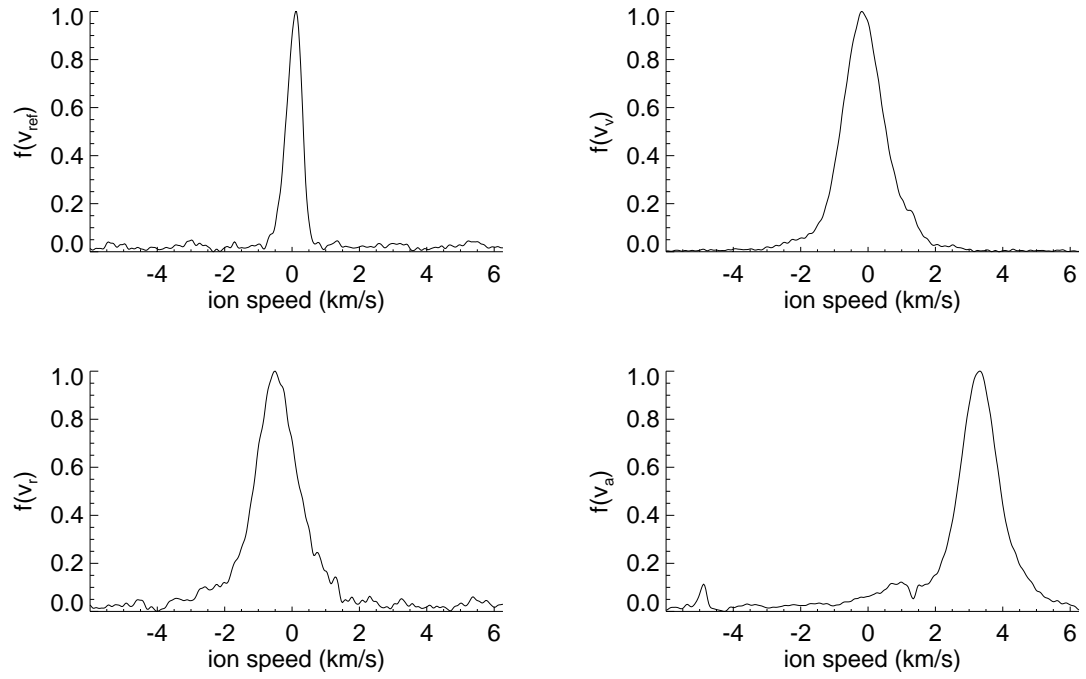


Figure B.4: Deconvolved $f(v_k)$ & curve-fit at 3 kW, $(x, y) = (10.01, 8.37)$ cm (3kwd).

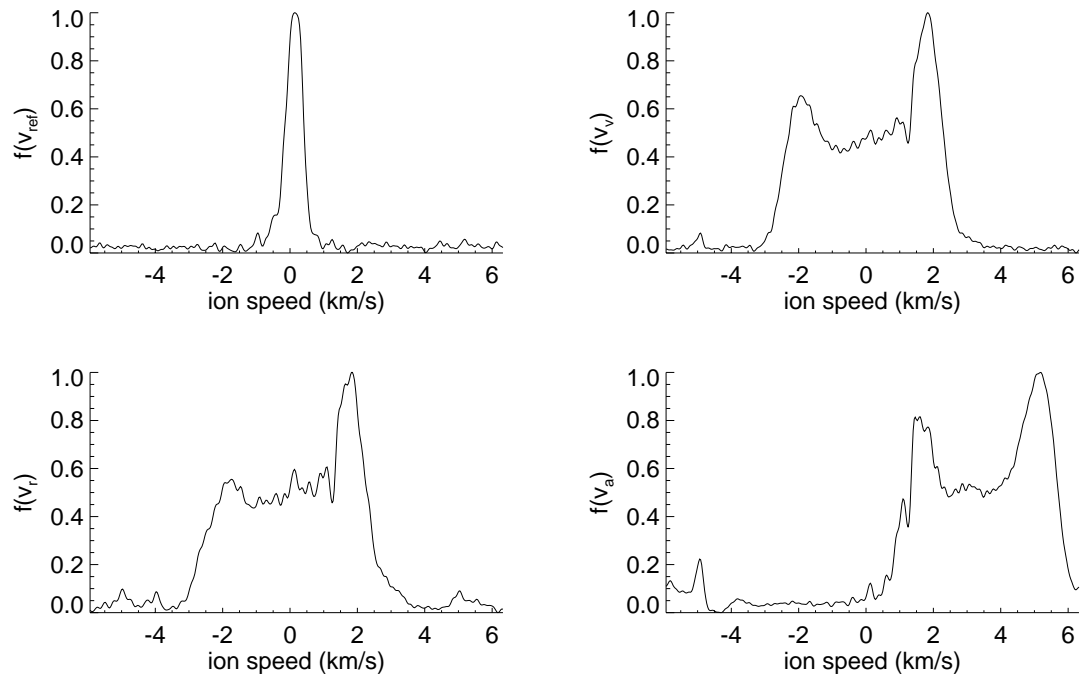


Figure B.5: Deconvolved $f(v_k)$ & curve-fit at 3 kW, $(x, y) = (50.02, 0.00)$ cm (3kwe).

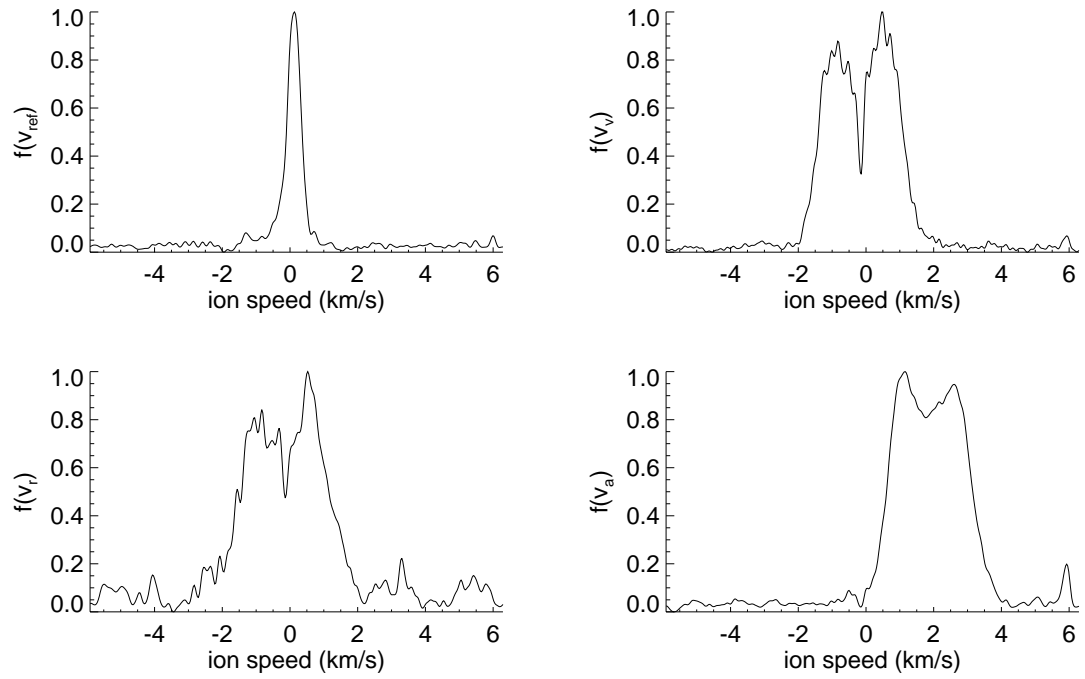
B.2 Test condition 9

Figure B.6: Deconvolved $f(v_k)$ & curve-fit at TC 9, $(x, y) = (50.02, 0.00)$ cm (tc9a).

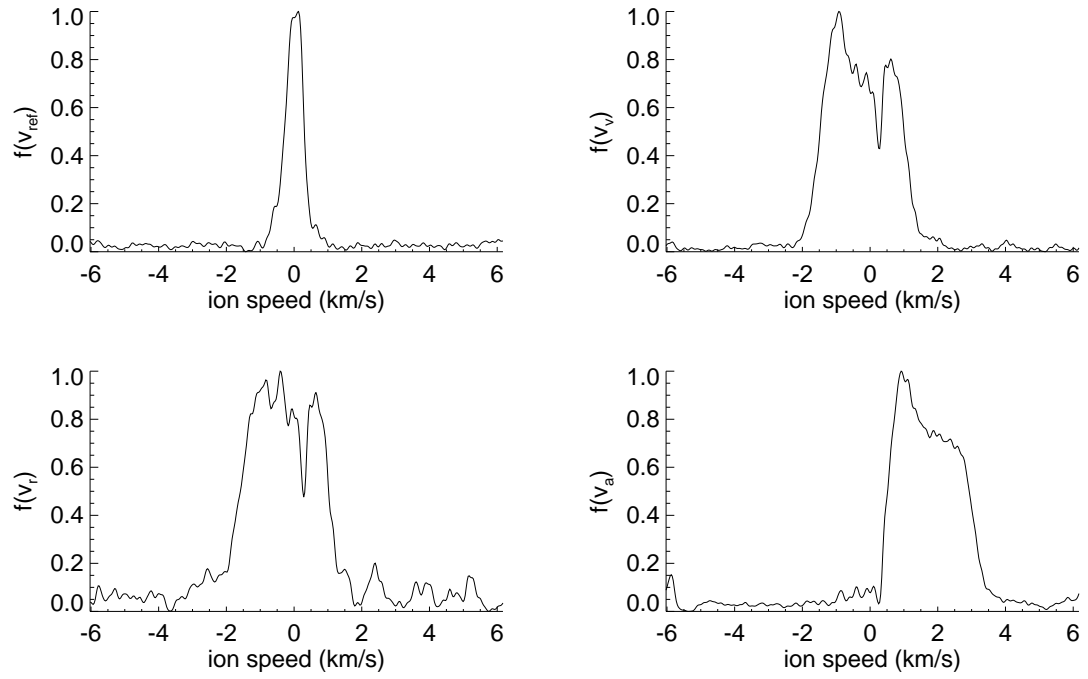


Figure B.7: Deconvolved $f(v_k)$ & curve-fit at TC 9, $(x, y) = (50.02, -1.00)$ cm (tc9b).

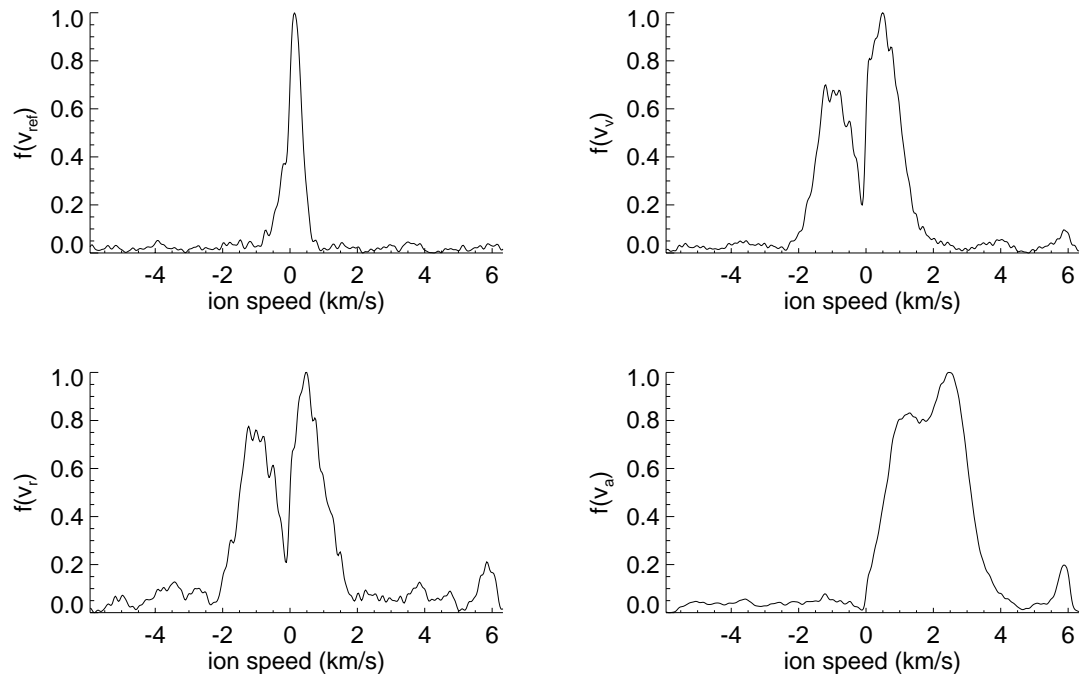


Figure B.8: Deconvolved $f(v_k)$ & curve-fit at TC 9, $(x, y) = (50.02, 1.00)$ cm (tc9c).

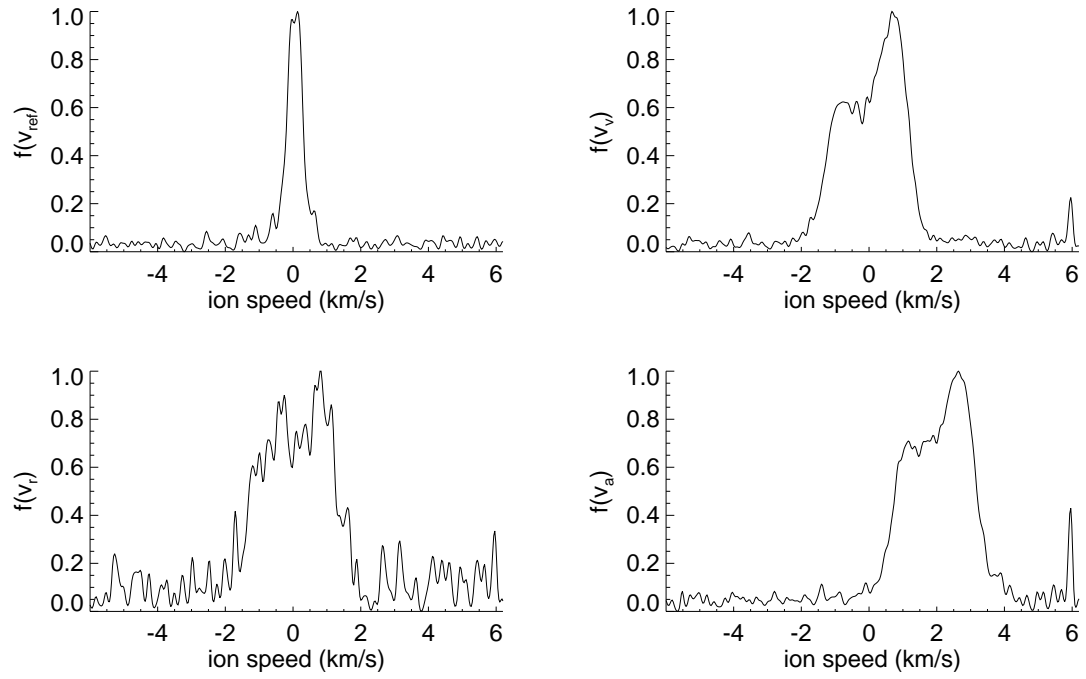


Figure B.9: Deconvolved $f(v_k)$ & curve-fit, TC 9, $(x, y) = (50.02, 2.00)$ cm (tc9d).

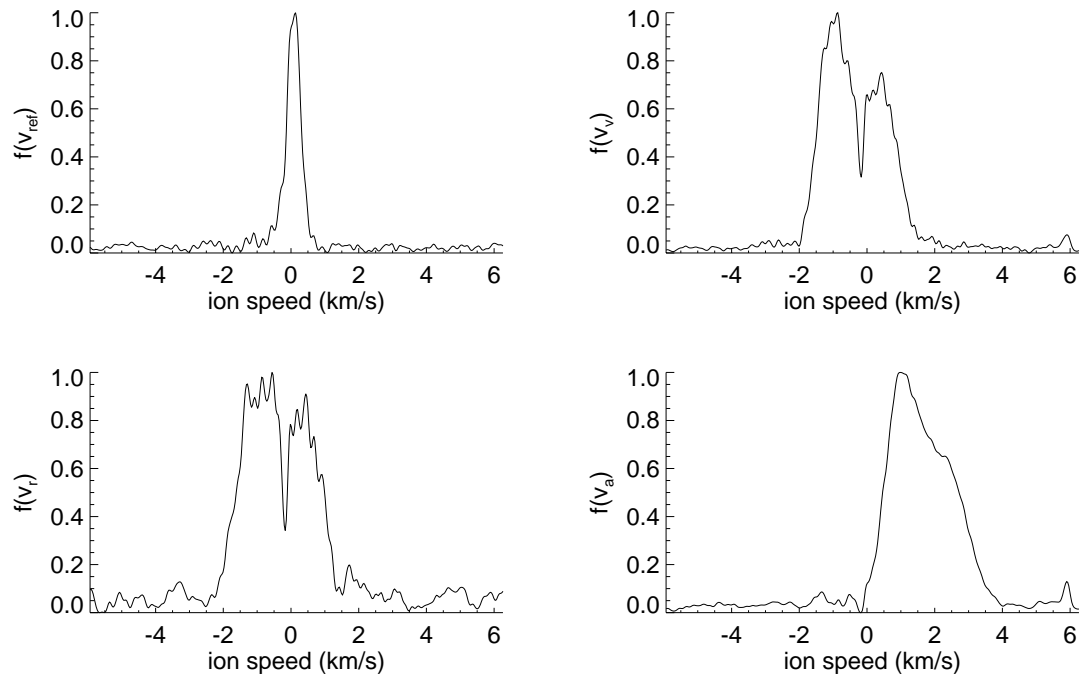


Figure B.10: Deconvolved $f(v_k)$ & curve-fit, TC 9, $(x, y) = (50.02, -2.00)$ cm (tc9e).

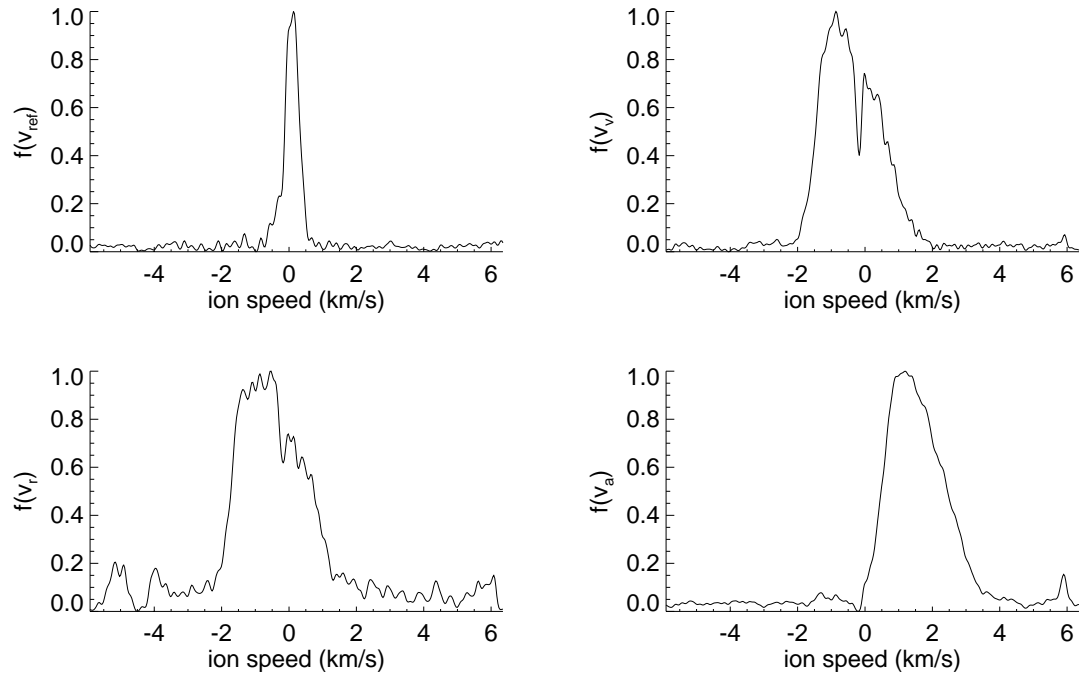


Figure B.11: Deconvolved $f(v_k)$ & curve-fit, TC 9, $(x, y) = (50.02, -5.00)$ cm (tc9f).

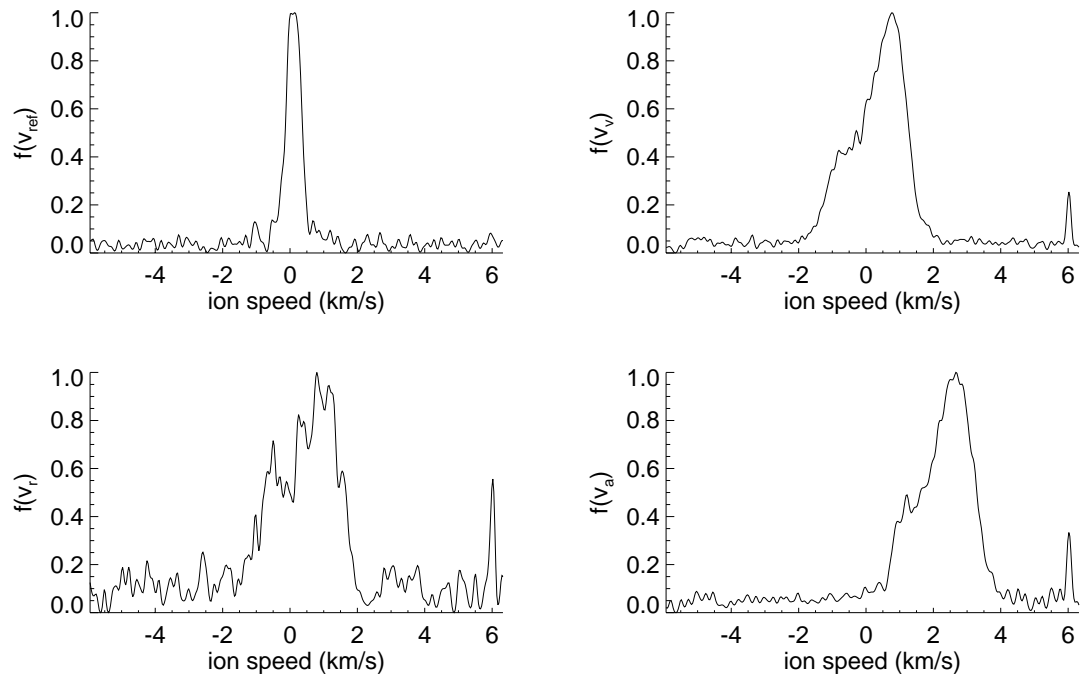


Figure B.12: Deconvolved $f(v_k)$ & curve-fit, TC 9, $(x, y) = (50.02, 5.00)$ cm (tc9g).

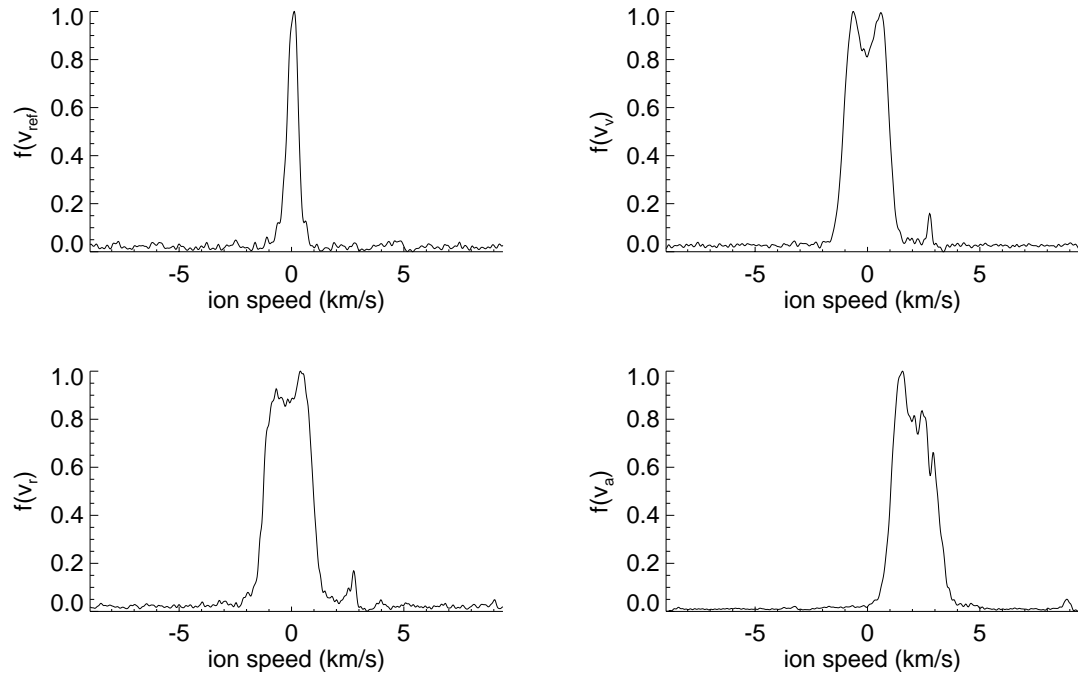


Figure B.13: Deconvolved $f(v_k)$ & curve-fit , TC 9, $(x, y) = (63.14, 0.00)$ cm (tc9h).

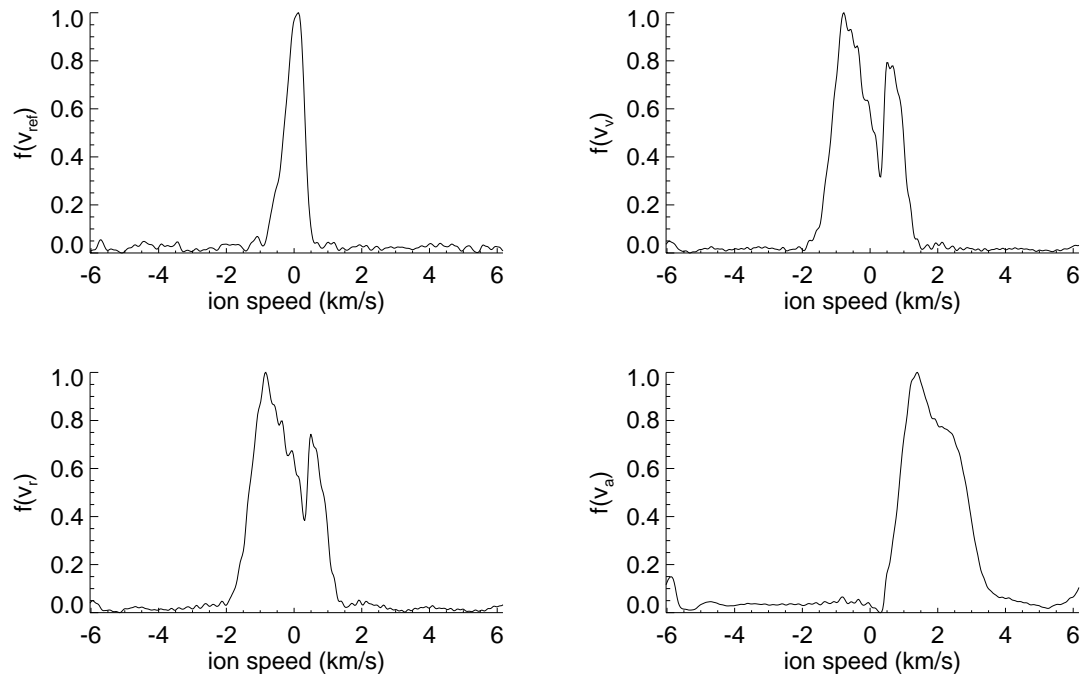


Figure B.14: Deconvolved $f(v_k)$ & curve-fit , TC 9, $(x, y) = (63.14, -1.00)$ cm (tc9i).

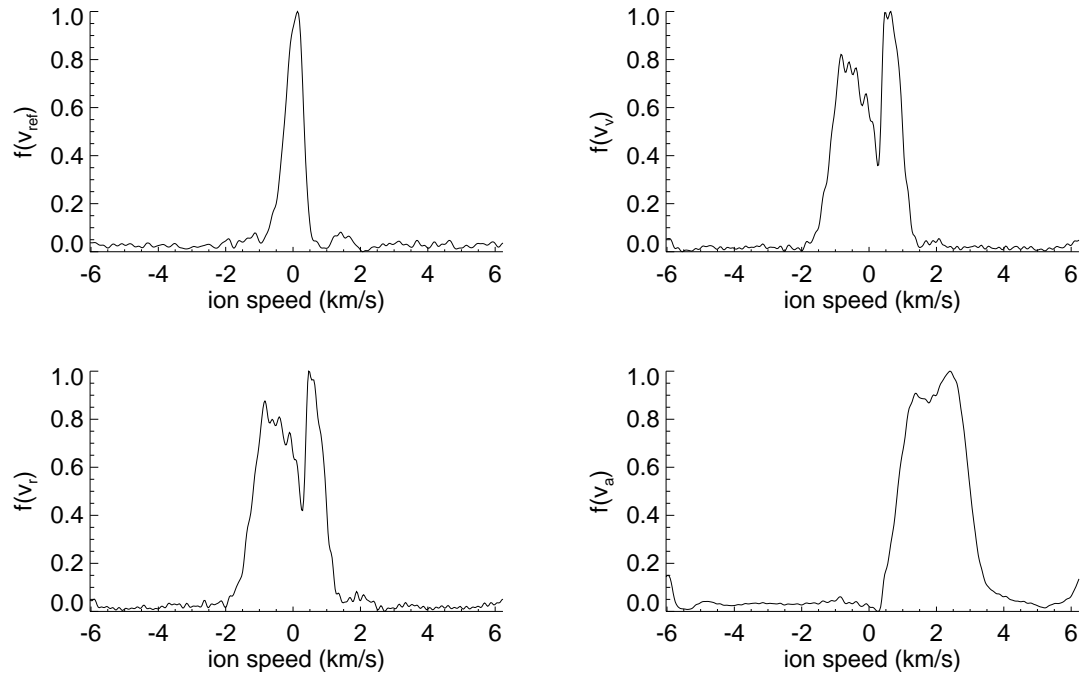


Figure B.15: Deconvolved $f(v_k)$ & curve-fit , TC 9, $(x, y) = (63.14, 1.00)$ cm (tc9j).

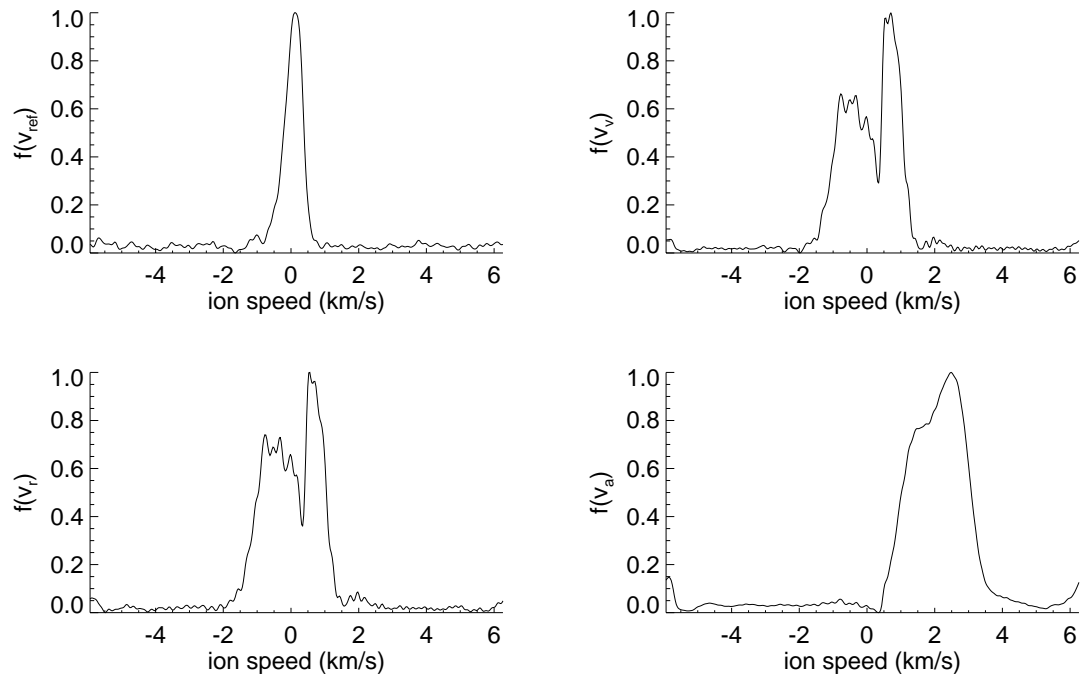


Figure B.16: Deconvolved $f(v_k)$ & curve-fit , TC 9, $(x, y) = (63.14, 2.00)$ cm (tc9k).

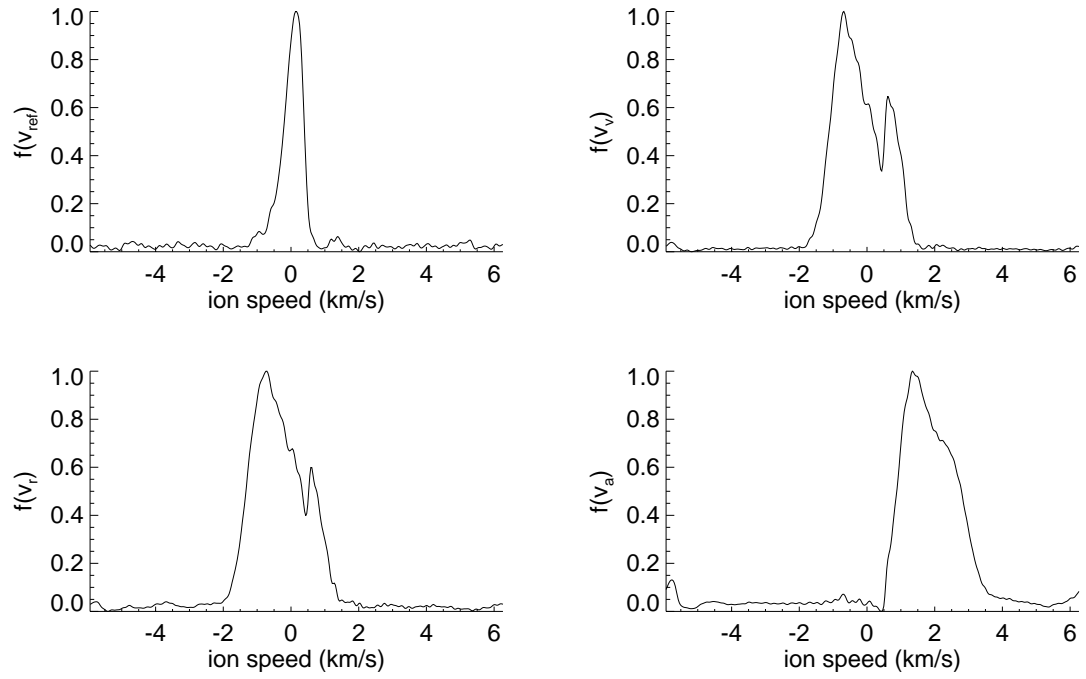


Figure B.17: Deconvolved $f(v_k)$ & curve-fit , TC 9, $(x, y) = (63.14, -2.00)$ cm (tc9l).

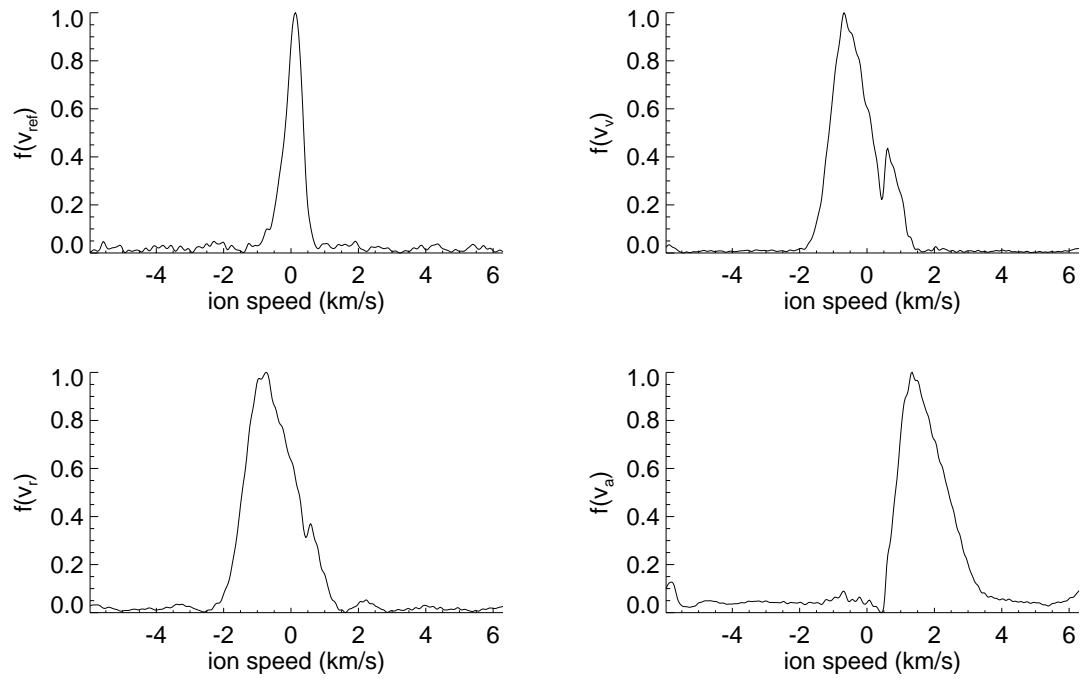


Figure B.18: Deconvolved $f(v_k)$ & curve-fit , TC 9, $(x, y) = (63.14, -5.00)$ cm (tc9m).

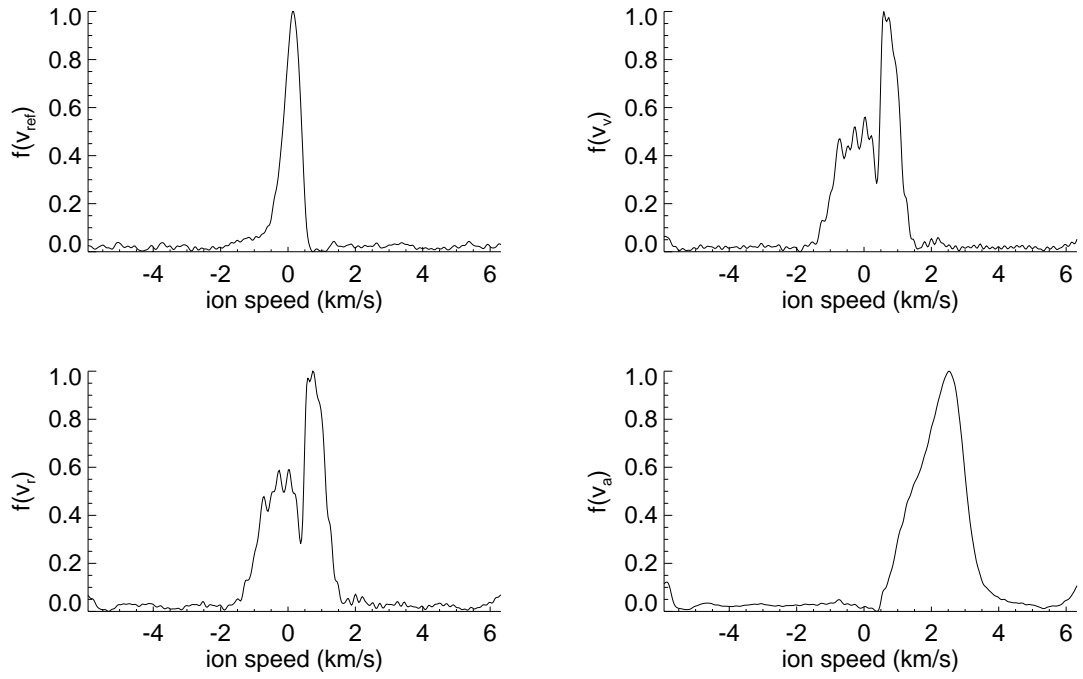


Figure B.19: Deconvolved $f(v_k)$ & curve-fit , TC 9, $(x, y) = (63.14, 5.00)$ cm (tc9n).

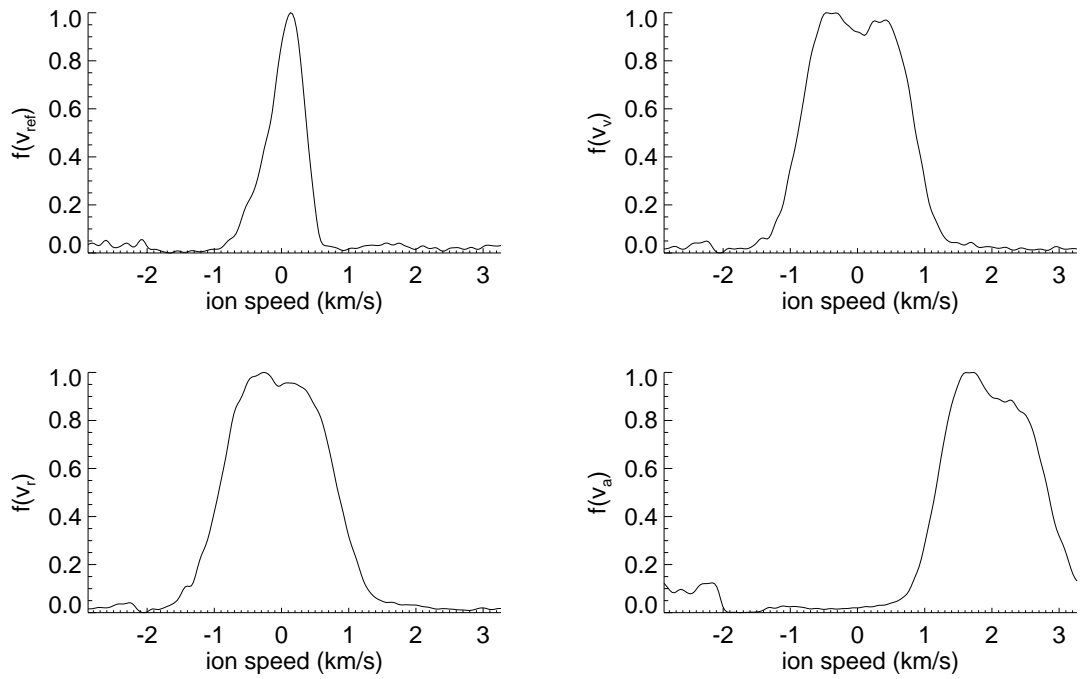


Figure B.20: Deconvolved $f(v_k)$ & curve-fit , TC 9, $(x, y) = (75.00, 0.00)$ cm (tc9o).

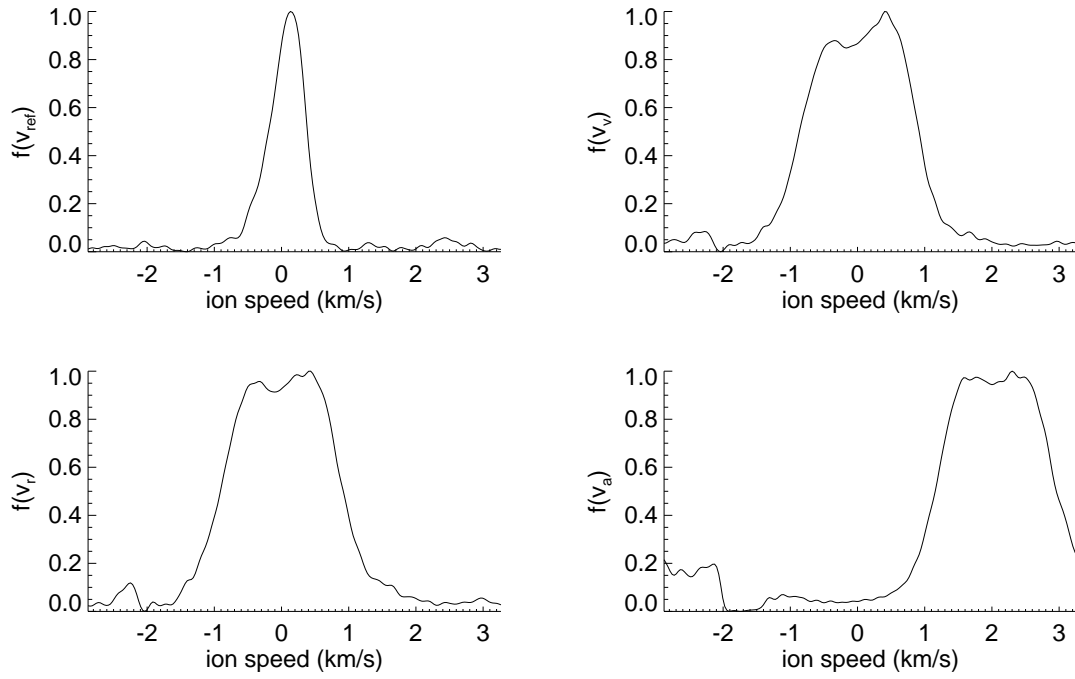


Figure B.21: Deconvolved $f(v_k)$ & curve-fit , TC 9, $(x, y) = (75.00, 1.00)$ cm (tc9p).

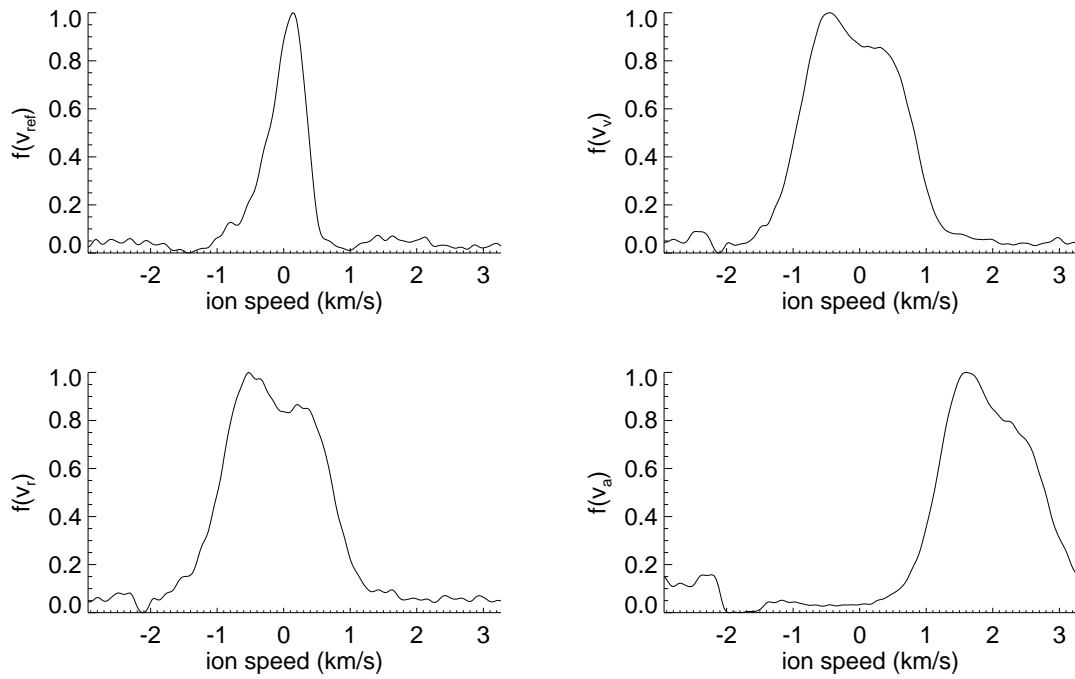


Figure B.22: Deconvolved $f(v_k)$ & curve-fit , TC 9, $(x, y) = (75.00, -1.00)$ cm (tc9q).

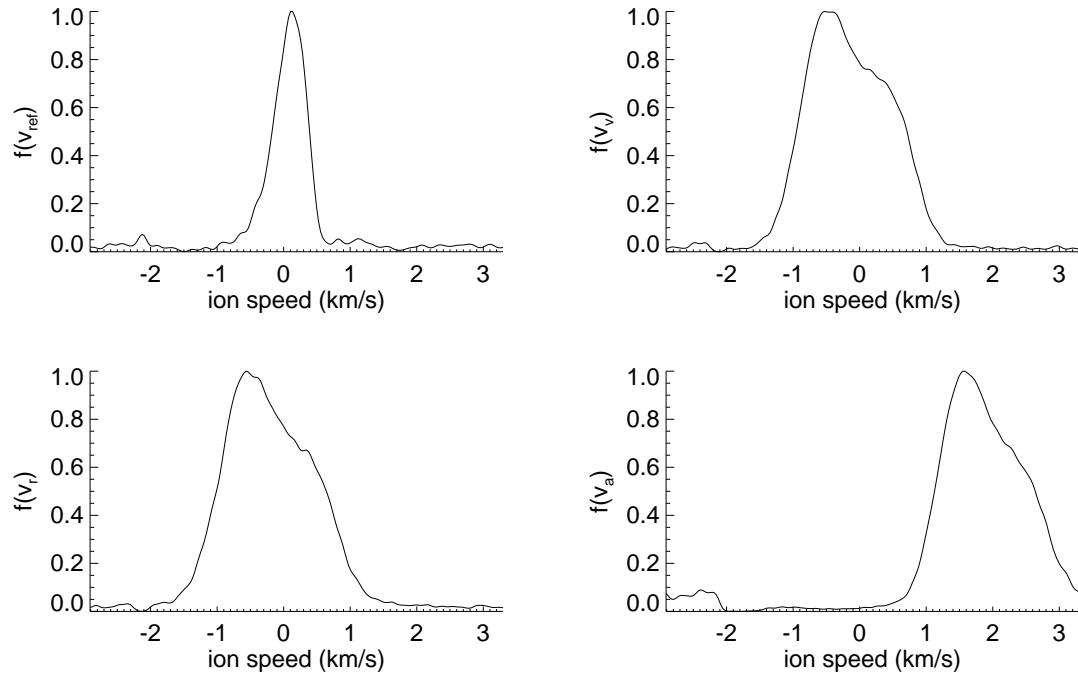


Figure B.23: Deconvolved $f(v_k)$ & curve-fit , TC 9, $(x, y) = (75.00, -2.00)$ cm (tc9r).

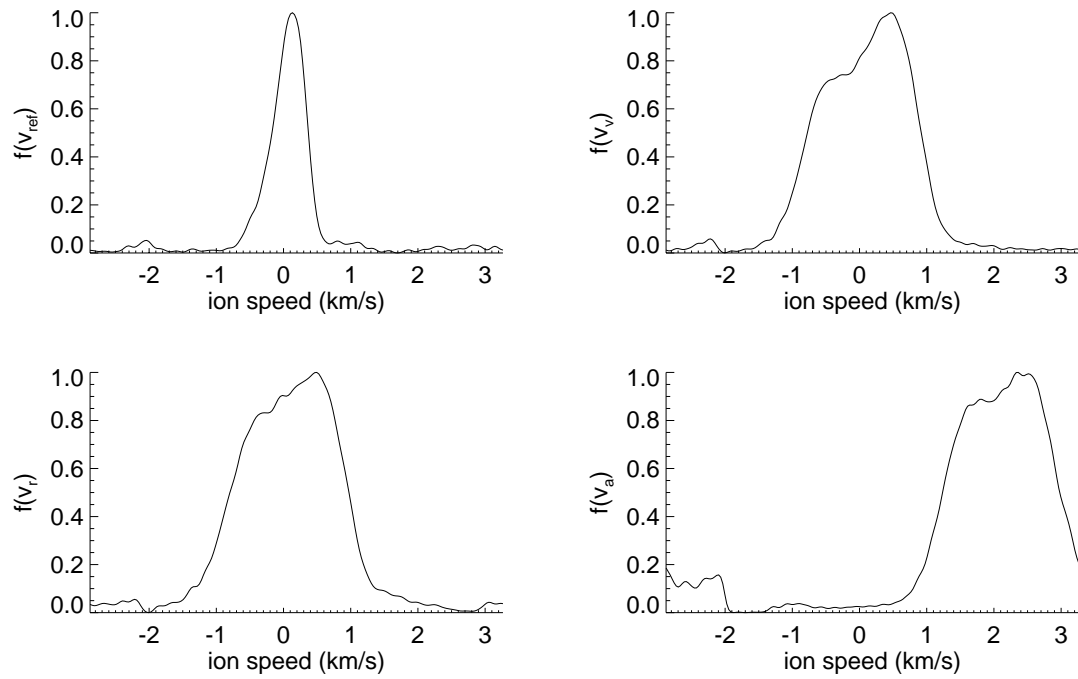


Figure B.24: Deconvolved $f(v_k)$ & curve-fit , TC 9, $(x, y) = (75.00, 2.00)$ cm (tc9s).

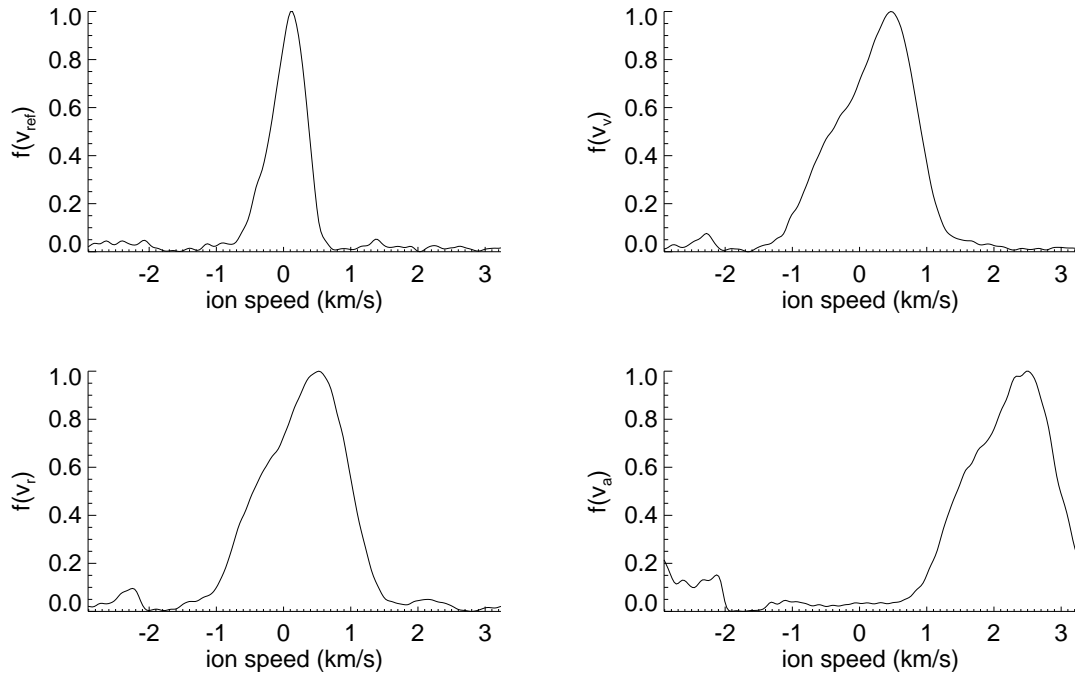


Figure B.25: Deconvolved $f(v_k)$ & curve-fit , TC 9, $(x, y) = (75.00, 5.00)$ cm (tc9t).

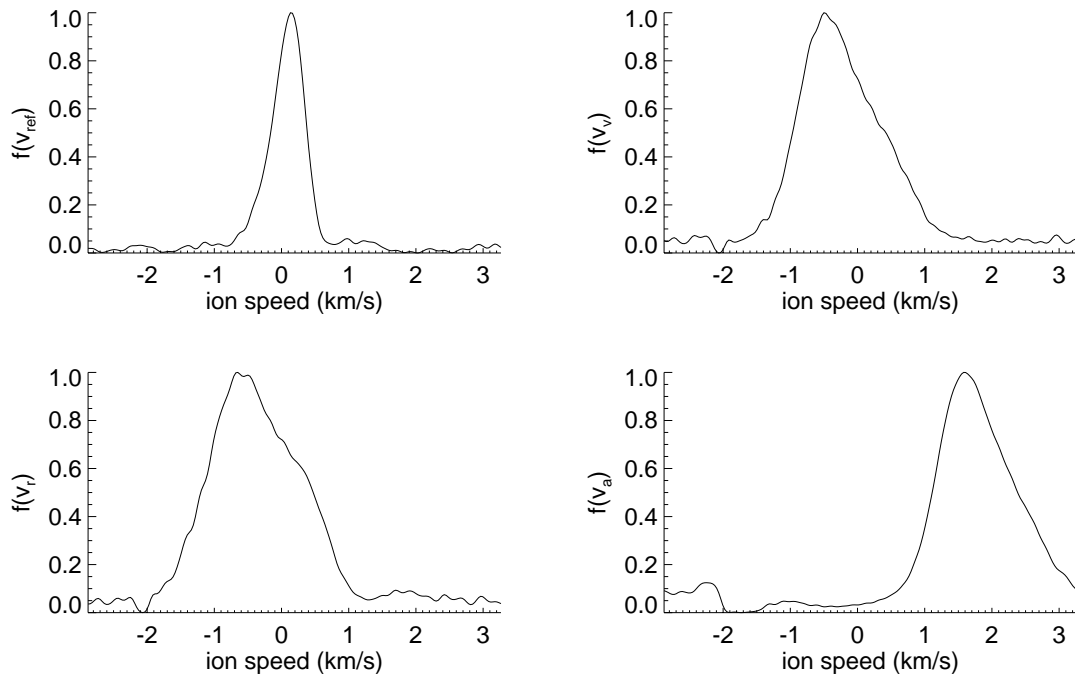


Figure B.26: Deconvolved $f(v_k)$ & curve-fit , TC 9, $(x, y) = (75.00, -5.00)$ cm (tc9u).

B.3 Test condition 10

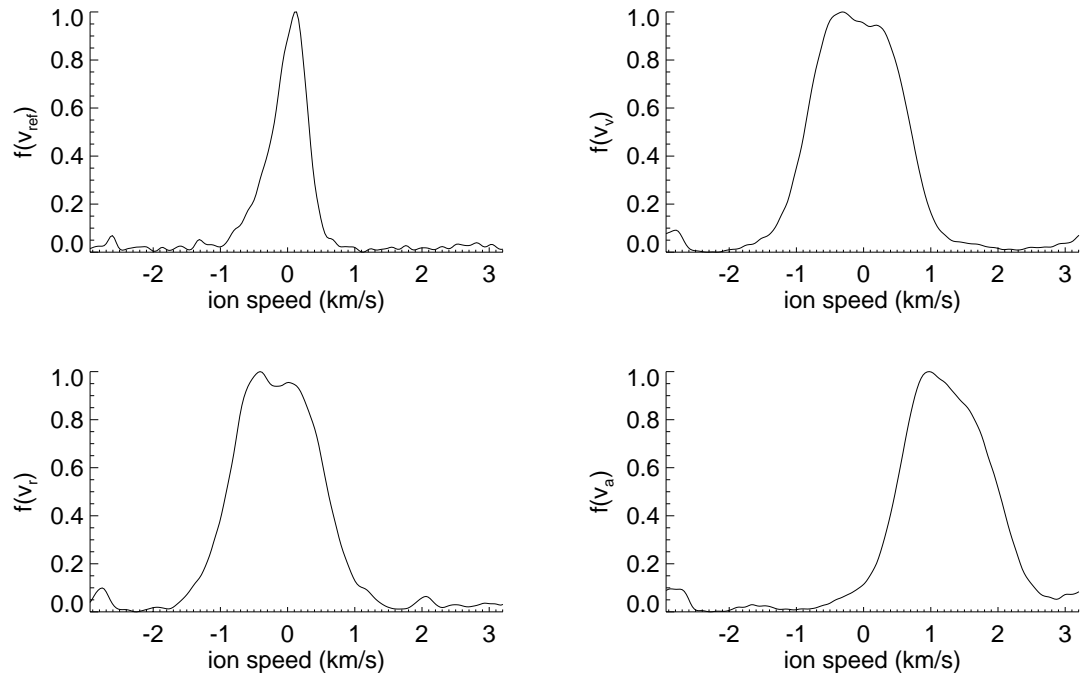


Figure B.27: Deconvolved $f(v_k)$ & curve-fit, TC 10, $(x, y) = (63.14, 0.00)$ cm (tc10a).

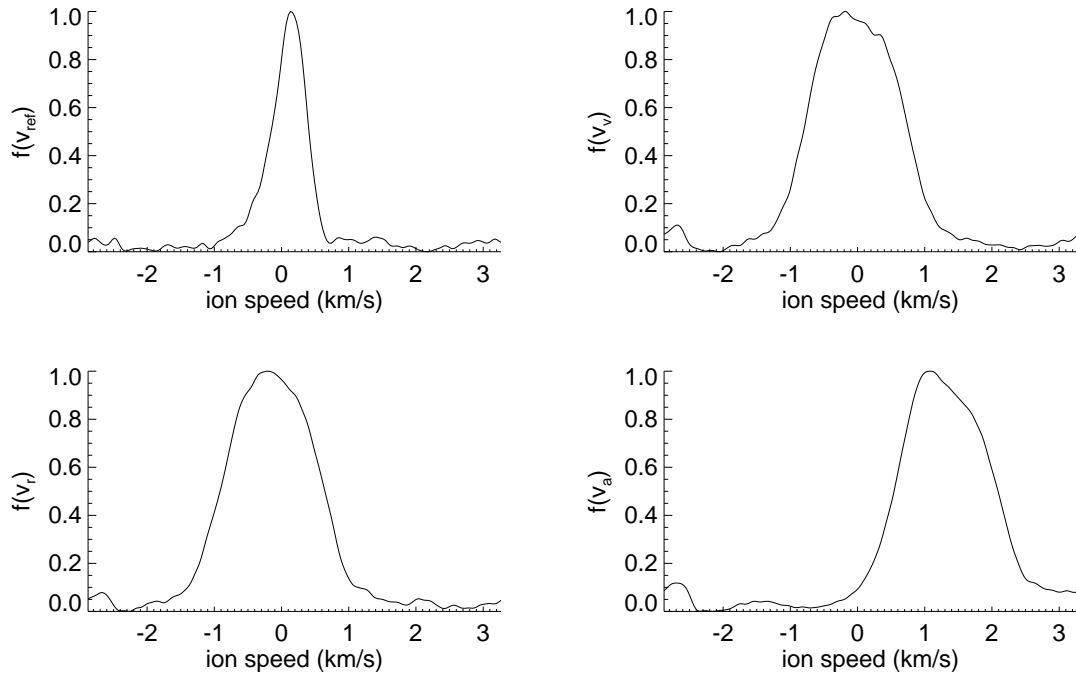


Figure B.28: Deconvolved $f(v_k)$ & fit, TC 10, $(x, y) = (63.14, -1.00)$ cm (tc10b).

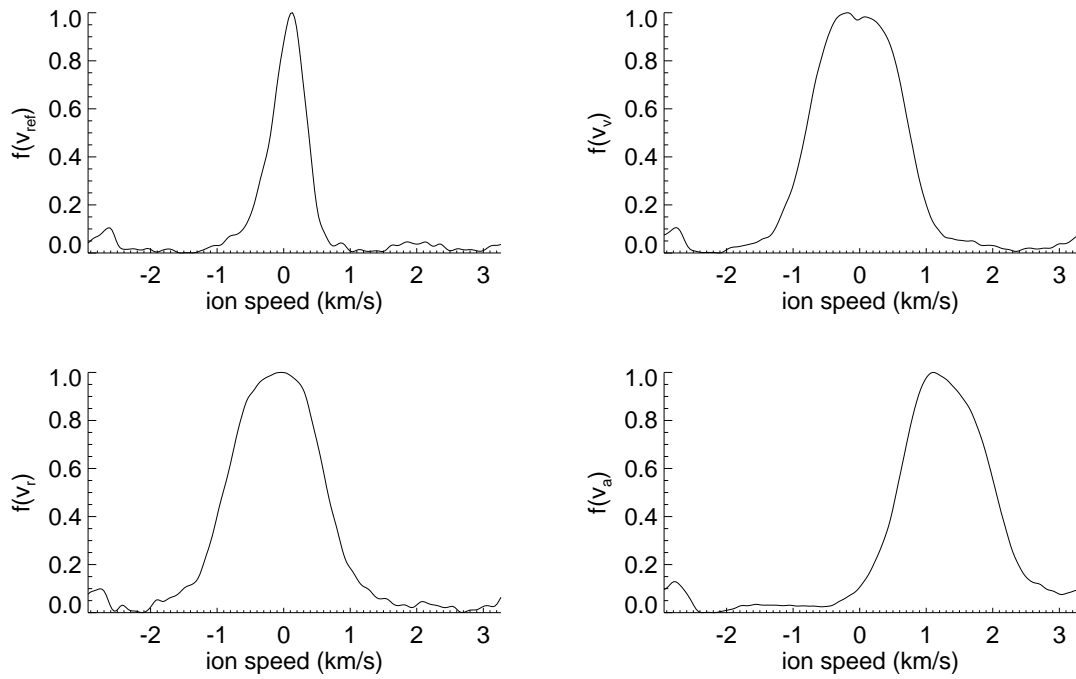


Figure B.29: Deconvolved $f(v_k)$ & curve-fit, TC 10, $(x, y) = (63.14, 1.00)$ cm (tc10c).

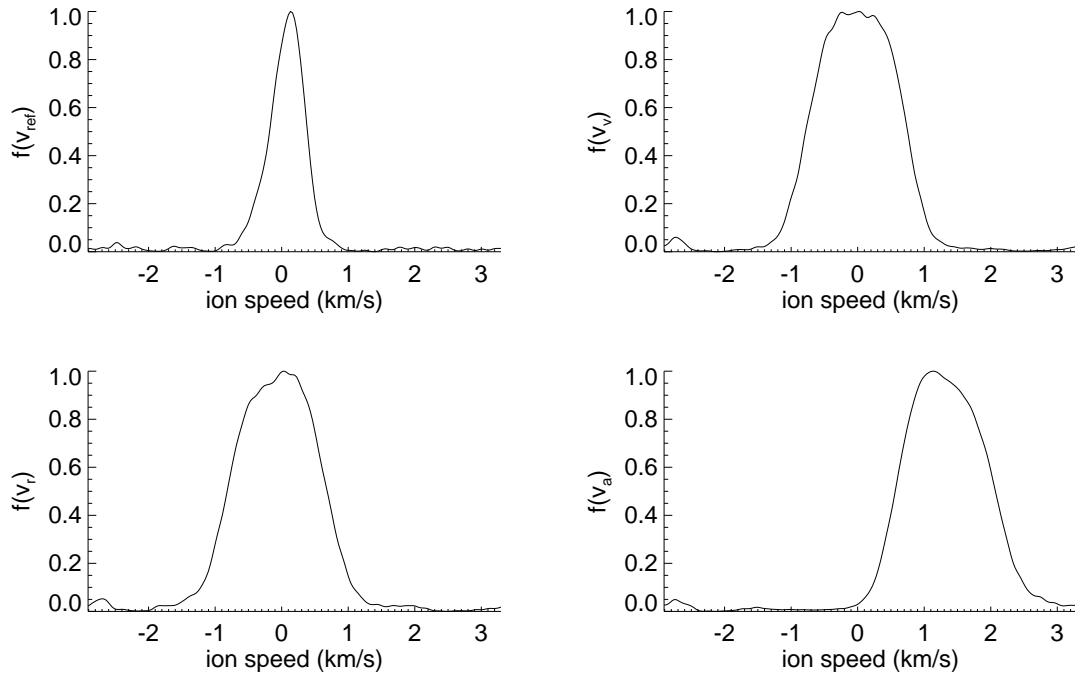


Figure B.30: Deconvolved $f(v_k)$ & curve-fit, TC 10, $(x, y) = (63.14, 2.00)$ cm (tc10d).

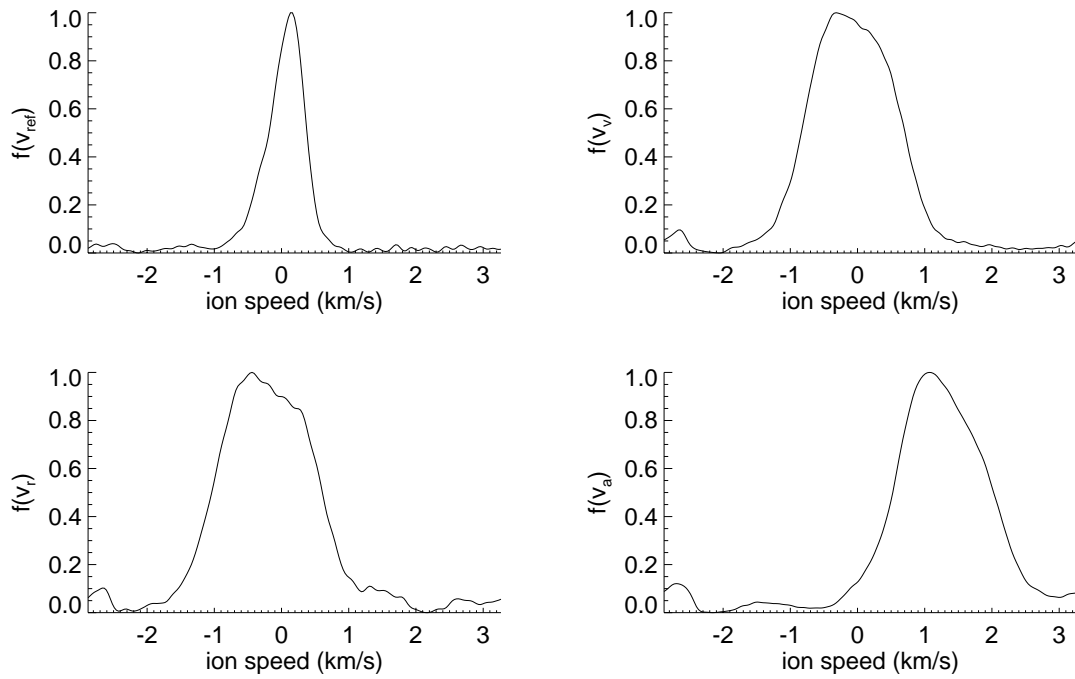


Figure B.31: Deconvolved $f(v_k)$ & fit, TC 10, $(x, y) = (63.14, -2.00)$ cm (tc10e).

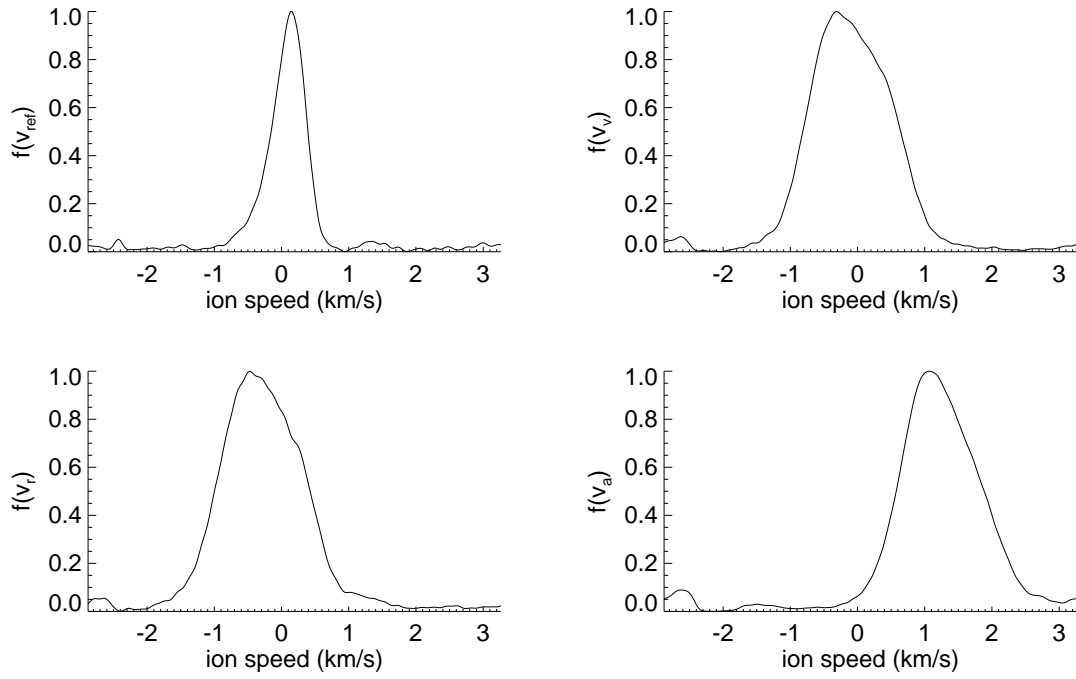


Figure B.32: Deconvolved $f(v_k)$ & fit, TC 10, $(x, y) = (63.14, -5.00)$ cm (tc10f).

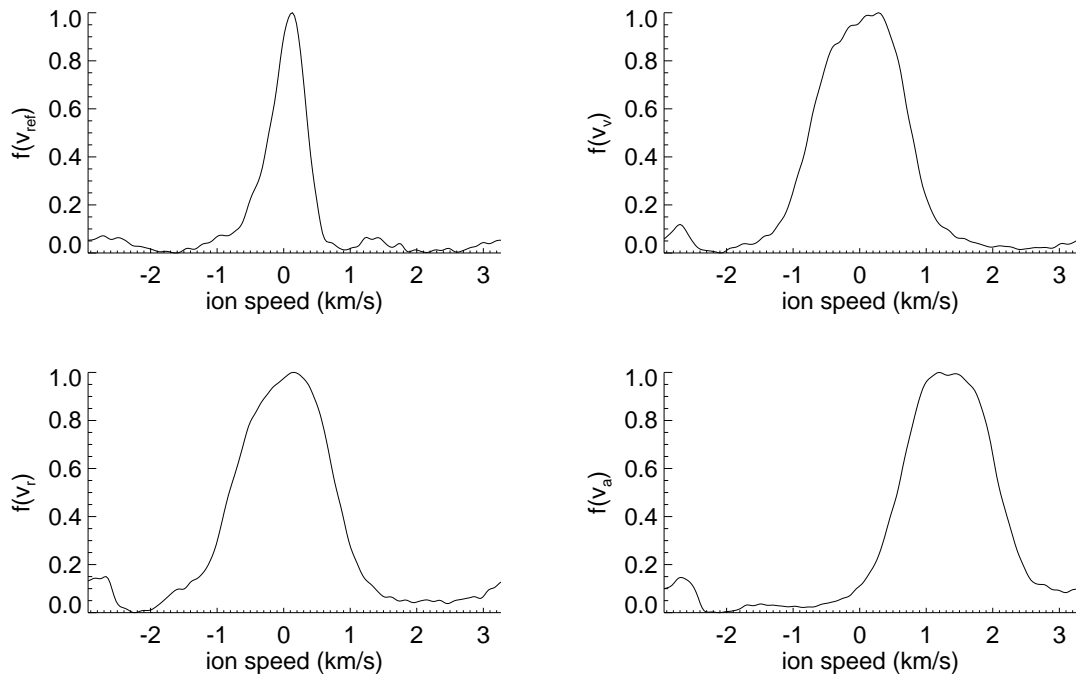


Figure B.33: Deconvolved $f(v_k)$ & curve-fit, TC 10, $(x, y) = (63.14, 5.00)$ cm (tc10g).

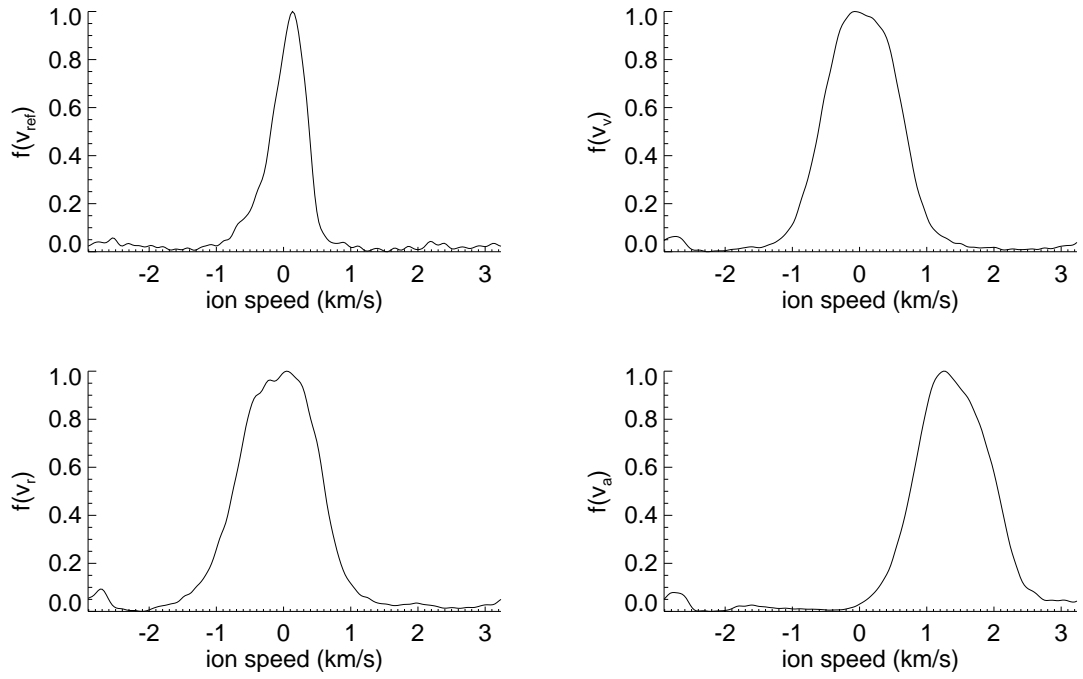


Figure B.34: Deconvolved $f(v_k)$ & curve-fit, TC 10, $(x, y) = (75.00, 0.00)$ cm (tc10h).

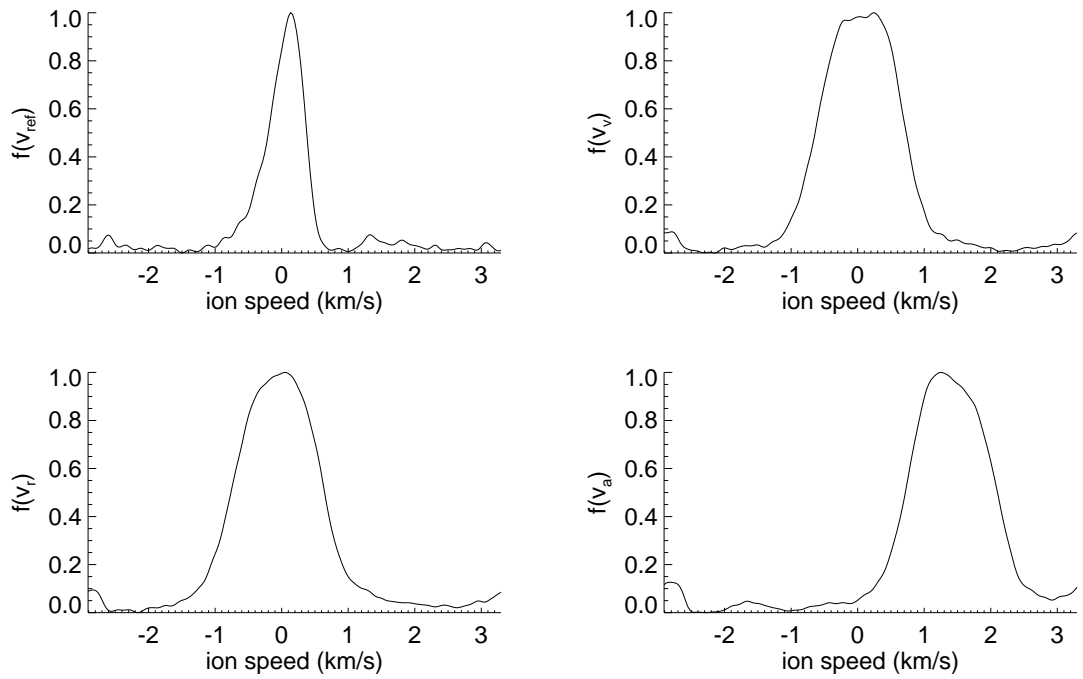


Figure B.35: Deconvolved $f(v_k)$ & curve-fit, TC 10, $(x, y) = (75.00, 1.00)$ cm (tc10i).

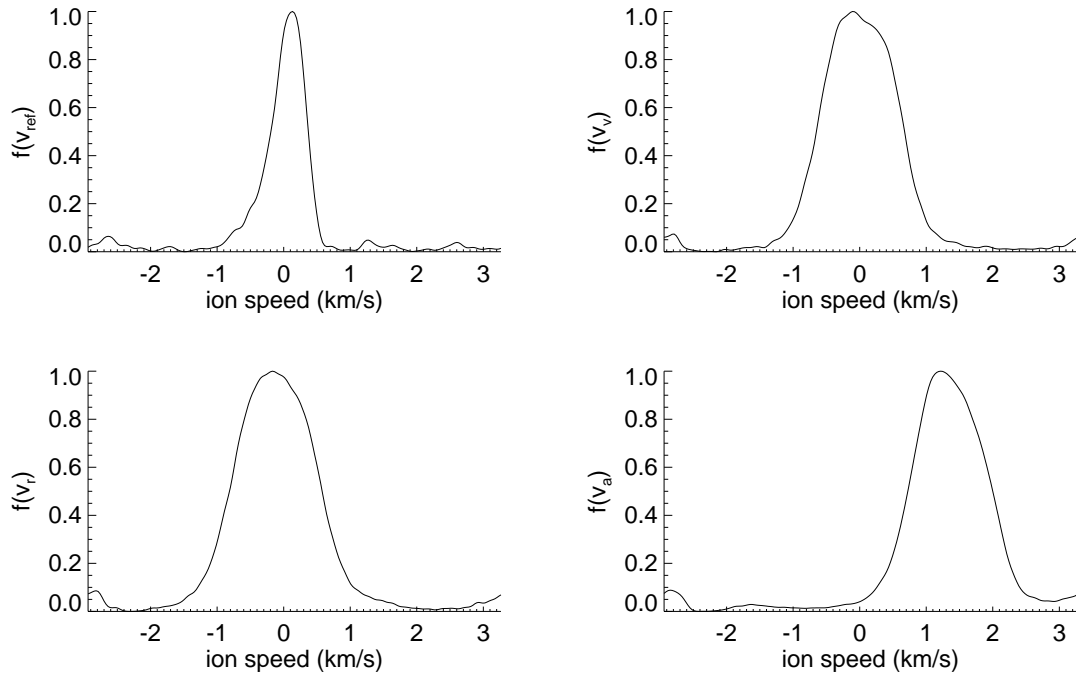


Figure B.36: Deconvolved $f(v_k)$ & fit, TC 10, $(x, y) = (75.00, -1.00)$ cm (tc10j).

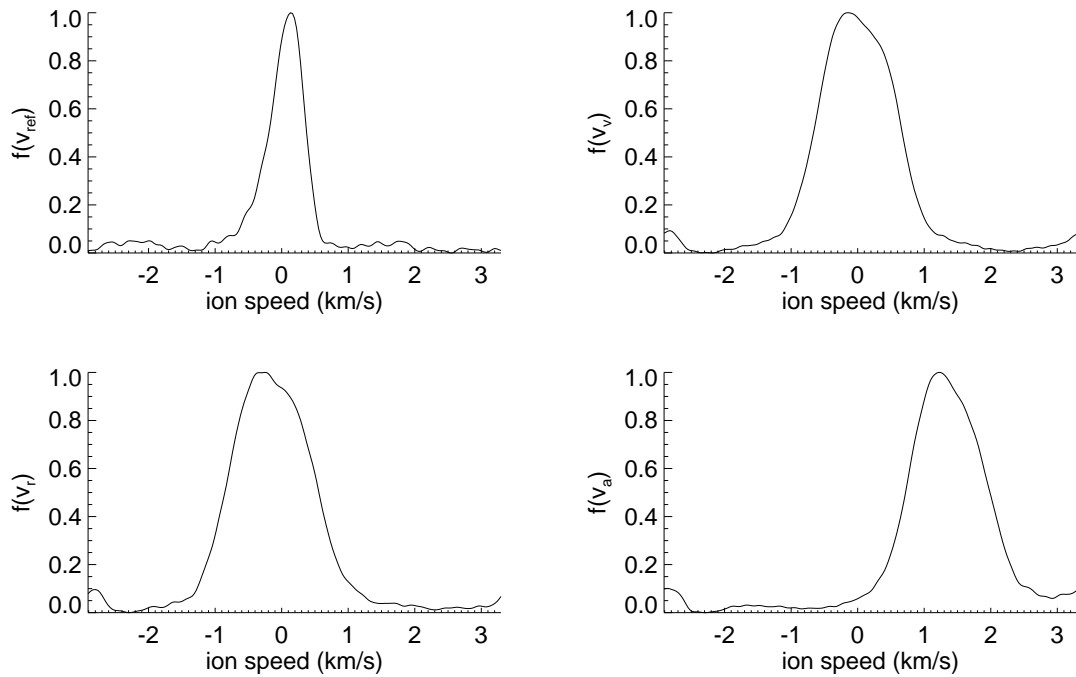


Figure B.37: Deconvolved $f(v_k)$ & fit, TC 10, $(x, y) = (75.00, -2.00)$ cm (tc10k).

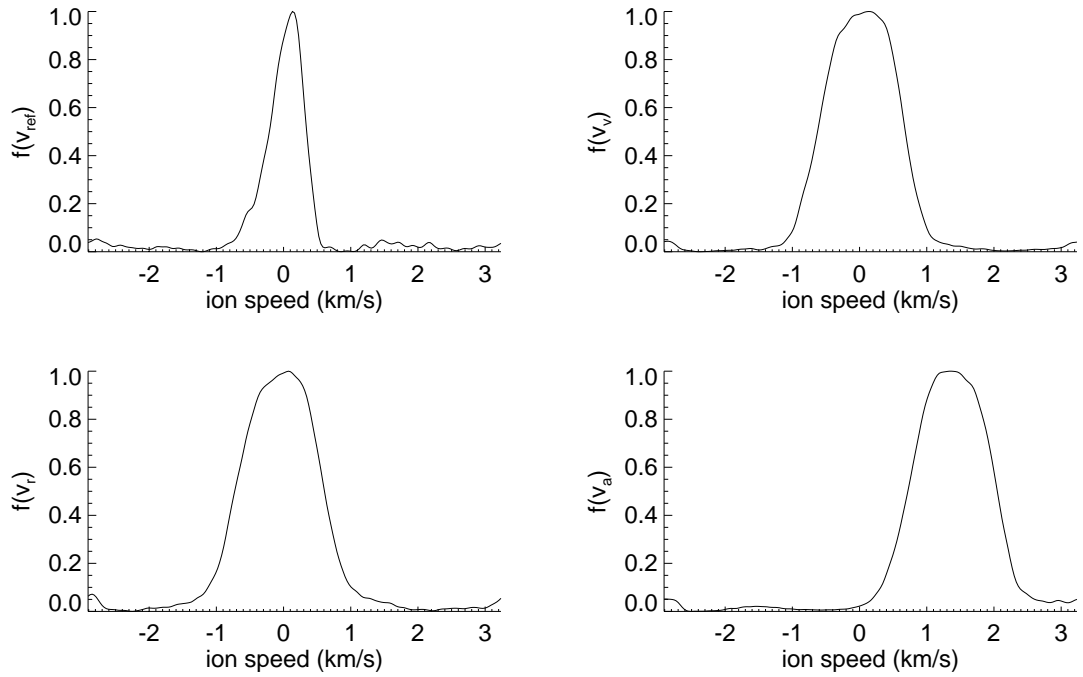


Figure B.38: Deconvolved $f(v_k)$ & curve-fit, TC 10, $(x, y) = (75.00, 2.00)$ cm (tc10l).

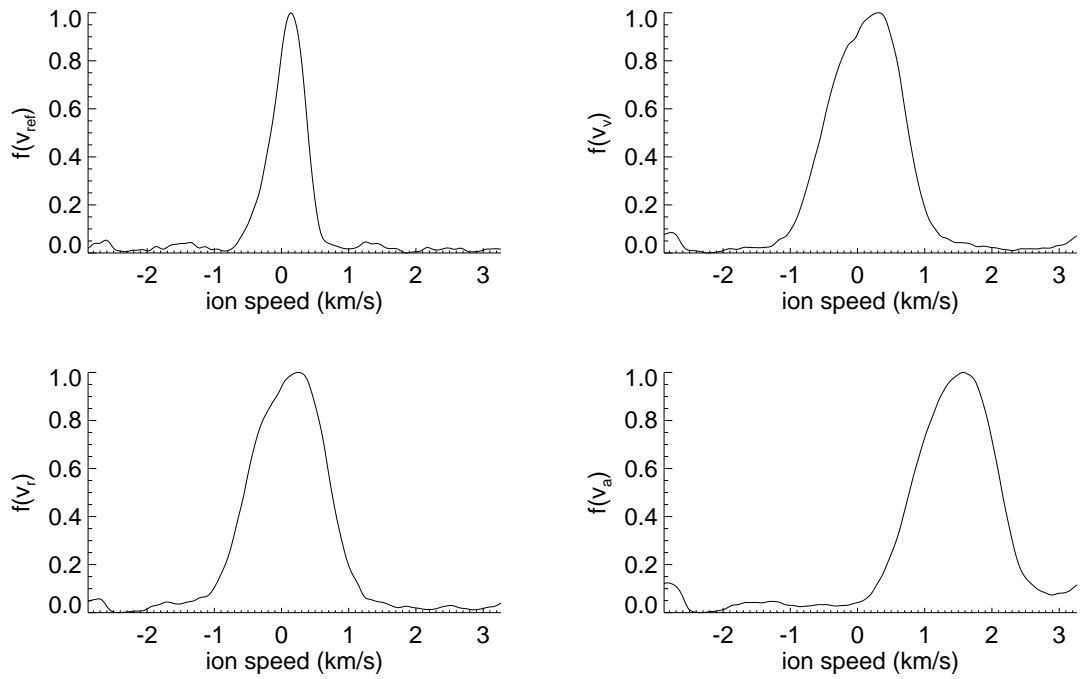


Figure B.39: Deconvolved $f(v_k)$ & curve-fit, TC 10, $(x, y) = (75.00, 5.00)$ cm (tc10m).

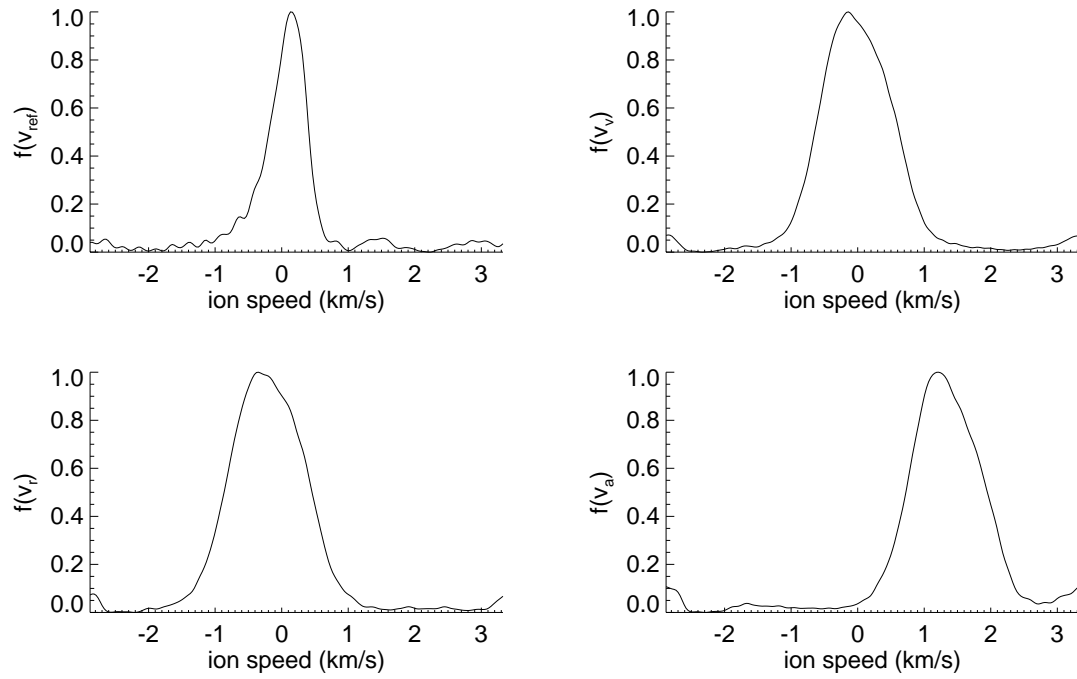


Figure B.40: Deconvolved $f(v_k)$ & curve-fit, TC 10, $(x, y) = (75.00, -5.00)$ cm (tc10n).

B.4 Test condition 1

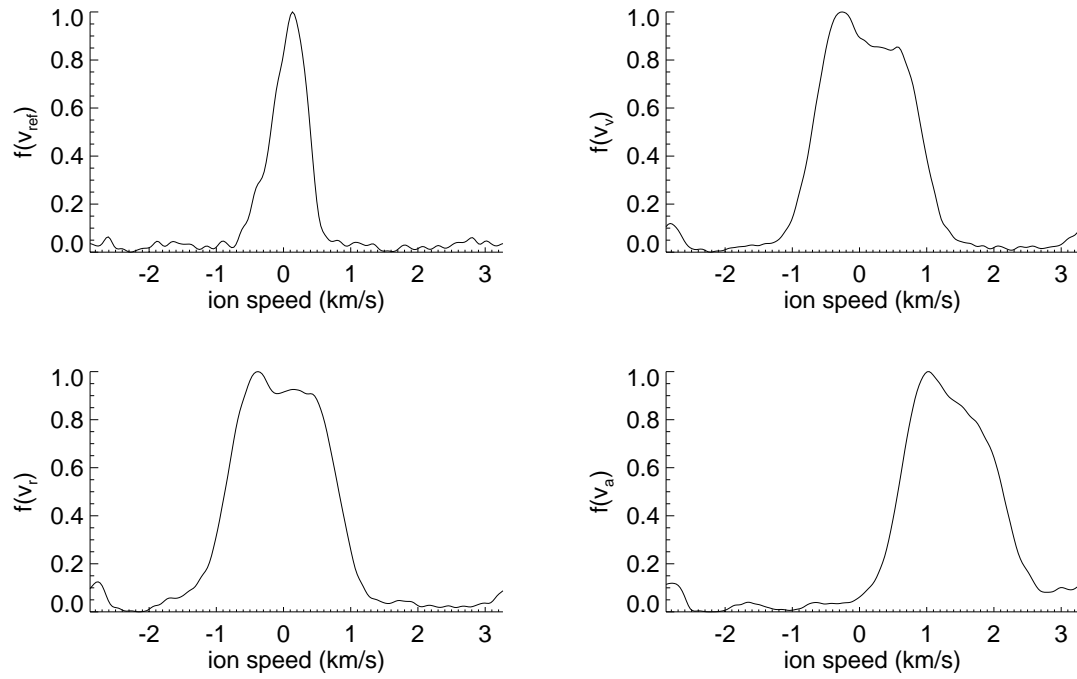


Figure B.41: Deconvolved $f(v_k)$ & curve-fit at TC 1, $(x, y) = (63.14, 0.00)$ cm (tc01a).

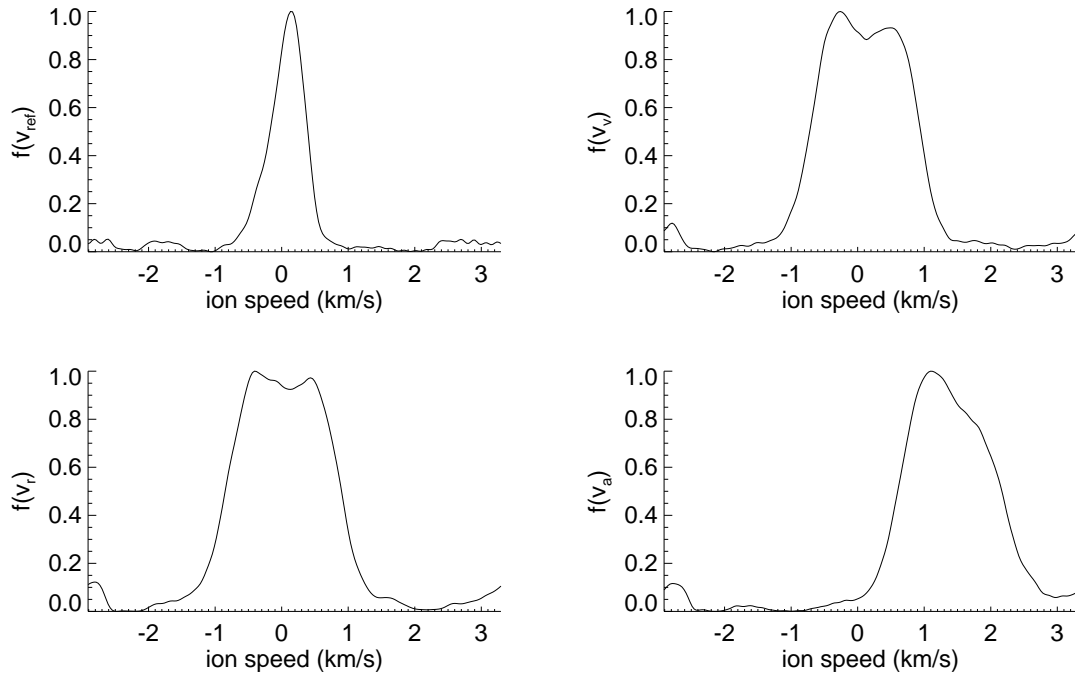


Figure B.42: Deconvolved $f(v_k)$ & fit at TC 1, $(x, y) = (63.14, -1.00)$ cm (tc01b).

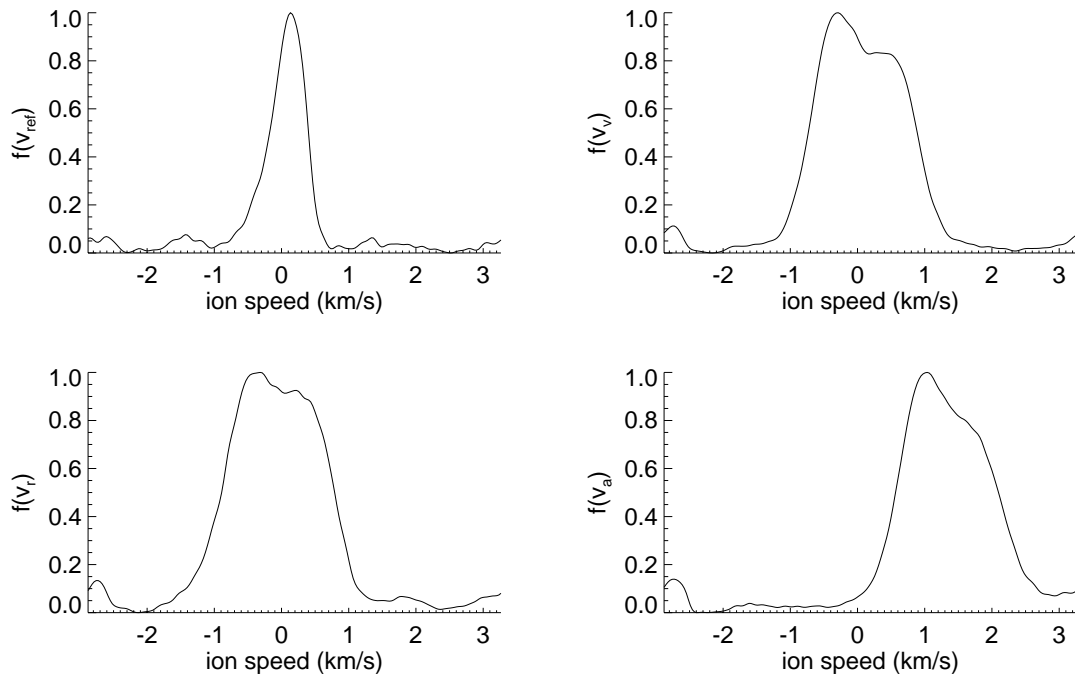


Figure B.43: Deconvolved $f(v_k)$ & curve-fit at TC 1, $(x, y) = (63.14, 1.00)$ cm (tc01c).

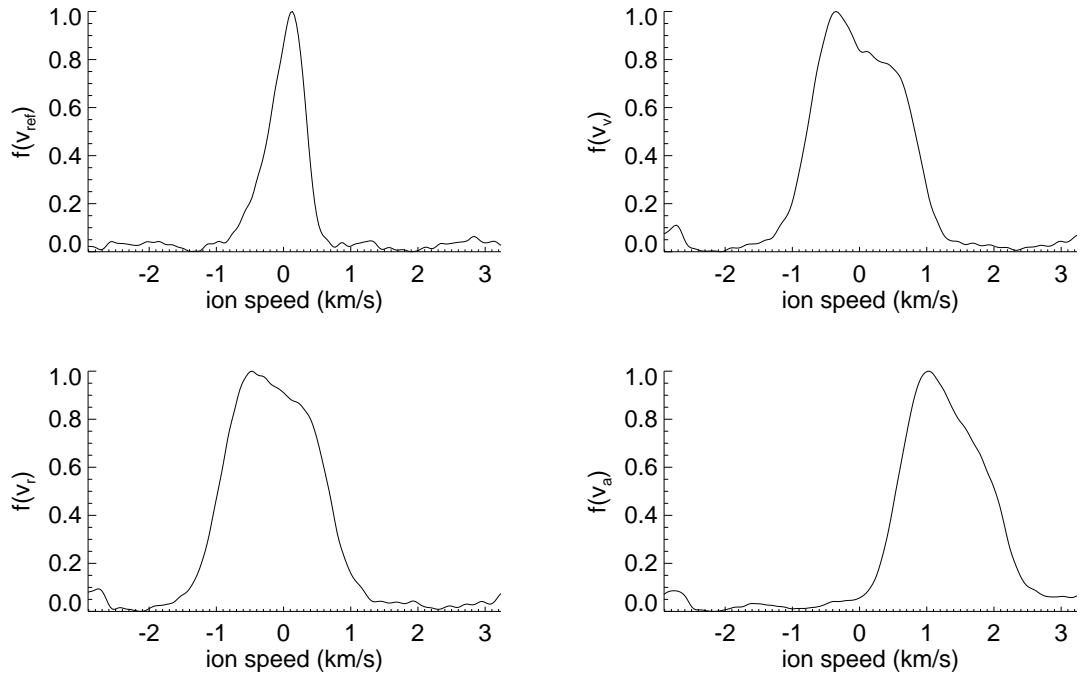


Figure B.44: Deconvolved $f(v_k)$ & curve-fit at TC 1, $(x, y) = (63.14, 2.00)$ cm (tc01d).

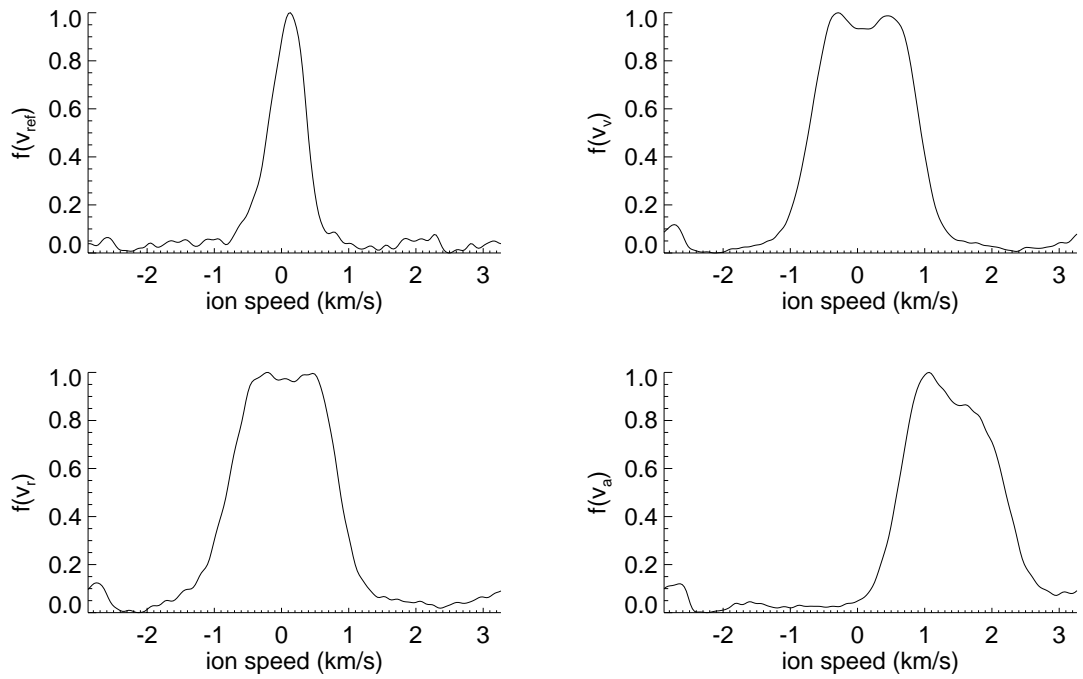


Figure B.45: Deconvolved $f(v_k)$ & fit at TC 1, $(x, y) = (63.14, -2.00)$ cm (tc01e).

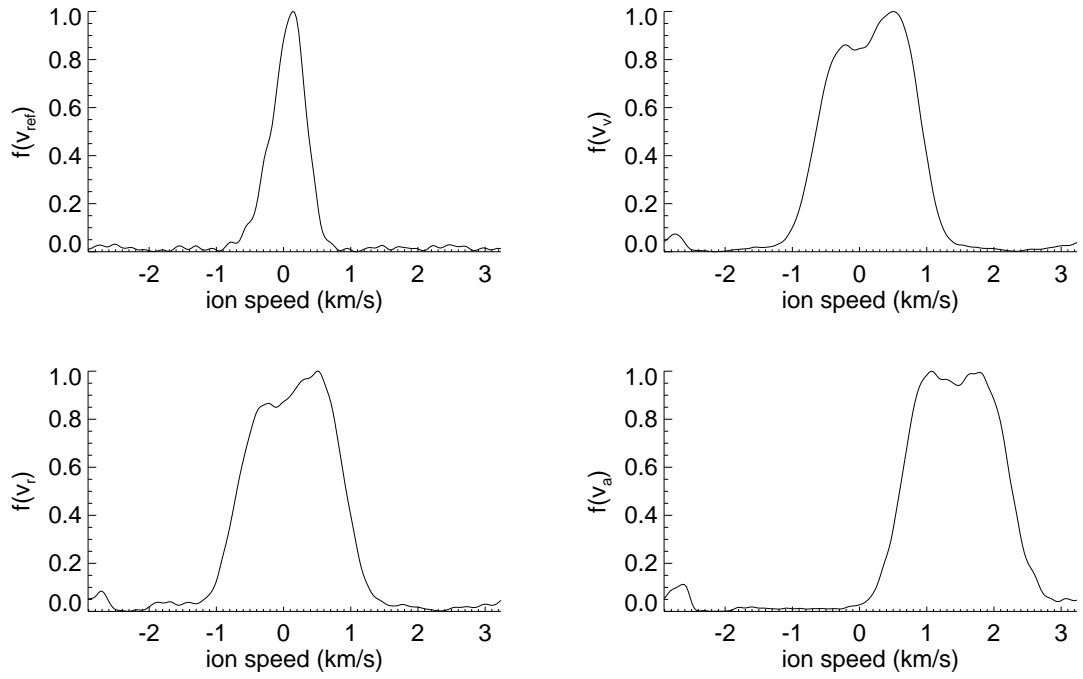


Figure B.46: Deconvolved $f(v_k)$ & fit at TC 1, $(x, y) = (63.14, -5.00)$ cm (tc01f).

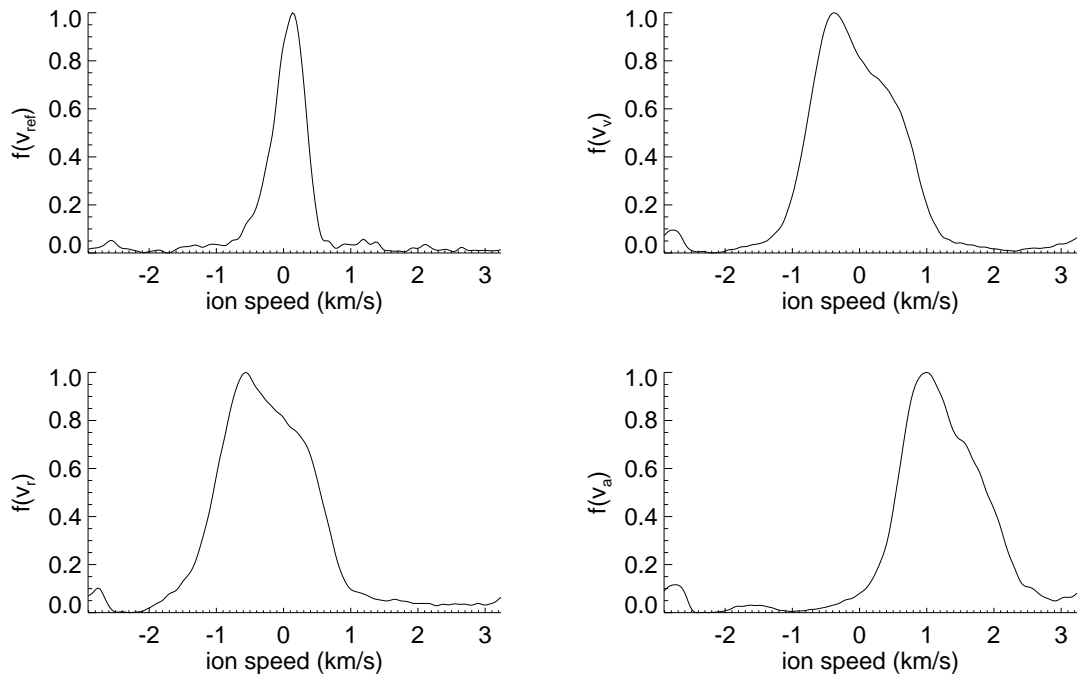


Figure B.47: Deconvolved $f(v_k)$ & curve-fit at TC 1, $(x, y) = (63.14, 5.00)$ cm (tc01g).

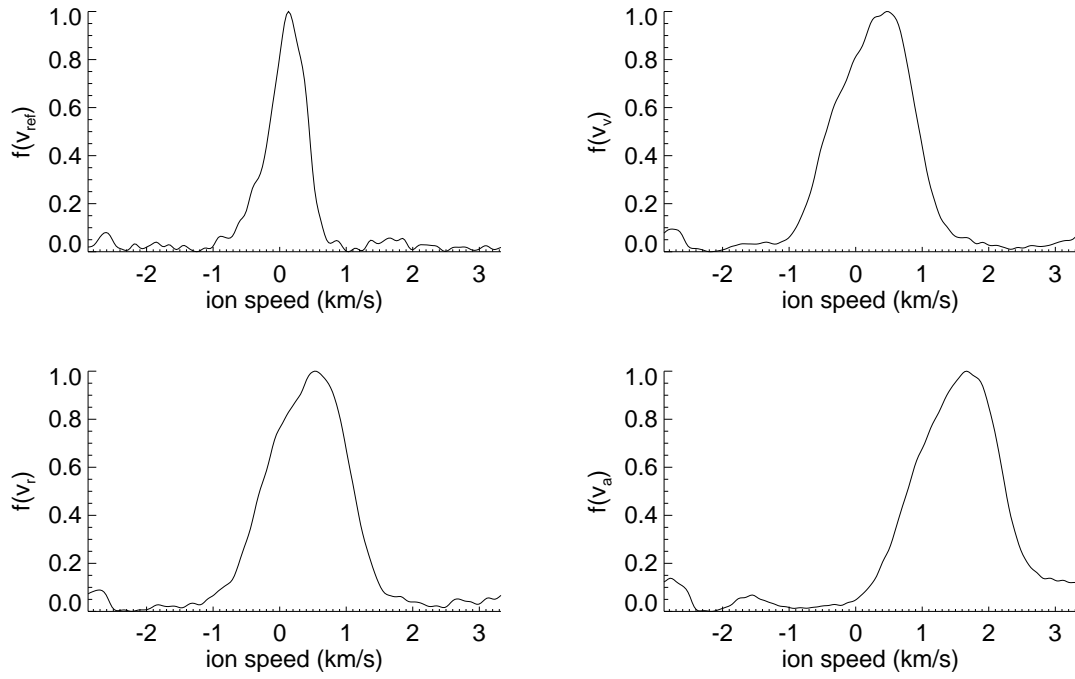


Figure B.48: Deconvolved $f(v_k)$ & fit at TC 1, $(x, y) = (63.14, 15.00)$ cm (tc01h).

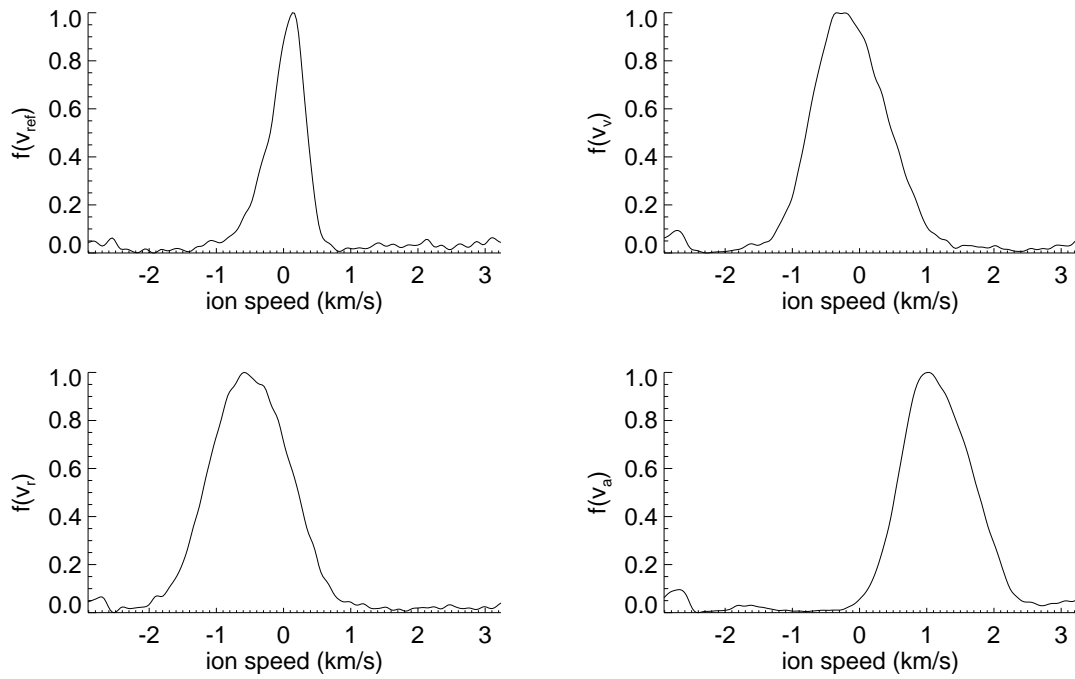


Figure B.49: Deconvolved $f(v_k)$ & fit at TC 1, $(x, y) = (63.14, -15.00)$ cm (tc01i).

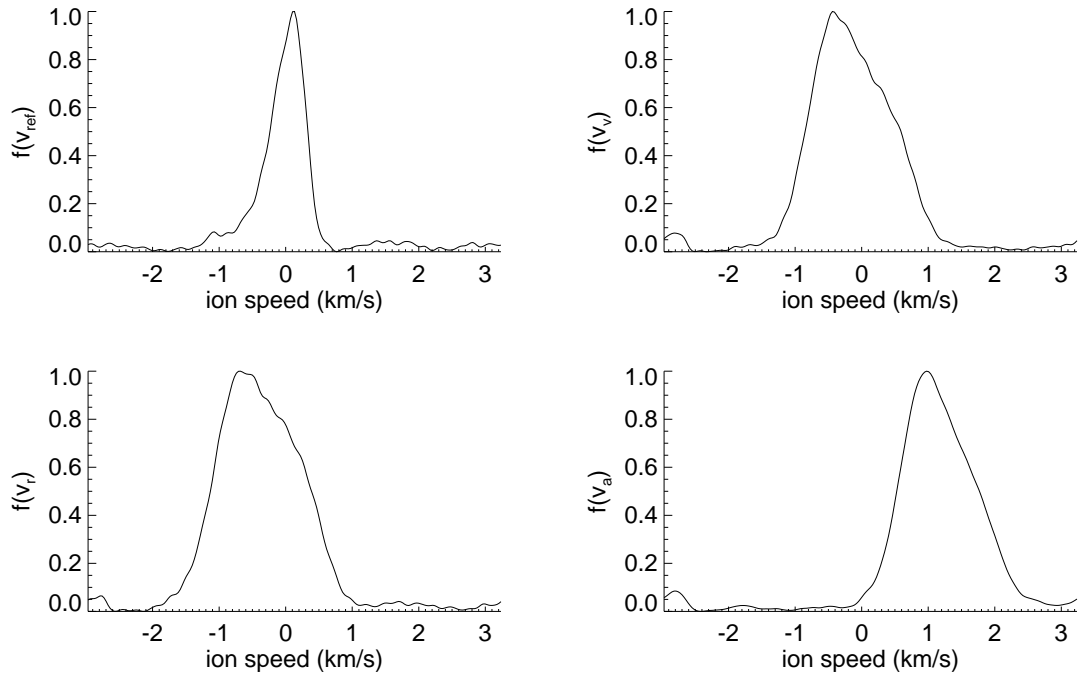


Figure B.50: Deconvolved $f(v_k)$ & fit at TC 1, $(x, y) = (63.14, -7.50)$ cm (tc01j).

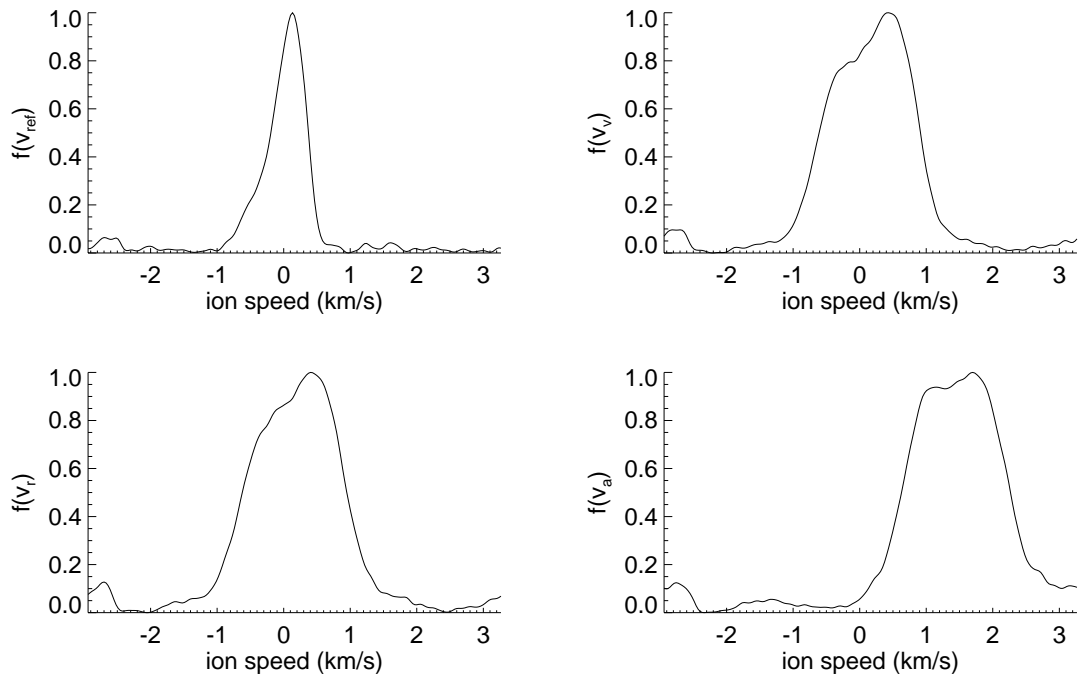


Figure B.51: Deconvolved $f(v_k)$ & curve-fit at TC 1, $(x, y) = (63.14, 7.50)$ cm (tc01k).

B.5 Test condition 2

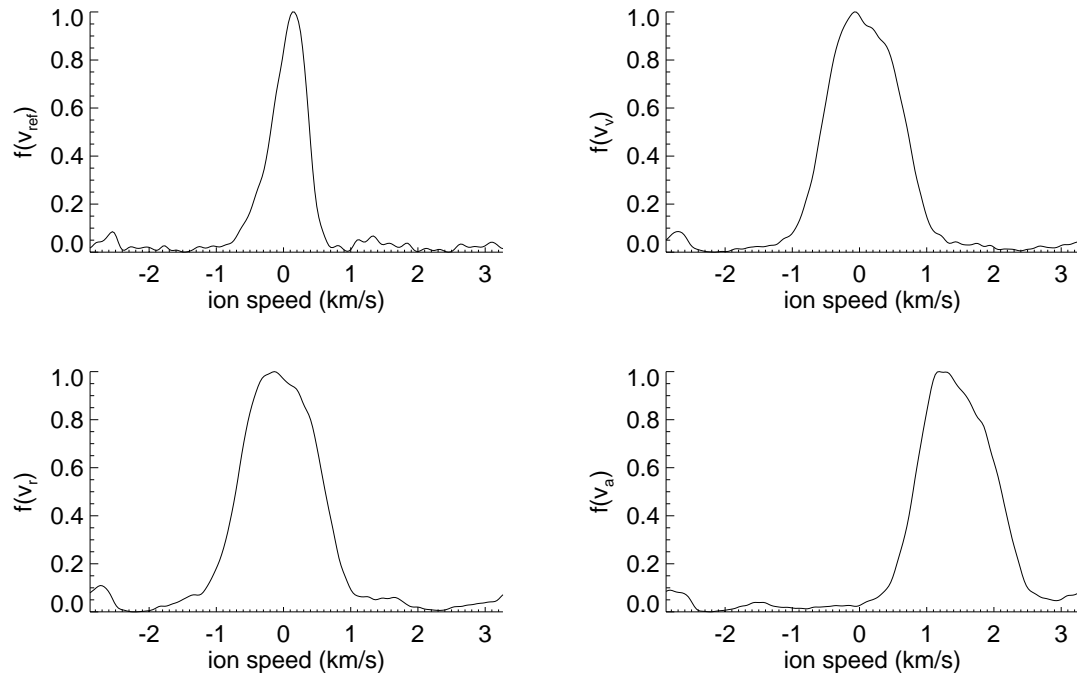


Figure B.52: Deconvolved $f(v_k)$ & curve-fit at TC 2, $(x, y) = (63.14, 0.00)$ cm (tc02a).

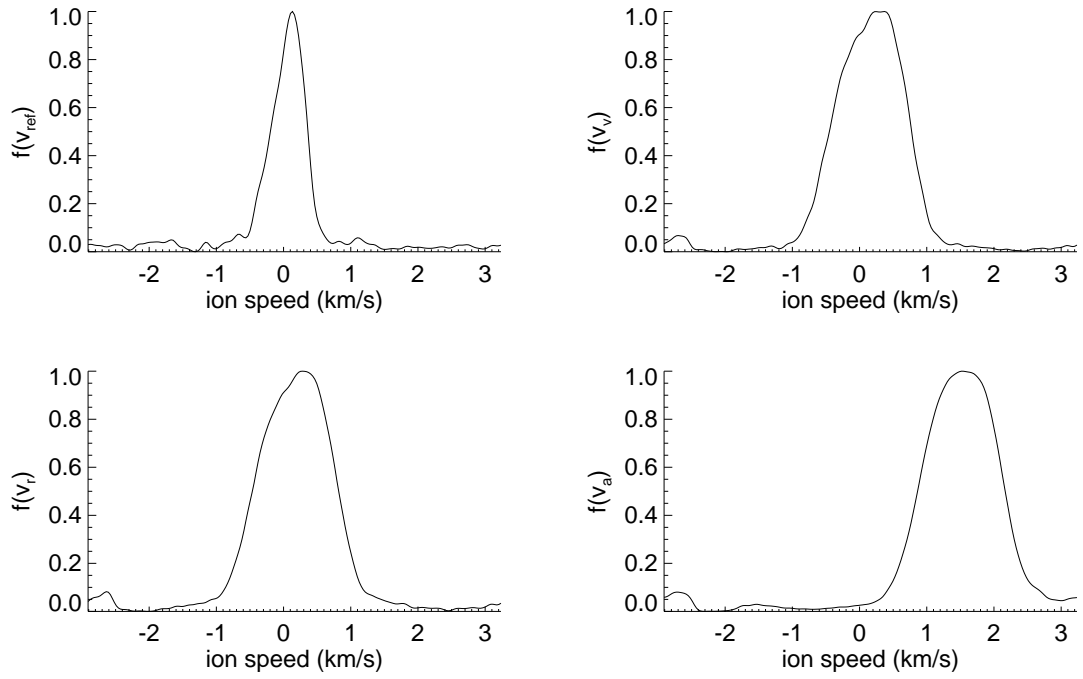


Figure B.53: Deconvolved $f(v_k)$ & curve-fit at TC 2, $(x, y) = (63.14, 7.50)$ cm (tc02b).

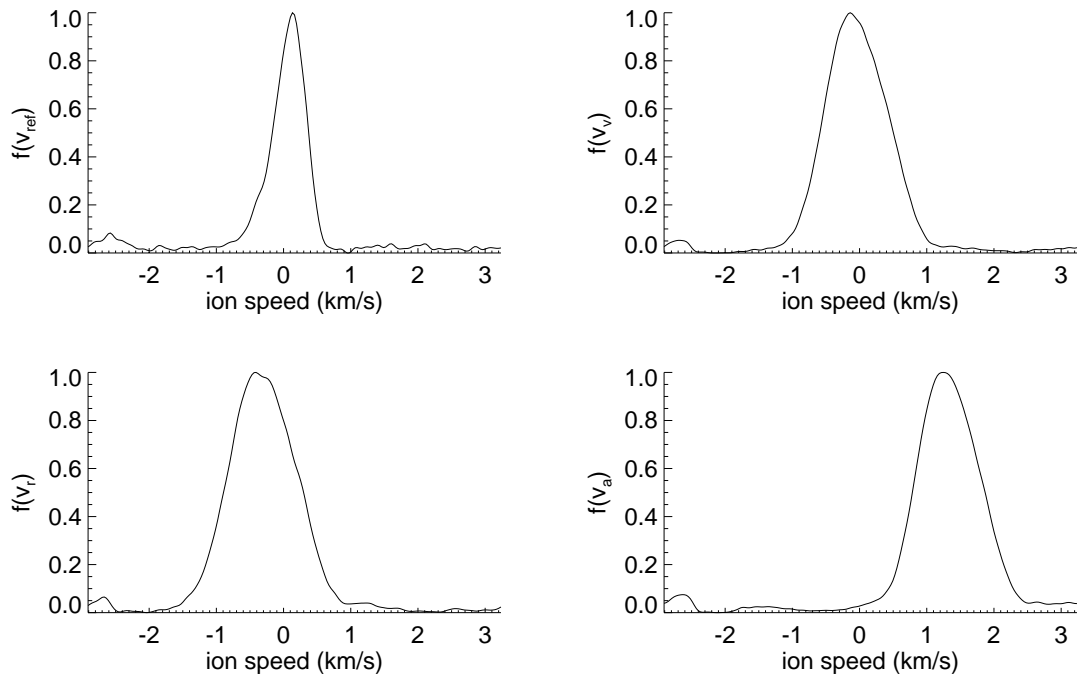


Figure B.54: Deconvolved $f(v_k)$ & fit at TC 2, $(x, y) = (63.14, -7.50)$ cm (tc02c).

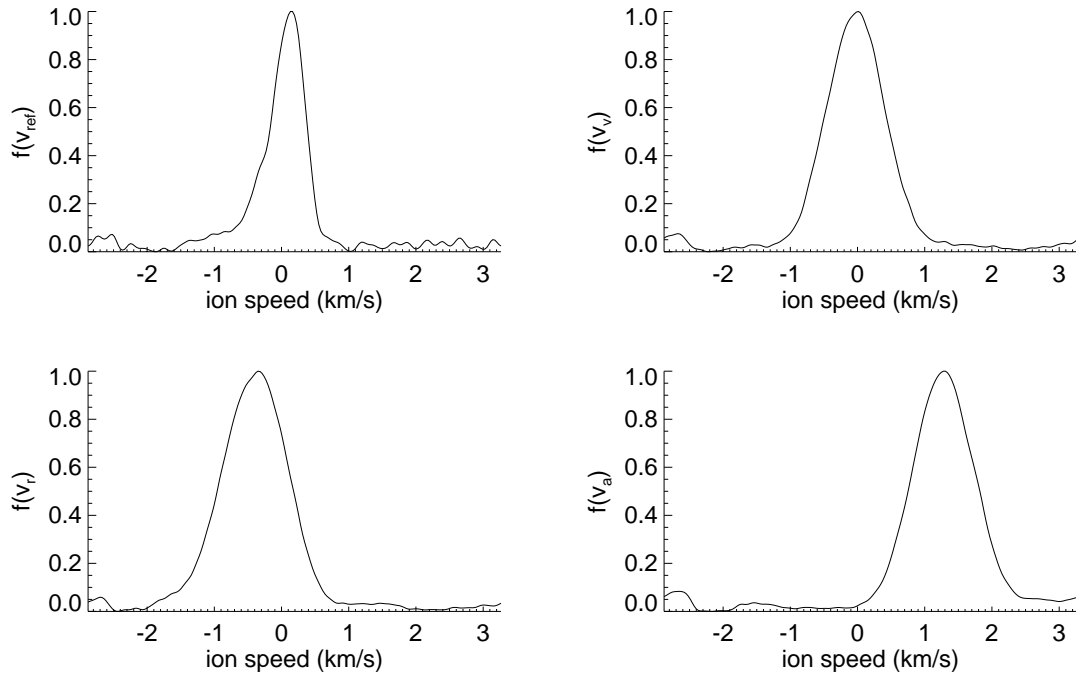


Figure B.55: Deconvolved $f(v_k)$ & fit at TC 2, $(x, y) = (63.14, -15.00)$ cm (tc02d).

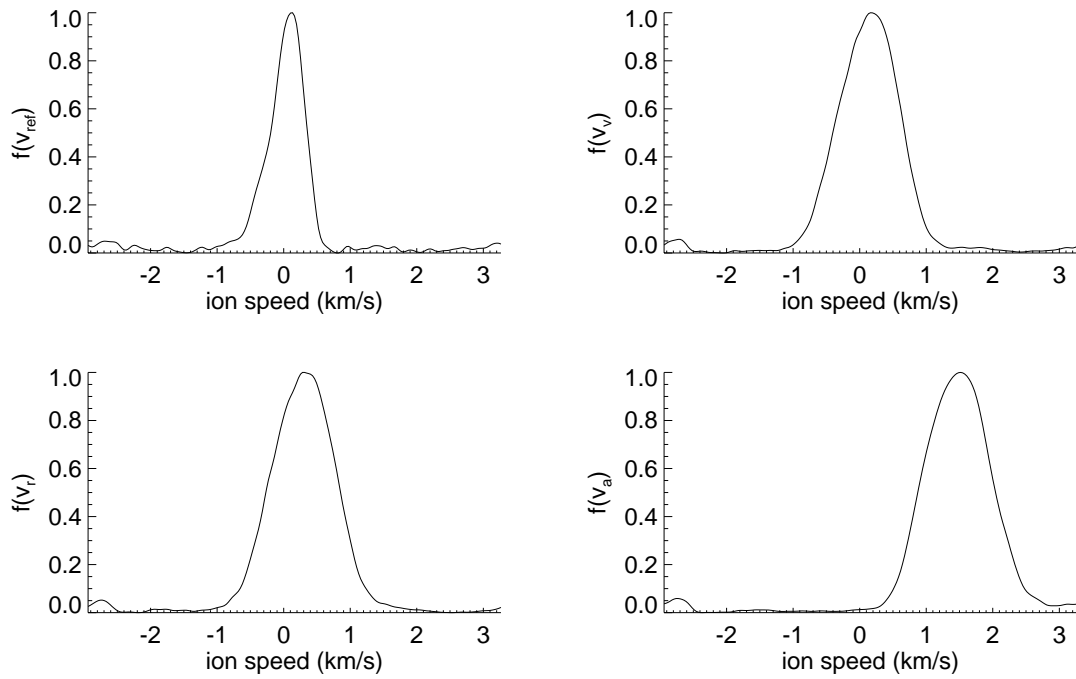


Figure B.56: Deconvolved $f(v_k)$ & fit at TC 2, $(x, y) = (63.14, 15.00)$ cm (tc02e).

APPENDIX C

FMT multiplex LIF: deconvolved velocity distributions

C.1 TH15 without neutralizer

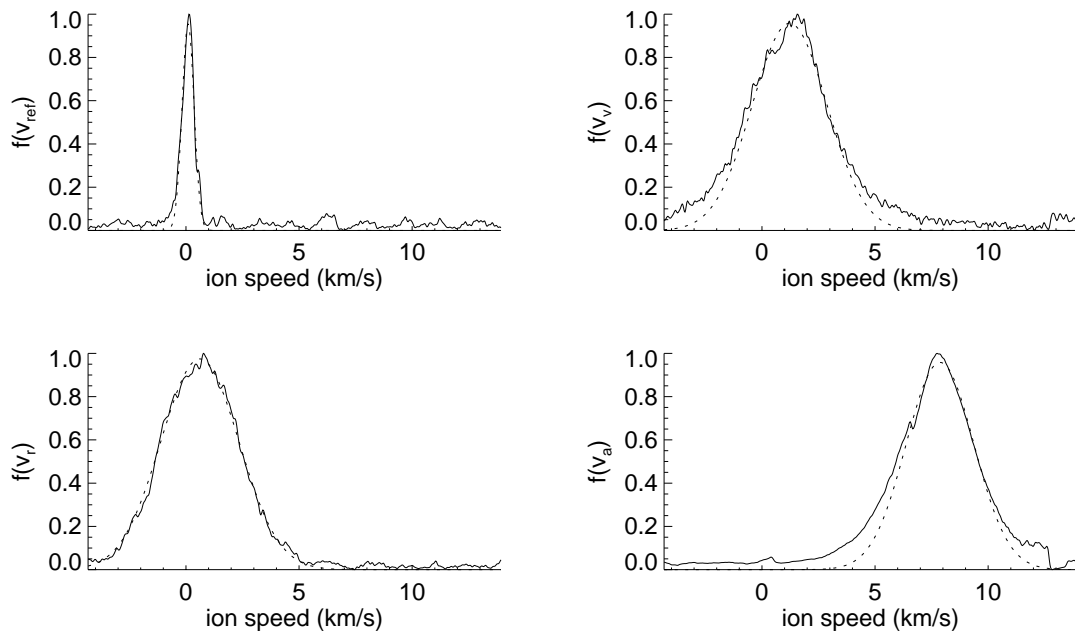


Figure C.1: Deconvolved $f(v)$ & curve-fit at TH15, $(x, y) = (0.14, 0.000)$ cm (th15a).

Figures C.1 through C.10 show velocity distributions taken 1.4 mm downstream of the FMT-2 accelerator grid. The solid line is the deconvolved distribution, while the dashed line is a curve-fit to a user-defined area.

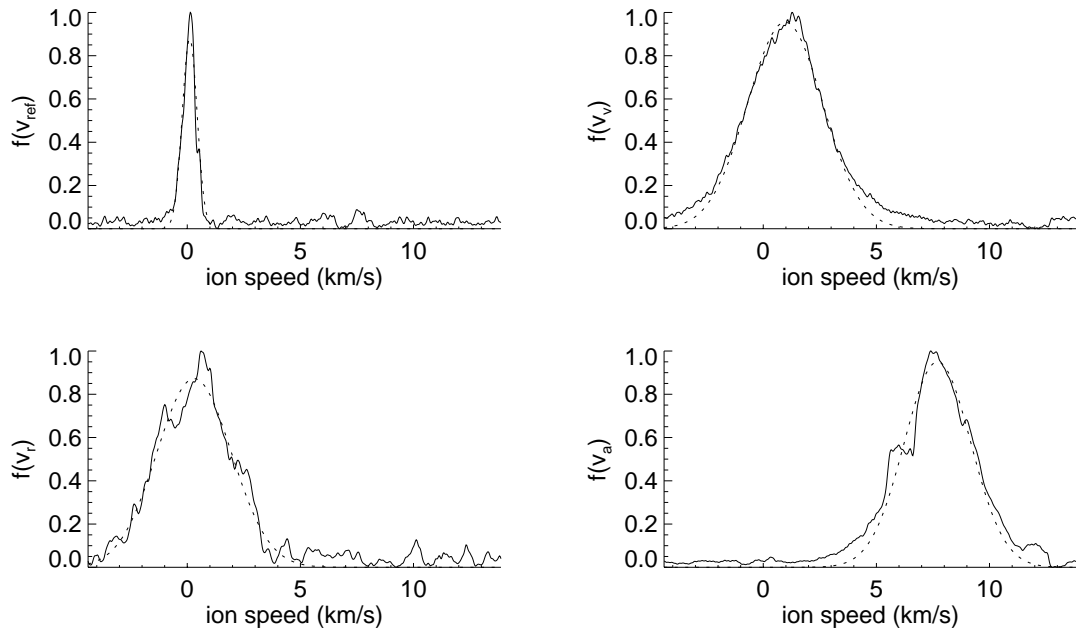


Figure C.2: Deconvolved $f(v)$ & curve-fit at TH15, $(x, y) = (0.14, 1.372)$ cm (th15b).

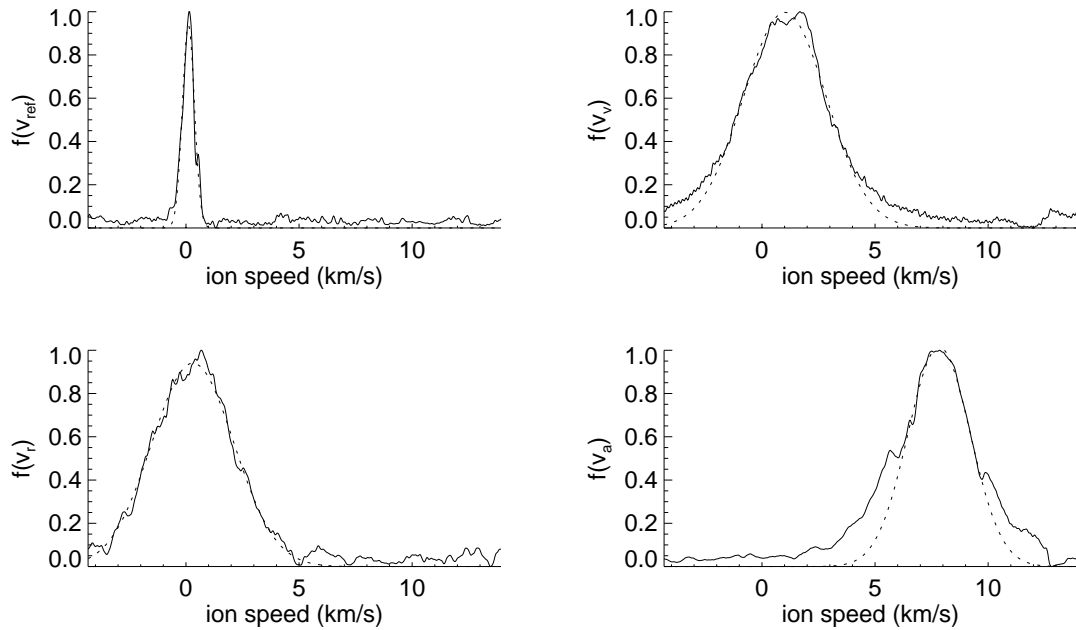


Figure C.3: Deconvolved $f(v)$ & curve-fit at TH15, $(x, y) = (0.14, 2.540)$ cm (th15c).

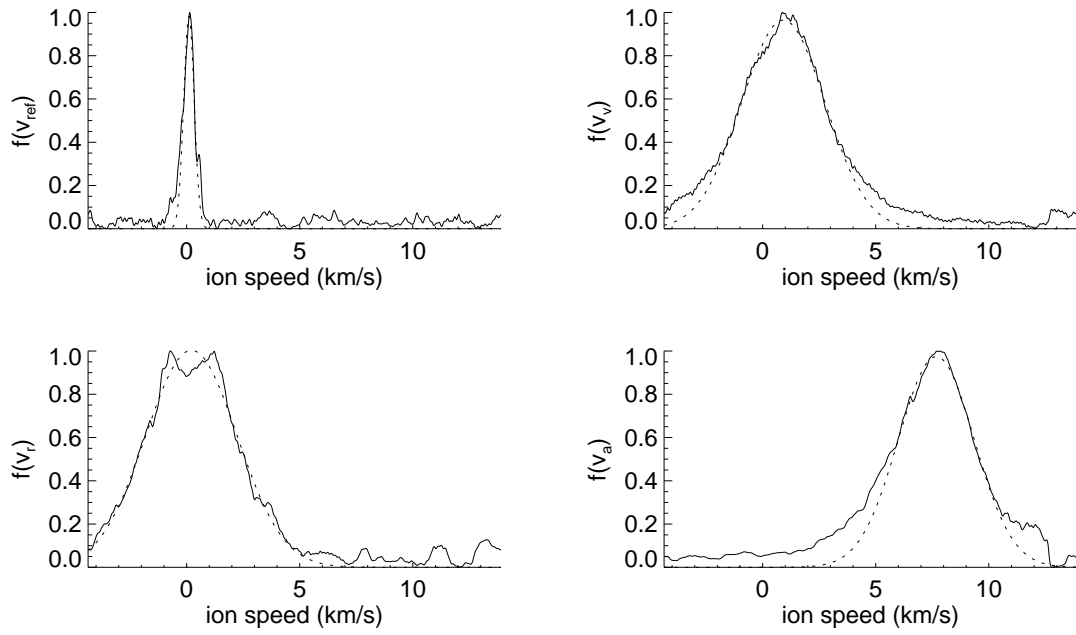


Figure C.4: Deconvolved $f(v)$ & curve-fit at TH15, $(x, y) = (0.14, 3.912)$ cm (th15d).

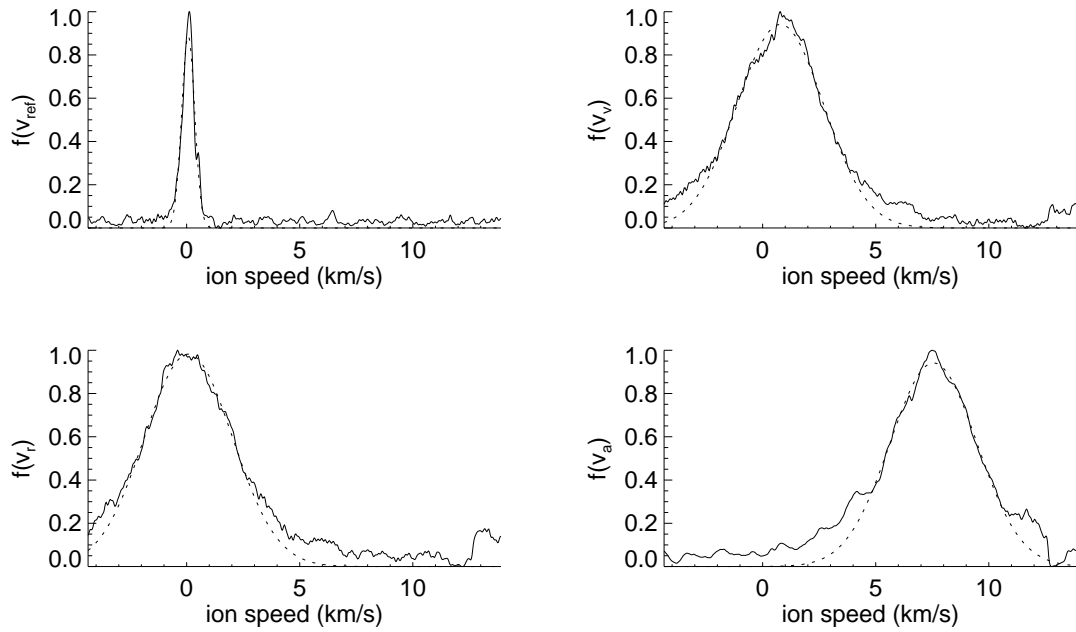


Figure C.5: Deconvolved $f(v)$ & curve-fit at TH15, $(x, y) = (0.14, 5.080)$ cm (th15e).

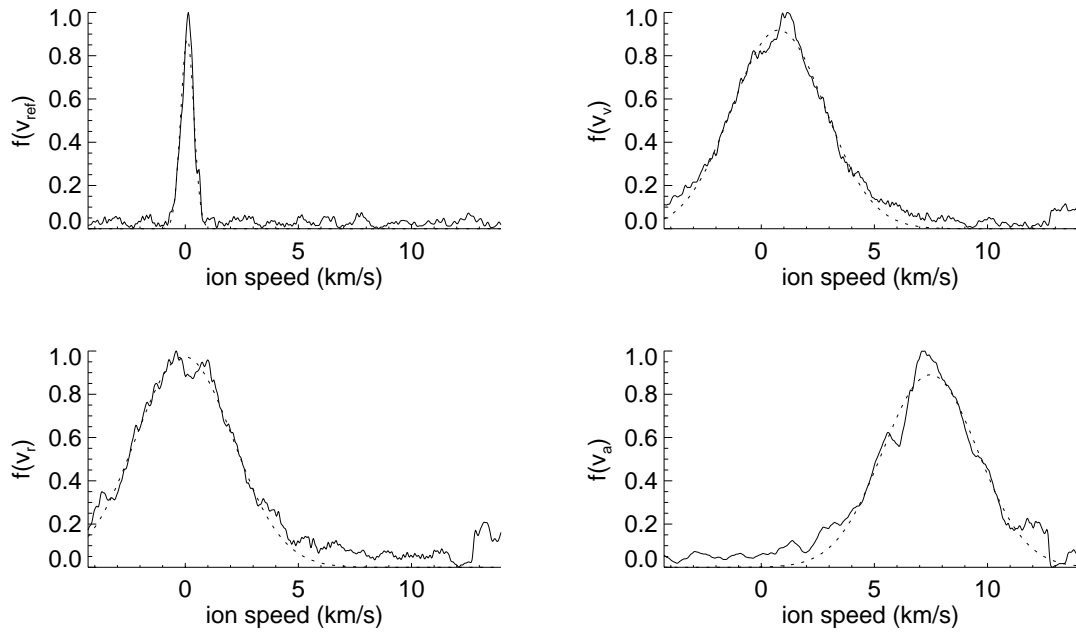


Figure C.6: Deconvolved $f(v)$ & curve-fit at TH15, $(x, y) = (0.14, 6.452)$ cm (th15f).

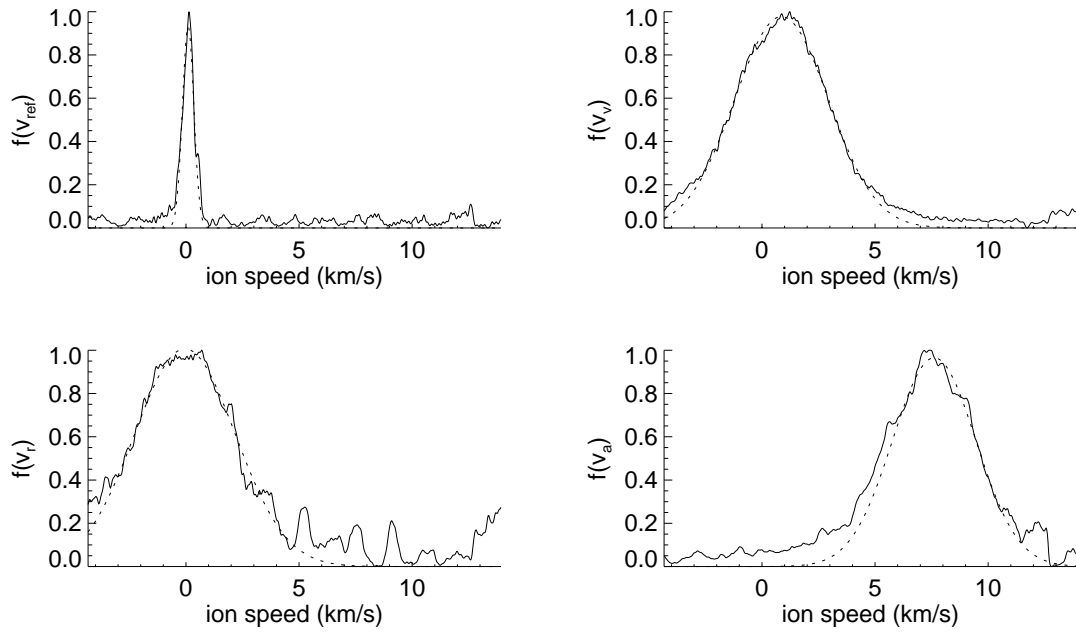


Figure C.7: Deconvolved $f(v)$ & curve-fit at TH15, $(x, y) = (0.14, 7.772)$ cm (th15g).

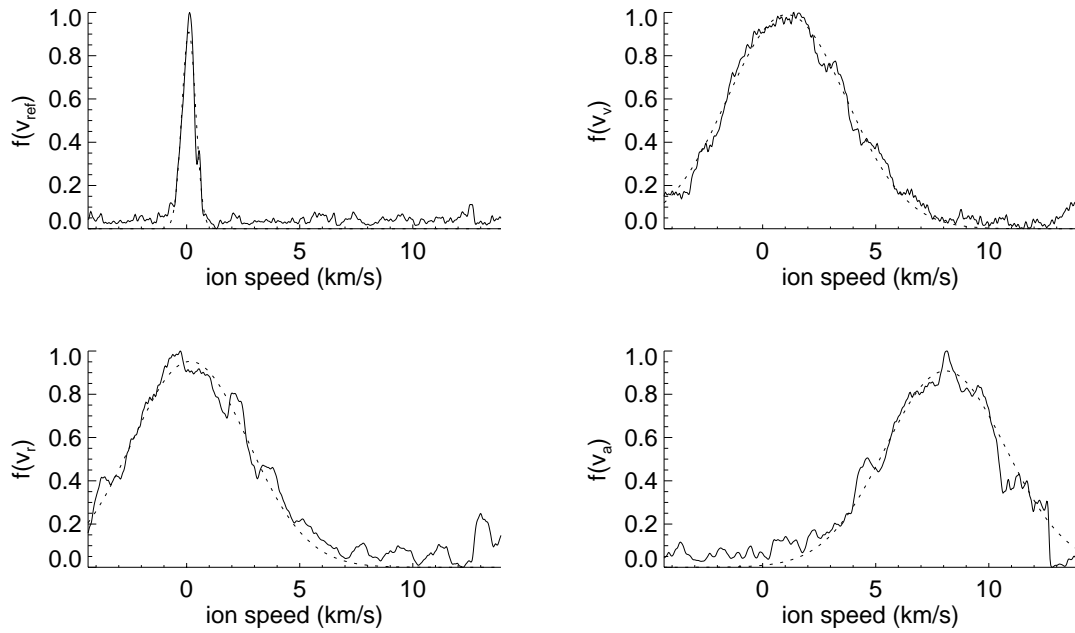


Figure C.8: Deconvolved $f(v)$ & curve-fit at TH15, $(x, y) = (0.14, 8.992)$ cm (th15h).

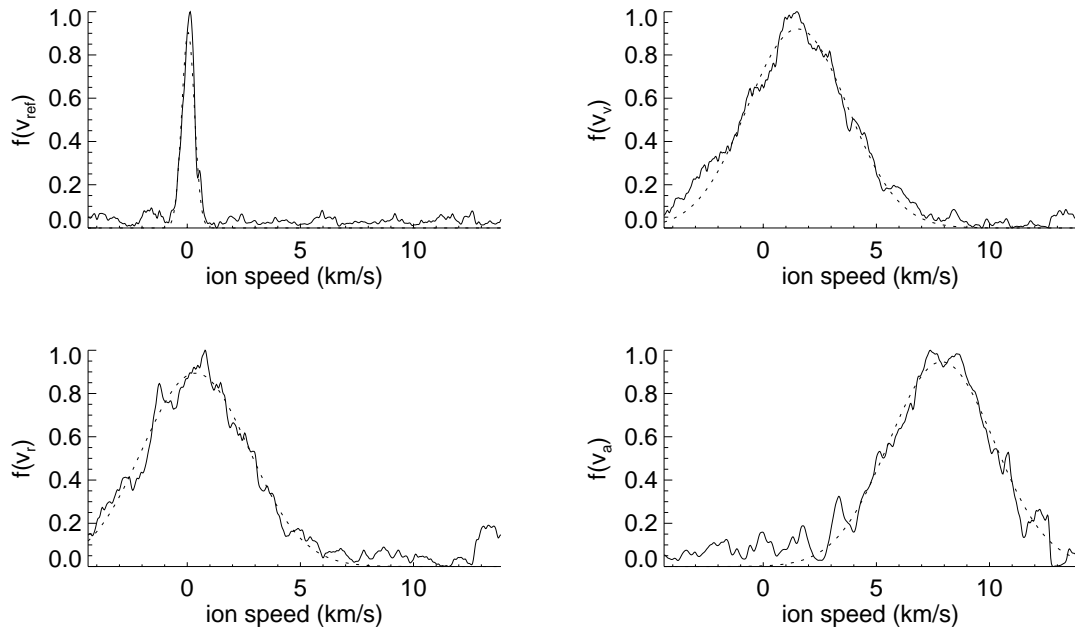


Figure C.9: Deconvolved $f(v)$ & curve-fit at TH15, $(x, y) = (0.14, 10.160)$ cm (th15i).

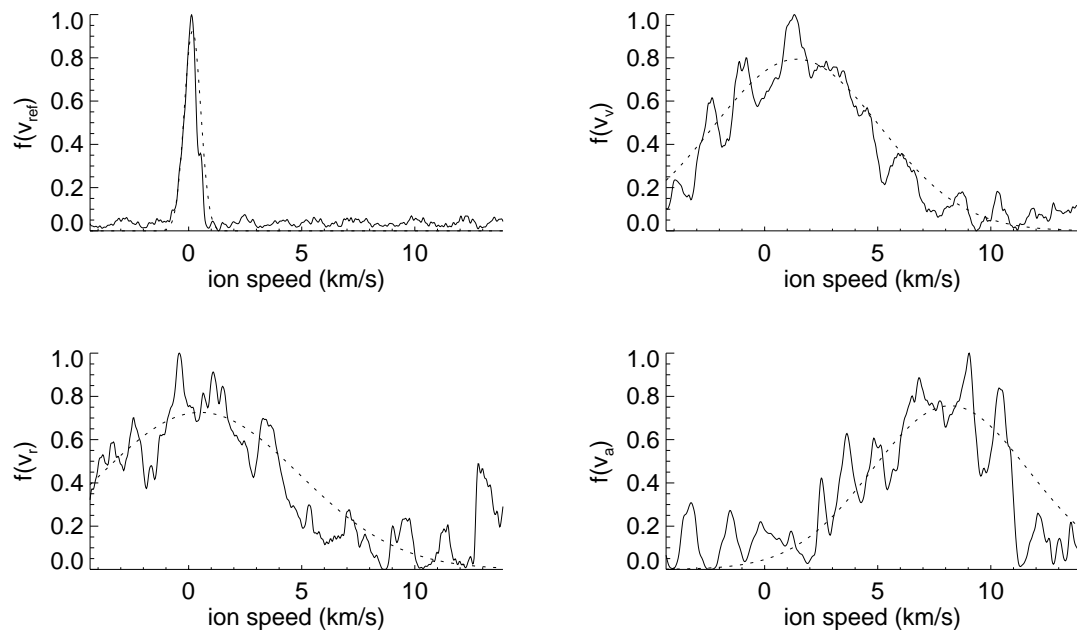


Figure C.10: Deconvolved $f(v)$ & curve-fit at TH15, $(x, y) = (0.14, 11.557)$ cm (th15j).

Figures C.11 through C.20 show velocity distributions taken 5 cm downstream of the FMT-2 accelerator grid. The solid line is the deconvolved distribution, while the dashed line is a Maxwellian curve-fit to a user-defined area.

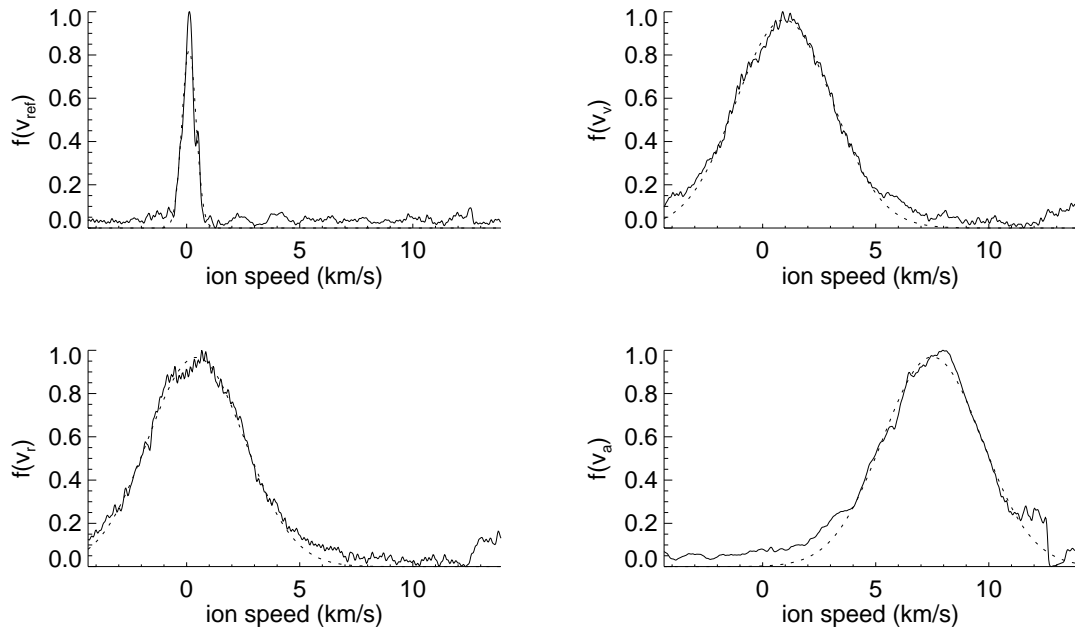


Figure C.11: Deconvolved $f(v)$ & curve-fit at TH15, $(x, y) = (5.02, 0.00)$ cm (th15l).

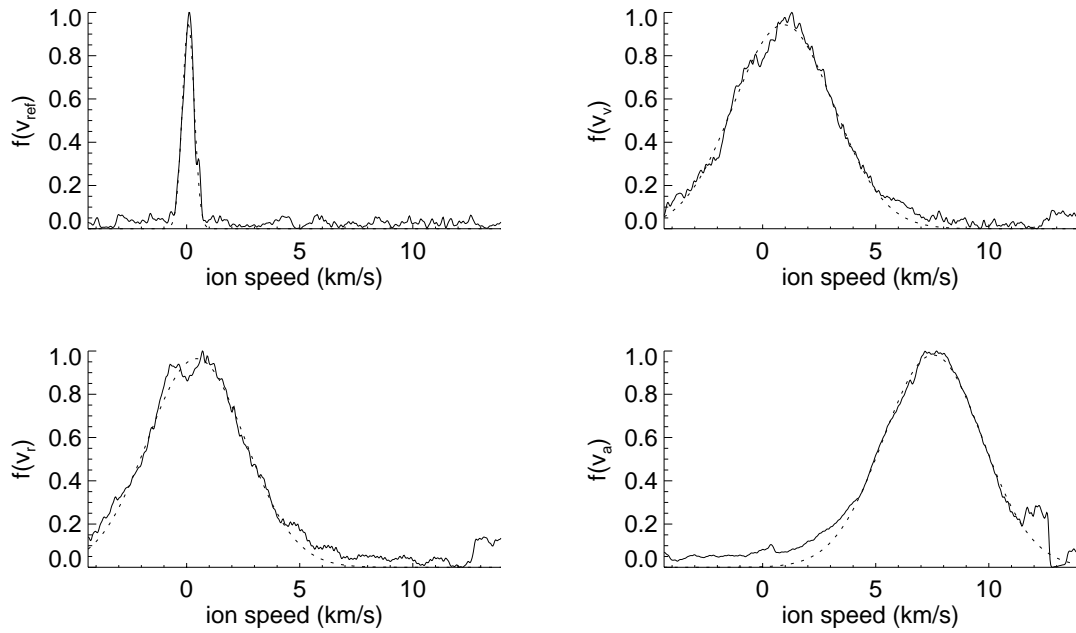


Figure C.12: Deconvolved $f(v)$ & curve-fit at TH15, $(x, y) = (5.02, 1.27)$ cm (th15m).

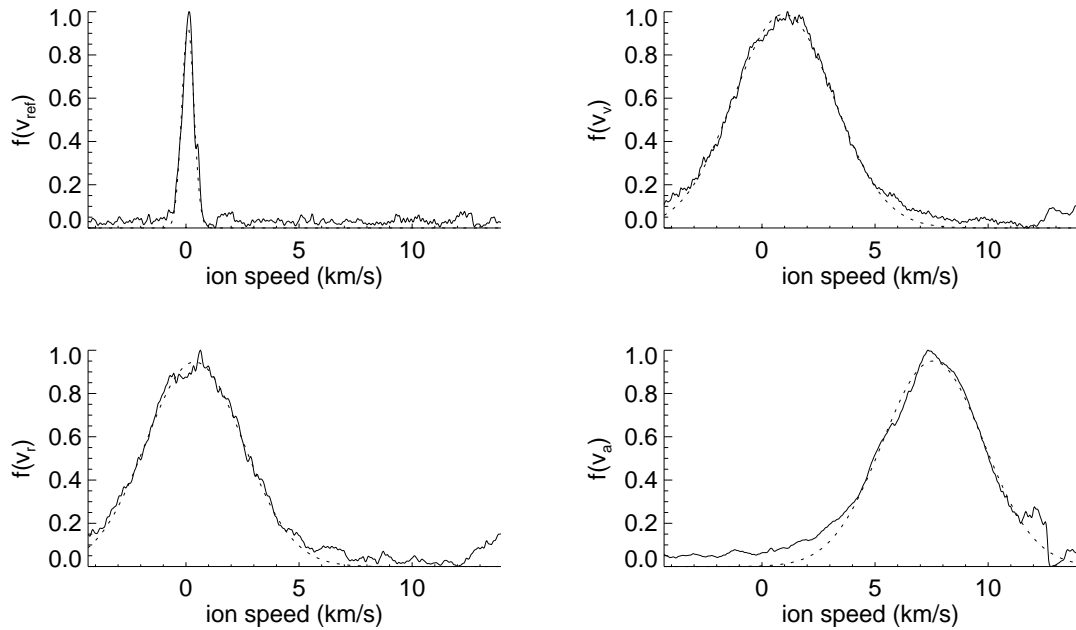


Figure C.13: Deconvolved $f(v)$ & curve-fit at TH15, $(x, y) = (5.02, 2.24)$ cm (th15n).

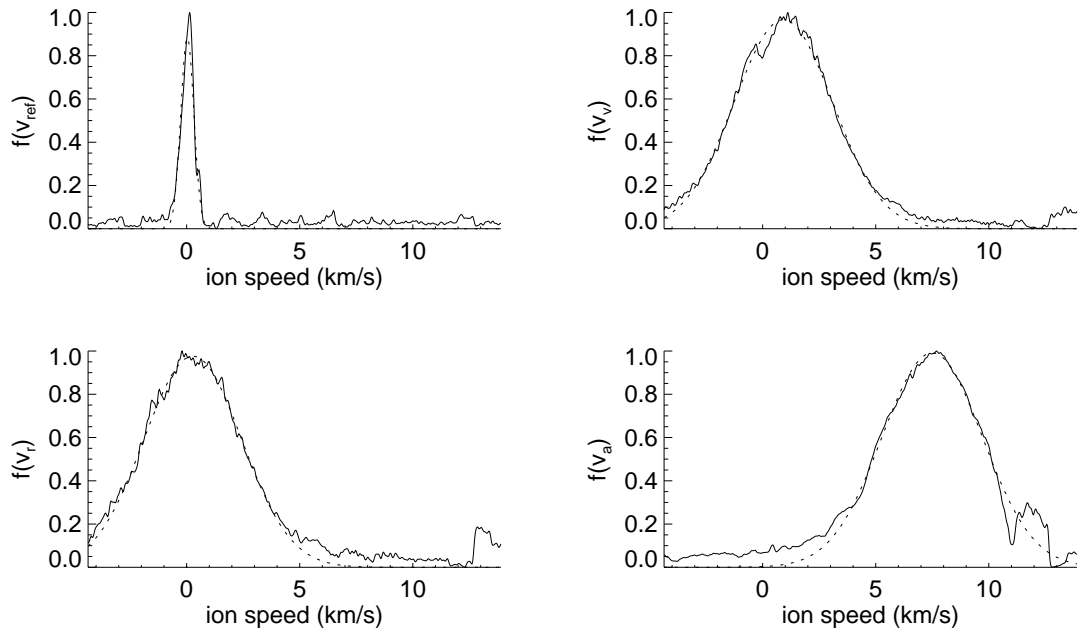


Figure C.14: Deconvolved $f(v)$ & curve-fit at TH15, $(x, y) = (5.02, 3.81)$ cm (th15o).

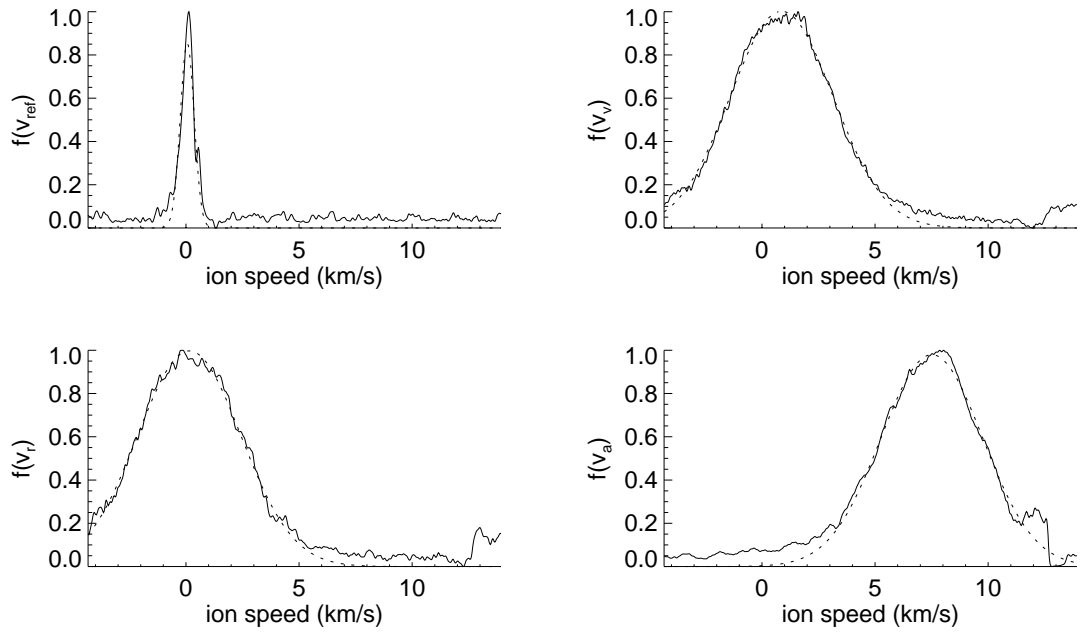


Figure C.15: Deconvolved $f(v)$ & curve-fit at TH15, $(x, y) = (5.02, 5.08)$ cm (th15p).

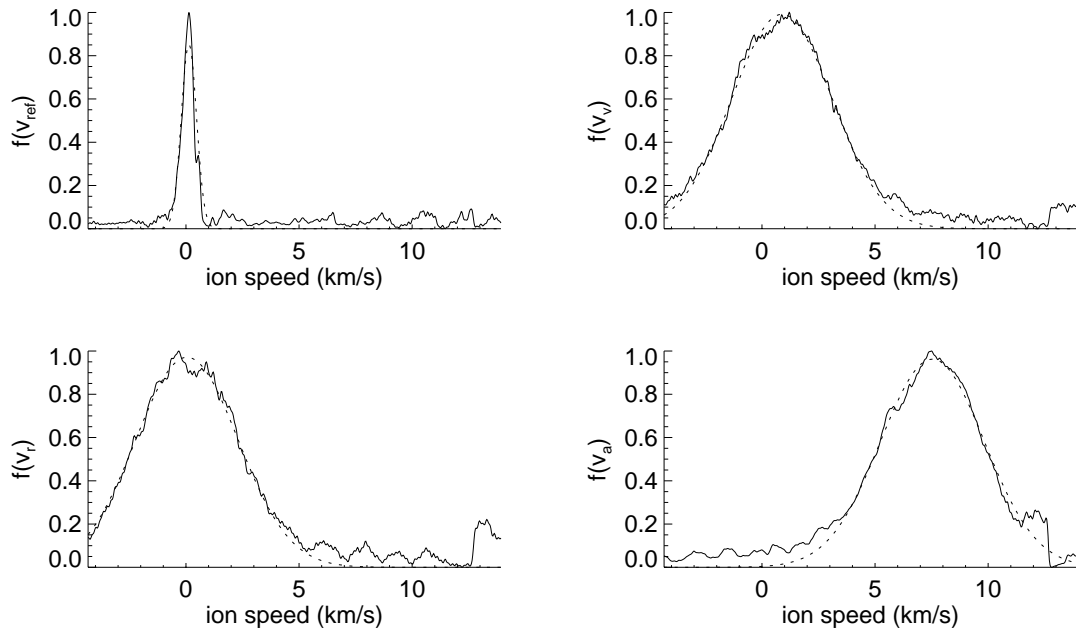


Figure C.16: Deconvolved $f(v)$ & curve-fit at TH15, $(x, y) = (5.02, 6.35)$ cm (th15q).

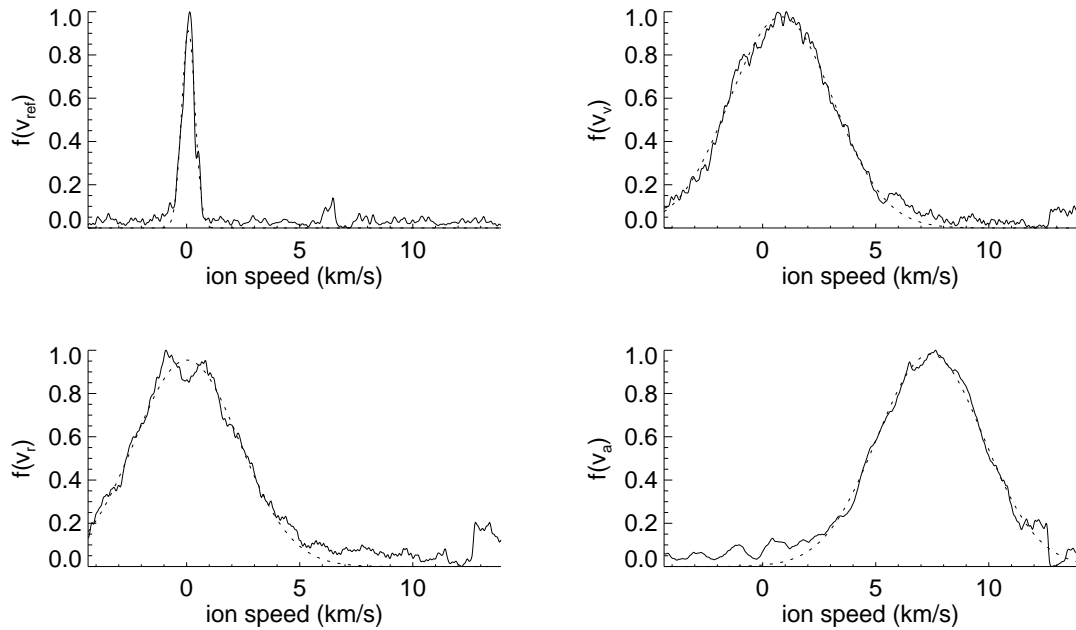


Figure C.17: Deconvolved $f(v)$ & curve-fit at TH15, $(x, y) = (5.02, 7.62)$ cm (th15r).

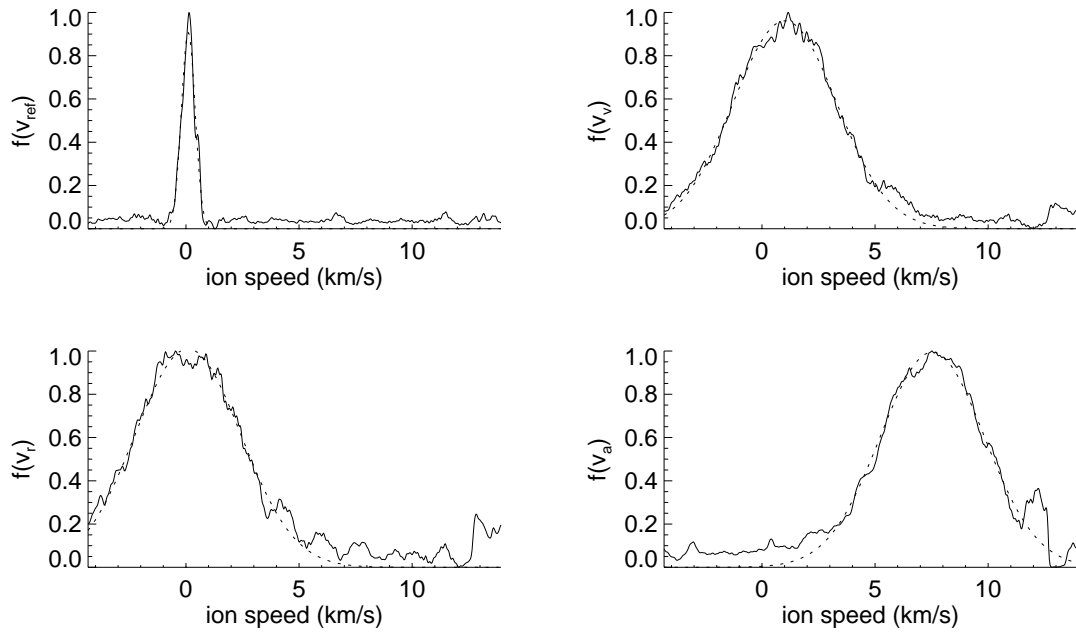


Figure C.18: Deconvolved $f(v)$ & curve-fit at TH15, $(x, y) = (5.02, 8.89)$ cm (th15s).

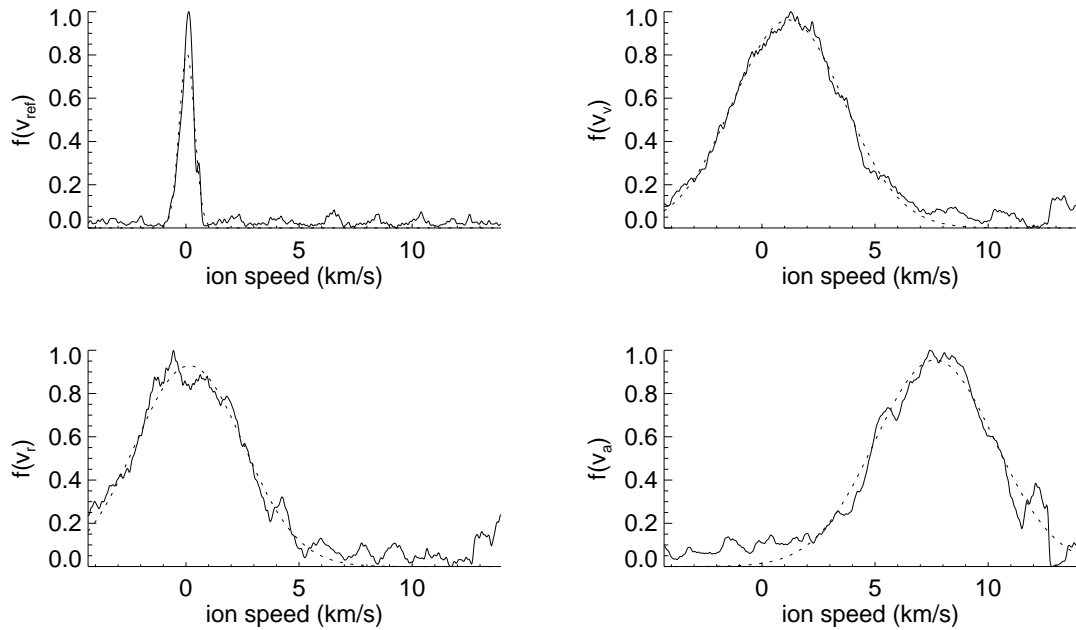


Figure C.19: Deconvolved $f(v)$ & curve-fit at TH15, $(x, y) = (5.02, 10.16)$ cm (th15t).

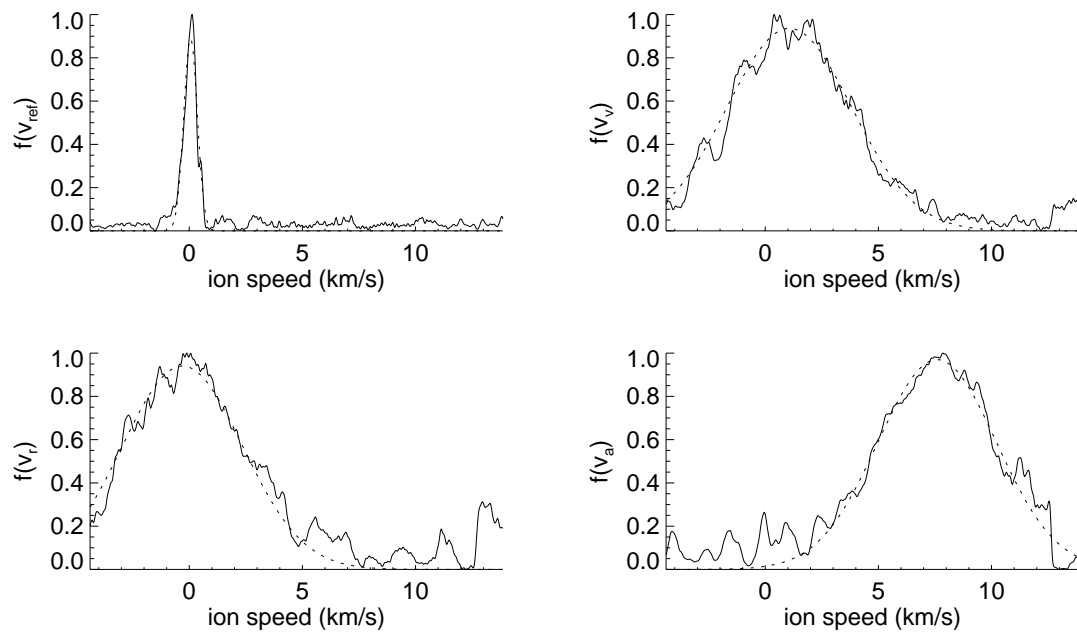


Figure C.20: Deconvolved $f(v)$ & curve-fit at TH15, $(x, y) = (5.02, 11.43)$ cm (th15u).

C.1.1 TH19 without neutralizer

Figures C.21 through C.27 show velocity distributions taken 5.09 cm downstream of the FMT-2 accelerator grid. The solid line is the deconvolved distribution, while the dashed line is a Maxwellian curve-fit to a user-defined area.

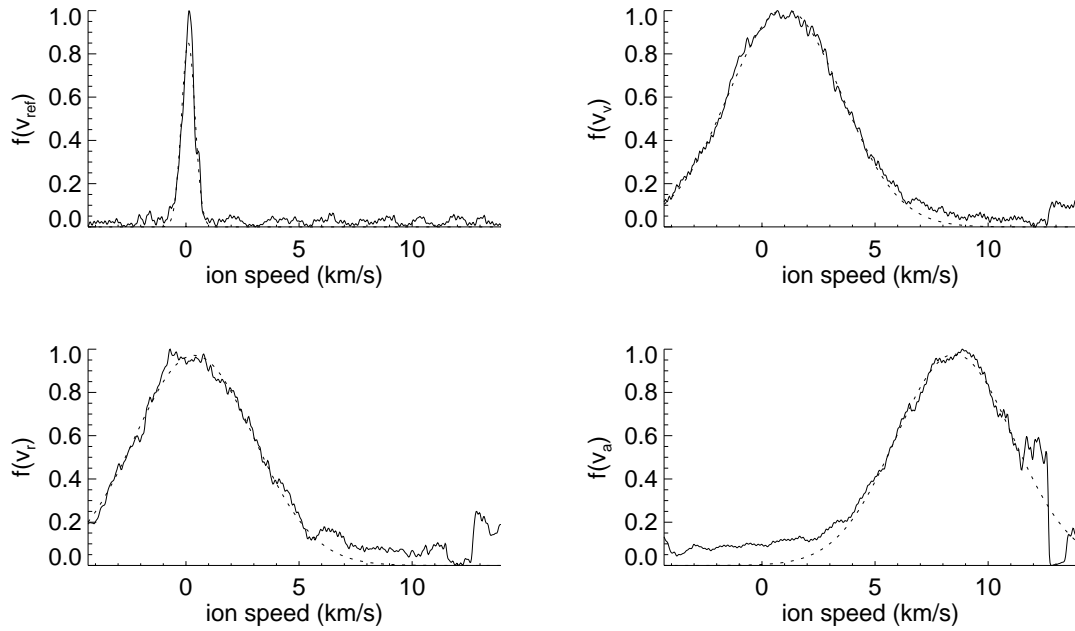


Figure C.21: Deconvolved $f(v)$ & curve-fit at TH19 w/ neutralizer, $(x, y) = (5.09, 0.00)$ cm (th19a).

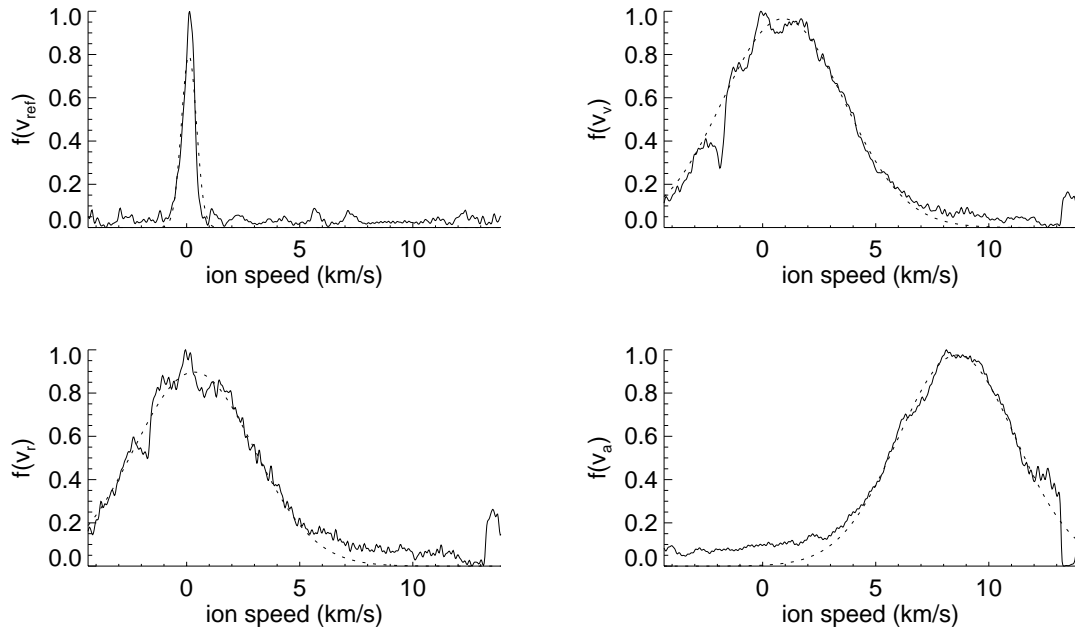


Figure C.22: Deconvolved $f(v)$ & curve-fit at TH19 w/ neutralizer, $(x, y) = (5.09, 1.27)$ cm (th19b).

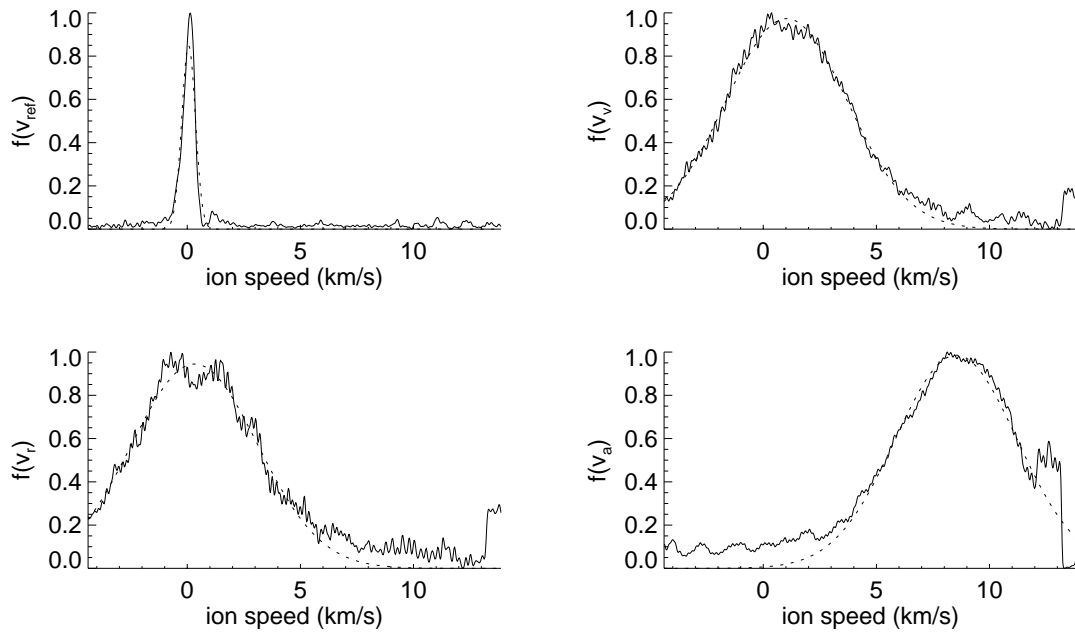


Figure C.23: Deconvolved $f(v)$ & curve-fit at TH19 w/ neutralizer, $(x, y) = (5.09, 2.54)$ cm (th19c).

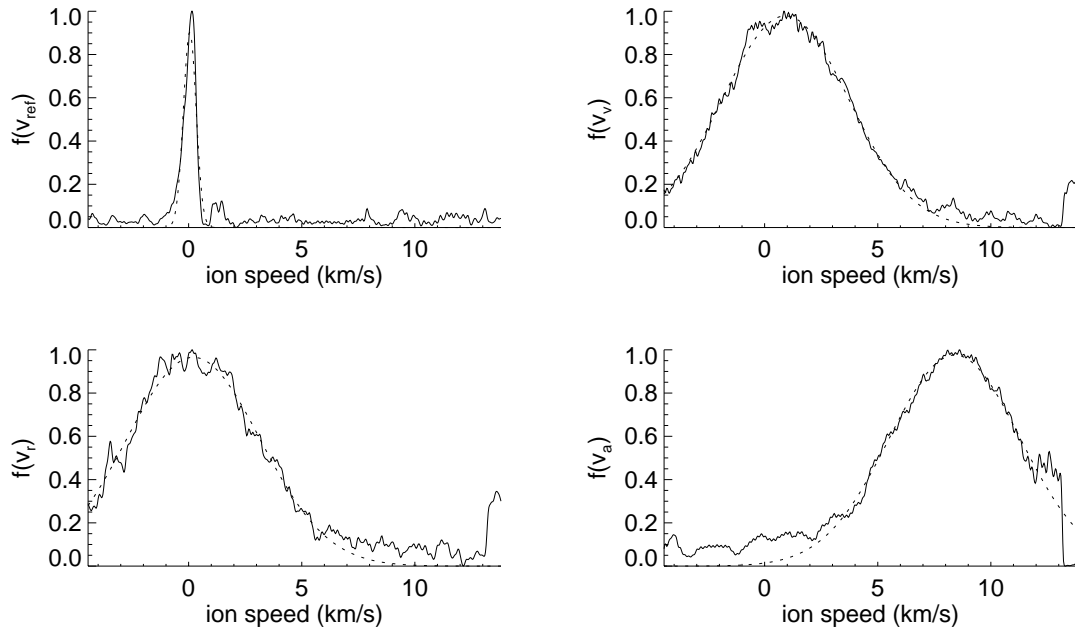


Figure C.24: Deconvolved $f(v)$ & curve-fit at TH19 w/ neutralizer, $(x, y) = (5.09, 3.81)$ cm (th19d).

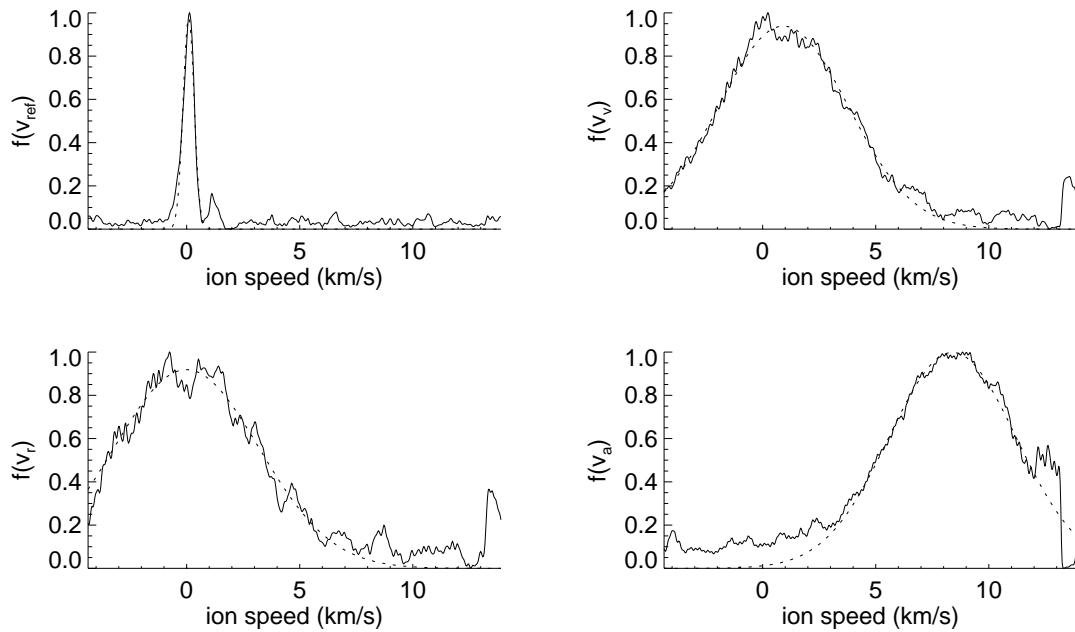


Figure C.25: Deconvolved $f(v)$ & curve-fit at TH19 w/ neutralizer, $(x, y) = (5.09, 5.08)$ cm (th19e).

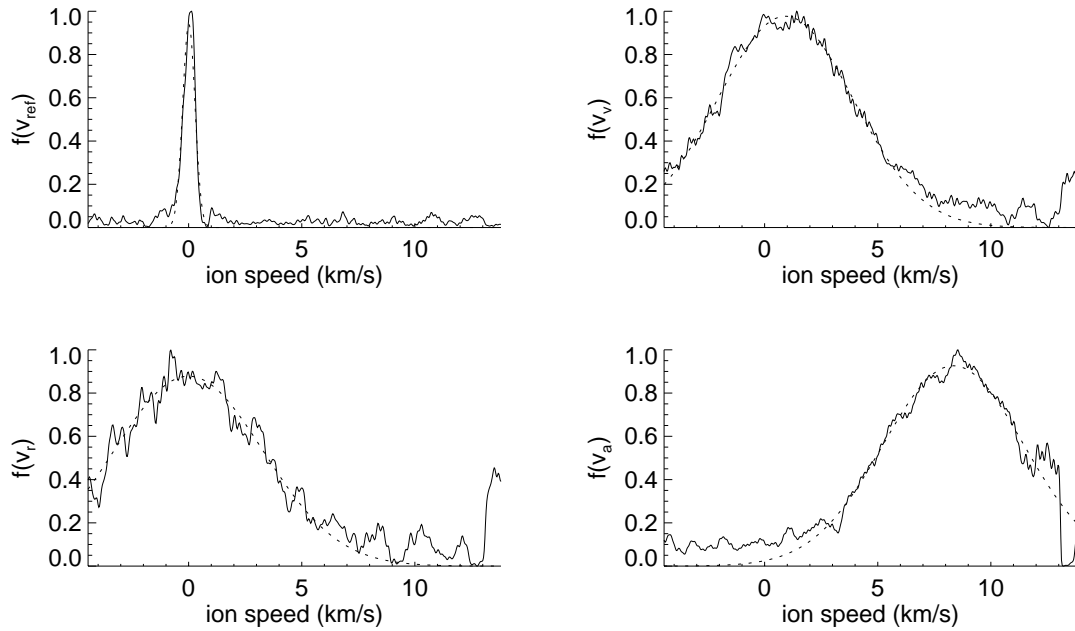


Figure C.26: Deconvolved $f(v)$ & curve-fit at TH19 w/ neutralizer, $(x, y) = (5.09, 6.35)$ cm (th19f).

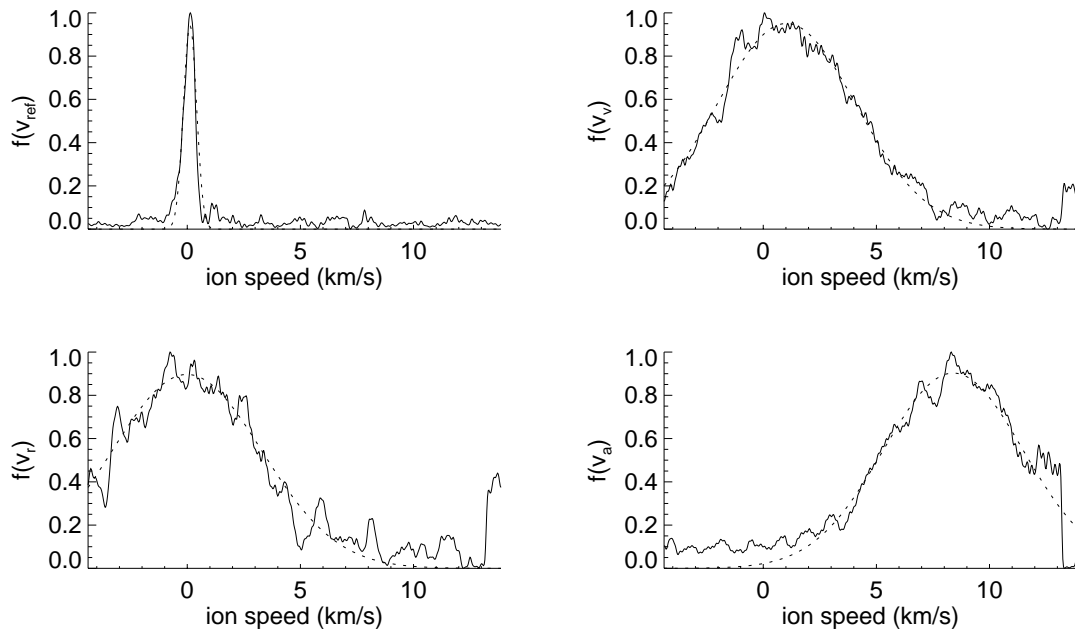


Figure C.27: Deconvolved $f(v)$ & curve-fit at TH19 w/ neutralizer, $(x, y) = (5.09, 7.62)$ cm (th19g).

C.1.2 TH15 with neutralizer

Figures C.28 through C.43 show velocity distributions taken along the FMT-2 centerline, from 1 mm to 30 cm downstream of the accelerator grid. The solid line is the deconvolved distribution, while the dashed line is a Maxwellian curve-fit to a user-defined area.

Note that the signal-to-noise ratio is still very good far downstream of the accelerator grid. This suggests that plume LIF could be measured much further downstream than we were able to move in this experiment.

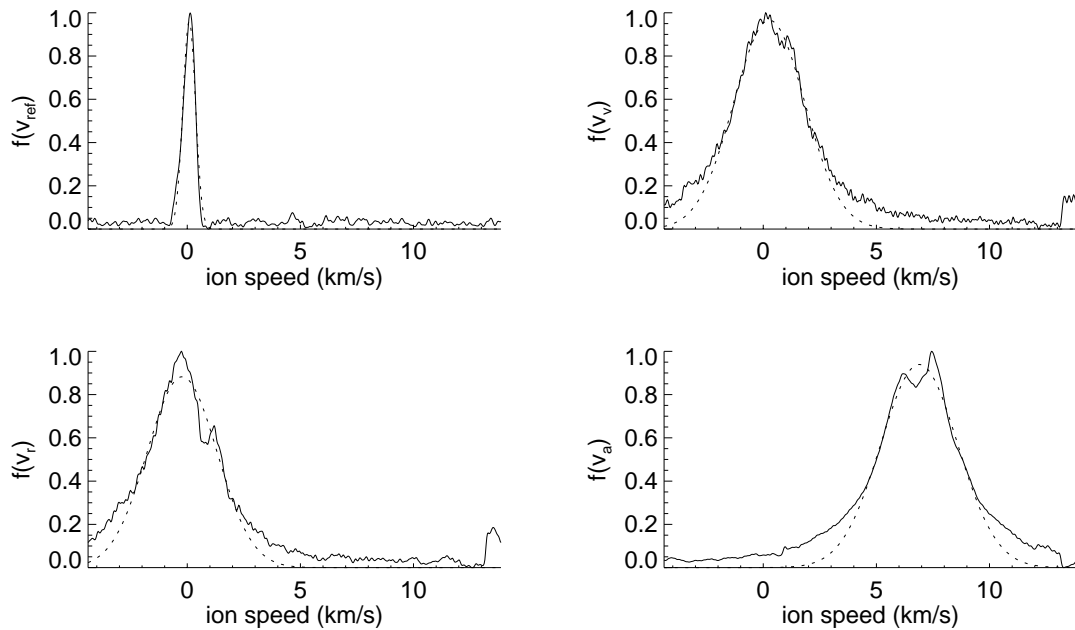


Figure C.28: Deconvolved $f(v)$ & curve-fit at TH15 w/ neutralizer, $(x, y) = (0.12\text{cm}, 0.00)\text{cm}$ (th15x0).

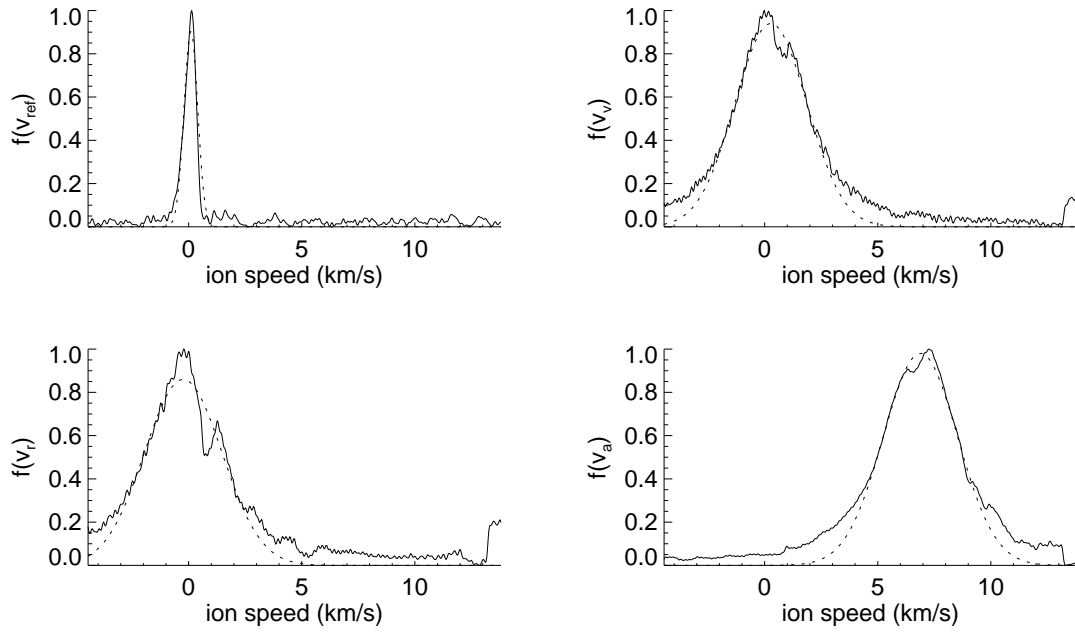


Figure C.29: Deconvolved $f(v)$ & curve-fit at TH15 w/ neutralizer, $(x, y) = (0.22, 0.00)$ cm (th15x1).

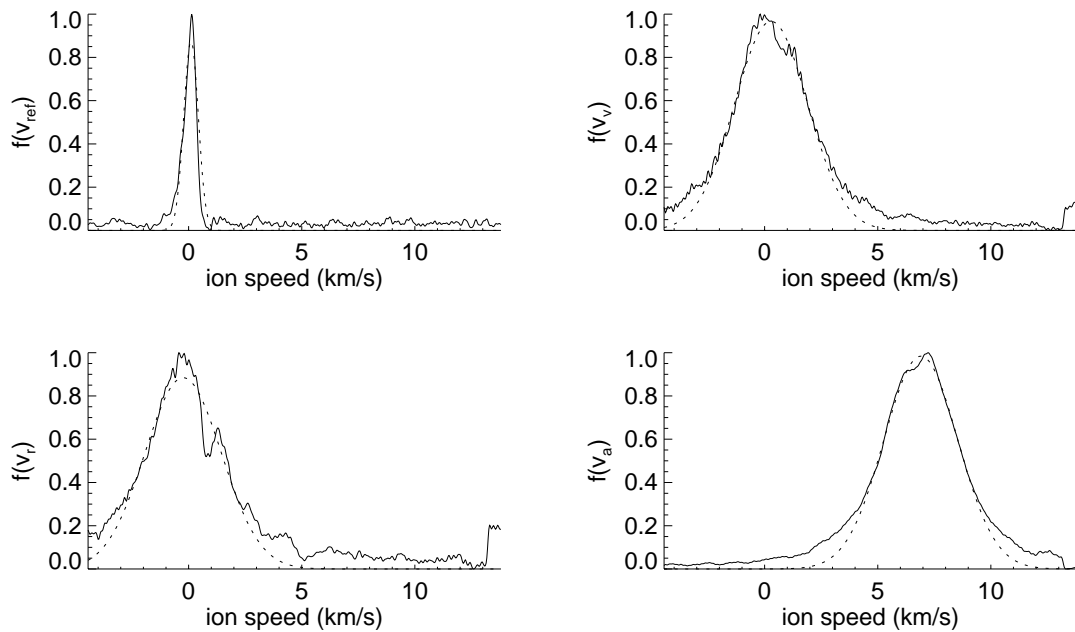


Figure C.30: Deconvolved $f(v)$ & curve-fit at TH15 w/ neutralizer, $(x, y) = (0.35, 0.00)$ cm (th15x2).

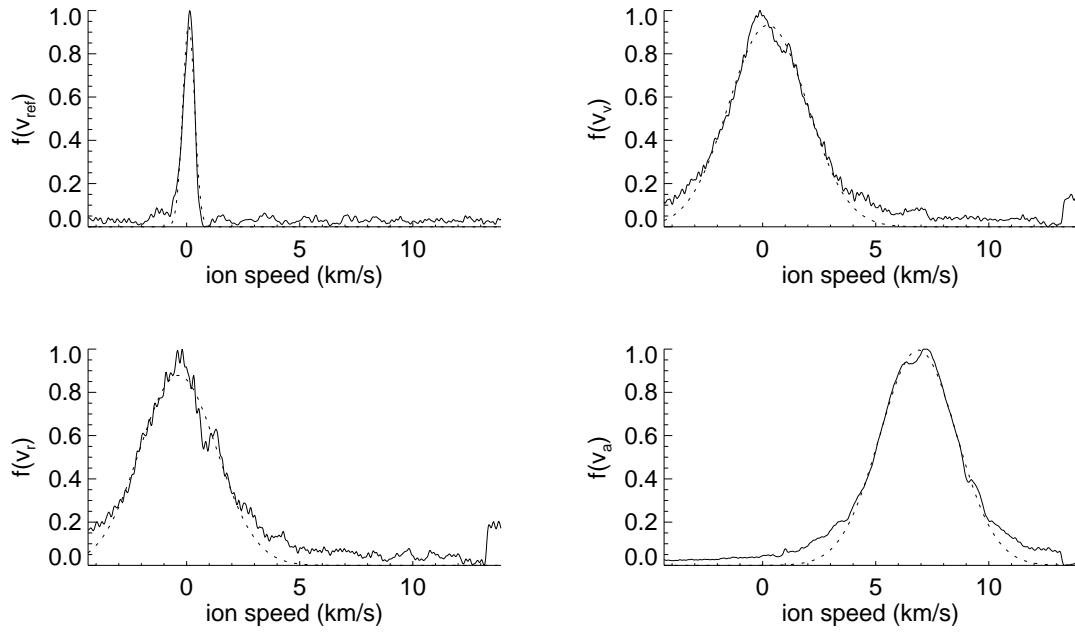


Figure C.31: Deconvolved $f(v)$ & curve-fit at TH15 w/ neutralizer, $(x, y) = (0.411, 0.00)$ cm (th15x3).

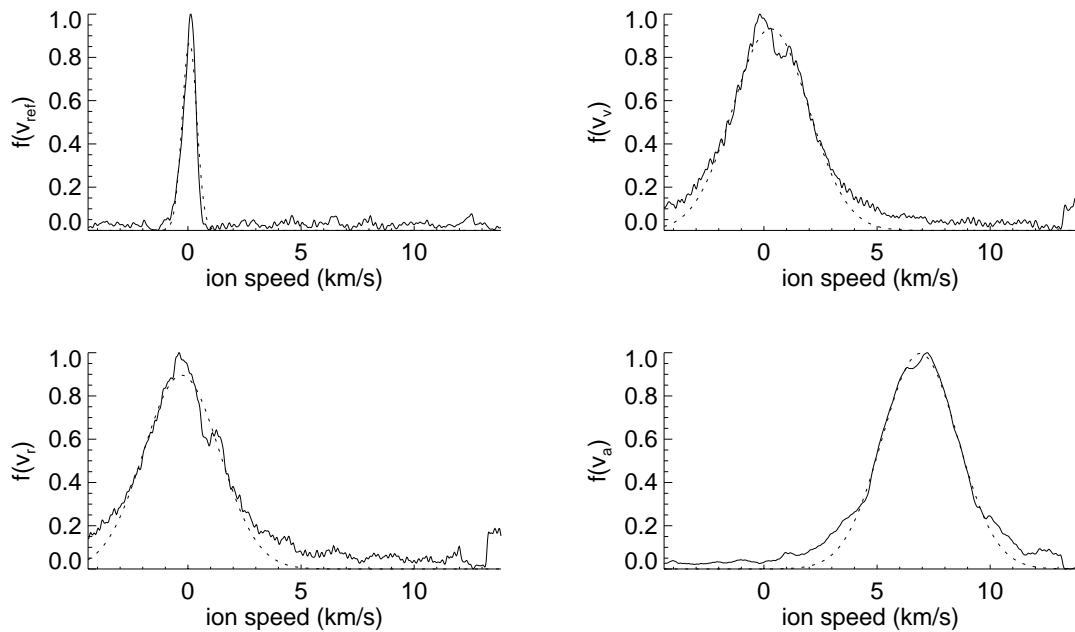


Figure C.32: Deconvolved $f(v)$ & curve-fit at TH15 w/ neutralizer, $(x, y) = (0.505, 0.00)$ cm (th15x4).

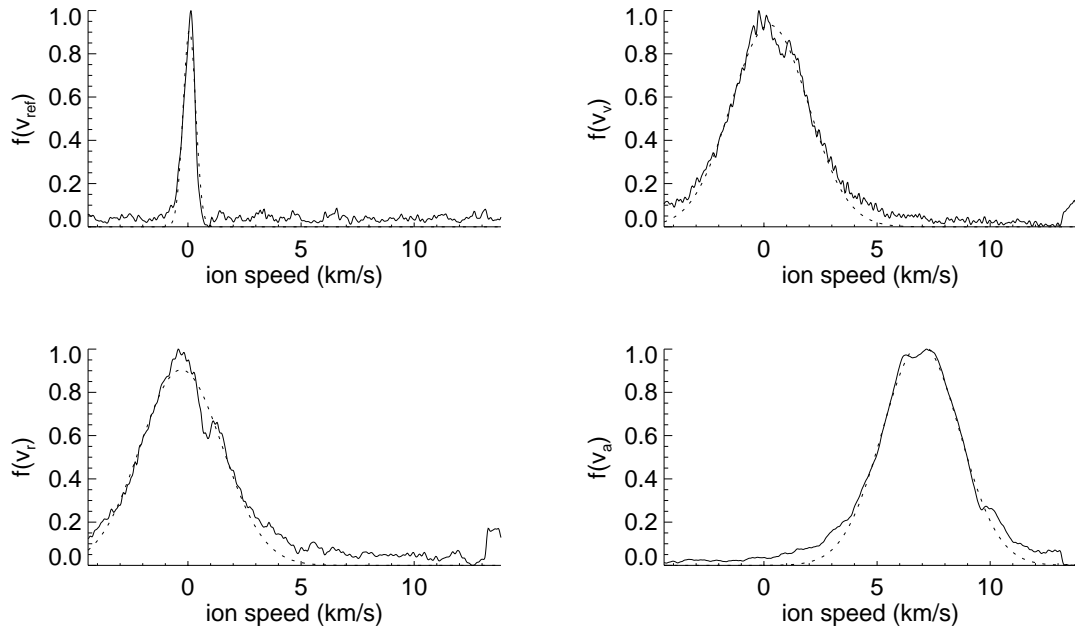


Figure C.33: Deconvolved $f(v)$ & curve-fit at TH15 w/ neutralizer, $(x, y) = (0.696, 0.00)$ cm (th15x5).

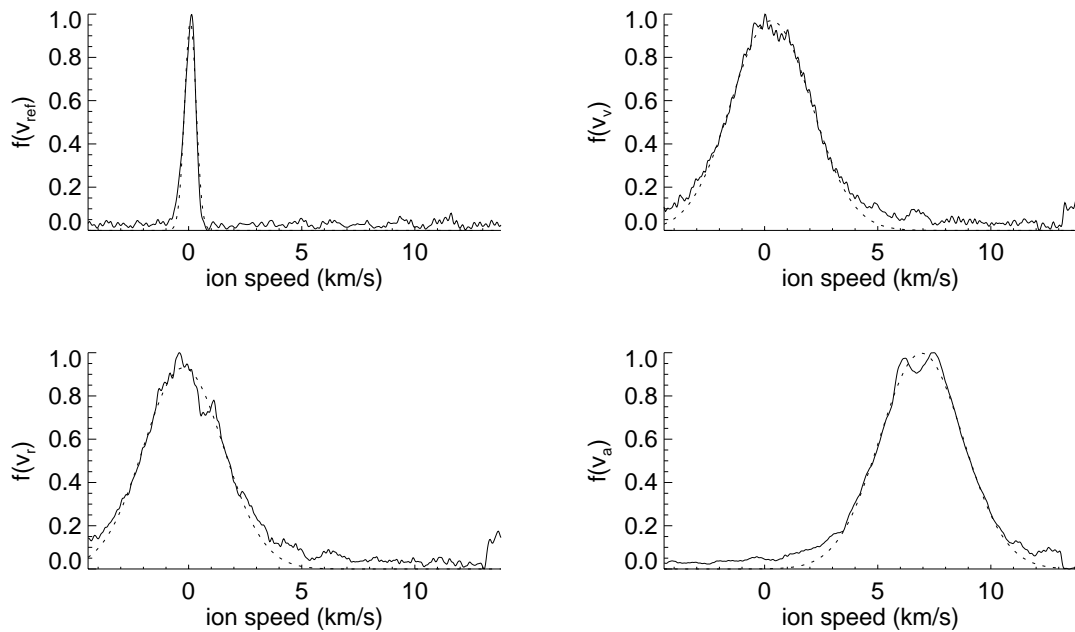


Figure C.34: Deconvolved $f(v)$ & curve-fit at TH15 w/ neutralizer, $(x, y) = (1.008, 0.00)$ cm (th15x6).

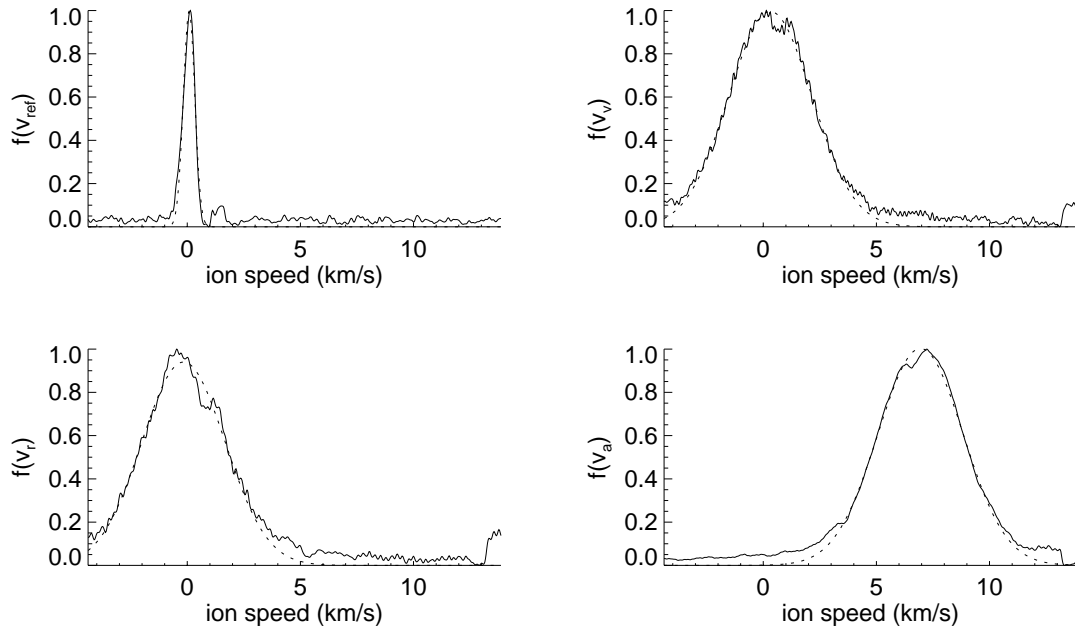


Figure C.35: Deconvolved $f(v)$ & curve-fit at TH15 w/ neutralizer, $(x, y) = (1.394, 0.00)$ cm (th15x7).

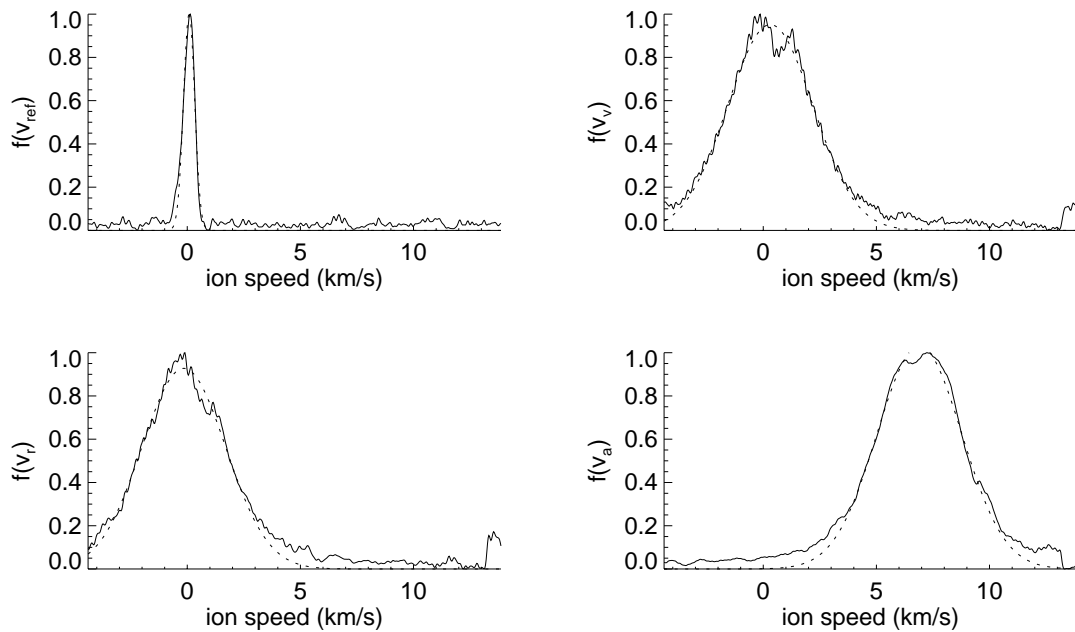


Figure C.36: Deconvolved $f(v)$ & curve-fit at TH15 w/ neutralizer, $(x, y) = (1.890, 0.00)$ cm (th15x8).

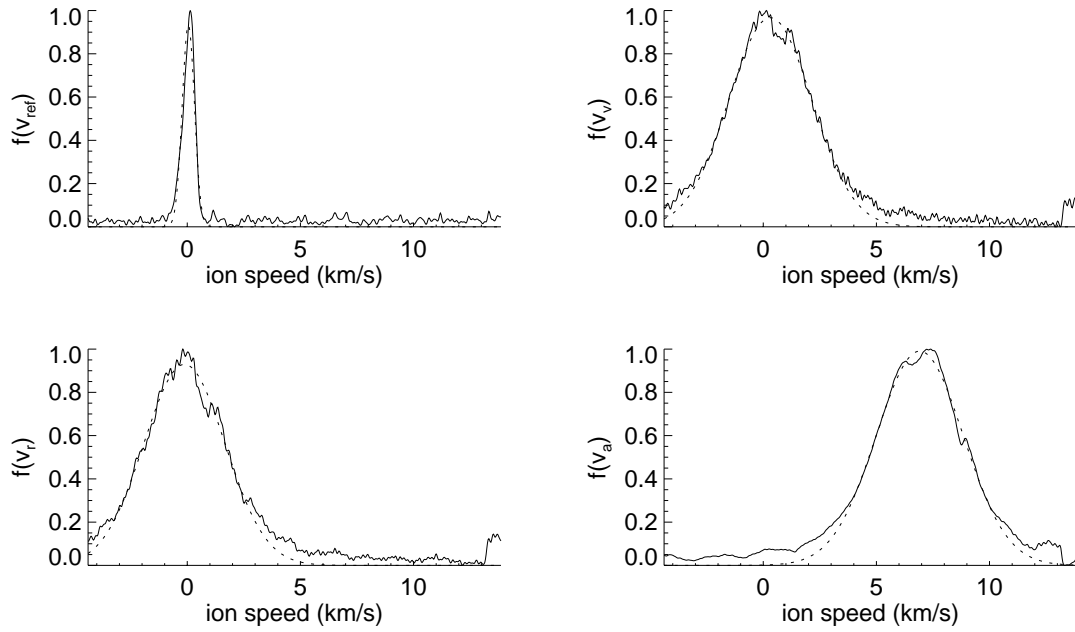


Figure C.37: Deconvolved $f(v)$ & curve-fit at TH15 w/ neutralizer, $(x, y) = (2.492, 0.00)$ cm (th15x9).

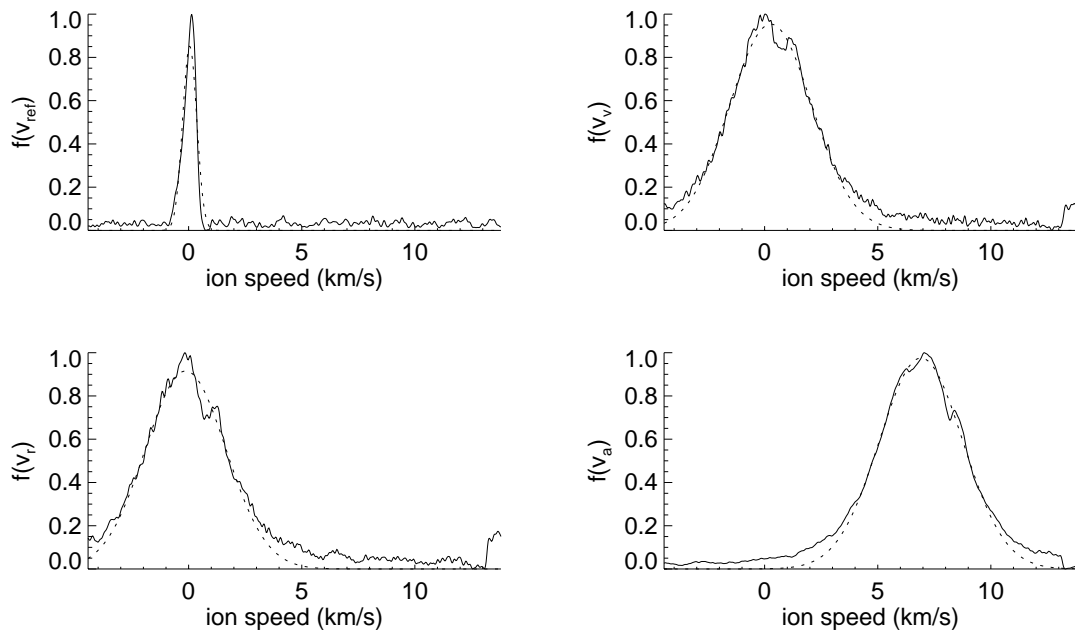


Figure C.38: Deconvolved $f(v)$ & curve-fit at TH15 w/ neutralizer, $(x, y) = (3.495, 0.00)$ cm (th15x10).

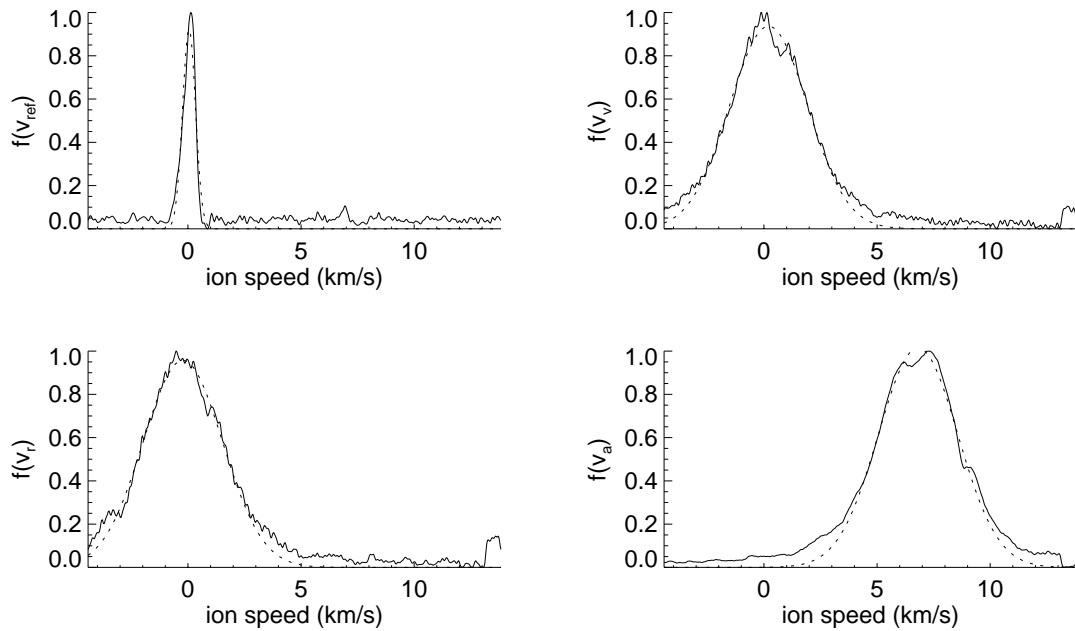


Figure C.39: Deconvolved $f(v)$ & curve-fit at TH15 w/ neutralizer, $(x, y) = (7.008, 0.00)$ cm (th15x11).

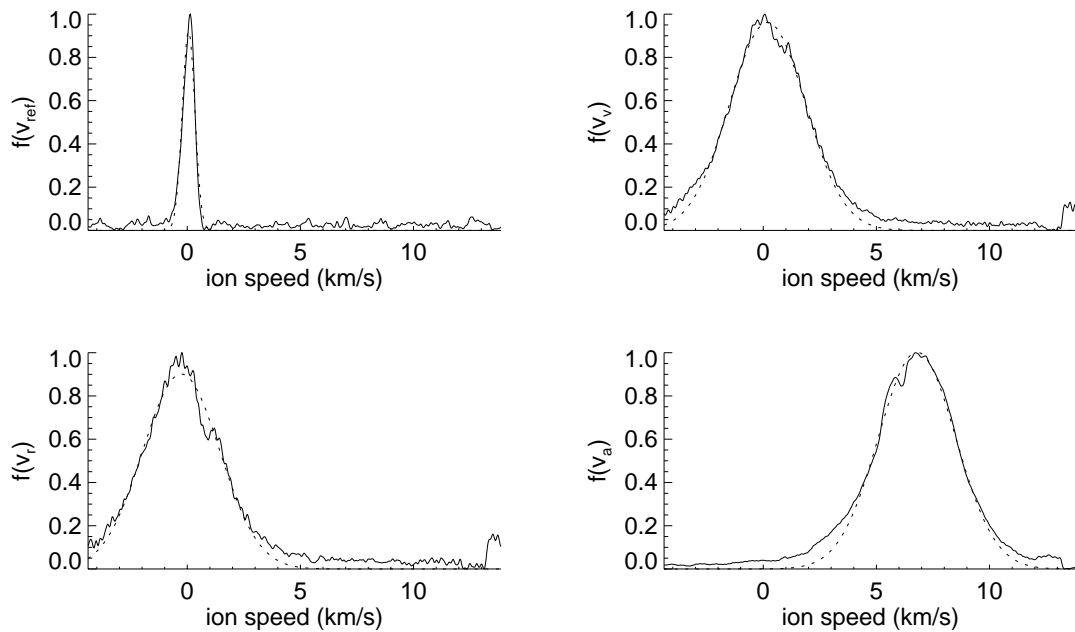


Figure C.40: Deconvolved $f(v)$ & curve-fit at TH15 w/ neutralizer, $(x, y) = (15.004, 0.00)$ cm (th15x12).

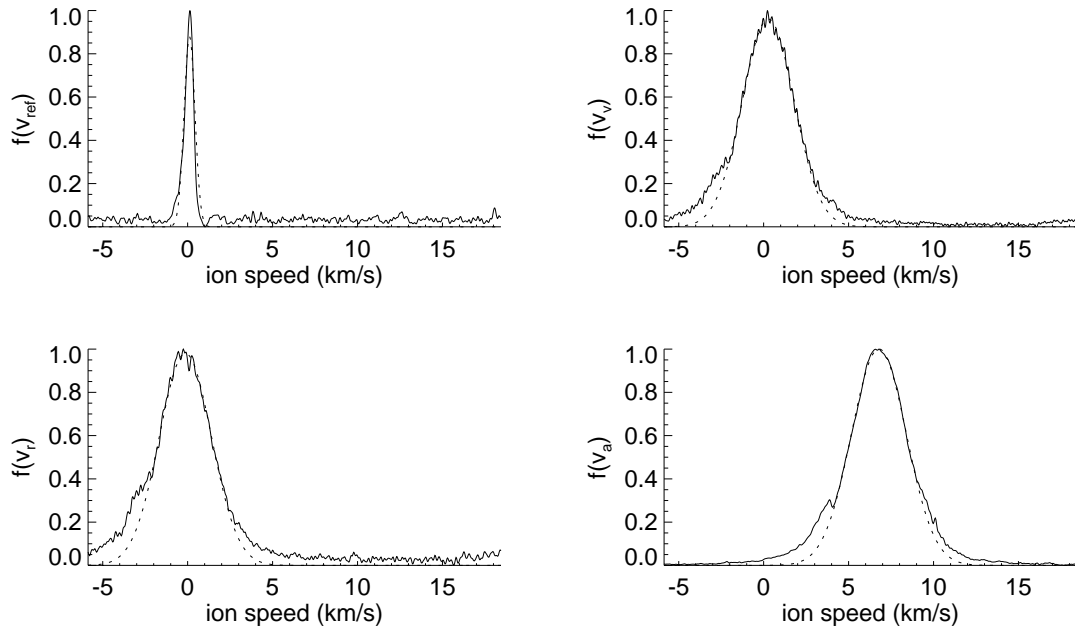


Figure C.41: Deconvolved $f(v)$ & curve-fit at TH15 w/ neutralizer, $(x, y) = (15.004, 0.00)$ cm (th15x13).

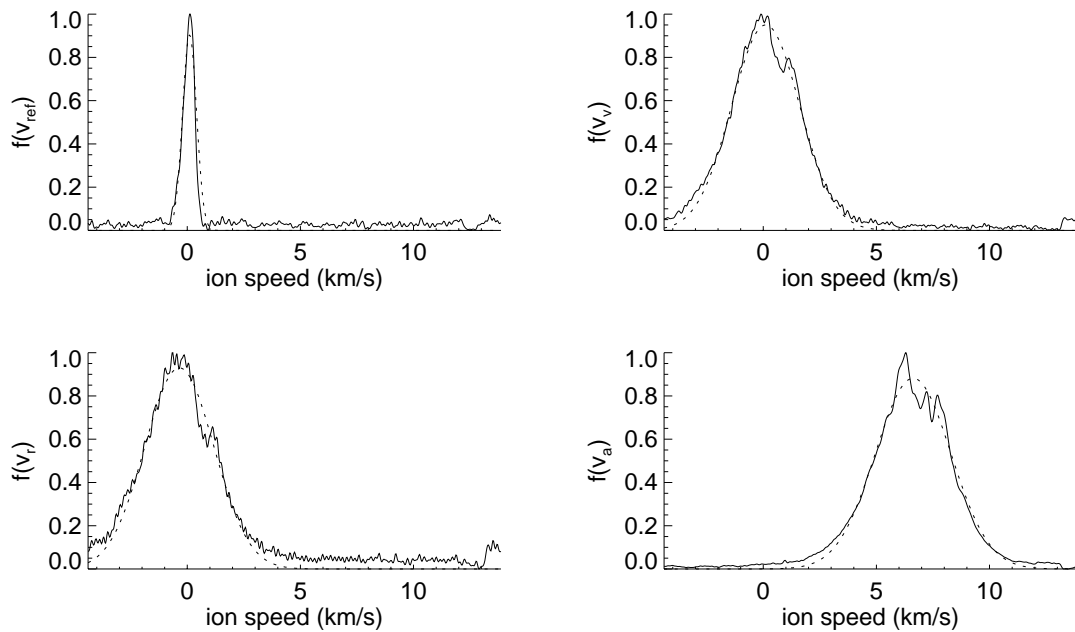


Figure C.42: Deconvolved $f(v)$ & curve-fit at TH15 w/ neutralizer, $(x, y) = (30.013, 0.00)$ cm (th15x14).

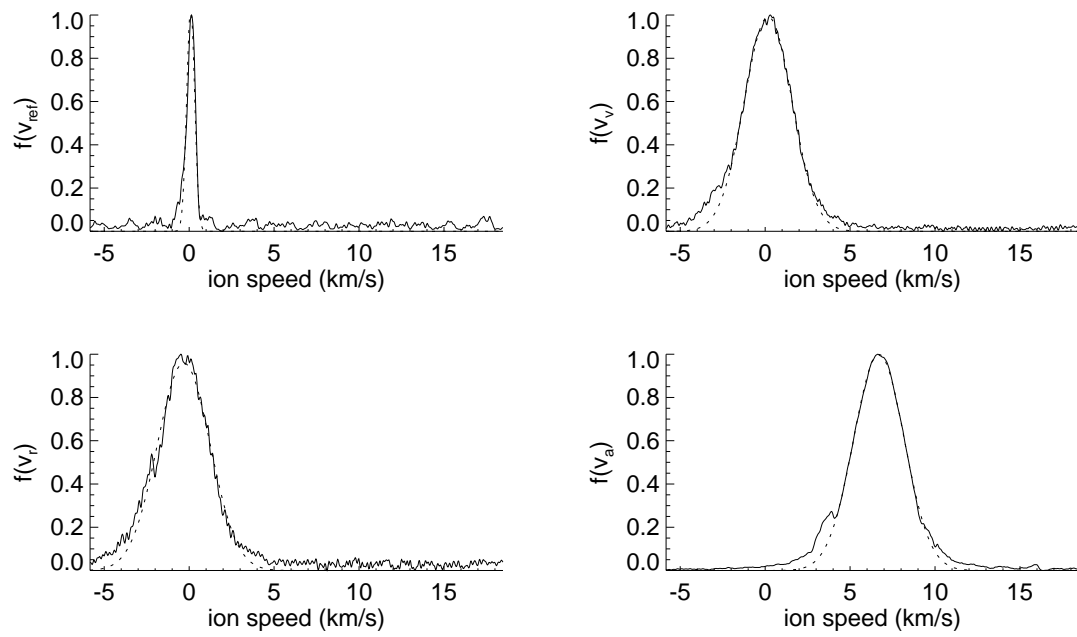


Figure C.43: Deconvolved $f(v)$ & curve-fit at TH15 w/ neutralizer, $(x, y) = (30.013, 0.00)$ cm (th15x15).

C.1.3 TH19 with neutralizer

Figures C.44 through C.58 show velocity distributions taken 0.142 and 5.09 cm downstream of the FMT-2 accelerator grid. The solid line is the deconvolved distribution, while the dashed line is a Maxwellian curve-fit to a user-defined area.

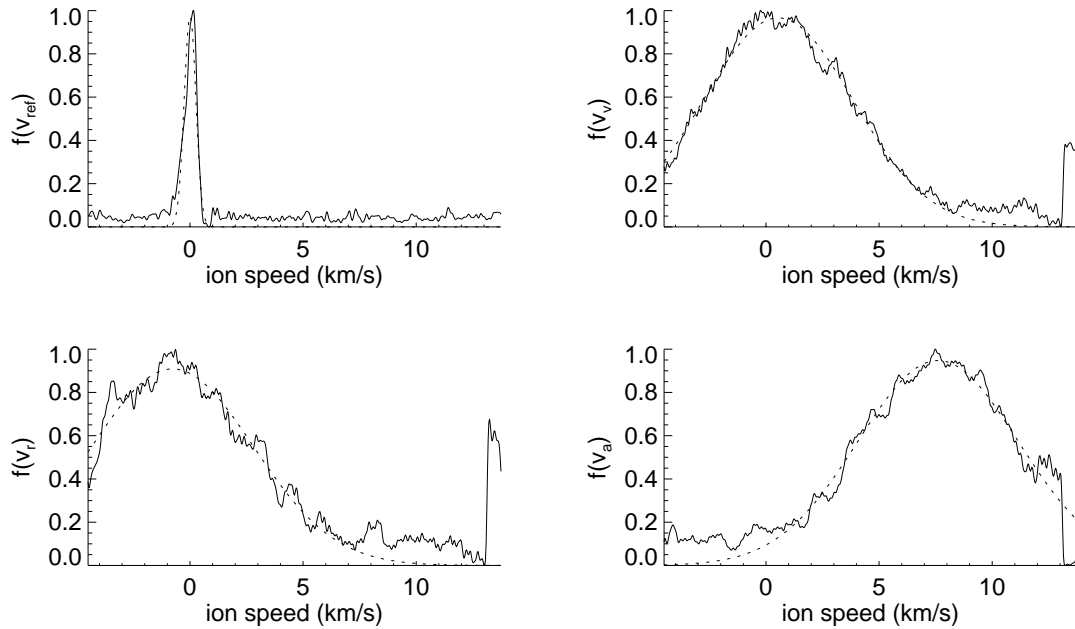


Figure C.44: Deconvolved $f(v)$ & Maxwellian curve-fit at TH19 w/ neutralizer, $(x, y) = (5.10, 10.160)$ cm (th19i1).

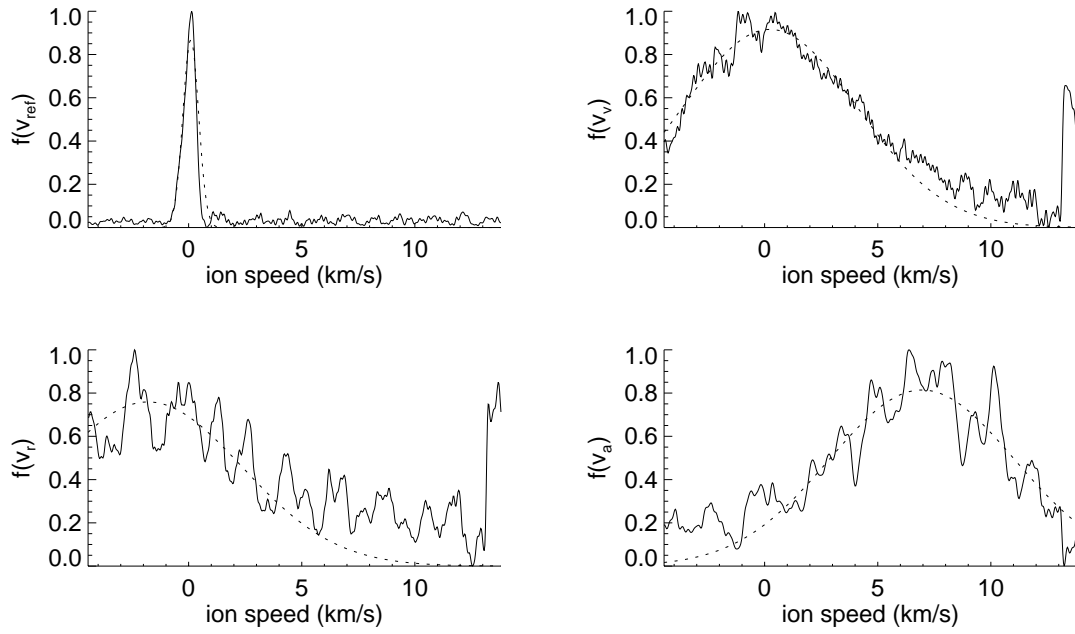


Figure C.45: Deconvolved $f(v)$ & Maxwellian curve-fit at TH19 w/ neutralizer, $(x, y) = (5.10, 11.430)$ cm (th19j).

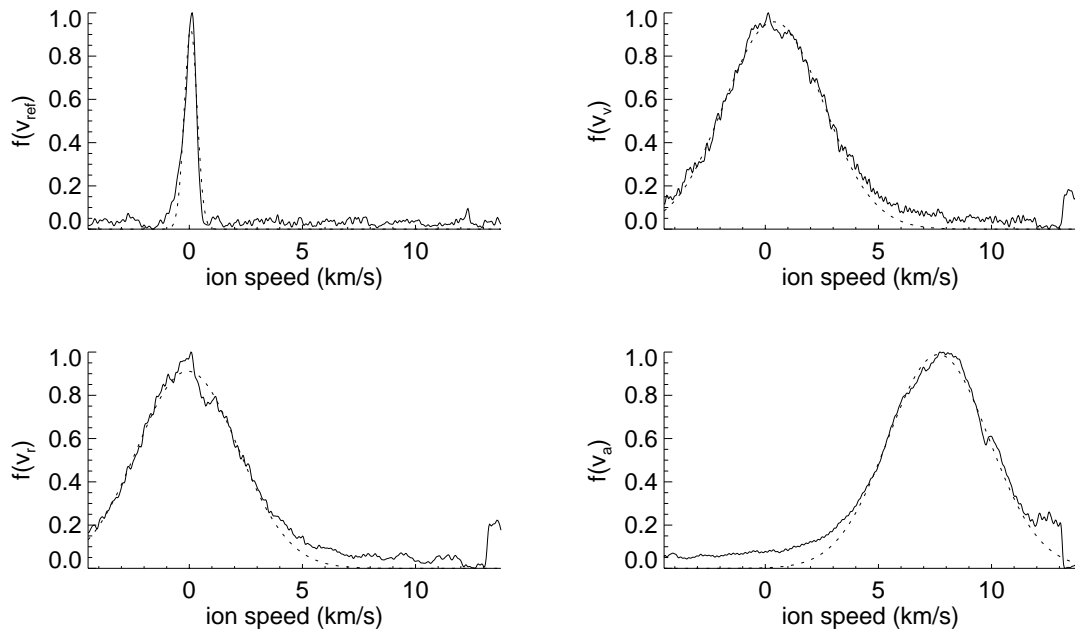


Figure C.46: Deconvolved $f(v)$ & Maxwellian curve-fit at TH19 w/ neutralizer, $(x, y) = (5.10, 0.000)$ cm (th19l).

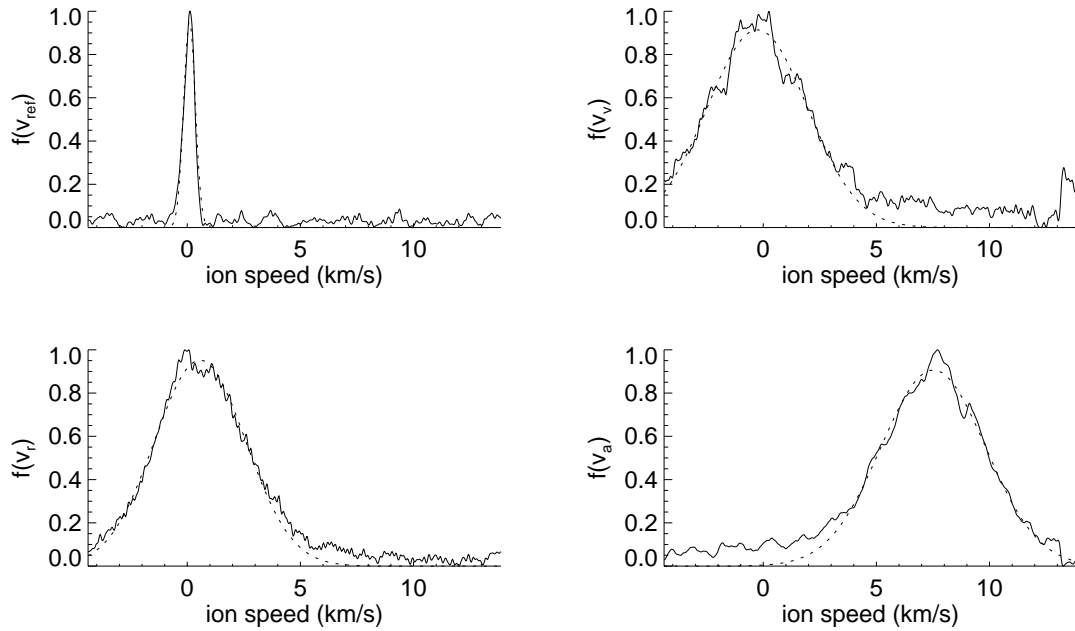


Figure C.47: Deconvolved $f(v)$ & Maxwellian curve-fit at TH19 w/ neutralizer, $(x, y) = (5.10, 5.080)$ cm (th19m).

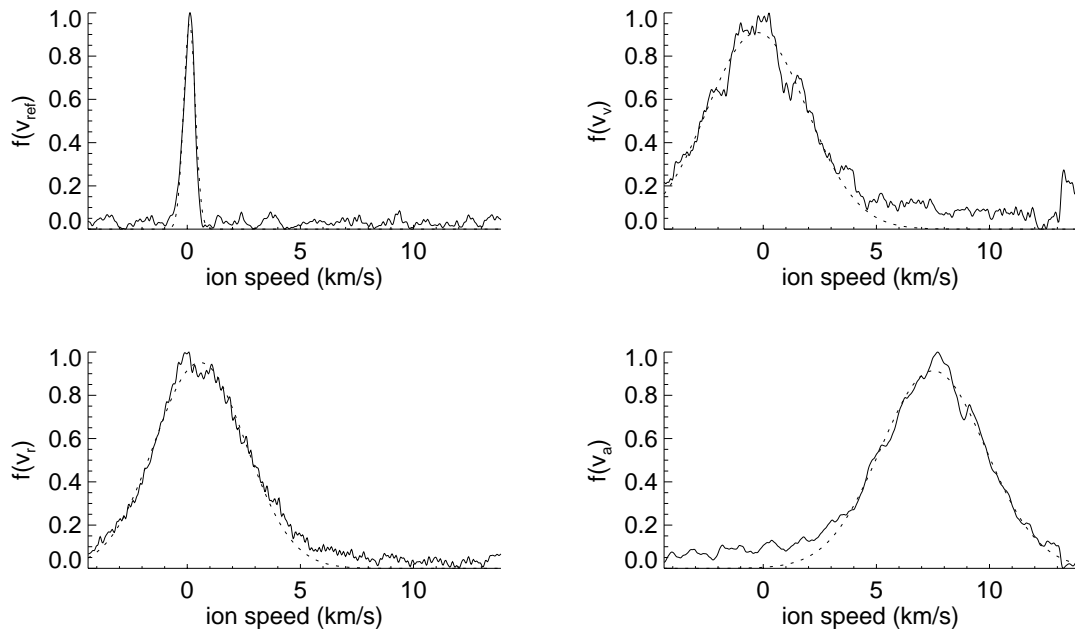


Figure C.48: Deconvolved $f(v)$ & Maxwellian curve-fit at TH19 w/ neutralizer, $(x, y) = (0.14, 0.254)$ cm (th19n0).

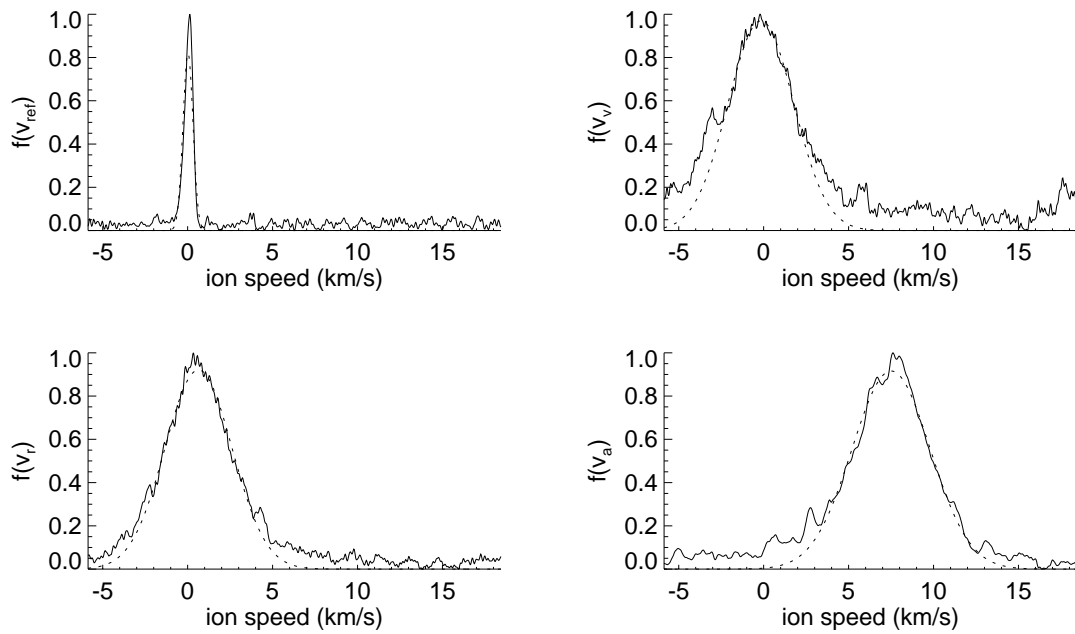


Figure C.49: Deconvolved $f(v)$ & Maxwellian curve-fit at TH19 w/ neutralizer, $(x, y) = (0.14, 0.254)$ cm (th19n1).

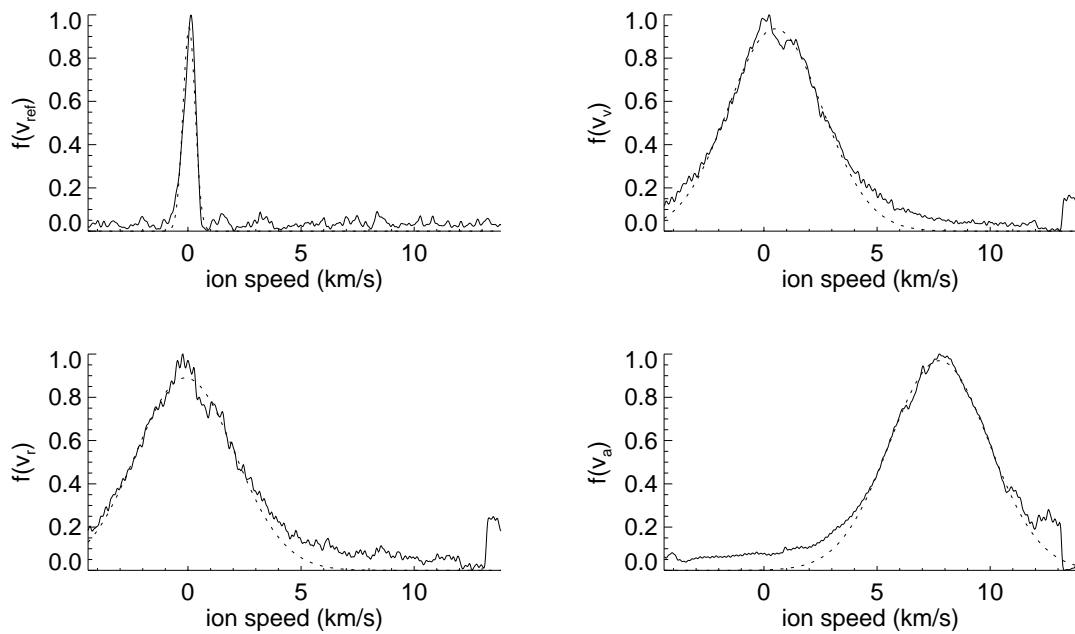


Figure C.50: Deconvolved $f(v)$ & Maxwellian curve-fit at TH19 w/ neutralizer, $(x, y) = (0.14, 1.270)$ cm (th19o).

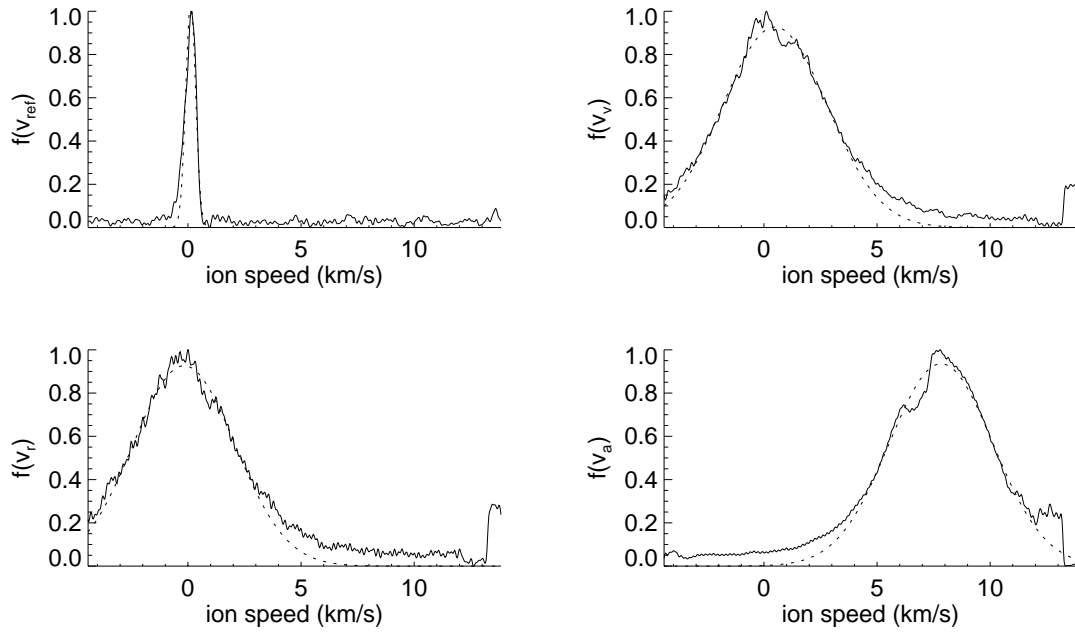


Figure C.51: Deconvolved $f(v)$ & Maxwellian curve-fit at TH19 w/ neutralizer, $(x, y) = (0.14, 2.616)$ cm (th19p).

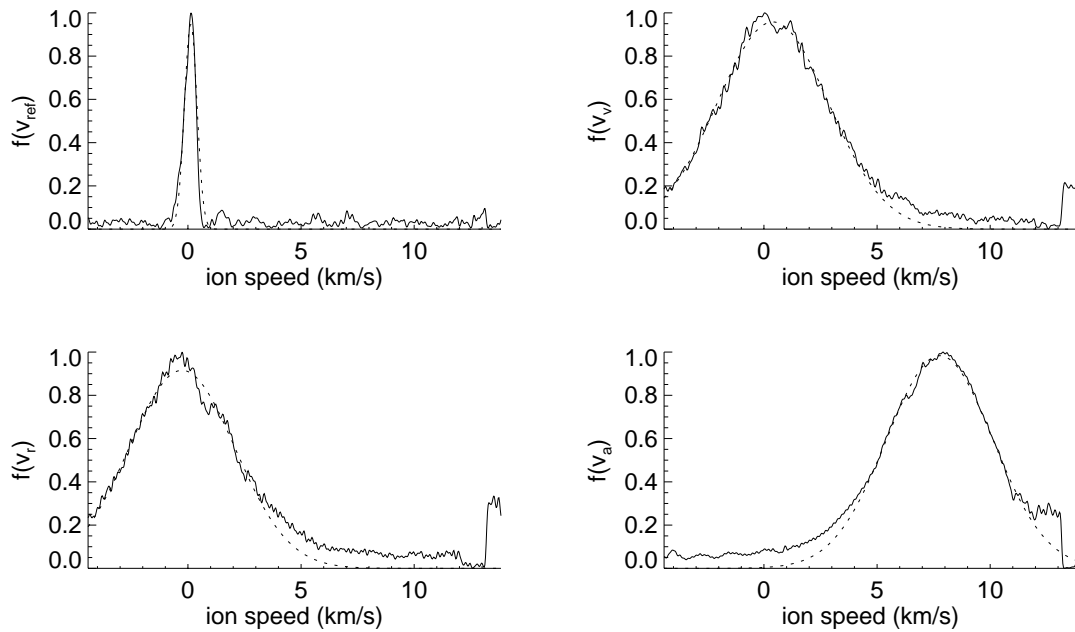


Figure C.52: Deconvolved $f(v)$ & Maxwellian curve-fit at TH19 w/ neutralizer, $(x, y) = (0.14, 3.759)$ cm (th19q).

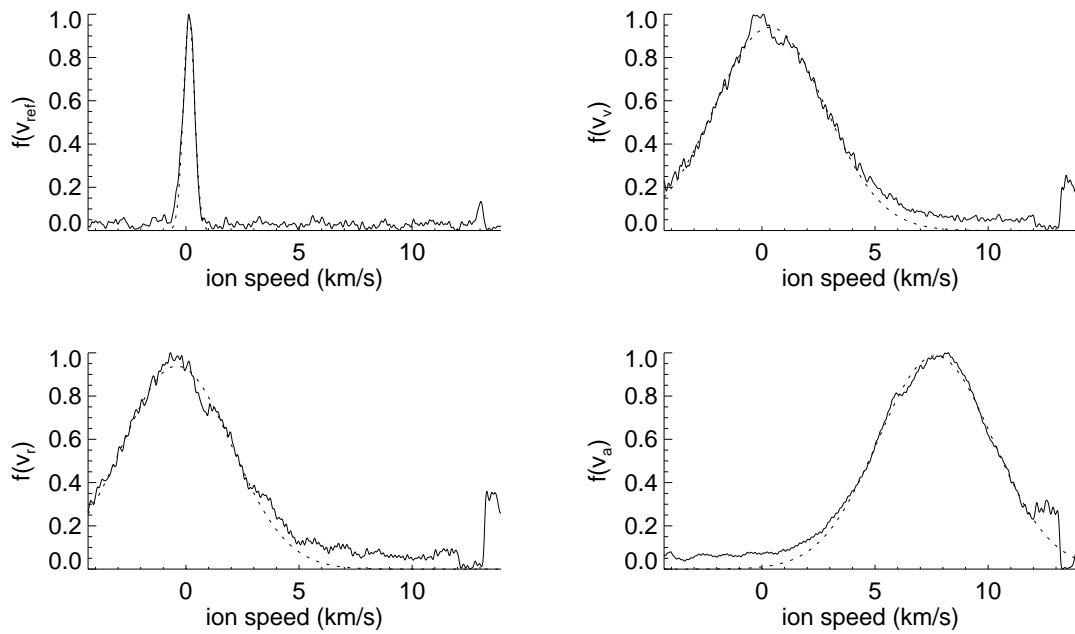


Figure C.53: Deconvolved $f(v)$ & Maxwellian curve-fit at TH19 w/ neutralizer, $(x, y) = (0.14, 5.131)$ cm (th19r0).

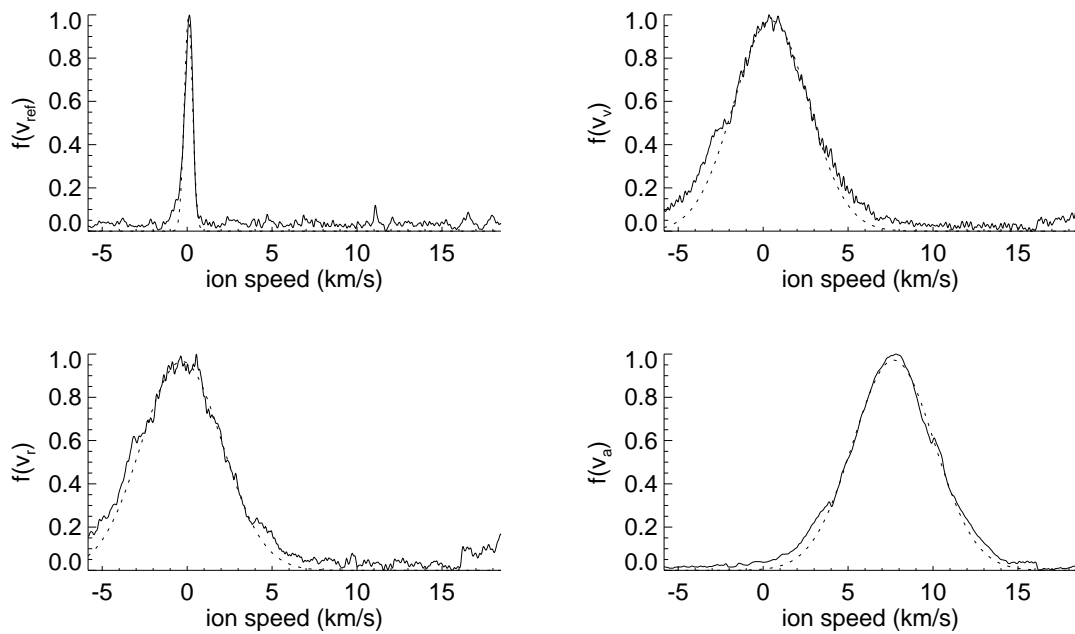


Figure C.54: Deconvolved $f(v)$ & Maxwellian curve-fit at TH19 w/ neutralizer, $(x, y) = (0.14, 5.131)$ cm (th19r1).

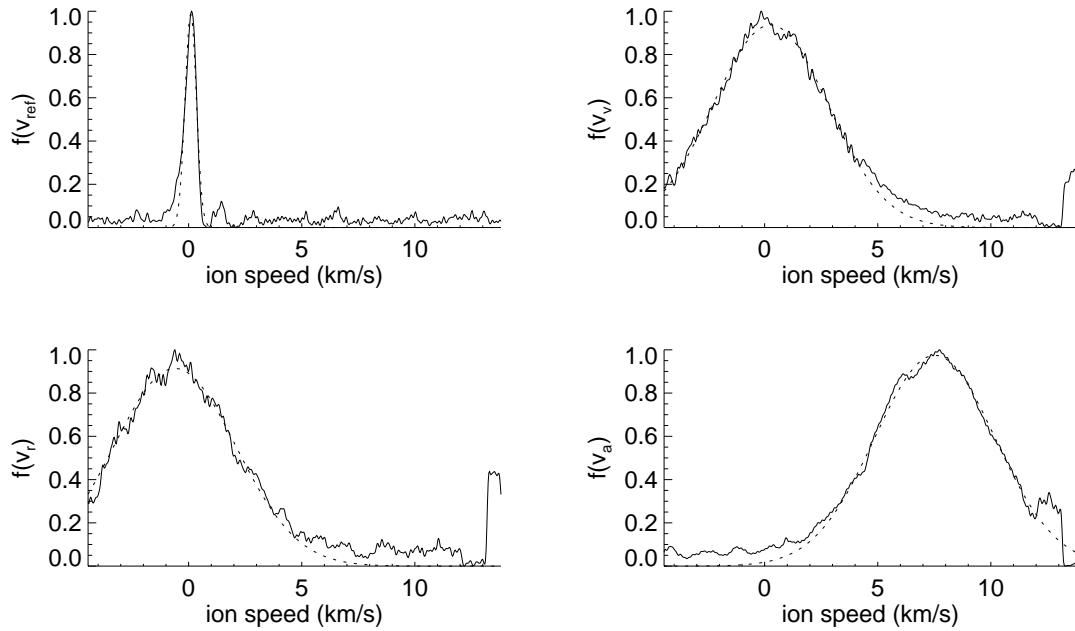


Figure C.55: Deconvolved $f(v)$ & Maxwellian curve-fit at TH19 w/ neutralizer, $(x, y) = (0.14, 6.299)$ cm (th19s).

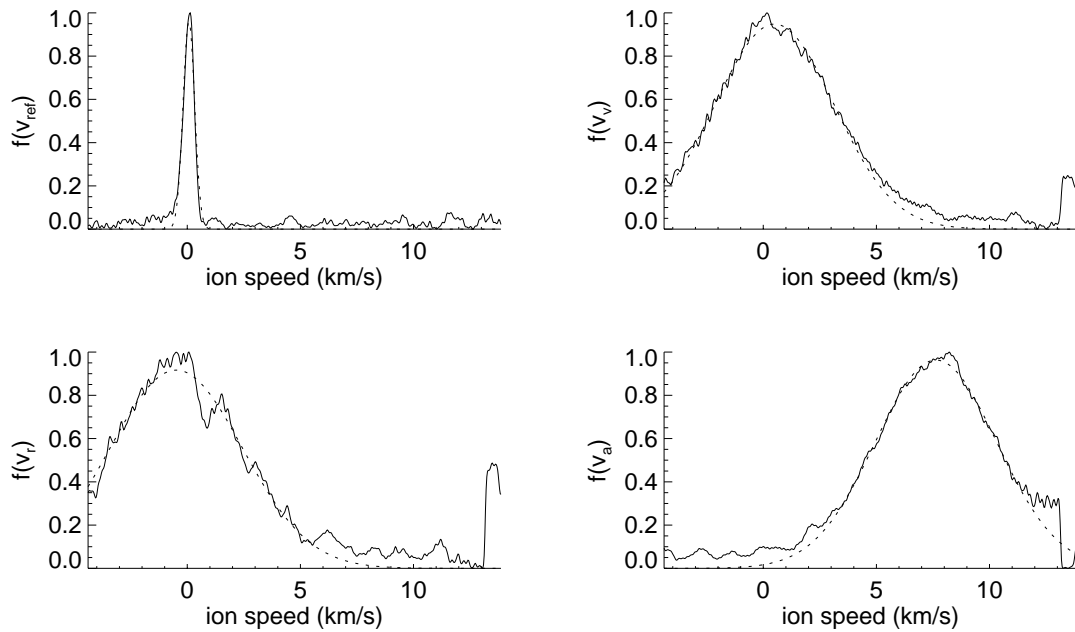


Figure C.56: Deconvolved $f(v)$ & Maxwellian curve-fit at TH19 w/ neutralizer, $(x, y) = (0.14, 7.671)$ cm (th19t).

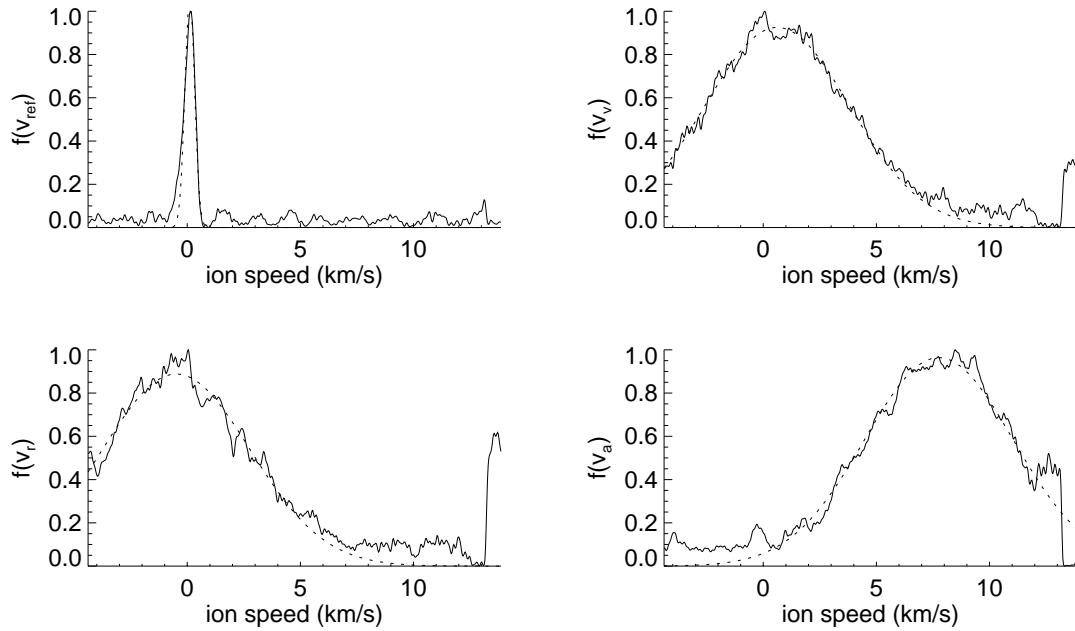


Figure C.57: Deconvolved $f(v)$ & Maxwellian curve-fit at TH19 w/ neutralizer, $(x, y) = (0.14, 8.839)$ cm (th19u).

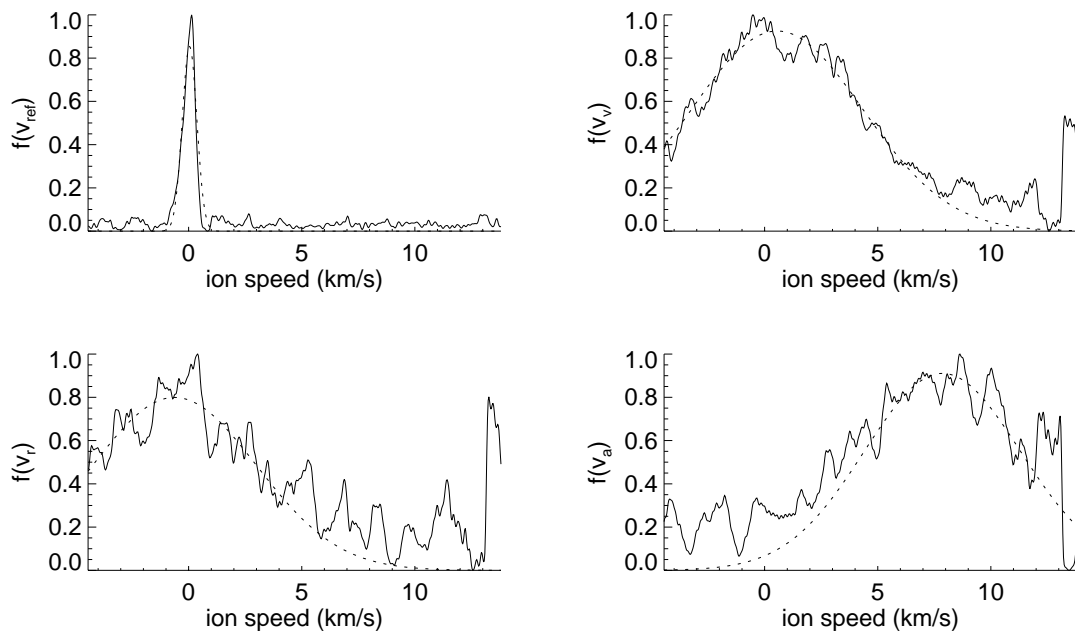


Figure C.58: Deconvolved $f(v)$ & Maxwellian curve-fit at TH19 w/ neutralizer, $(x, y) = (0.14, 10.185)$ cm (th19v).

BIBLIOGRAPHY

BIBLIOGRAPHY

- [1] F. Dyson. *Disturbing the Universe*. Harper & Row, 1979, p. 9.
- [2] R. Koslover and R. McWilliams. "Measurement of multidimensional ion velocity distributions by optical tomography." *Review of Scientific Instruments* **57**(1986) 2441-2448.
- [3] R. A. Dressler, J. P. M. Beijers, H. Meyer, S. M. Penn, V. M. Bierbaum and S. R. Leone. "Laser probing of ion velocity distributions in drift fields: Parallel and perpendicular temperatures and mobility for Ba⁺ in He." *Journal of Chemical Physics* **89**(1988) 4707-4715.
- [4] M. Zintl and R. McWilliams. "Improved optical tomography device." *Review of Scientific Instruments* **65**(1994) 2574-2579.
- [5] D. A. Edrich, R. McWilliams and N. S. Wolf. "Single beam laser induced fluorescence technique for plasma transport measurements." *Review of Scientific Instruments* **67**(1996) 2812-2817.
- [6] N. Sadeghi, N. Dorval, J. Bonnet, D. Pigache, C. Kadlec-Phillipe, and A. Bouchoule. "Velocity measurement of Xe⁺ in stationary plasma thruster using LIF." In *Proceedings of the 35th Joint Propulsion Conference*. AIAA-99-2429, June 1999.
- [7] R. J. Cedolin, W. A. Hargus, P. V. Storm, R. K. Hanson and M. K. Cappelli. "Laser-induced fluorescence study of a xenon Hall thruster." In *Proceedings of the 33rd Joint Propulsion Conference*. AIAA-97-3053, July 1997.
- [8] R. J. Cedolin, W. A. Hargus, P. V. Storm, R. K. Hanson and M. K. Cappelli. "Laser-induced fluorescence study of a xenon Hall thruster." *Applied Physics B* **65**(1997) 459-469.
- [9] R. J. Cedolin. *Laser-induced fluorescence diagnostics of xenon plasmas*. Ph.D. dissertation, Dept. of Mechanical Engineering, Stanford University, June 1997.
- [10] D. Keefer. "Multiplexed LIF and Langmuir probe diagnostic measurements in the TAL D-55 thruster." In *Proceedings of the 35th Joint Propulsion Conference*. AIAA-99-2425, June, 1999.

- [11] G. J. Williams Jr., T. B. Smith, F. S. Gulczinski III, B. E. Beal, A. D. Gallimore, and R. P. Drake. "Laser induced fluorescence measurement of ion velocities in the plume of a Hall effect thruster." In *Proceedings of the 35th Joint Propulsion Conference*. AIAA-99-2424, June 1999.
- [12] G. J. Williams Jr. "The use of laser-induced fluorescence to characterize discharge cathode erosion in a 30 cm ring-cusp ion thruster." Ph.D. dissertation, Dept. of Aerospace Engineering, University of Michigan, October 2000.
- [13] W. A. Hargus Jr and M. A. Cappelli. "Laser-induced fluorescence measurements of velocity within a Hall discharge." *Applied Physics B* **B72**(2001) 961-969.
- [14] W. A. Hargus Jr. *Investigation of the plasma acceleration mechanism within a coaxial Hall thruster*. Ph.D. dissertation, Dept. of Mechanical Engineering, Stanford University, March 2001.
- [15] R. H. Smith. Personal communication, 1974.¹
- [16] J. C. Maxwell. "Illustrations of the dynamical theory of gases. I. On the motions and collisions of perfectly elastic spheres." *Philosophical Magazine* **19**(1860) 19-32. Quoted by T. I. Gombosi. *Gaskinetic Theory*. Cambridge University Press, 1994, p. 57.
- [17] R. H. Goddard. "Report on conditions for minimum mass of propellant," 27 August 1929. In *The Papers of Robert H. Goddard*, E. C. Goddard and G. E. Pendray, ed. McGraw-Hill, 1970.
- [18] E. B. Wilson Jr. *An Introduction to Scientific Research*. McGraw-Hill, 1952, p. 2.
- [19] E. Stuhlinger. Ch. 1 in *Ion Propulsion for Space Flight*. McGraw-Hill, 1964.
- [20] W. E. Burrows. Ch. 6 in *This New Ocean: the Story of the First Space Age*. Random House, 1999.
- [21] R. G. Jahn. *Physics of Electric Propulsion*. McGraw-Hill, 1968.
- [22] R. Myers. "Overview of electric propulsion activities in industry." In *Proceedings of the 36th Joint Propulsion Conference*. AIAA-00-3147, July 2000. Quoted in [12], p. 3.
- [23] G. P. Sutton. *Rocket Propulsion Elements: An Introduction to the Engineering of Rockets*. 6th ed., Wiley-Interscience, 1992.
- [24] J. E. Polk, et al. "An Overview of the Results from an 8200 Hour Wear Test of the NSTAR Ion Thruster." In *Proceedings of the 35th Joint Propulsion Conference*. AIAA-99-2446, June 1999.

¹Actually, she said "Just because everybody else is doing it doesn't mean you should do it, too." Your mom probably said something similar.

- [25] F. F. Chen. *Introduction to Plasma Physics and Controlled Fusion: Plasma Physics*. 2nd ed., Plenum Publishing, 1984.
- [26] H. R. Kaufman. "Technology of closed-drift thrusters." *AIAA Journal* **23**(1983) 78-87.
- [27] R. R. Hofer and R. S. Jankovsky. "A Hall thruster performance model incorporating the effects of a multiply-charged plasma." In *Proceedings of the 37th Joint Propulsion Conference*. AIAA-01-3322, July 2001.
- [28] E. Y. Choueiri. "Plasma oscillations in Hall thrusters." *Physics of Plasmas* **8**(2001) 1411-1426.
- [29] J. F. James. *A Student's Guide to Fourier Transforms with Applications in Physics and Engineering*. Cambridge University Press, 1995, p.ix.
- [30] R. N. Bracewell. *The Fourier Transform and Its Applications*. McGraw-Hill, 1965.
- [31] B. R. Frieden. "Image enhancement and restoration." Ch. 5 in *Topics in Applied Physics: Picture Processing and Digital Filtering*, T. S. Huang, ed. Springer-Verlag, 1975.
- [32] R. N. Bracewell. "Restoration in the presence of errors." *Proceedings of the Institute of Radio Engineers* **46**(1958) 106-111.
- [33] C. W. Helstrom "Image restoration by the method of least squares." *Journal of the Optical Society of America* **57**(1967) 297-303.
- [34] N. Wiener. *Extrapolation, Interpolation and Smoothing of Stationary Time Series*. John Wiley & Sons, 1949. Cited in [32] and [33].
- [35] J. Conrad. *Lord Jim*. Doubleday & McClure, 1900.
- [36] C. H. Townes. *How the Laser Happened : Adventures of a Scientist* Oxford University Press, 1999.
- [37] N. Taylor. *Laser : the Inventor, the Nobel Laureate, and the Thirty-Year Patent War* Simon & Schuster, 2000.
- [38] T. H. Maiman. "Stimulated optical radiation in ruby." *Nature* **187**(1960) 493.
- [39] A. Javan, W. R. Bennett Jr., and D. R. Herriott. "Population inversion and continuous optical maser oscillation in a gas discharge containing a He-Ne mixture." *Physical Review Letters* **6**(1961), 106-110.
- [40] O. B. Peterson, S. A. Tuccio, and B. B. Snavely. "CW operation of an organic dye solution laser." *Applied Physics Letters* **17**(1970), 245-247. Cited in [42].
- [41] P. K. Runge and R. Rosenberg. "Unconfined flowing-dye films for cw dye lasers." *IEEE Journal of Quantum Electronics* **QE-8**(1970) 910-911. Cited in [42].

- [42] L. Hollberg. "CW dye lasers." Ch. 5 in *Dye Laser Principles: With Applications*. Academic Press, 1990.
- [43] W. Demtröder. *Laser Spectroscopy: Basic Concepts and Instrumentation*. Springer-Verlag, 1996.
- [44] A. Yariv. *Quantum Electronics*. 3rd ed., Wiley, 1989.
- [45] M. Zimmerman and R. B. Miles. "Hypersonic-helium-flowfield measurements with the resonant Doppler velocimeter." *Applied Physics Letters* **37**(1980), 885-887.
- [46] D. A. Erwin, G. C. Pham-Van-Diep and W. D. Dieninger. "Laser-induced fluorescence measurements of flow velocity in high-power arcjet thruster plumes." *AIAA Journal* **29**(1991), 1298-1303.
- [47] J. G. Liebeskind, R. K. Hanson and M. K. Cappelli. "Velocity measurements in a hydrogen arcjet using LIF." In *Proceedings of the 24th AIAA Plasmadynamics and Lasers Conference*. AIAA-91-2112, June 1991.
- [48] J. G. Liebeskind, D. H. Manzella, C. R. Ruthling, R. K. Hanson and M. K. Cappelli. "Optical diagnostics of a low power hydrogen arcjet." In *Proceedings of the 22nd International Electric Propulsion Conference*. IEPC-91-091, October 1991.
- [49] J. G. Liebeskind, R. K. Hanson and M. K. Cappelli. "LIF measurements of species velocities in an arcjet plume." In *Proceedings of the 22nd International Electric Propulsion Conference*. IEPC-91-091, October 1991.
- [50] J. G. Liebeskind, R. K. Hanson and M. K. Cappelli. "LIF of atomic H in an arcjet thruster." In *Proceedings of the 30th AIAA Aerospace Sciences Meeting*. AIAA-92-0678, January 1992.
- [51] J. G. Liebeskind, R. K. Hanson and M. K. Cappelli. "Flow diagnostics of an arcjet using laser-induced fluorescence." In *Proceedings of the 28th Joint Propulsion Conference*. AIAA-92-3243, July 1992.
- [52] J. G. Liebeskind, R. K. Hanson and M. K. Cappelli. "Laser-induced fluorescence diagnostic for temperature and velocity measurements in a hydrogen arcjet plume." *Applied Optics* **32**(1993) 6117-6127.
- [53] D. Keefer et al. "Multiplexed laser induced fluorescence and non-equilibrium processes in arcjets." In *Proceedings of the 25th AIAA Plasmadynamics and Lasers Conference*. AIAA-94-2656, July 1992.
- [54] J. A. Pobst and I. J. Wysong. "Laser induced fluorescence of ground state hydrogen atoms at nozzle exit of an arcjet plume." In *Proceedings of the 26th AIAA Plasmadynamics and Lasers Conference*. AIAA-95-1973, June 1995.
- [55] C. J. Gaeta, R. S. Turley, J. N. Matossian, J. R. Beattie and W. S. Williamson. "Plasma erosion rate diagnostics using laser-induced fluorescence." *Review of Scientific Instruments* **63**(1992) 3090-3095.

- [56] C. J. Gaeta, J. N. Matossian, R. S. Turley, J. R. Beattie, J. D. Williams and W. S. Williamson. "Erosion rate diagnostics in ion thrusters using laser-induced fluorescence." *Journal of Propulsion and Power* **9**(1993) 369-376.
- [57] D. H. Manzella. "Stationary plasma thruster ion velocity distribution." In *Proceedings of the 30th Joint Propulsion Conference*. AIAA-94-3141, June 1994.
- [58] G. J. Williams Jr., T. B. Smith, M. T. Domonkos, K. J. Shand, A. D. Gallimore and R. P. Drake. "Laser induced fluorescence measurement of ion emitted from hollow cathode." In *Proceedings of the 35th Joint Propulsion Conference*. AIAA-99-2862, June 1999.
- [59] J. E. Pollard and E. J. Beiting. "Measurements of xenon ion velocities of the SPT-140 using laser induced fluorescence." In *Proceedings of the 3rd International Conference on Spacecraft Propulsion*. ESA-SP-465, Oct 2000, 789-797.
- [60] N. Dorval, J. Bonnet, J. P. Marque and D. Pigache. "Laser induced fluorescence measurements in xenon plasma thrusters." In *Proceedings of the 3rd International Conference on Spacecraft Propulsion*. ESA-SP-465, Oct 2000, 797-805. Quoted in [61].
- [61] N. Dorval, J. Bonnet, J. P. Marque, E. Rosencher, S. Chable, F. Rogier and P. Lasgorceix. "Determination of the ionization and acceleration zones in a stationary plasma thruster by optical spectroscopy study: Experiments and model." *Journal of Applied Physics* **91**(2002) 4811-4817.
- [62] J. E. Hansen and W. Persson. "Revised analysis of singly ionized xenon, Xe II." *Physica Scripta* **36**(1987) 602-643.
- [63] G. Herzberg. *Atomic Spectra and Atomic Structure*. 2nd ed., Dover, 1944, p.65.
- [64] W. C. Martin and W. L. Wiese. "Atomic spectroscopy: an introduction." Ch. 10 in *Atomic, Molecular and Optical Physics Handbook*, G. W. F. Drake, ed. AIP Press, 1996. Web version ;<http://sed.nist.gov/Pubs/AtSpec/total.html>;
- [65] S. Svanberg. *Atomic and Molecular Spectroscopy: Basic Aspects and Practical Applications*. 3rd ed., Springer-Verlag, 2001.
- [66] N. V. Vitanov, B. W. Shore, L. Yatsenko, K. Böhmer, T. Halfmann, T. Rickes, and K. Bergmann. "Power broadening revisited: theory and experiment." *Optics Communications* **199** (2001) 117-126.
- [67] E. Browne. *Table of Isotopes*, C. M. Lederer and V. S. Shirley, ed. 7th ed., Wiley, 1978.
- [68] H. Kopfermann. *Nuclear Moments*. Academic Press, 1958.
- [69] C. C. Candler. *Atomic Spectra and the Vector Model*. Van Nostrand, 1964.

- [70] S. D. Rosner, T. D. Gaily, and R. A. Holt. "Laser-fluorescence ion-beam magnetic resonance: Xe⁺ hyperfine structure." *Physical Review Letters* **40**(1978) 851-853.
- [71] C. R. Bingham, M. L. Gaillard, D. J. Pegg, H. K. Carter, R. L. Mlekodaj, J. D. Cole, and P. M. Griffin. "Collinear fast-beam laser spectroscopy experiment: measurement of hyperfine structure and isotope shifts in Xe II." *Nuclear Instruments and Methods* **202**(1982) 147-152.
- [72] G. Borghs, P. De Bisschop, R. E. Silerans, M. Van Hove, and J. M. Van den Cruyce. "Hyperfine structures and isotope shifts of the $5d^4 D_{7/2} - 6p^4 P_{5/2}^0$ transition in xenon ions." *Zeitschrift fur Physik A* **299**(1981) 11-13.
- [73] L. Bröstrom, A. Kastberg, J. Lidberg, and S. Mannervik. "Hyperfine-structure measurements in Xe II." *Physical Review A* **53**(1996) 109-112.
- [74] L. Bröstrom, S. Mannervik, A. Passian and G. Sundström. "Investigation of some transitions and lifetimes in Xe II." *Physical Review A* **49**(1994) 3333-3337.
- [75] P. A. Jansson. *Deconvolution of images and spectra*. Academic Press, 1997.
- [76] G. Arfken. *Mathematical Methods for Physicists*. Academic Press, 1966.
- [77] J. T. Verdeyen. *Laser Electronics*. 3rd ed., Prentice-Hall, 1995.
- [78] J. O. Berg and W. L. Shackelford. "Rotational redistribution effect on saturated laser-induced fluorescence." *Applied Optics* **18**(1979) 2093-2094.
- [79] A. C. Eckbreth. *Laser Diagnostics for Combustion Temperature and Species*. Overseas Publishers Association, 1996.
- [80] R. C. Hilborn. "Einstein coefficients, cross sections, f values, dipole moments, and all that." *American Journal of Physics* **50**(1982) 982-986.
- [81] S. L. Kaufman. "High-resolution laser spectroscopy in fast beams." *Optics Communications* **17**(1976) 309-312.
- [82] T. B. Smith, D. A. Herman, A. D. Gallimore, and R. P. Drake. "Deconvolution of axial velocity distributions from Hall thruster LIF spectra." In *Proceedings of the 27th International Electric Propulsion Conference*. IEPC-01-0019, October 2001.
- [83] T. S. Geisel. *How the Grinch Stole Christmas*. Random House, 1957.
- [84] C. S. Ruf. Personal communication, 2002.
- [85] E. Nesbit. *The Magic City*. MacMillan, 1910. Quoted in [1].
- [86] J. M. Haas. "Performance characteristics of a 5 kw laboratory Hall thruster." *Low-perturbation interrogation of the internal and near-field plasma structure of a Hall thruster using a high-speed probe positioning system*. Ph.D. dissertation, Dept. of Aerospace Engineering, University of Michigan, January 2001.

- [87] S. Dushman. *Scientific Foundations of Vacuum Technique*, vol 4. John Wiley & Sons, 1958.
- [88] J. M. Haas, F. S. Gulczinski III, A. D. Gallimore, G. G. Spanjers, and R. A. Spores. "Performance characteristics of a 5 kw laboratory Hall thruster." In *Proceedings of the 34th Joint Propulsion Conference*. AIAA 98-3503, July 1998.
- [89] B. E. Gilchrist, S. G. Bilen, E. Choiniere, A. D. Gallimore, and T. B Smith. "Analysis of chamber simulations of long collecting probes in high-speed, dense plasmas." *IEEE Transactions on Plasma Science* **30**, to be published in October 2002 issue.
- [90] H. W. Coleman and W. G. Steele Jr. *Experimentation and uncertainty analysis for engineers*. John Wiley & Sons, 1989.
- [91] F. S. Gulczinski and A. D. Gallimore. "Near-field ion energy and species measurements of a 5 kW laboratory Hall thruster." In *Proceedings of the 35th Joint Propulsion Conference*. AIAA 99-2430, June 1999.
- [92] F. S. Gulczinski. *Examination of the structure and evolution of ion energy properties of a 5 kw class laboratory Hall effect thruster at various operational conditions*. Ph.D. dissertation, Dept. of Aerospace Engineering, University of Michigan, August 1999.
- [93] G. R. Fowles. *Introduction to Modern Optics*. 2nd ed., Dover, 1975.
- [94] E. J. Beitung and J. E. Pollard. "Measurements of xenon ion velocities of the SPT-140 using laser-induced fluorescence." In *Proceedings of the 3rd International Conference on Spacecraft Propulsion*. ESA SP-465, 897-900, December 2000.
- [95] B. E. Beal, A. D. Gallimore and W. A. Hargus. "Preliminary plume characterization of a low-power Hall thruster cluster." In *Proceedings of the 38th Joint Propulsion Conference*. AIAA 02-4251, July 2002.

ABSTRACT

DECONVOLUTION OF ION VELOCITY DISTRIBUTIONS FROM LASER-INDUCED FLUORESCENCE SPECTRA OF XENON ELECTROSTATIC THRUSTER PLUMES

by

Timothy B. Smith

Chairperson: Associate Professor A.D. Gallimore

This thesis presents a method for extracting singly-ionized xenon (Xe II) velocity distribution estimates from single-point laser-induced fluorescence (LIF) spectra at 605.1 nm. Unlike currently-popular curve-fitting methods for extracting bulk velocity and temperature data from LIF spectra, this method makes no assumptions about the velocity distribution, and thus remains valid for non-equilibrium and counterstreaming plasmas.

The well-established hyperfine structure and lifetime of the $5d^4 D_{7/2} - 6p^4 P_{5/2}^0$ transition of Xe II provide the computational basis for a Fourier-transform deconvolution. Computational studies of three candidate deconvolution methods show that, in the absence of *a priori* knowledge of the power spectra of the velocity distribution and noise function, a Gaussian inverse filter provides an optimal balance between noise amplification and filter broadening.

Deconvolution of axial-injection and multiplex LIF spectra from the P5 Hall thruster plume yields near-field and far-field axial velocity distributions. Near-field LIF spectra provide velocity distributions that cannot be measured by probe-based methods, while far-field LIF spectra provide a basis for comparison with mass spectrometer data. Transforming far-field ion axial velocity distributions to an ion energy basis reproduces all Xe II features found in mass spectrometer data taken at the same location and conditions. Axial profiles of ion axial velocity show a zone of increasing velocity extending 20 cm downstream of the thruster exit plane, with decreasing velocity from 20 to 50 cm, and demonstrate repeatabilities within 2%. Vertical-beam LIF reveals unexpectedly strong interactions between counterflowing streams in the inward divergence region at the thruster centerline.

Deconvolution of multiplex LIF spectra taken from the FMT-2 ion engine plume provides beamwise velocity distributions from 1.4 mm to 30 cm. Axial profiles of axial velocity fail to disclose the location of the neutralization plane, while radial sweeps of axial velocity show no discernable trend. Radial profiles of radial velocity show increasing divergence with radial position.